DISS. ETH NO. 26761

Quantum information processing with mixed-species ion crystals

A thesis submitted to attain the degree of

DOCTOR OF SCIENCE of ETH ZÜRICH

(Dr. sc. ETH ZÜRICH)

presented by

MATTEO MARINELLI

MSc ETH Zurich

born on 19.11.1990

citizen of Italy

Abstract

Trapped ions are among the leading platforms for the realization of scalable quantum information processing (QIP). A hybrid system composed of different species of ions extends the control capabilities of the system by providing new capabilities and extra degrees of freedom. A significant advantage of using two species of ion is the ability to individually manipulate and read out the state of one ion species without disturbing the quantum information stored in the internal states of the other.

In this thesis I demonstrate different elements required for the control of mixed-species ion chains composed of calcium and beryllium ions. One of the main results is the first realization of repeated measurements of quantum correlations of two beryllium ions that preserve their quantum entanglement. This is possible by reading out a co-trapped calcium ion that has previously interacted with the beryllium ions. Real-time feedback of the classical control system allows us to prepare and retain entangled states for up to fifty measurement rounds. The measurements consist of a series of quantum gates between the three ions, which involve mixed-species gates between beryllium hyperfine states and calcium electronic states. Independent experiments, also described in this thesis, show mixed-species entangled state fidelities of 98.4(9)% for two ions, and 93.8(5)% for three ions. The low-crosstalk mixed-species operations demonstrated in this work can be useful in quantum error correction as well as quantum metrology.

The abilities of the classical control system and the precise control of mixed-species chains are further exploited to deterministically realize an arbitrary unitary operation on a single ion two-level system (qubit) using measurement-base quantum computing (MBQC). Within this framework, sequences of adaptive measurements on entangled states in a larger multi-qubit Hilbert space are used to realize quantum operations on the two-dimensional space of a single target qubit. As opposed to standard MBQC, entanglement is created on demand when needed in this thesis to minimize the additional resources required to control the target qubit. The work presented in this thesis provides the first not post-selected realization of single-qubit unitaries in the MBQC paradigm.

Future algorithms will involve the manipulation of multiple ion chains of different types whose structure is continuously reconfigured through transport and splitting/recombination. This thesis also discusses the characterization of transport and separation of single and mixed-species ion chains. It shows the reliable splitting of single-species chains composed of two ions with a residual motional excitation below 1.6 quanta for calcium and below 0.7 quanta for beryllium. Mixed-species transport and splitting are also investigated. However, more characterization is required to make these processes reliable.

Finally, this thesis also describes technical advancements in the software interface used for controlling and calibrating experiments. The interface consists of a low-level structure written in C++ that controls all the physical details of the apparatus, and provides a set of command structures that are independent of details of the physical setup and allow the users to write control scripts at a high level of abstraction. These tools are complemented by an improved graphical user interface that provides users with a significant degree of automation and sophisticated scheduling of calibration experiments through a Python-based scripting interface.

This is the second edition of the thesis, released on the 22$^{\text{th}}$ of May 2020. The first edition was released on the 25$^{\text{th}}$ of March 2020.

Riassunto

Gli ioni intrappolati rappresentano una delle piattaforme più promettenti per la realizzazione di un computer quantistico capace di risolvere problemi attualmente irrisolvibili. Le capacità di controllo del sistema quantistico possono essere estese tramite un approccio ibrido basato sull'utilizzo di diverse specie di ioni. In particolare, la possibilità di manipolare e misurare lo stato di ciascuna specie, senza influenzare l'informazione quantistica memorizzata nell'altra, rappresenta un vantaggio significativo di questo approccio.

In questa tesi sono discussi diversi requisiti necessari per il controllo di catene di ioni formate da calcio e berillio. Tra i risultati principali presentiamo il primo esperimento in grado di misurare ripetutamente le correlazioni quantistiche tra due ioni berillio preservando il loro stato di entanglement quantistico. Ciò è possibile attraverso la misura dello stato di uno ione calcio presente nella stessa trappola. L'informazione derivante dalla misura viene processata in tempo reale dal nostro sistema di controllo permettendo di stabilizzare gli stati di entanglement fino a cinquanta ripetizioni della misura. L'estrazione delle correlazioni è basata su sequenze di operazioni che sfruttano l'interazione tra due livelli iperfini del berillio e due livelli elettronici del calcio. L'accuratezza di queste operazioni, misurata con esperimenti specifici anch'essi discussi in questa tesi, si attesta attorno al 98.4(9)% per operazioni tra due ioni e attorno al 93.8(5)% per operazioni con tre ioni. Le tecniche utilizzate in questo esperimento possono essere direttamente impiegate per algoritmi di correzione quantistica e metrologia.

In un secondo esperimento dimostriamo la prima realizzazione deterministica di operazioni unitarie su un sistema a due livelli (qubit) nel formalismo di measurement-based quantum computing (MBQC). In quest'approccio, operazioni quantistiche vengono eseguite tramite sequenze di misure adattive su stati di entanglement estesi su molti qubit. A differenza dell'approccio definito nell'ambito di MBQC, nel nostro esperimento l'entanglement viene creato solamente quando necessario consentendo di diminuire il numero di risorse necessarie ad eseguire l'algoritmo. Anche in questo caso sfruttiamo le principali proprietà del nostro sistema di controllo e le tecniche di manipolazione di catene di ioni con specie differenti.

Esperimenti futuri, basati sulla tecnologia degli ioni intrappolati, richiederanno la manipolazione di molteplici catene di ioni la cui struttura sarà continuamente modificata attraverso sequenze di trasporto e separazione/ricombinazione. Per garantire la massima accuratezza delle operazioni è fondamentale ridurre il più possibile l'eccitazione meccanica derivante da imperfezioni sperimentali. Nell'arco di questa tesi abbiamo caratterizzato il trasporto e la separazione di catene di ioni formate da due ioni della stessa specie e di due specie diverse. Sebbene la separazione di specie differenti non sia ancora affidabile dimostriamo ottimi risultati per la separazione di catene con due ioni della stessa specie. Nel caso del berillio otteniamo eccitazioni residue inferiori a 0.7 quanti di moto, mentre per il calcio le eccitazioni sono inferiori a 1.6 quanti.

Per finire, questa tesi presenta dei progressi tecnici sull'interfaccia di programmazione utilizzata per la scrittura di esperimenti e per la calibrazione di parametri sperimentali. In particolare, viene descritta un'interfaccia di basso livello sviluppata in C++ che incapsula tutti i dettagli dell'apparato sperimentale garantendo la possibilità di programmare esperimenti ad un alto livello di astrazione. Questi strumenti sono combinati con un'interfaccia grafica migliorata che consente una maggiore automazione e una pianificazione sofisticata degli esperimenti di calibrazione attraverso un'interfaccia di scripting basata su Python.

Questa è la seconda edizione della tesi pubblicata il 22 Maggio 2020. La prima edizione è stat pubblicata il 25 Marzo 2020.

Acknowledgements

I've now been part of the group since the spring semester of 2013, first as a master student and later as a Ph.D. candidate. I have had the privilege to meet and work with almost every member that joined the group since its creation. Each one of you, with your own distinct character, contributed to a fantastic working environment that it is hard to find elsewhere.

Foremost I would like to thank Prof Jonathan Home. After a few days of work as a semester student, I had my first simulation of Rabi oscillations. One afternoon you came and enthusiastically spent an hour playing with plots and parameter giving me some insights about the physics of trapped ions. It was inspiring, and luckily it was not a unique event; you kept doing it until now even if the group grew larger. Your creativity and motivation were crucial for the work presented in this thesis. I reluctantly have to admit that your "good progress" on every single result that I thought was the final one, really improved the quality of my work. So thanks for all the discussions we had on physics but also on general topics.

I owe a lot to all the members, past and present of the segtrap experiment. I should really thank Vlad Negnevitsky, who has been my partner in most of the work discussed here. Every time I think about our data taking I remember of the Tony Abbot simulator, the disgusting smell of your garlic cream cheese that you ate every day at midnight, and your bottles full of Joylent (oh god, I cannot believe I'm mentioning that rubbish in my thesis). Aside from work, spending time with you has always been enjoyable and I had very interesting conversations on any possible topic. Karan Mehta also played a crucial role in the mixed-species experiment. I should really thank you for your insistence on discussing and understanding every small detail of the experiment. You made me re-think everything I thought I knew, and that really improved my knowledge. For the MBQC results, I should also thank Tanja Behrle. Since the beginning, you tirelessly worked with me on the setup and on the SDK code. You impressively learned a lot in a short time. The experimental system is now in good hands, just remember to remove "il foglietto di merda" when you load. Aside from work, I have had a lot of fun with you. Thanks for sharing with me all the juicy gossips that you know I love discussing. Over the last few years, I also worked closely with Francesco Lancellotti, aka Mister Micromotion. You have been given a tough research project, but I'm sure that your work will enable great experiments. I cannot recall all the 2D plots we have been looking at together. If you are really going to put them all in your thesis, be sure to buy a stack of blue and yellow colors for the printer. Recently I have also been working with Brennan MacDonand-de Neeve. Thanks for taking over the burden of Ionizer and implementing all the new features that people desperately want. I should also thank you for making me lose so many games of kicker; it is impressive how much you suck. Okay, I'm joking! I owe a lot also to the past members of the segtrap team. Daniel Kienzler and Hsiang-Yu Lo, I always found your experience and knowledge very impressive. Thanks for your patience in teaching me how to run experiments and for helping me fix all the stupid mistakes I did at the beginning. I spent several nights with Ludwig deClerq trying to get the parallel gate paper. As I'm sure you remember, everything is awesome (oh no, now that song is stuck in my head...again). Many thanks also to Christa Fluehmann

that always took great care of the 729 setup. It has been fun working with you, even if we often did not agree on many things. I should also thank David Nadlinger. You have been working with us almost every day for a few years, and I cannot count the number of improvements you made to our setup, from the devil server to the death's code. Discussing with you has always been very stimulating. I will never forget that great coincidence (was it?) when one night you said: "guys, I'm just going to restart the devil server, nothing will change." As you pushed the enter button, the apocalypse started (no light, two broken fiber amplifiers, and one faulty seed laser). Finally, I should also thank Ben Keitch, who started all the technical work in our lab. I really wonder what the lab would look like if you were not there.

These were just the people that contributed to the segtrap experiment. The rest of the group has been crucial for other memories and for setting up a great environment. To thank you, I will go in order of office number so that I don't risk forgetting anyone. Many thanks to Mirjam Bruttin, our incredible group secretary. Everyone would agree with me that without you, the group would be lost. Probably half of us would also be in jail for forgetting to pay most of the bills. Thanks for your efficiency and for solving any possible issue incredibly quickly. Many thanks to Tobias Saegesser and Nick Schwegler for being great office companions. I haven't yet decided who of you will get my office spot, so you can still bribe me. However, for the health of the office, it is better if Tobias gets it; otherwise, you will all turn into penguins or polar bears. Many thanks also to Chi Zhang. I'm really impressed by how you changed over the past years. I love your sarcasm and the way you made fun of me. We often worked together, and it has been a lot of fun, especially when you get frustrated at the setup and start laughing. Many thanks to Christoph Fischer. You started as my master's student working on the cavity that I initially built. It never worked, but you kept trying until you wisely decided to throw it in the bin. Thanks for not killing me for all these years. Thanks for all the atomic physics discussions too. Aside from work, I have lots of great memories. Climbing, skiing, mountaineering, to name a few. Spending time with you has been a pleasure! Thanks to Chris Axline. You have also been my climbing partner and my personal chauffeur in all our climbing trips. Thanks for that, James! You witnessed my near-death climbing experience, but just five minutes before that, it has been hilarious to see you hanging like salami on an anchor point (that was not an anchor point) only one meter above a ledge (for the record I'm laughing now). Many thanks to Oliver Wipfli. You have been my conference buddy on various occasions. I have a lot of funny memories, especially around our beloved kicker table. I must mention the ballometer and its chat; every single Physics2 TA wanted to kill you that day. However, it was entertaining and a good antidote against the depression that originated from bad students' exams. Thanks also to Simon Ragg. I'm delighted that we went to Russia together. There I got to know you better, and since then I had a lot of fun in the office with you. Thanks to Florentin Reiter, who is our group theorist. Thanks for clearly explaining theoretical works to poor experimentalists. Thanks to Martin Stadler. You are an excellent asset to the group. Thanks for your tireless work on the control system.Thanks for not killing me even if I kept asking you lots of features or changes. Thanks to our engineers Utku Altunkaya., Cagri Oneal and Peter Clemens. Thanks for talking about electronics in a very understandable way. I'm so looking forward to playing with your new electronics for the control system. Many thanks to Chiara Decaroli. Thanks for the interesting discussions and for bringing a bit of art and colors in our gray physics minds. Thanks to Thanh-Long Nguyen. I have to admit that at the beginning I couldn't say if you were joking or not. Now I know that you mostly joke even when the situation is desperate. Thanks for your positive attitude. By

Contents

1 Introduction

In a remarkable paper published in 1936 [1], Alan Turing proposed an abstract notion of a computing device, now known as the universal *Turing machine*, that is capable of solving any mathematical problem that can be expressed in a symbolic form. A few years later, John von Neumann introduced a theoretical model (still used in modern computers) describing a simple structure for practically building a computing device that is as capable as the universal Turing machine. This concept implies that all computers, independently of the physical implementation, are equivalent in terms of the type of tasks they can solve. Finding the solution to a problem then transforms into developing an algorithm using a convenient mathematical framework (e.g., the Turing machine), instead of inventing a new computing technique on some physical device.

Since these early works, modern computers facilitated many technological advancements and are now indispensable to our everyday lives. However, the classical nature of the information theory that governs modern computers is just an approximation of physical reality; nature is quantum, not classical. While, in theory, a classical computer could be used to simulate phenomena described by quantum mechanics, it appears to be impossible to do it in an *efficient* way[1]. Devices that process information at the quantum level, known as *quantum computers*, offer a speed advantage over classical computers. In 1985, David Deutsch described a quantum model for computation, the Quantum Turing Machine, and showed that it could efficiently solve problems that are not efficiently solvable on a classical Turing machine [2]. This result laid the ground for the development of quantum mechanical computers.

1.1 Quantum information processing

The main properties at the core of Quantum Information Processing (QIP) are quantum superposition, interference, and entanglement. Similarly to the classical *bit* ($'0'$ or $'1'$), introduced by Shannon in 1948 [3] as the unit of classical information, the *qubit* is the unit of quantum information. The general state of a qubit can be written as $\alpha \left| 0 \right\rangle + \beta \left| 1 \right\rangle$[2], where $\left| 0 \right\rangle$ and $\left| 1 \right\rangle$ are two discrete states, and α and β are complex numbers.

There are several areas in which quantum information processing could be advantageous. One of them is the simulation of quantum systems, as proposed by Richard Feynman in 1982 [4]. In principle, classical simulation can be used to simulate quantum systems. In this approach, quantum systems are encoded in a quantum memory (i.e., a register of qubits) that is proportional in size with the system state. A classical register can then describe each qubit, and the interaction between qubits could in principle be simulated with a classical computer. However, adding one extra qubit to the classical register *doubles* the classical memory required, due to the possibility of quantum entanglement [5, 6]. As a result, a quantum system described by approximately 50 interacting qubits is at the limit

---

[1]Roughly speaking, an efficient algorithm solves a problem in time polynomial in the problem's size.
[2]In the next chapters the qubit states $\left| 0 \right\rangle$ and $\left| 1 \right\rangle$ are replaced with the states $\left| \uparrow \right\rangle$ and $\left| \downarrow \right\rangle$, as they refer to two particular energy levels of a trapped ion.

of the computational power of modern classical supercomputers. These complex systems appear in various fields, such as solid-state physics, chemistry, material science and biology [7]. To solve these problems more efficiently, with *quantum simulation* [5, 8], we simulate the behavior of a quantum system by controlling the quantum register describing the system. More recently, hybrid approaches that combine the strength of classical and quantum computation have been proposed to simulate complex quantum chemistry operations [9, 10].

In addition to problems in quantum physics and related derivatives, it has also been shown that a quantum computer offers a speed-up for problems like the factorization of large integers [11] [3], solving a linear system of equations [12], and searching unsorted databases [13].

The long term goal for quantum information processing is the realization of a large-scale universal quantum computer that is capable of executing any quantum algorithm that can be encoded in its register. There are five necessary conditions required for building a quantum computer, as discussed by Di Vincenzo [14]: a scalable physical system with well-defined qubits, the ability to initialize the qubit in a particular state, robust storage of information, a "universal" set of gates, and the ability of reading out the state of the qubit. Several physical platforms have been investigated for potentially building a quantum computer. Superconducting qubits [15, 16] and trapped atomic ions [17, 18, 19] are among the leading candidates.

1.2   Trapped ions for QIP

In the trapped-ion approach, two particular electronic energy states of a single ion implement the qubit. What makes ions an ideal choice for qubits is that ions of the same species are identical by nature and that the atomic properties are well understood. The fact that they are charged also allows the possibility of confining them with electromagnetic forces. Typically the ions are stored and manipulated in vacuum at pressures below 10^{-11} mbar to decouple them from the environment and to minimize collisions with background gases [20]. As a result, ions can be stably trapped, allowing robust information storage. For QIP purposes, the most common ion trap design is the Paul trap [21]. Paul traps use a combination of static and radio-frequency (rf) voltages applied on specific electrodes to confine ions in specific locations.

There are two possible types of qubits and both are used in the work included in this thesis: *ground state* qubits and *optical* qubits [18]. Ground state qubits consist of two energy levels in the ground state manifold of an ion; optical qubits are instead implemented between one energy level in the ground state manifold and one in a metastable excited state. While optical qubits offer some technical advantages, they exhibit a lifetime of approximately 1 s (the time it takes for an ion in the higher energy qubit state to spontaneously decay to a lower energy level) and stabilizing optical frequencies to the same frequency stability as microwave oscillators is a major challenge. Ground state qubits have a lifetime which can be years long, and, in some cases, information can be robustly stored for several minutes [22, 23]. However, if the ground state manifold possesses additional states beyond those defining the qubit, there could be mechanisms that lead to a leakage of the population outside the qubit subspace. It is possible to account for this type of error in a large scale quantum computer but this comes at the cost of more resources [24].

---

[3]However, it has not been proven yet that no classical factorization algorithms exist that are equally efficient or better than the quantum algorithm.

In our experiments, we use a ground state qubit defined between two energy levels in the hyperfine ground state of a beryllium ion (^{9}Be$^+$), and an optical qubit defined on a dipole forbidden transition of a calcium ion (^{40}Ca$^+$). All qubit operations, such as state initialization, quantum gates, and state detection, are performed with lasers. When two or more ions are stored in a single potential well, they couple to one another via their mutual repulsion. We use this coupling to transfer quantum information between ions and to generate entanglement [25]. The motion of the ions is also cooled with lasers to achieve the highest gate accuracy. Details about all these operations will follow in later chapters.

A large scale quantum computer based on trapped ions requires to be able to control and manipulate thousands of ions. Within a single potential well, only a few tens of ions can likely be manipulated with the precise control required for executing quantum algorithms. A more promising approach is the 'Quantum Charge-Coupled Device' (QCCD) architecture [26, 27]. In this framework, a complex set of electrodes is used to create physically separated trapping locations. Each region is then used for qubit readout, manipulation and storage. Ions are shuttled between different regions by varying the electrode voltages. This architecture is more scalable than the single well approach; however, it requires careful management of ion transport, a large number of electronic connections, and a large number of lasers beams. Various techniques like chip-integrated beam delivery [28, 29] and integrated voltage sources [30] have been explored in recent years to address these issues. One other proposal that is gaining more interest is a modular approach. Here multiple "unit-cell traps", each holding few tens of ions, are linked together by photonic interfaces to perform large-scale algorithms [31, 19, 32]. Although recent results showed the preparation of entangled states through a photonic interface at a higher-rates and with improved fidelities [33] compared to prior studies, more research is needed to reach the levels required by complex protocols.

1.3 Mixed-species for QIP

One of the first proposed application of mixed-species is the sympathetic cooling of one type of ion by a second one of a different species [27]. Scalable QIP experiments indeed require the ability to cool the motion of ions close to the quantum ground state while preserving the quantum information stored in the qubit. The dissipation process induced by direct laser cooling destroys the quantum superposition of the qubit states. Therefore, co-trapping another species of ion allows to laser cool the second species, while the the first one is sympathetically cooled due to the Coulomb repulsion. Early demonstrations of sympathetic cooling date back to the 1980s [34, 35].

More recently two species of ions have been used in QIP experiments for high-fidelity detection of one species with quantum non-demolition measurements [36], state initialization and readout of molecular ions using quantum-logic spectroscopy [37, 38], the preparation of entangled states [39, 40, 41, 42] and the teleportation of a gate between separated qubits [43].

One other application for a mixed-species processor is quantum error correction (QEC). Coping with errors arising from noise and imperfect gate operations is a primary challenge in the quest of large-scale quantum computers. QEC relies on the ability to encode one or more logical qubits in multiple physical qubits. Individual errors in the physical qubits have to be detected and corrected without perturbing the state of the logical qubit [44, 45]. The most prominent protocols for QEC, detect errors using ancillary qubits to perform

measurements of the quantum correlations between multiple qubits [6, 46]. With trapped ions, state detection relies on photon scattering, which heats the motion of the ions. This limits the ability to perform further gates, which usually require the ions motion to be cooled close to the motional ground state. For this reason, using two species of ions, one for the ancilla and the other for the data qubits, is beneficial for QEC. If there is enough spectroscopic separation between the two species, the detection of the ancilla does not perturb the information stored in the data qubits. Moreover, the ancilla ion can be used to cool the motion of the ions sympathetically after detection, and the same ancilla qubit could be re-initialized for a new round of measurement.

In this thesis, we used a mixed-species setup to perform joint measurements of the state of two beryllium ions using a calcium ion as an ancilla. We further used the ability of our control system to modify the experimental sequence in real time to prepare and stabilize entangled states [42].

A second significant result discussed in this thesis is the deterministic realization of an arbitrary single-qubit gate in the Measurement-Based Quantum Computation (MBQC) formalism. As opposed to the circuit model, that is a direct quantum generalization of the classical construct, MBQC is a conceptually different paradigm for quantum computation. Quantum operations are not performed by applying a sequence of quantum gates, but rather a series of adaptive measurements on an entangled state of qubits. A general single-qubit unitary in the MBQC formalism requires an entangled state of four qubits and three adaptive measurements. In this work, the single-qubit unitary is performed using a mixed-species chain composed of two qubits, where entanglement is created on demand to reduce the number of resources.

1.4   Thesis outline

Chapter 2 presents the experimental apparatus used in this thesis. After a short description of the segmented trap, I introduce the concepts of normal modes, single-qubit coherent operations, the relevant level structures of $^{40}\text{Ca}^+$ and $^{9}\text{Be}^+$ ions, and I will summarize dissipative operations including cooling, state detection and preparation. I then conclude the chapter introducing the normal modes of motion of mixed-species ion chains.

Chapter 3 is dedicated to the techniques required for state readout. In the trapped-ion architecture, state dependent fluorescence is the most common method for qubit detection. The first part of the chapter describes the most common techniques for state discrimination. The rest of the chapter is dedicated to the description of processes that lead to population leakage during detection. Depending on the choice of qubit, these processes can lead to readout errors if not taken into account. I will present real-time detection techniques that make use of the temporal information carried by the detected photons to improve state discrimination.

Having covered the basic techniques for ion trapping, cooling and detection, Chapter 4 discusses the main features of the experimental control system. At first, I will present the most recent software modifications introduced for the flexible control of arbitrary mixed-species ion chains. The chapter continues summarizing ion transport and separation operations, and the experiments used to characterize their performance with mixed-species chains. Finally, the chapter is concluded with the description of various experimental techniques such as ion reordering and recrystallization that are necessary for the experiments discussed in later chapters.

Chapter 5, discusses various coherent experiments performed in this thesis to better characterize the experimental setup. These include Ramsey sequences to measure motional coherence and the spectral isolation between the two ion species, the characterization of mixed-species normal modes, and finally theory and results of mixed-species entangling gates.

With all mixed-species techniques in place, Chapter 6 discusses the experimental realization of a protocol for the repeated extraction of quantum correlations of two beryllium ions using a co-trapped calcium ion. We use the ability of our control system to feedback upon calcium detection to stabilize the beryllium qubit in a parity subspace for a sequence including up to 50 rounds of measurements. Using similar techniques we also show the deterministic preparation and stabilization of Bell states. The chapter discusses the various details of this experiment, from the pulse sequence to the analysis of the data with a focus on the modeling of the experiment.

In Chapter 7 I will discuss the experimental realization of an arbitrary single-qubit operation in the measurement based quantum computing (MBQC) formalism. The chapter starts with an introduction to MBQC where I highlight the main differences with the standard circuit model approach. I will then continue with a circuit model derivation of an arbitrary single-qubit gate in the MBQC architecture. The chapter is then concluded with preliminary experimental results.

Chapter 8 concludes this thesis providing a summary of the main experimental results and future outlooks.

2 Mixed-species setup

The long term vision behind the setup is the QCCD architecture introduced in the previous chapter (*quantum charged-coupled device*) in which ion transport, separation/recombination as well as sympathetic cooling with a second ion species play an essential role. The trap used for all the experimental results shown in this thesis is a segmented, linear design, which was specifically designed to trap calcium and beryllium ions simultaneously.

Within this chapter, I first introduce the segmented trap, briefly review the main concepts about qubit manipulation and present the techniques for state preparation, manipulation, and readout for both calcium and beryllium. I conclude with an overview of the physics and the experimental challenges of working with both ion species trapped in the same potential well.

2.1 Segmented trap overview

The segmented trap, designed and fabricated by Daniel Kienzler, consists of a stack of gold plated alumina wafers. An exploded view of the wafer stack, and a cross-section of the design is shown in Figure 2.1. The stack is mounted onto a filter board and placed inside a vacuum chamber. Further details about the setup can be found in the thesis of Daniel Kienzler and Hsiang-Yu Lo [47, 48]. The central two electrode wafers form the linear Paul trap, and each contains one radio-frequency (rf) electrode and 15 dc electrodes[1]. The segmented structure of the dc electrodes along the axis is designed to provide two loading zones, three zones for experimental quantum control or ion storage, and two splitting/recombination regions. On both ends of the trap, there are two loading zones through each of which neutral atom beams from one calcium and one beryllium oven pass. This configuration allows flexibility while loading, and limits the charging effect from the photo-ionization lasers to this area of the trap. The electrodes in the loading zones are the widest (500 µm), and the maximum axial trapping frequencies are smaller than those achievable in the central regions with the same maximum voltage. The three experimental/storage regions realize a simplified version of the QCCD architecture and are the dedicated areas for the quantum control of the ion chains. Each of those is centered on an electrode of width 300 µm. In between each of the experimental regions there is a zone consisting of three finger-electrodes (150 µm wide) optimized to achieve tight axial confinement during splitting and recombination operations.

A custom arbitrary-waveform generator [49] produces the dc voltages required to control the time-varying potential wells. For most of the experiments discussed in this thesis, the ions are manipulated in the center of the trap at 20 µm from the geometrical center (Figure 2.1e). The main reason for not working precisely in the center is that at 20 µm, the axial pseudo-potential gradient is lower (see Section 5.2.1 for more details.) The ions are loaded in the left loading zone of the trap (electrodes 2-17 in Figure 2.1e) at −1870 µm from the trap center and are then transported to the central experimental zone. For this

---

[1]dc stands for direct current. In the ion trapping community though it is usually a synonym of static fields and the electrodes that are used to form the static fields ('dc electrodes'). This sometimes inaccurate convention is used throughout the text to adhere to the convention.

operation, we use a "loading conveyor" waveform, which starts with simultaneous wells in the loading and experimental zones that are merged in the experiment zone by the transport waveform.

We apply an rf voltage at $\Omega_{\mathrm{rf}} \approx 2\pi \times 113.5$ MHz with a peak-to-peak amplitude of $V_{\mathrm{rf}} \sim 700$ V to the radio-frequency (rf) electrodes. This is generated by a stable rf source[2] followed by a helical resonator. An ion near the center of the trap $(x, y, z = 0)$ is confined by an approximate electric potential given by

$$V(x, y, z, t) = \frac{1}{2} V_{\mathrm{dc}} (\alpha_z z^2 - \alpha_x x^2 - \alpha_y y^2) + \frac{1}{2} V_{\mathrm{rf}} (\beta_x x^2 + \beta_y y^2) \cos(\Omega_{\mathrm{rf}} t) \qquad (2.1)$$

in which α_i and β_j $(i, j \in x, y, z)$ are geometric factors. The rf potential confines the ion along the radial direction $x - y$ while the dc potential confines it along the trap axis z. For an ion with mass m, the motion along the trap axis is mostly static, with an oscillation frequency of

$$\omega_z = \sqrt{e \alpha_z V_{\mathrm{dc}}/m} \ . \qquad (2.2)$$

Along the radial direction, the equations of motion are found by solving $d^2 u/dt^2 = -e/m \partial^2 V(x, y, z, t)/\partial u^2$ for $u = x, y$ which can be written in terms of a Mathieu equations [26, 21] with parameters

$$a_u = -\frac{4e\alpha_u V_{\mathrm{dc}}}{m\Omega_{\mathrm{rf}}^2},$$
$$q_x = -q_y = \frac{2e\beta_x V_{\mathrm{rf}}}{m\Omega_{\mathrm{rf}}^2} \ . \qquad (2.3)$$

An exponential series is used to solve the Mathieu equations [50]. The lowest order of the solutions yield *secular* harmonic oscillations at frequencies

$$\omega_{\mathrm{rf},u} = \frac{\Omega_{\mathrm{rf}}}{2} \sqrt{a_u + \frac{q_u^2}{2}} \qquad (2.4)$$

superposed with a small excursion at the trap frequency Ω_{rf}, called *micromotion*, whose amplitude is proportional to m^{-1}.

In the ideal case, along the trap axis $(x = 0, y = 0)$, there is no radial micromotion since the rf potential is null. Fabrication defects or poor alignment can lead to a rf component in the axial direction, which in turn causes *intrinsic micromotion*. Stray electric fields shift the ion equilibrium position away from the trap axis, causing *excess micromotion*, which is primarily radial. Compensating stray fields is of crucial importance, especially when working with mixed-species since the radial displacement varies depending on the mass of the ions. This induces a deformation of the crystal and consequently changes the amplitude, frequency and direction of the normal modes of motion, which are critical for laser cooling and multi-qubit gates.

To compensate *excess micromotion*, we use a set of 28 electrodes hosted in two wafers below and above the central dc/rf electrodes (Figure 2.1b) and controlled by a slow DAC (Digital to Analog Converter) embedded in our control system[3]. The reason for the large electrode count is the need to simultaneously compensate excess micromotion in different regions of the trap.

---

[2]Rohde&Schwarz SMC100A rf signal generator
[3]Analog devices' AD5371 evaluation board
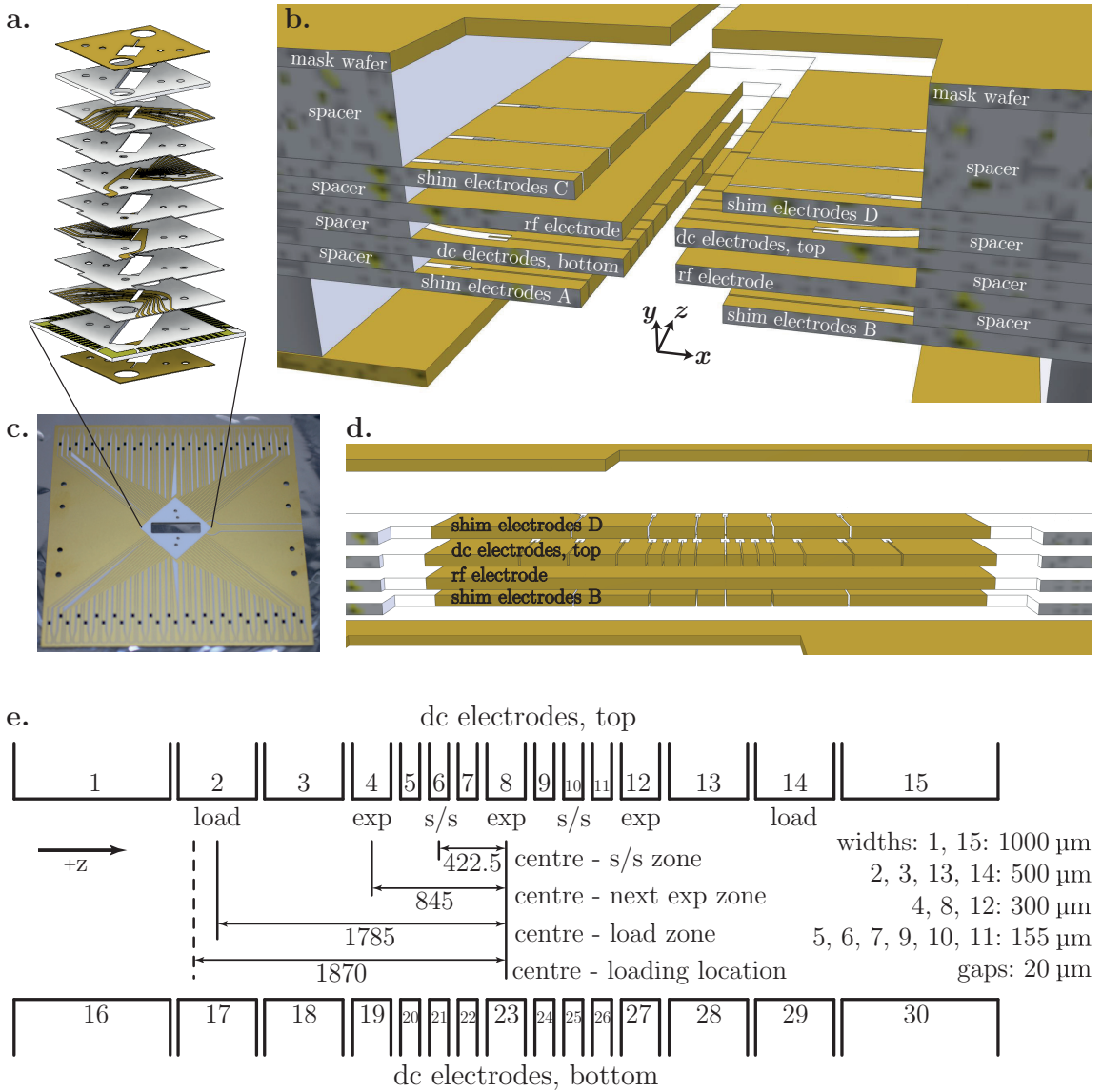
Figure 2.1: Segmented trap: **a.** Assembly of the wafer stack. **b.** Detailed view of the assembly close to the trap electrodes. **c.** Empty filter board. **d.** View of the trap showing the position and dimension of the shim electrodes relative to the dc ones. **e.** Dc electrode numbering and dimension (in μm). The ion to electrode distance is ≃180 μm.

2.2   Normal modes of motion

The derivation presented in this section follows closely the one described in [51]. The task is to the calculate the equilibrium position and the motional oscillations for a set of N ions trapped in a single potential well. For this purpose, we assume the temperature of the ions to be low enough such that the oscillations around their equilibrium position is small compared to the ion-ion distance. We also assume that each ion has a mass m_j (with $j \in [1, N]$), and that the charge $+e$ carried by each ion is the same.

For convenience, we also denote the ions coordinates as $3N$ scalars $z_1, \ldots, z_{3N}$ ($\{z_i\}, i \in [1, 3N]$) which are used to define the N vectors describing the ions position $\mathbf{r}_1, \ldots, \mathbf{r}_N$ ($\{\mathbf{r}_j\}, j \in [1, N]$). Since we are only interested at the dynamics of the secular motion with

coordinate $\mathbf{r}_j$, the potential described by Equation 2.1, can be approximated by

$$\Phi(\boldsymbol{r}_j, m_j) = \phi_{\mathrm{st}}(\boldsymbol{r}_j) + \Phi_{\mathrm{pond}}(\boldsymbol{r}_j, m_j) \ , \tag{2.5}$$

where ϕ_{st} is the static term of Equation 2.1, and the ponderomotive term Φ_{pond} is

$$\Phi_{\mathrm{pond}}\left(\mathbf{r}_j, m\right) = \frac{e|\nabla\phi_{\mathrm{rf}}|^2}{4m_j\Omega_{\mathrm{rf}}^2} \ . \tag{2.6}$$

This last expression is derived by averaging the kinetic energy of the driven micromotion at frequency Ω_{rf}. Further discussion about the validity of this approximation can be found in [52].

With these assumptions, we can write the kinetic energy T, and potential energy U of N ions in a potential described by Equation 2.5:

$$
\begin{aligned}
T &= \sum_{j=1}^{N} \frac{m_j}{2}\dot{\boldsymbol{r}}_j^2 \\
U &= \sum_{j=1}^{N} e\Phi\left(\boldsymbol{r}_j, m_j\right) + \frac{1}{2}\sum_{j,l=1,j\neq l}^{N}\frac{1}{4\pi\varepsilon_0}\frac{e^2}{|\boldsymbol{r}_l - \boldsymbol{r}_j|}
\end{aligned}
\tag{2.7}
$$

The equilibrium position $\{z_i^0\}$ can be found by solving $\partial U/\partial z_i = 0$, which in general requires numerical methods. The $3N \times 3N$ symmetric Hessian matrix, required to calculate the normal modes, can be found by a Taylor expansion of the potential around the equilibrium position:

$$H'_{ik} = \frac{1}{\sqrt{m_i m_k}}\frac{\partial^2 U}{\partial z_i \partial z_k}\bigg|_{\{z_i\}} \ . \tag{2.8}$$

For mixed-species ion chains, it is convenient to rewrite the coordinates z_i with mass-weighted coordinates $z'_i = \sqrt{m_i}z_i$ [51]. The normal modes are then found by solving the Lagrangian equations of motion, defined in terms of the displacement from the equilibrium position $\zeta'_i = z'_i - z_i^{0\prime}$:

$$\ddot{\zeta}'_k + \sum_{i=1}^{3N} H'_{ik}\zeta'_i = 0. \tag{2.9}$$

Assuming $\zeta'_k = \zeta_k^0 e^{i\omega t}$ as an Ansatz yield a linear system of equations. The normal modes of motion are then defined by the eigenvalues and eigenvectors of the Hessian matrix H'_{ik}. The eigenvalues are ω_α^2, where ω_α is the motional frequency of the α normal mode with $\alpha \in [1, 3N]$. The individual ion coordinates ζ'_i can be written in terms of the eigenvectors $e'_{i,\alpha}$ as

$$\zeta'_i = \sum_{\alpha=1}^{3N} e'_{i,\alpha}\zeta'_\alpha \ . \tag{2.10}$$

High-fidelity experiments generally require the motional modes to be close to the ground state. In this scenario, we consider the ion motion to be well described by a quantum harmonic oscillator. Each normal mode is described as an independent oscillator, and the motion can be quantized by defining the position and momentum operators as

$$
\begin{aligned}
\hat{\zeta}'_\alpha &= \frac{\sigma'_\alpha}{\sqrt{2}}\left(\hat{a}_\alpha + \hat{a}_\alpha^\dagger\right), \\
\hat{p}'_\alpha &= i\frac{\hbar}{\sqrt{2}\sigma'_\alpha}\left(\hat{a}_\alpha - \hat{a}_\alpha^\dagger\right).
\end{aligned}
\tag{2.11}
$$

where $\sigma'_\alpha = \sqrt{\hbar/\omega_\alpha}$ and $\hat{a}_\alpha$ $(\hat{a}^\dagger_\alpha)$ is a lowering (rising) ladder operator. Further discussion about the normal modes properties for a mixed-species ion chain can be found in Section 2.8.1.

2.3   Coherent laser-ion interaction

As explained in the previous section, a trapped ion can be modeled as a particle confined in a quadratic potential along the axial and the radial directions. For the experiments described in this thesis, the ion motion in a certain normal mode can then be well-described by a quantum harmonic oscillator, with energy-eigenstates $\{|n\rangle_m\}$ $(n \in \mathbb{N})$ and frequency ω_m. In our experiments, the motional frequencies range from $\sim 2\pi \times 300\,\mathrm{kHz}$ to $\sim 2\pi \times 13\,\mathrm{MHz}$. The qubit is a unit of quantum information and can be stored in any chosen pair of internal levels. These two internal states of the ion are modeled as a two-level system with states $|\downarrow\rangle$ and $|\uparrow\rangle$. Throughout this thesis, state $|\downarrow\rangle$ always refers to the lower energy state. With that, the definition of the operators introduced in this section iapplies to any choice of the qubit. The energy difference $\hbar\omega_0$ between the internal states $|\downarrow\rangle$ and $|\uparrow\rangle$ varies depending on the qubit choice. In our experiments the qubit transition frequency for beryllium is $\omega_0 \sim 2\pi \times 1\,\mathrm{GHz}$; for calcium instead, it ranges from $\sim 2\pi \times 330\,\mathrm{MHz}$ in the case of the ground state qubit to $\sim 2\pi \times 400\,\mathrm{THz}$ for the optical qubit.

The Hamiltonian for the ion and motion is

$$H_0 = H_{\mathrm{qubit}} + H_{\mathrm{motion}} = \frac{\hbar\omega_0}{2}\hat{\sigma}_z + \sum_i \hbar\omega_{m,i}(\hat{a}^\dagger_i \hat{a}_i + 1/2) \ , \qquad (2.12)$$

where $\hat{\sigma}_z$ is the Pauli operator $\hat{\sigma}_z = |\uparrow\rangle\langle\uparrow| - |\downarrow\rangle\langle\downarrow|$, and $\hat{a}_i$ $(\hat{a}^\dagger_i)$ is the the lowering (raising) operator for the harmonic oscillator of the i motional mode.

Lasers or rf fields are used to coherently manipulate the state of the system. Following a standard treatment found in [50], the Hamiltonian that describes the interaction of an ion with a laser with frequency ω_l and phase ϕ can be written under the appropriate approximations [50] as

$$H_I = \frac{\hbar\Omega_0}{2}e^{i\mathbf{k}\cdot\mathbf{R}}e^{i(\phi-\omega_l t)}\hat{\sigma}_+ + H.c. \ , \qquad (2.13)$$

where $\mathbf{k}$ is the wave-vector of the laser field, $\mathbf{R}$ the external position operator for the ion center of mass written in a coordinate system that lines up with the directions of the normal mode vectors of the ion motion in the trap, $\hat{\sigma}_+ = |\uparrow\rangle\langle\downarrow|$ the spin flip operator, and Ω_0 is the resonant Rabi frequency which depends on atomic parameters and the laser/microwave field strength. For a single ion, the term $\mathbf{k}\cdot\mathbf{R}$ can be rewritten introducing the the *Lamb-Dicke parameter* η_i as

$$\mathbf{k}\cdot\mathbf{R} = \sum_{i=1}^{3}\eta_i\left(\hat{a}^\dagger_i + \hat{a}_i\right), \quad \eta_i = k_i\sqrt{\frac{\hbar}{2m\omega_{m,i}}} \ , \qquad (2.14)$$

in which k_i represents the projection of the laser wave-vector onto the axis of the i-th motional mode. In our setup, for typical axial trapping frequencies of $\sim 2\pi \times 2\,\mathrm{MHz}$, the Lamb-Dicke parameter is $\eta \approx 0.05$ for the calcium 729 nm qubit manipulation beam which is at 45 degrees to the trap axis (Section 2.5.2), while in the case of the beryllium Raman beams it can be as large as $\eta \approx 0.4$ (Section 2.5.1).

Moving into the interaction picture with respect to the bare Hamiltonian H_0, and considering only one motional mode [4], we can rewrite Equation 2.13 as

$$H'_I = \frac{\hbar}{2}\Omega_0 \exp\left[i\eta\left(\hat{a}^\dagger e^{i\omega_m t} + \hat{a}e^{-i\omega_m t}\right)\right]\hat{\sigma}_+ e^{i(\phi-\delta t)} + h.c\ ,\qquad(2.15)$$

where $\delta = \omega_l - \omega_0$ is the detuning between the laser and the qubit frequency. Making use of the *rotating-wave approximation* (RWA), this Hamiltonian features resonances for $\delta = s\omega_m$, with s being an integer. The three most relevant ones are the *carrier*, at $\delta = 0$, the *red sideband* at $\delta = -\omega_m$, and the *blue sideband* for $\delta = +\omega_m$. More generally for any s the Rabi frequency for the transition $|\downarrow, n\rangle \leftrightarrow |\uparrow, n+s\rangle$ is

$$\begin{aligned}\Omega_{n+s,n} &= \Omega_0 \left|\left\langle n+s\left|e^{i\eta(\hat{a}+\hat{a}^\dagger)}\right|n\right\rangle\right| \\ &= \Omega_0 \exp\left(-\eta^2/2\right)\eta^{|s|}\sqrt{\frac{n_{\min}!}{n_{\max}!}}L^{(|s|)}_{n_{\min}}\left(\eta^2\right)\ ,\end{aligned}\qquad(2.16)$$

where $n_{\min} = \min(n, n+s)$, and $n_{\max} = \max(n, n+s)$, and $L^{(|s|)}_{n_{\min}}\left(\eta^2\right)$ are the generalized Laguerre polynomials

$$L^{(|s|)}_{n_{\min}}\left(\eta^2\right) = \sum_{k=0}^{n_{\min}}(-1)^k\left(\begin{array}{c}n_{\min}+|s|\\ n_{\min}-k\end{array}\right)\frac{\eta^{2k}}{k!}\ .\qquad(2.17)$$

A considerable simplification to Equation 2.15 comes when working in the *Lamb-Dicke regime*, which is applicable when $\eta\sqrt{\left\langle\left(\hat{a}^\dagger+\hat{a}\right)^2\right\rangle}\ll 1$. Under this assumption, and making use of the RWA, the three main transitions introduced above take the form of simpler Hamiltonians

$$\begin{aligned}H_{\text{carr}} &= \frac{\hbar}{2}\Omega_0\left(\hat{\sigma}_+ e^{i\phi} + \hat{\sigma}_- e^{-i\phi}\right)\ , \\ H_{\text{rsb}} &= \frac{\hbar}{2}\Omega_0\eta\left(i\hat{a}\hat{\sigma}_+ e^{i\phi} - i\hat{a}^\dagger\hat{\sigma}_- e^{-i\phi}\right)\ , \\ H_{\text{bsb}} &= \frac{\hbar}{2}\Omega_0\eta\left(i\hat{a}^\dagger\hat{\sigma}_+ e^{i\phi} - i\hat{a}\hat{\sigma}_- e^{-i\phi}\right)\ .\end{aligned}\qquad(2.18)$$

An ion initialized in $|\downarrow, 1\rangle$ will thus exhibit resonant Rabi oscillations between states $|\downarrow, 1\rangle \leftrightarrow |\uparrow, 1\rangle$, $|\downarrow, 1\rangle \leftrightarrow |\uparrow, 0\rangle$ and $|\downarrow, 1\rangle \leftrightarrow |\uparrow, 2\rangle$ under the effect of the carrier, the red and blue sideband Hamiltonian respectively. In the *Lamb-Dicke regime*, Equation 2.16 for the carrier and the two sidebands Rabi frequencies simplifies to

$$\Omega_{carr} = \Omega_0\ ,\Omega_{rsb,n,n-1} = \Omega_0\eta\sqrt{n}\text{ and }\Omega_{bsb,n,n+1} = \Omega_0\eta\sqrt{n+1}\ .\qquad(2.19)$$

Figure 2.2 gives a graphical representation of the coupled ion-oscillator system, showing the transitions driven by the carrier and first red/blue sideband Hamiltonians. It is important to note that one can get resonant Rabi oscillations also without the the *Lamb-Dicke regime* approximation, but the matrix elements are different from the approximate values (see Figure 2.2b).

---

[4]For this assumption to hold, we assume that the laser is tuned close to a resonance which involves only one motional mode (i.e. the axial) such that excitations on other modes can be neglected (*weak coupling regime*).
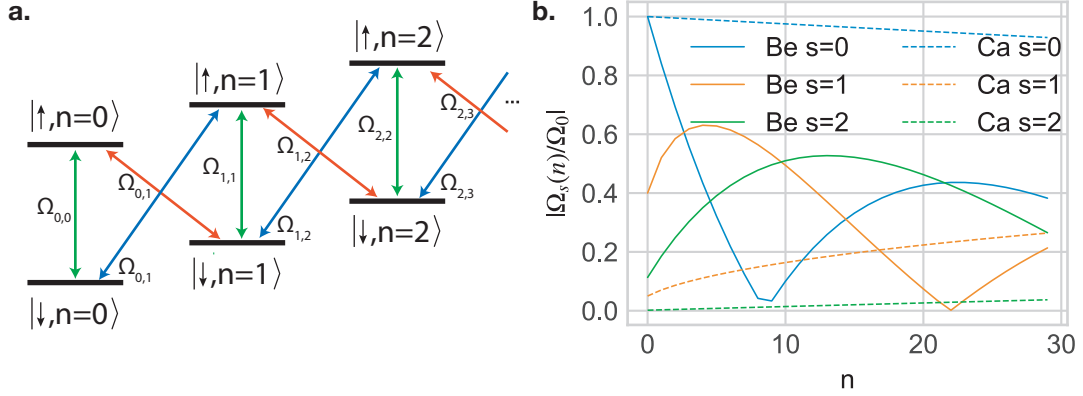
Figure 2.2: Spin-motion structure. **a** Energy ladder for the coupled spin-motion system. High-lighted are the three main transition frequencies: carrier (green), the red sideband (red), and the blue sideband (blue) **b** Rabi frequency strength as a function of the phonon occupancy obtained from Equation 2.16 for $|s| = 0, 1$ and 2. The solid lines are for a Lamb-Dicke parameter $\eta = 0.4$, which is a typical value for the experiments involving only one beryllium ion presented in this thesis. The dashed lines are for $\eta = 0.05$, which is the value we have for our calcium $729\,\text{nm}$ beam.

2.3.1 Rabi oscillations and single qubit rotations

A general superposition $|\Psi(t)\rangle$ of the states shown in Figure 2.2a can be written as

$$|\Psi(t)\rangle = \sum_{n=0}^{\infty} c_{\downarrow,n}(t) \, |\downarrow, n\rangle + c_{\uparrow,n}(t) \, |\uparrow, n\rangle \; . \tag{2.20}$$

The evolution under the Hamiltonian of Equation 2.15 can be analytically solved to obtain the rotation operator R

$$\begin{pmatrix} c_{\uparrow,n+s}(t) \\ c_{\downarrow,n}(t) \end{pmatrix} = R_n^s(t, \delta, \phi) \begin{pmatrix} c_{\uparrow,n+s}(0) \\ c_{\downarrow,n}(0) \end{pmatrix} \tag{2.21}$$

with

$$R_n^s(t, \delta, \phi) = \begin{bmatrix} e^{-i\delta't/2}\left(\cos\frac{\tilde{\Omega}_n^s t}{2} + i\frac{\delta'}{\tilde{\Omega}_n^s}\sin\frac{\tilde{\Omega}_n^s t}{2}\right) & e^{-i\delta't/2}\left(-i\frac{\Omega_{n+s,n}}{f_n^s}e^{i\left(\phi+|s|\frac{\pi}{2}\right)}\right)\sin\frac{\tilde{\Omega}_n^s t}{2} \\ e^{i\delta't/2}\left(-i\frac{\Omega_{n+s,n}}{\tilde{\Omega}_n^s}e^{-i\left(\phi+|s|\frac{\pi}{2}\right)}\right)\sin\frac{\tilde{\Omega}_n^s t}{2} & e^{i\delta't/2}\left(\cos\frac{\tilde{\Omega}_n^s t}{2} - i\frac{\delta'}{\tilde{\Omega}_n^s}\sin\frac{\tilde{\Omega}_n^s t}{2}\right) \end{bmatrix}$$
$$\tag{2.22}$$

where $\delta' = \delta - s\omega_m$ is laser the detuning from the s sideband frequency and $\tilde{\Omega}_n^s = \sqrt{\Omega_{n+s,n}^2 \delta'^2}$ is the effective Rabi frequency.

Assuming that the laser field is on resonance with either the carrier or one sideband, $\delta' = 0$, the rotation operator $R_{n,\,\text{res}}^s(t, \phi)$ that describes a generalized form of Rabi oscillation between pairs of states is

$$R_{n,\,\text{res}}^s(\theta_{n+s,n}, \phi) = \begin{bmatrix} \cos\frac{\theta_{n+s,n}}{2} & -ie^{i\left(\phi+|s|\frac{\pi}{2}\right)}\sin\frac{\theta_{n+s,n}}{2} \\ -ie^{-i\left(\phi+|s|\frac{\pi}{2}\right)}\sin\frac{\theta_{n+s,n}}{2} & \cos\frac{\theta_{n+s,n}}{2} \end{bmatrix}, \tag{2.23}$$

where $\theta_{n+s,n} = \Omega_{n+s,n}t$ and ϕ describe the rotation angles of the rotation matrix $R_{n,\,\text{res}}^s$.

For carrier rotations and in the Lamb-Dicke approximation, $\theta = \Omega_0 t$ and the rotation matrix can be simply written as:

$$R(\theta, \phi) = \left[\begin{array}{cc} \cos \frac{\theta}{2} & -ie^{i(\phi)} \sin \frac{\theta}{2} \\ -ie^{-i(\phi)} \sin \frac{\theta}{2} & \cos \frac{\theta}{2} \end{array} \right]. \tag{2.24}$$

2.4 Stages of an experiment

Each run of the experiments presented in this thesis consists of a similar sequence of steps. Depending on the crystal characteristics each step might vary, but broadly speaking, the typical sequence is as follow:

1. Cooling of motional modes

2. Internal state preparation

3. Qubit manipulation

4. Internal state detection

In our notation, a sequence of these four steps is called an experimental *shot*. We then repeat the same shot up to several thousand times to gather statistics and infer the state population. In our notation, we call the sequence of experimental shots a data *point*. Scans are a collection of data points where, for each point, a different setting of the control parameters is used.

Within the next sections, the first three stages will be presented together with the experimental details for both calcium and beryllium. Chapter 3 introduces the basics of internal state detection and describes the techniques for state discrimination.

2.5 Beryllium and calcium ions

2.5.1 Beryllium ion

Beryllium is the lightest ion species commonly used for QIP, giving the advantage of tighter confinement and stronger coupling of the motion to light fields. It features a hyperfine ground state with two manifolds, $\mathbf{F} = 1$ and $\mathbf{F} = 2$ deriving from the coupling of the total electron angular momentum $\mathbf{J}$ with the nuclear spin $\mathbf{I} = 3/2$. In our experiment, a magnetic field of 119.45 G splits the degeneracy of the hyperfine ground states, thus allowing us to isolate individual transitions between different m_F states. These transition can be driven with microwaves fields [53] or two-photon stimulated Raman transitions [26, 54]. In our experiment, coherent manipulation of these transitions is performed using a two-photon stimulated Raman process that couples the $S_{1/2}, F = 1$ and $S_{1/2}, F = 2$ manifolds through the $P_{1/2}$ states. At this magnetic field, the energy splitting of the transition $|F = 2, m_F = 0\rangle \leftrightarrow |F = 1, m_F = 1\rangle$ is, to first order, insensitive to magnetic field fluctuations. We call this qubit transition FIQ (field-independent qubit), and it exhibits a coherence time[5] of $\sim 4\,\text{s}$ [48].

---

[5]In quantum information processing, a qubit is said to be coherent as long as there is a well-defined phase relationship between the two states defining the qubit. If the qubit is perfectly isolated, coherence would be maintained indefinitely, but no qubit manipulation would be possible. Coupling the qubit to the
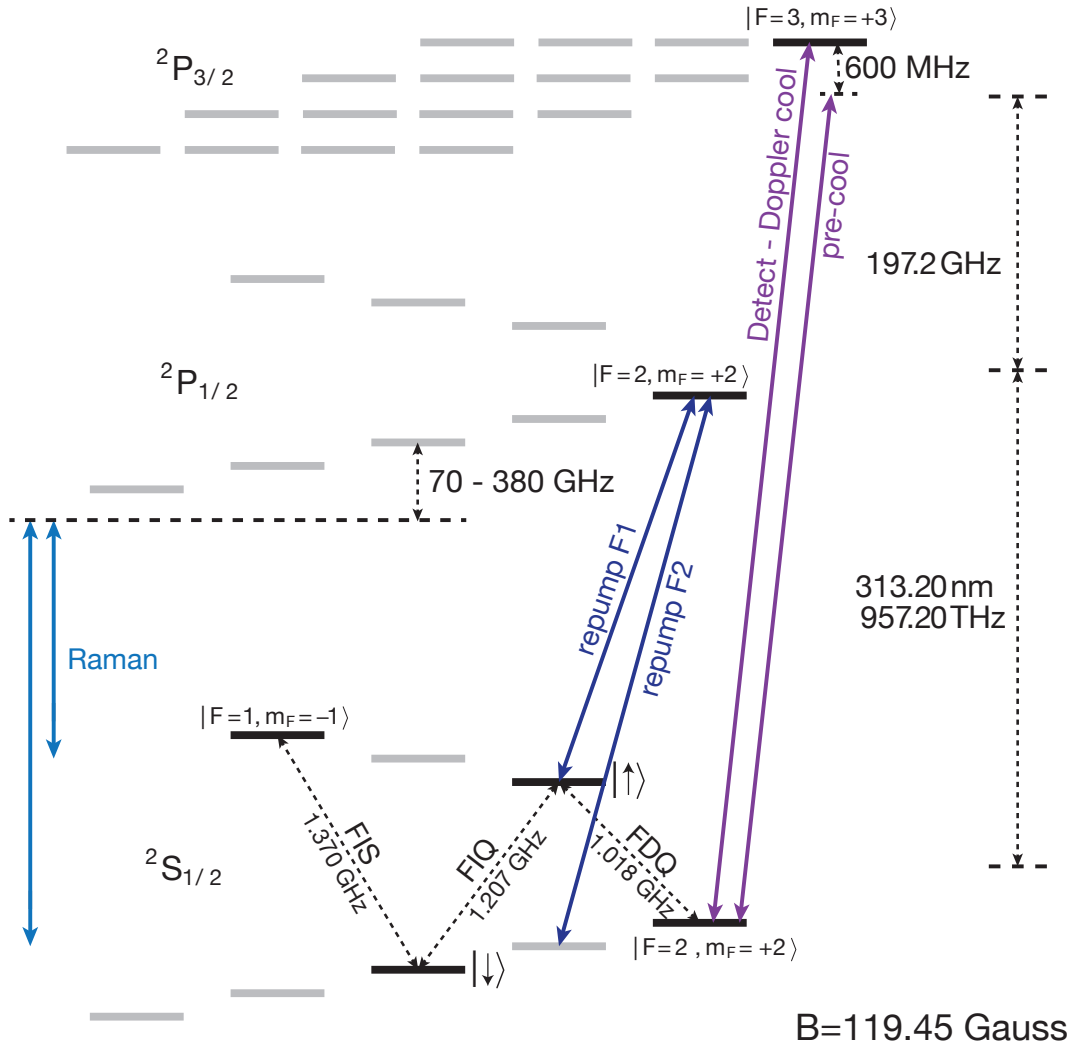
Figure 2.3: ^{9}Be$^+$ level structure at a magnetic field of 119.45 G. The hyperfine levels that are accessible throughout a typical experimental sequence are highlighted in black. The solid lines represent the lasers used for the manipulation. The Raman beams can be tuned to drive the FDQ, FIQ, FIS transition.

Figure 2.3 shows the level scheme of beryllium at the magnetic field value used in this thesis, and Figure 2.4 shows the beam configuration with respect to the vacuum chamber. All transitions are driven with lasers around 313 nm. State readout is performed on the closed $\left|S_{1/2}, F = 2, m_F = 2\right\rangle \leftrightarrow \left|P_{3/2}, F = 3, m_F = 3\right\rangle$ transition, which has a natural linewidth of $2\pi \times 19.4$ MHz. For this transition to be closed, the laser coupling the two states needs to be purely σ_+ polarized. If the ion is initially in the state $\left|S_{1/2}, F = 2, m_F = 2\right\rangle$, it will be excited to the $\left|P_{3/2}, F = 3, m_F = 3\right\rangle$ level from which it will decay emitting photons at 313 nm that can be detected with photomultiplier tube (PMT) or a camera. Ideally, if the ion is in any other state in the $S_{1/2}$ manifold, it will not scatter any photon. There are two main sources of infidelity associated with this readout scheme: the first one is polariza-

---

external world opens a channel for information loss. In trapped-ions, magnetic field noise is one of the leading mechanisms for the loss of information. Noise in the magnetic field perturbs the relative energy difference of the qubit states and thus their relative phase in an uncontrolled way.

tion impurity of the readout beam, which leads to a small chance of decaying to other $S_{1/2}$ states outside the readout cycling transition [55, 48, 56]. The other is off-resonant pumping of the dark states into the bright $\left|S_{1/2}, F = 2, m_F = 2\right\rangle$ level [56, 57, 55, 58]. Chapter 3 goes more into the details of state readout and illustrates tools that can mitigate these sources of infidelity. Doppler cooling (see Section 2.7.1)is also performed on the readout transition.

State initialization and repumping are carried out with two laser beams, close to resonance with the $\left|S_{1/2}, F = 2, m_F = 1\right\rangle \leftrightarrow \left|P_{1/2}, F = 2, m_F = 2\right\rangle$ and $\left|F = 1, m_F = 1\right\rangle \leftrightarrow \left|P_{1/2}, F = 2, m_F = 2\right\rangle$ transitions. Together they are used to optically pump the population to $\left|S_{1/2}, F = 2, m_F = 2\right\rangle$.

Along with the FIQ transition mentioned earlier, we also employ two other transitions depicted in Figure 2.3 as FDQ (field-dependent qubit) and FIS (shelving for the field-independent qubit). The first one is the simplest to drive, thus we use it in state preparation (Section 2.6)and for sideband cooling (Section 2.7.4), where optical pumping is performed repeatedly. The second shelves the state $|F = 2, m_F = 0\rangle$ for better detection fidelity.

The detuning of the Raman lasers from the $P_{1/2}$ manifold is $\sim 230\,\mathrm{GHz}$, as a tradeoff between sufficiently large Rabi frequency and low scattering rate. The effective Raman Rabi frequency can be derived assuming two monochromatic laser fields that couple the qubits states though the different excited states $|e_m\rangle$ that compose the P manifolds. The two fields, E_r and E_b can be written as $\mathbf{E}_i = \hat{\epsilon}_i E_i \cos\left(\mathbf{k}_i \cdot \mathbf{r} - \omega_i t + \phi_i\right)$ for $i \in \{b, r\}$, where E_i and $\hat{\epsilon}_i$ are the amplitude and polarization of the electric fields, $\mathbf{k}_i$ is the wave vector, and ω_i and ϕ_i the frequency and phase of the laser. For Raman carrier operations, the frequency of the two lasers is chosen such that $\omega_0 = \omega_b - \omega_r$, with ω_0 the qubit transition frequency. Assuming that the "blue" Raman beam couples the levels $|\downarrow\rangle$ and $|e_m\rangle$, while the "red" Raman beam the states $|\uparrow\rangle$ and $|e_m\rangle$, one can define the single-photon Rabi frequencies as $g_{r,e_m} \equiv \frac{E_r \langle e_m|\mathbf{d}\cdot\hat{\epsilon}_r|\uparrow\rangle}{h}$ and $g_{b,e_m} \equiv \frac{E_b \langle e_m|\mathbf{d}\cdot\hat{\epsilon}_b|\downarrow\rangle}{h}$, where $\mathbf{d}$ is the atomic dipole. Under the assumption of large Raman detuning ($\Delta \gg g_{r,e_m}, g_{r,e_m}$ for all m) it can then be shown that the effective Raman Rabi frequency is [48]

$$
\begin{aligned}
|\Omega| = \Omega_0 &= \sum_m \frac{g_{b,e_m} g_{r,e_m}^*}{2\Delta} \\
&= \frac{E_b E_r}{2\hbar^2} \sum_m \frac{\langle 2|\mathbf{d}\cdot\hat{\epsilon}_r|e_m\rangle \langle e_m|\mathbf{d}\cdot\hat{\epsilon}_b|1\rangle}{\Delta_m}
\end{aligned}
\tag{2.25}
$$

Associated with the Raman process, there are two well-known sources of infidelities: Raman and Rayleigh scattering [59]. In both cases, it is an undesired off-resonant scattering from the P manifolds. A detailed description of the two scattering processes can be found in the thesis of Hsiang-Yu Lo [48]. The Raman off-resonant scattering rate is proportional to $1/\Delta^2$, and it can be mitigated by increasing the detuning at the cost of reducing the Rabi frequency.

Figure 2.4 shows a schematic of the configurations for the Raman beams which are available in our apparatus. We can choose to drive any transition either with co-propagating beams or with lasers at 90 degrees to each other. The difference is in the effective $\mathbf{k} = \mathbf{k_b} - \mathbf{k_r}$ wave-vector, is, in turn, related to the Lamb-Dicke parameter η through Equation 2.14. In the case of co-propagating beams, the effective $\mathbf{k_{co}}$ vector value is $k_{co} \approx 30\,\mathrm{m}^{-1}$, which is almost negligible compared to $|\mathbf{k_r}|$ and $|\mathbf{k_b}|$. Therefore the Lamb-Dicke parameter is $\eta \approx 0$ making this configuration ideal to drive motion-insensitive transitions, since it largely decouples the operations from motional imperfections like Rabi frequency fluctuations due
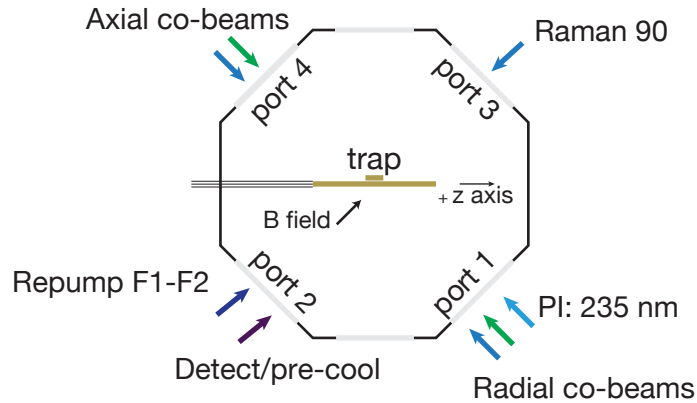
Figure 2.4: Top-down view of the vacuum chamber showing the different orientations of the beryllium lasers. Considering only the Raman beams, the green arrow marks the direction of the $\mathbf{k_b}$ wave-vector, while the blue arrow the $\mathbf{k_r}$ wave-vector. In the optical setup, a flip mirror determines whether the co-propagating Raman beams enter through port 4 or port 1. Depending on the choice, the resulting $\mathbf{k_{90}}$ wave-vector (see text) is either parallel or perpendicular to the trap axis, allowing to couple to either the axial or the radial modes of motion.

to micromotion and imperfect cooling. We make use of this feature for the FDQ and FIS pulses that prepare the ion before readout of the FIQ populations. Another relevant property of this configuration is that the relative path difference between the two beams is small, resulting in a relatively stable phase relationship over the course of taking an data point that is important for the experiments described in later chapters.

In the case of beams at 90 deg, the effective $\mathbf{k_{90}}$ vector is $k_{90} \approx 2.8 \times 10^8 \mathrm{m}^{-1}$, that is on the order of $|\mathbf{k_r}|$ and $|\mathbf{k_b}|$ themselves. This configuration is used for driving motion-sensitive transitions. Depending on the pair of beams that we choose to use, $\mathbf{k_{90}}$ is parallel to the trap axis or perpendicular to it giving access to either the axial modes of motion or the radials.

One important imperfection in our trap is that the beryllium ions exhibit strong axial micromotion, which we cannot compensate by controlling the dc voltages of the shim electrodes introduced in Section 2.1. The effect is a modulation of the axial position of the ion in phase with the trap rf frequency $\Omega_{\mathrm{rf}} \sim 2\pi \times 113.5\,\mathrm{MHz}$. In the frame of reference of the ion, the Doppler shift induced by axial micromotion adds sidebands to the laser spectrum at integer multiples of the drive frequency. The strength of these sidebands is parameterized by a beam-dependent modulation index β given by [60]

$$\beta = k_z z_{\mathrm{mm}}, \tag{2.26}$$

where axial component of the k_z beam wave vector and z_{mm} is the micromotion amplitude. We counterbalance the Doppler shifts by modulating the frequency of the cooling, repump, detection, and Raman beams in phase with the trap rf frequency with the use of EOMs. A more detailed description of the setup and the EOM tuning procedures for the detection beams can be found in the Ph.D. thesis of Hsiang-Yu Lo [48], while for the Raman beams in the one of Vlad Negnevitsky [61].
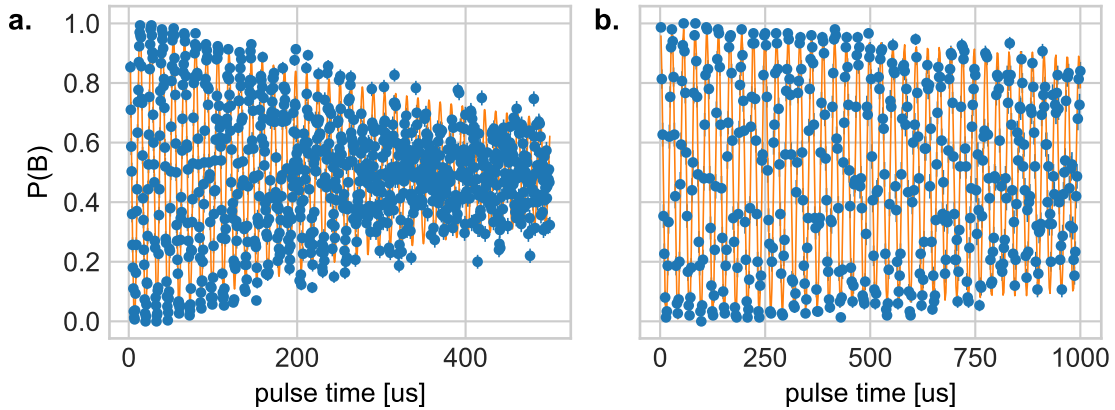
Figure 2.5: FIQ Rabi oscillations before and after the breadboard installation. For both plots, the pulse time in the x-axis is such that there should be visible up to 70π Rabi oscillations. Fitting the damping rate of the oscillation's contrast, we measure a $20\times$ improvement after the installation of the breadboard. We believe that most of the improvements derive from the suppression of non-common mode vibrations due to the rigid connection to the vacuum chamber.

Setup improvements

Throughout my Ph.D., we spent much effort trying to improve the overall fidelity of the beryllium gates, with a focus on Rabi frequency noise, through improvements of the apparatus.

The generation of a high power source at 313 nm has been discussed in depth in the Ph.D. thesis of Hsiang-Yu Lo [48] and follows the approach demonstrated in [62]. It consists of two stages: first, a sum-frequency generation stage (SFG), which generates light at 626.546 nm using two input lasers at 1551.44 nm and 1050.98 nm. The 626 nm light is then coupled into a polarization-maintaining fiber and sent to a frequency doubling cavity that generates the light at 313.273 nm. For the experiments presented in Chapter 6, the doubling cavity was installed by Hsiang-Yu Lo and was based on the design described in [62]. With this cavity, we measured fast intensity noise (from 50 kHz to 500 kHz) on the 313 nm output of $\sim 10\%$. After the results of Chapter 6, we replaced the cavity with a commercial solution offered by Toptica. The double piezo locking system installed by Toptica improved the overall stability of the lock, and we also noticed a reduction in the fast intensity noise (from 50 kHz to 500 kHz) at 313 nm to $< 2\%$ in daily operations.

To mitigate beam pointing fluctuations of the Raman beams, we worked on the mechanical elements right before the vacuum chamber. The chamber is surrounded by four optical breadboards that supply the beams at the four different viewports. The last mechanical element before the viewports is a housing box that is rigidly connected to the chamber. It contains optics to overlap and focus beams with different wavelengths. To improve the mechanical stability, we re-designed the breadboards and the focusing box of viewport 3 and 4 of Figure 2.4. We rigidly connected the breadboard to the chamber, making all the vibration common mode, and also added the possibility to enclose the laser beam path completely to mitigate beam pointing fluctuations caused by turbulent airflow. A second improvement to beam pointing fluctuations came from the use of UV-capable photonic crystal fibers [63], which replaced the periscopes that connected the optical table to the breadboards. Figure 2.5 shows a comparison of Rabi oscillations before and after the setup
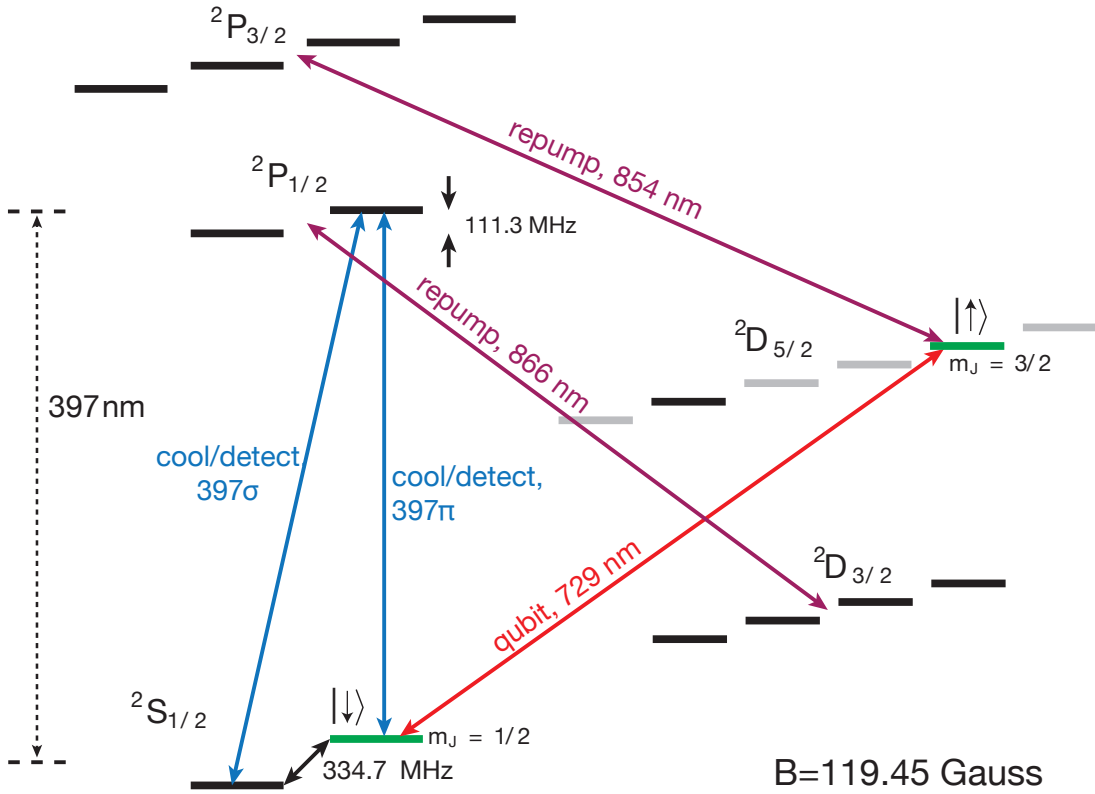
Figure 2.6: $^{40}Ca^+$ level structure at a magnetic field of 119.45 G. In dark are highlighted all the accessible levels, while in green the two qubit levels used throughout this thesis.The solid lines represent the lasers used for the ion manipulation.

improvements. Since both changes happened at the same time, it is hard to say which of the two contributed the most to the improvement.

2.5.2 Calcium ion

The other ion species used in our setup is calcium, $^{40}Ca^+$. Compared to beryllium, it is approximately four times heavier, it has low-lying D manifolds, and it has no nuclear spin, which reduces the number of ground-state electronic levels due to the lack of hyperfine structure. Figure 2.6 shows the level structure of calcium at the magnetic field of 119.45 G, and Figure 2.7 shows the orientation of the lasers used for the manipulation of the ion.

There are two typical choices for the qubit. The first one, not yet used in our experiments, is between the two ground-state levels whose frequency difference is $\omega_0 = 2\pi \times 334.7$ MHz [64]. The second one is on the quadrupole transition between the ground state and the excited $D_{5/2}$ manifold. The latter is usually called the optical qubit, and it is driven with a narrow linewidth laser at 729.35 nm. With the current beam configuration, there are two possible choices for the optical qubit. One is between the states $\left|S_{1/2}, m_J = 1/2\right\rangle \leftrightarrow \left|D_{5/2}, m_J = -3/2\right\rangle$, and the second between $\left|S_{1/2}, m_J = 1/2\right\rangle \leftrightarrow \left|D_{5/2}, m_J = +3/2\right\rangle$. For the purpose of this thesis, only the second transition is relevant, and the qubit states are highlighted in green in Figure 2.6. Experiments described in [65] and conducted by Christa Flühmannn also made use of the other transition. These were performed coincident with the work in this thesis.
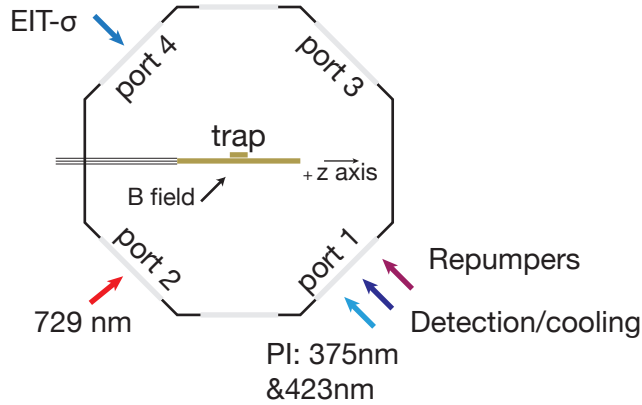
Figure 2.7: Top-down view of the vacuum chamber showing the different directions for the calcium lasers

Compared to the 4 s coherence time of the field-independent qubit of beryllium, the coherence time of the optical qubit in calcium is only ~1.7 ms. One of the reasons is the transition frequency sensitivity to the magnetic field, which is 1.12 MHz/G. We measured that, on the millisecond timescale, the magnetic field fluctuates with standard deviation $\sigma_m \approx 81\,\mu G$. The other source of decoherence is laser linewidth, which we estimated to be $\sigma_l \approx 2\pi \times 99$ Hz. More details about these measurements, including the techniques employed for the magnetic field stabilization and the 729 laser setup, can be found in [66].

For typical axial trapping frequencies $\omega_z \simeq 2\pi \times 2$ MHz, the Lamb-Dicke parameter for the 729 nm beam at 45° to the trap axis is $\eta \simeq 0.05$. As a consequence, the Lamb-Dicke approximation introduced in Section 2.3 is fulfilled for a broad set of motional levels $\{n\}$ ($n < 50$), making calcium an ideal choice for motional state engineering [67, 68, 69, 70, 71, 67, 48, 66].

State readout, cooling, and state preparation are on the transition between $S_{1/2} \leftrightarrow P_{1/2}$ at 396.96 nm. This transition has a linewidth of roughly $2\pi \times 22.7$ MHz, and it is not closed: an ion in the $P_{1/2}$ level can decay either to the $S_{1/2}$ states or to the meta-stable $D_{3/2}$ manifold with an approximate branching ration of 20 : 1. Experimentally we repump the population decayed into $D_{3/2}$ with an 866.45 nm laser with two different frequencies. Two frequencies are needed due to the large Zeeman's shift of $D_{3/2}$ states caused by the magnetic field at 119.45 G [47]. The light has a mixture of $\hat{\sigma}_+$ and $\hat{\sigma}_-$ polarization, thus allowing the repumping from all relevant states in the $D_{3/2}$ manifold.

The $D_{5/2}$ manifold is repumped to the ground state manifold by coupling to the short-lived $P_{3/2}$ manifold with a laser at 854.44 nm. The ion quickly decays to from the $P_{3/2}$ state to the $S_{1/2}$ manifold emitting a photon at 393 nm.

2.6 Internal state preparation

The qubit is defined between two particular atomic states. State preparation ensures that the ion population is initialized into a specific state. The most common technique used for state preparation is optical pumping [72]. During this process, a laser beam couples the undesired states to a short-lived state, which has a non-zero probability of decaying to the

desired state. The desired state is the dark state of the process, and its population increases as photons are scattered. For trapped ions, the state preparation fidelity can easily be above 99%, mostly limited by laser imperfections such as polarization impurity [18].

Calcium

We depopulate the unwanted ground-state level $\left|S_{1/2}, m_J = -1/2\right\rangle$ by coupling a σ_+-polarized 397 laser resonantly to the transition $\left|S_{1/2}, m_J = -1/2\right\rangle \leftrightarrow \left|P_{1/2}, m_J = 1/2\right\rangle$. After a few μs, approximately 99.7% of the population is in the $\left|\downarrow\right\rangle$ state. The main source of infidelity comes from $\pi-$polarization impurity [47]. As mentioned before, the 397 nm laser has both σ_+ and σ_- components. Therefore we solely rely on frequency selectivity since the σ_- component is 444 MHz detuned from resonance. Further discussion about discrepancies of the experimental results from simulations can be found in Daniel Kienzler's thesis [47].

Beryllium

As mentioned in Section 2.5.1, state initialization and repumping is performed with a pair of σ_+ polarized beams that optically repump the states $\left|F = 1, m_F = 1\right\rangle$ and $\left|F = 2, m_F = 1\right\rangle$ to $\left|F = 2, m_F = 2\right\rangle$. Experimentally we observe that imperfect polarization of these beams is the major source of infidelity for state preparation.

To describe the state preparation infidelity we can assume that one of the repump beams, the one that couples the states $\left|S_{1/2}, F = 1, m_F = 1\right\rangle \rightarrow \left|P_{1/2}\right\rangle$ has some impure π polarization component [48]. This assumption is justified since this beam is the closest to resonance $\left|S_{1/2}, F = 2, m_F = 2\right\rangle \rightarrow \left|P_{1/2}\right\rangle$, which can lead to a population leakage outside the $\left|S_{1/2}, F = 2, m_F = 2\right\rangle$ state through a non σ_+ transition. An ion initially in state $\left|S_{1/2}, F = 2, m_F = 2\right\rangle$ can off-resonantly absorb a π polarized photon and get excited in the state $\left|P_{1/2}, F = 2, m_F = 2\right\rangle$, from which it will decay to $\left|S_{1/2}, F = 2, m_F = 1\right\rangle$ or $\left|S_{1/2}, F = 1, m_F = 1\right\rangle$. The infidelity caused by this process can be shown to be [48]:

$$e_{\text{init}} = \frac{4(1 + s_0)\epsilon_\pi}{1 + s_0 + 4\delta_\pi^2/\Gamma^2}, \tag{2.27}$$

where s_0 is the beam saturation intensity, ϵ_π the π polarization component, δ_π the detuning from resonance (for beryllium at 119.45 gauss, $\delta_\pi = 2\pi \times 142.7$ MHz) and Γ is the transition linewidth.

Experimentally, we then optimize the repump beam polarization by measuring how often the ion is found in the bright state $\left|S_{1/2}, F = 2, m_F = 2\right\rangle$. Figure 2.8a shows an example of imperfect state preparation, where at zero photon counts, there still is a significant amount of population, implying that part of the population leaked outside the $\left|S_{1/2}, F = 2, m_F = 2\right\rangle$ state. By adjusting the polarization of the beams with a $\lambda/4$ and $\lambda/2$ waveplates right before the viewport of the vacuum chamber, it is possible to suppress the dark state population, as shown in Figure 2.8b.

Another step of state preparation is necessary when working with the magnetic field-insensitive qubit. For this purpose, a resonant FDQ π-pulse transfers the population to the state $\left|F = 1, m_F = 1\right\rangle$. For the best transfer fidelity, the transition is driven with co-propagating Raman beams in order to decouple the operation from motional imperfections.

Chapter 3 explains in more detail why for intermediate counts the histogram shape does not follow exactly the Poisson distribution.
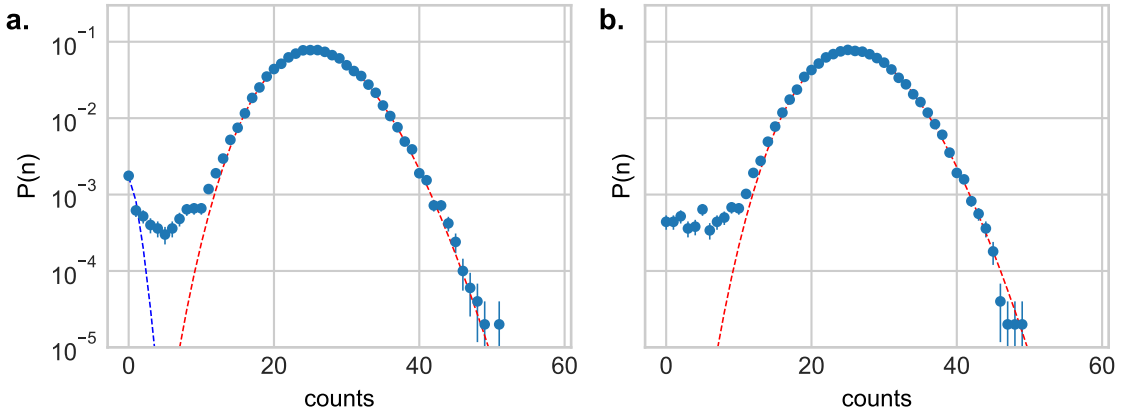
Figure 2.8: Photon count distribution for an ion prepared in the bright state. Panel **a**: histogram in the case of imperfect state preparation, where the blue dashed line is the simple Poisson fit for an ion in the dark state. The fitted residual population in the dark state is 0.3(1)%. The red dashed line is the fit for a Poisson distribution for a bright ion. Panel **b**: After optimizing the polarization, the dark state population at 0 counts is suppressed. Only the bright-to-dark leakage is still visible. For both plots, the data is a collection of 50000 detections.

2.7 Cooling of motional modes

High-fidelity gates usually require the motional modes of an ion crystal to be as close as possible to the ground state. To achieve this limit, we make use of a combination of steps. First, we apply Doppler cooling using a laser beam far detuned from an allowed dipole transition. This has a large capture range and thus is used to recover from large motional excitation. The second stage is a standard Doppler cooling sequence to reach the resolved-sideband regime on all the modes. For calcium, the next step is Electromagnetically-induced transparency (EIT) cooling, which is a fast and broadband cooling technique used to bring the population of all the calcium modes below $\bar{n} = 1$. For beryllium, this technique is not applicable with the current laser setup. As the last step, resolved-sideband cooling is useful to cool very close to the motional ground state.

An introduction to each of those cooling techniques together with ion-specific implementation details is given in the following subsections.

2.7.1 Doppler cooling

For the description of the Doppler cooling technique I will follow a similar approach to the one explained in [51]. In particular, I will assume the Doppler cooling of a single trapped ion, where, in a simplified picture, the ion is a two-level system interacting with a light field red-detuned from the resonance of a dipole-allowed transition. We also assume that the motional frequency ω_m is smaller than the transition linewidth Γ. We call this regime the weak-binding limit [73].

Following a semi classical treatment [74], the probability of finding the ion in the excited state is

$$p_{ee} = \frac{s/2}{1 + s + (2\Delta/\Gamma)^2},$$

(2.28)

where $s = 2|\Omega_0|^2/\Gamma^2$ is the saturation parameter which depends on the on-resonance Rabi frequency Ω_0, and Δ is the detuning from resonance.

The rate at which the ion kinetic energy is cooled is then [51]

$$\frac{dE_K}{dt} = \frac{2\hbar\Gamma}{m}\left(\frac{dp_{ee}}{d\Delta}\right)\frac{(\mathbf{k}\cdot\mathbf{p})^2}{2m},\tag{2.29}$$

where m is the mass of the ion, $\mathbf{k}$ is the cooling laser wave vector, and $\mathbf{p}$ is the ion momentum. The term $\mathbf{k}\cdot\mathbf{p}$ can be written in terms of the normal modes coordinates (see Section 2.2) as [51]

$$\mathbf{k}\cdot\mathbf{p} = \sum_{\alpha=1}^{3}\sqrt{m}\mathbf{k}\cdot\mathbf{e}'_\alpha p'_\alpha\tag{2.30}$$

where $\mathbf{e}'_\alpha$ is the vector of the normal modes eigenvectors.

Assuming a quantized harmonic oscillator, the term p'_α can be written as in Equation 2.11. As a result the cooling rate for mode α can be written in terms of quanta per seconds as

$$\frac{dn_\alpha}{dt} = 2\omega_\alpha\eta_\alpha^2(n_\alpha + 1/2)\Gamma\left(\frac{dp_{ee}}{d\Delta}\right).\tag{2.31}$$

From the latter equation we can see that the cooling rate is proportional to the Lamb-Dicke parameter for mode α, and that it is largest when the detuning is set to be at the steepest point of the absorption profile $\Delta = \Gamma\sqrt{1+s}/2$.

The cooling process is limited by the random nature of photon absorption and emission which lead to a momentum diffusion that heats the ion [51, 50]. The absorption and emission of photons can be considered to be independent under the assumption of weak Rabi frequency ($\Omega \ll \Delta, \Gamma$). In this case, the heating rate can be described by

$$\frac{dn_\alpha}{dt} = \Gamma p_{ee}\left(\eta_\alpha^2 + \frac{2/5\hbar^2|\mathbf{k}|^2|\mathbf{e}_\alpha|^2}{2m}\right).\tag{2.32}$$

The first term is simply the absorption of a photon from the laser, while the second term describes the recoil effect during spontaneous emission. In this particular expression, the recoil term assumes a dipole emission pattern, and is an average over all the possible emission directions. This assumption is justified in the case of beryllium, where the emission pattern is that of a dipole since it only emits σ_+ photons. However, the emission pattern of calcium is a mixture of σ_+ and π polarization; in this case, Equation 2.32 needs to be modified to take it into account. Since it is not too important for the purpose of this thesis, and for simplicity, I will ignore this difference.

At equilibrium, the cooling and heating rates will balance, and the motional modes will reach an equilibrium temperature [50]. Assuming $\Delta = \Gamma\sqrt{1+s}/2$, the lowest achievable temperature is [50]

$$T_D = \frac{\hbar\Gamma\sqrt{1+s}}{4k_B}(1 + 2/5).\tag{2.33}$$

Calcium

Calcium Doppler cooling makes use of two laser frequency components at $397\,\mathrm{nm}$. The first one is π-polarized and couples the $\left|S_{1/2}, m_J = 1/2\right\rangle \leftrightarrow \left|P_{1/2}, m_J = 1/2\right\rangle$, the second one is σ_+-polarized and couples $\left|S_{1/2}, m_J = -1/2\right\rangle \leftrightarrow \left|P_{1/2}, m_J = 1/2\right\rangle$. We drive those

transitions at roughly half the saturation intensity with a detuning $\sim 5-10\,\text{MHz}$ red from the resonance for about $600\,\mu\text{s}$. Typical trapping frequencies used in our experiments are $\omega_z \simeq 2\pi \times 1.5\,\text{MHz}$ for the axial modes, and $\omega_x \simeq 2\pi \times 2.5\,\text{MHz}$ and $\omega_y \simeq 2\pi \times 3.5\,\text{MHz}$, for the two radial modes. The corresponding mean thermal occupancy for the axial and radial modes after cooling is $\bar{n}_{ax} \simeq 5$ and $\bar{n}_{rad} \simeq 3 - 4$.

Beryllium

Beryllium Doppler cooling utilizes the cycling transition that couples the $\left|S_{1/2}, F = 2, m_F = 2\right\rangle$ level to the $\left|P_{3/2}, F = 3, m_F = 3\right\rangle$ state. The beam is $\sim 10\,\text{MHz}$ red detuned and has an intensity of $\approx 2.5\,\mu\text{W}$ focused on $\sim 60\,\mu\text{m}$ spot size. The beam propagates along the B field and is σ_+ polarized. To ensure polarization purity, we use a Glan-Laser polarizer[6] and a set of $\lambda/2$ and $\lambda/4$ waveplates to correct for birefringence on the vacuum chamber viewport.

Imperfect polarization of the cooling beam leads to leakage pathways outside the cycling transition. The two states that get mostly populated are $|F = 2, m_F = 1\rangle$ and $|F = 1, m_F = 1\rangle$. During Doppler cooling, we continuously repump those states to $\left|S_{1/2}, F = 2, m_F = 2\right\rangle$ with the repump beams introduced in Section 2.5.1.

The typical trapping frequencies for beryllium are $\sim 2\pi \times 2.5\,\text{MHz}$ for the axial mode and $\sim 2\pi \times 10-12\,\text{MHz}$ for the two radial ones. After a cycle of Doppler cooling, which usually lasts for $600\,\mu\text{s}$, the average thermal state occupancy is $\bar{n}_{ax} \simeq 4$ and $\bar{n}_{rad} \simeq 1$ for the axial and the radial modes, respectively.

2.7.2 Far-detuned Doppler cooling

Far red-detuned Doppler cooling usually referred to as *pre-cooling*, is usually the first stage of the cooling sequence. Background gas collisions, imperfect transport, frequency drifts of the resonant detection laser might lead to large motional excitations. Therefore, a standard cooling mechanism such as Doppler cooling will be less effective due to a Doppler shift of the resonant transition frequency. Pre-cooling usually lasts for several milliseconds, and its large capture range decreases the probability of losing the ions.

Calcium

We use the π-polarized component of $397\,\text{nm}$ laser, that is red detuned by $\approx 40\,\text{MHz}$ from the $\left|S_{1/2}, m_J = 1/2\right\rangle \leftrightarrow \left|P_{1/2}, m_J = 1/2\right\rangle$ transition and at ≈ 100 saturation intensities [47]. The presence of just π polarized light implies that, as the photons are scattered, both ground state levels will be occupied with populations depending on the decay branching ratio from the excited $P_{1/2}$ manifold. For an ion in state $\left|S_{1/2}, m_J = -1/2\right\rangle$ the pre-cooling laser is detuned by $\approx 200\,\text{MHz}$ from the $\left|S_{1/2}, m_J = -1/2\right\rangle \leftrightarrow \left|P_{1/2}, m_J = -1/2\right\rangle$.

Beryllium

The pre-cooling laser has an intensity of $\sim 1\,\text{mW}$ focused to a waist of $\sim 60\,\mu\text{m}$, and is $\sim 600\,\text{MHz}$ detuned from the $\left|S_{1/2}, F = 2, m_F = 2\right\rangle \leftrightarrow \left|P_{3/2}, F = 3, m_F = 3\right\rangle$ transition. The pulse lasts on average for $2-3\,\text{ms}$. In beryllium, pre-cooling does not just recover from large excitations of the motion but also serves as an off-resonant repumper for the dark states in the $S_{1/2}$ manifold. The high optical power increases the probability of scattering

---

[6]Thorlabs GLB10-UV
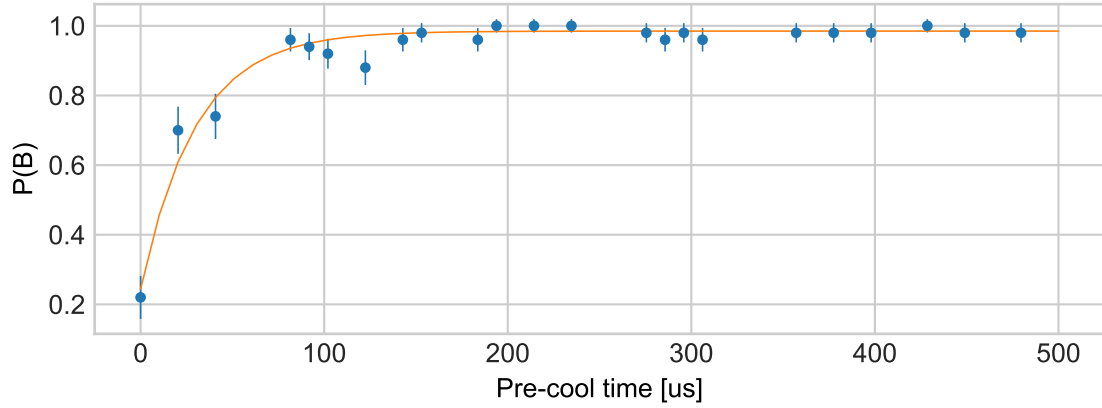
Figure 2.9: Pre-cooling repumping time trace. For an ion intially prepared in the shelved state $|F = 1, m_F = -1\rangle$ we measure the probability of detecting the ion in state $|F = 2, m_F = 2\rangle$ as a function of the pre-cooling pumping time.
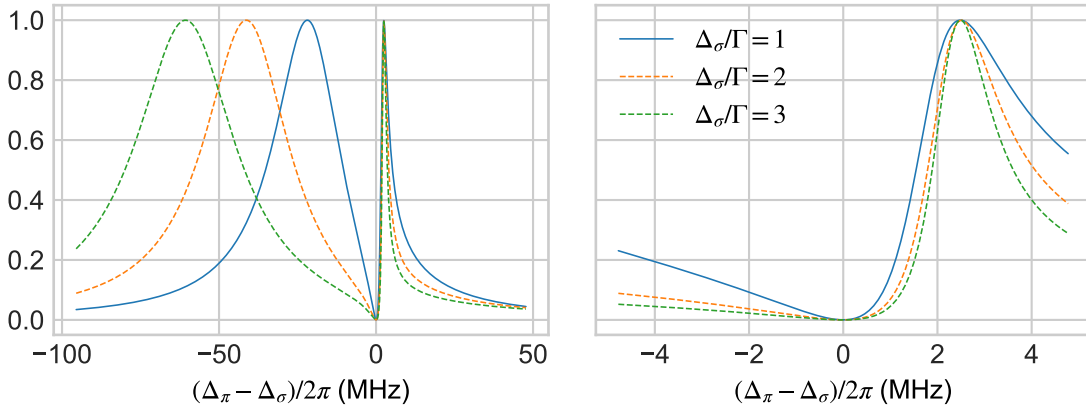
Figure 2.10: EIT lineshape as a function of the π detuning, for three different values of σ detuning. In each case the Ω_σ is adjusted such that the EIT resonance is at $\Delta = 2\pi \times 2.5$ MHz, which corresponds to the typical lowest radial freqeuncy we have with calcium experiments. $\Omega_\pi = \Omega_\sigma/100$ and $\Gamma = 2\pi \times 22.7$ MHz

photons off-resonantly from any of those levels, and the σ_+ polarization ensures that this shifts the population towards the $|S_{1/2}, F = 2, m_F = 2\rangle$ state.

The repumping time of an ion initially prepared in the shelved state $|F = 1, m_F = -1\rangle$ is used as a diagnostic for optimizing the detuned beam alignment. Figure 2.9 shows the probability of detecting the ion in the $|F = 2, m_F = 2\rangle$ state a function of the pre-cooling pulse time for an ion initially prepared in the shelved state.

2.7.3   Electromagnetically-induced transparency cooling

To go beyond the Doppler limit with a calcium ion, we use Electromagnetically-Induced Transparency (EIT) cooling [75], which acts on the $S_{1/2} \leftrightarrow P_{1/2}$ transition. The Doppler temperature is limited by the natural linewidth of the cooling transition, which for calcium

is $2\pi \times 22.7$ MHz. EIT cooling goes beyond the Doppler limit by creating a spectral feature that is narrower than the natural linewidth of the $S_{1/2} \leftrightarrow P_{1/2}$ transition. With the current optical setup, EIT cooling can only be performed on calcium.

A detailed theoretical description of EIT cooling can be found in [50, 76]. In our setup, we make use of two counter-propagating 397 nm beams at 45 degrees to the trap axis such that there is sufficient overlap of the difference wave vector $\mathbf{k}$ to all the modes. One of the beams is σ_+ polarized[7], and drives the transition $\left|S_{1/2}, m_J = -1/2\right\rangle \leftrightarrow \left|P_{1/2}, m_J = 1/2\right\rangle$, blue detuned by $\Delta_\sigma \sim 10$ MHz. The other one is weaker, purely π polarized, and couples the transition $\left|S_{1/2}, m_J = 1/2\right\rangle \leftrightarrow \left|P_{1/2}, m_J = 1/2\right\rangle$ with a similar blue detuning $\Delta_\pi \approx \Delta_\sigma$. We also assume that the excited state $|e\rangle = \left|P_{1/2}, m_J = 1/2\right\rangle$ decays to the states $\left|S_{1/2}, m_J = -1/2\right\rangle$ and $\left|S_{1/2}, m_J = 1/2\right\rangle$ at a rate rate Γ_σ and Γ_π, respectively.

The strong coupling of the σ_+ laser to the excited $\left|P_{1/2}, m_J = 1/2\right\rangle$ state creates an absorption profile for the weaker π-polarized laser that is advantageous for cooling. In particular, it can be shown that the scattering rate on the π-transition $\left|S_{1/2}, m_J = 1/2\right\rangle \leftrightarrow \left|P_{1/2}, m_J = 1/2\right\rangle$ is [50]

$$W(\delta) = \Gamma \rho_{ee}(\delta) = \frac{4\delta^2 \Omega_\pi^2 \Omega_\sigma^2 \Gamma^2}{D} \ , \tag{2.34}$$

where $\Gamma = \Gamma_\pi + \Gamma_\sigma$ is the total decay rate, ρ_{ee} is the population of the excited state as a function of the detuning $\delta = \Delta_\pi - \Delta_\sigma$, Ω_π (Ω_σ) is the Rabi frequency associated to the π (σ) transition and the denominator is [8]

$$\begin{aligned} D =& 8\delta^2 \Omega_\sigma^2 \Omega_\pi^2 \Gamma + 4\delta^2 \Gamma^2 \left(\Omega_\sigma^2 \Gamma_\pi + \Omega_\pi^2 \Gamma_\sigma\right) \\ &+ 16\delta^2 \left[\Delta_\sigma^2 \Omega_\pi^2 \Gamma_\sigma + \Delta_\pi^2 \Omega_\sigma^2 \Gamma_\pi\right] + 8\Delta_\sigma \delta \Omega_\pi^4 \Gamma_\sigma \\ &- 8\Delta_\pi \delta \Omega_\sigma^4 \Gamma_\pi + \left(\Omega_\sigma^2 + \Omega_\pi^2\right)^2 \left(\Omega_\sigma^2 \Gamma_\pi + \Omega_\pi^2 \Gamma_\sigma\right) \ . \end{aligned} \tag{2.35}$$

The lineshape as a function of the detuning Δ_π is shown in Figure 2.10. For $\Omega_\sigma \gg \Omega_\pi$, it features a zero for $\Delta_\pi = \Delta_\sigma$, and a sharp resonance centered at $\Delta_\pi = \Delta_\sigma + \delta$ [50, 76, 75], with

$$\Delta = \frac{\sqrt{\Delta_\sigma^2 + \Omega_\sigma^2} - |\Delta_\sigma|}{2} \tag{2.36}$$

originating from the ac Stark shift of the σ_+ laser. For optimal cooling of mode m, it is possible to adjust the parameters $(\Delta_\sigma, \Omega_\sigma)$ such that $\Delta = \omega_m$, with ω_m the frequency of the motional mode. In this case, and for $\Delta_\pi = \Delta_\sigma$, the ion can resonantly absorb a π-polarized photon at the cost of one quantum of motion $\hbar \omega_m$ leading to cooling. The absorption at $\Delta_\pi = \Delta_\sigma - \omega_m$ sets the cooling limit, which for $\Delta = +\omega_m$ happens at a lower rate since $W(-\omega_m) < W(\omega_m)$. It can be shown that for $\Delta = \omega_m$, the motional occupancy of mode m after EIT cooling is a thermal state with an average phonon number of [76, 50]

$$\bar{n} \simeq \left(\frac{\Gamma}{4\Delta_\sigma}\right)^2 \ . \tag{2.37}$$

---

[7]In our setup, the σ_+ beam does not have a pure polarization, but it is in an equal mixture of σ_+ and σ_- polarization. Since the σ_- component is about 20 linewidths detuned from the undesired transition $\left|S_{1/2}, m_J = 1/2\right\rangle \leftrightarrow \left|P_{1/2}, m_J = -1/2\right\rangle$, it results in a negligible contribution to the heating.

[8]In the literature, there are two slightly different expressions for the denominator that originates from two different sources. The first is in [77], while the second is [78]. In [77], the Bloch equations are not given; thus, it is not possible to verify the result. It may be that they made a particular assumption to the decay rates, which are not stated in the paper. The difference is mostly visible in the width of the EIT resonance. From a qualitative comparison of the expected lineshape with the experimental parameters given in the text, the width of the resonance can be up to twice as broad for [77].
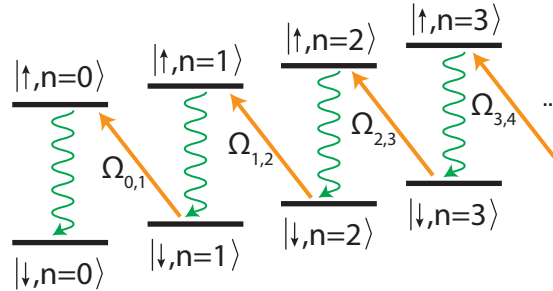
Figure 2.11: One cycle of resolved-sideband cooling. First a a red sideband pulse is applyed (orange arrows) and consequently the spin in reset to the ground state (green arrows). Repeating this cycle several times gradually pumps the population in $|\downarrow, n = 0\rangle$.

A thermal occupancy close to the ground state of motion is thus achievable for large detunings $\Delta_\sigma + \Delta_\pi \gg \Gamma$, at the cost of higher σ Rabi frequency (Equation 2.36). One implicit assumption that we made in this treatment is that spontaneous emission does not alter the average motional quantum number. This assumption is valid as long as we start in the Lamb-Dicke regime [76], as the spontaneous emission predominantly happens through carrier scattering, thus leaving the motional states mostly untouched (in general, the average energy per scattering event is $\eta^2\Omega$).

In the experiment we mostly work in the low detuning regime, with $\Delta_\sigma \approx \Gamma$. This allow us to bring all the calcium motional modes below $\bar{n} = 1$ within $\sim 300\,\mu$s of EIT cooling. To reach the ground state of motion we then apply sideband cooling.

2.7.4   Resolved-sideband cooling

Resolved-sideband cooling, also referred to as *sideband cooling*, is applied as the last cooling step, and it is used to cool specific motional modes near the ground state of motion. It works in the strong-binding regime [73], where the linewidth Γ of the transition used for cooling is small compared to motional mode frequency ω_m. Sideband cooling generally relies on the manipulation of the qubit transition $|\downarrow\rangle \leftrightarrow |\uparrow\rangle$ to optically pump into the state $|\downarrow, n = 0\rangle$, where $n = 0$ is the harmonic oscillator ground state. A cycle of sideband cooling consists of two steps. For an ion initially in state $|\downarrow, n\rangle$, we first drive the $|\downarrow, n\rangle \leftrightarrow |\uparrow, n - 1\rangle$ red sideband transition, to remove a quantum of motion. In a second step, the internal state of the qubit is reset to $|\downarrow\rangle$ by coupling the excited state $|\uparrow\rangle$ to a short-lived atomic level that decays to $|\downarrow\rangle$. The process is then repeated until the system reaches the ground state $|\downarrow, n = 0\rangle$. A schematics diagram of the process can be seen in Figure 2.11.

Generally, the initial population is not in a well defined Fock state but rather in a thermal distribution with an average phonon number $\bar{n}$, in which each motional state has its own red sideband Rabi frequency (Section 2.3). As the population shifts towards the motional ground state, the average red sideband Rabi frequency decreases. To partially mitigate this effect and to increase the cooling efficiency, at each cycle, we lengthen the red sideband pulse time.

The primary heating mechanisms are off-resonant driving of the carrier transition and blue sideband transitions. Carrier excitations happen with probability $[\Omega/(2\omega_m)]^2$, but will mostly decay back on the carrier transition [50]. Heating occurs if there is a decay along the blue sideband transition after a carrier excitation. The rate at which this happens is $[\Omega/(2\omega_m)]^2\tilde{\eta}^2\Gamma$, where $\tilde{\eta}$ is the Lamb-Dicke parameter for this decay path[9]. The other heating mechanism is the off-resonant excitation of the blue sideband transition followed by a decay on the carrier transition. The rate at which this decay process happens is $[\eta\Omega/(4\omega_m)]^2\Gamma$, with η the Lamb-Dicke parameter for the sideband excitation. Finally, it can be shown that these two heating mechanisms limit the ground state occupancy to $p_0 \approx 1 - (\Gamma/2\omega_m)^2$, which is close to 1 [50].

In calcium, the small Lamb-Dicke parameter $\eta \simeq 0.05$, makes the sideband transition more susceptible to the off-resonant excitation of the carrier and blue sideband. We mitigate this effect by shaping the sideband pulse amplitude to reduce the spectral power at the carrier and blue sideband frequencies.

The figure of merit for the calibration of sideband cooling parameters is the contrast of the blue sideband Rabi oscillations. Consider a single ion initially prepared in $|\downarrow\rangle$ and with a motional state probability distribution $\{p_n\}$. For thermal states, it can be written as $p_{n,\text{therm}} = \bar{n}^n/(1+\bar{n})^{n+1}$, where the the term $\bar{n}$ is the average motional state occupancy. Under the application of a resonant blue sideband pulse, it can be shown from Equation 2.22 that state $|\downarrow\rangle$ evolves according to

$$
\begin{aligned}
p_\downarrow(t) = 1 - p_\uparrow(t) &= 1 - \sum_{n=0}^{\infty} p_n \sin^2 \frac{\Omega_{n+1,n}t}{2} \\
&= \frac{1}{2} + \frac{1}{2}\sum_{n=0}^{\infty} p_n \cos(\Omega_{n+1,n}t) \ ,
\end{aligned}
\tag{2.38}
$$

where the resonant blue sideband Rabi frequency, $\Omega_{n+1,n}$, can be calculated from Equation 2.16. Figure 2.12, shows a set of possible blue sideband Rabi oscillations for beryllium (panel a) and for calcium (panel b) for a thermal state distribution with $\bar{n} \in [0,5]$. In the ideal case of perfect cooling ($\bar{n} = 0$), oscillations are between the states $|\downarrow,0\rangle \leftrightarrow |\uparrow,1\rangle$. Experimentally, blue sideband pulses with duration in the highlighted green area provide a sensitive measure to minimize the temperature of the ion. At the end of the optimization, a fit of Equation 2.38 to the experimental blue sideband oscillations, assuming a thermal probability distribution, give a measure of the average motional state occupancy $\bar{n}$.

Experimentally, we replace the blue sideband pulse with a carrier π-pulse followed by a red sideband pulse. The effect is analogous to driving the blue sideband, but it provides a direct calibration of the red sideband frequency, which is the parameter used in sideband cooling.

Beryllium

Due to the beam geometry (see Section 2.5.1), sideband cooling can either be performed on the axial or radial modes. In all the experiments described here, the axial modes are the only ones that are sideband cooled.

---

[9]In general, the Lamb-Dicke parameter $\tilde{\eta}$ for the decay along the blue sideband is different from the Lamb-Dicke parameter η that is related to the excitation of the sideband transition, since that photons can be emitted in any direction and not just along the cooling laser's wave vector. On top of this, some experimental realizations make use of three level system, for which the emitted photon can have a different wavelength from that of the cooling laser [50].
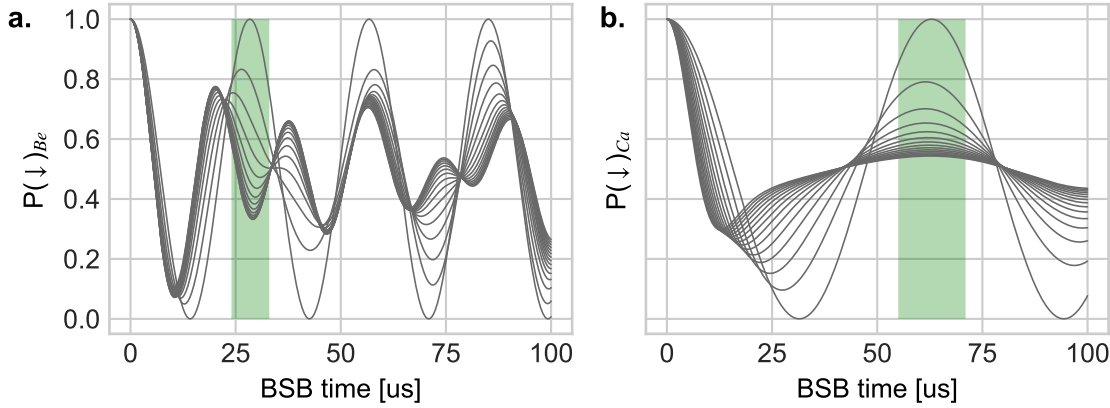
Figure 2.12: Blue sideband Rabi oscillations for beryllium (panel **a**) and calcium (panel **b**), assuming thermal state distribution with $\bar{n} \in [0, 5]$ (the curve with the biggest contrast corresponds to the lowest excitiation). In both cases, the Lamb-Dicke approximation is not applied. In the case of beryllium, the resonant carrier Rabi frequency is assumed to be $\Omega_0 = 2\pi \times 0.3\,\text{MHz}$ and $\eta = 0.4$ corresponding to the typical experimental parameters of the FDQ transition. For calcium $\Omega_0 = 2\pi \times 1\,\text{MHz}$ and $\eta = 0.05$.

Experimentally, Raman beams at a 90° drive the FDQ red sideband transition. For a single-species beryllium crystal, the red sideband Rabi frequency vanishes for motional state $n \approx 22$ due to the Lamb-Dicke paramter $\eta \approx 0.4$. For optimal cooling, it is necessary to pump the population from higher Fock states below this number. We found that a few rounds of second-order sideband cooling achieve this goal and improve the overall contrast of the carrier Rabi oscillations driven with the motion-sensitive configuration. For a mixed-species crystal this trick is not necessary since the motional modes can be sympathetically cooled below this point by calcium EIT cooling.

2.8   Mixed-species normal modes and basic sequence

In Section 2.2, I defined the normal modes of motion and introduced the basic operations to cool and initialize calcium and beryllium ions. Within this section, I will first present the main characteristics of mixed-species normal modes in the case of ion chains composed of calcium-beryllium and beryllium-calcium-beryllium. Finally, I will present the basic experimental sequence used for the mixed-species experiments described in this thesis.

2.8.1   Normal modes characteristics

In general, the normal modes of motion of mixed-species present several features, which mostly depend on the mass-ratio of the two species. In Table 2.1, is shown an example of the normal modes eigenfrequency and eigenvectors for the a beryllium-calcium ion chain. The values are the typical ones used in the mixed-species experiments presented in this thesis. The eigenvector $\mathbf{e}'_{i,\alpha}$ are in turn related to the Lamb-Dicke parameter $\eta_{j,\alpha}$ by

$$\eta_{j,\alpha} = \sqrt{\frac{\hbar}{2m_j\omega_\alpha}}\boldsymbol{k} \cdot \boldsymbol{e}'_{j,\alpha}, \tag{2.39}$$

where $\mathbf{k}$ is the laser wave vector used to couple to the normal mode α.

$\omega_\alpha/2\pi$ (MHz)	Be$^+$			Ca$^+$		
	$e'_{x1,\alpha}$	$e'_{y1,\alpha}$	$e'_{z1,\alpha}$	$e'_{x2,\alpha}$	$e'_{y2,\alpha}$	$e'_{z2,\alpha}$
1.779	0	0	0.272	0	0	0.962
2.145	0	−0.014	0	0	1	0
3.226	0.013	0	0	−1	0	0
4.614	0	0	0.962	0	0	−0.272
13.023	0	−1	0	0	−0.014	0
13.976	1	0	0	0.013	0	0

Table 2.1: Normal mode eigenfrequencies and mass-weighted eigenvectors for beryllium-calcium crystal. The single calcium secular frequencies used for the calculations are $[\omega_x, \omega_y, \omega_z] = 2\pi \times [2.4, 3.4, 1.5]$MHz. The calculated eigenfrequencies are the typical values used for the beryllium-calcium experiments presented in this thesis.
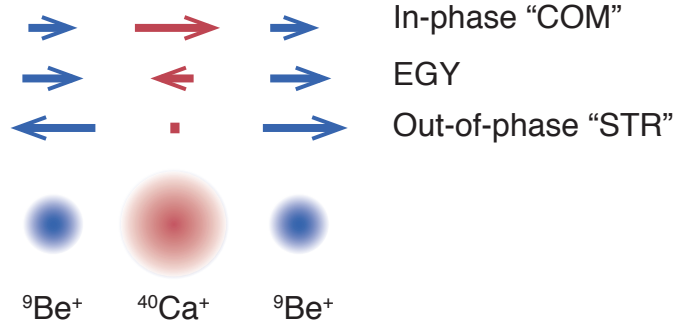
Figure 2.13: Axial motional modes of the beryllium-calcium-beryllium ion chain. The arrow lengths are not in scale with the amplitude of the oscialltions.

One interesting feature in Table 2.1, is that the radial modes of motion (x, y) for the two species are almost independent. To understand it, we have to remember the in the radial plane the confining potential felt by each species is proportional to m^{-1}. This means that if we consider the motion of the two species as independent (neglecting the Coulomb repulsion), the radial frequencies for the two ions would have different values. As a result, in the coupled case, the energy exchange due to the Coulomb coupling is far off-resonant and has a small effect on the resulting motion [51].

A similar behavior can also be observed in Table 2.2, where the normal modes frequencies and eigenvectors are shown for a beryllium-calcium-beryllium ion chain. Figure 2.13, shows the axial motional modes for this particular ion chain. It is worth noticing that for the motional mode labeled as "STR" (stretch mode), the two beryllium ions oscillates out-of-phase with respect to each other, while the calcium ion does not move. This feature is particularly important for the experiments presented in Chapter 6 because it means that the calcium lasers cannot excite, nor cool, this motional mode.

A detailed experimental investigation of shifts from the theoretical normal mode structure, can be found in Section 5.2.1.

$\omega_\alpha/2\pi$ (MHz)	Be$_1^+$ $e'_{x1,\alpha}$	$e'_{y1,\alpha}$	$e'_{z1,\alpha}$	Ca$^+$ $e'_{x2,\alpha}$	$e'_{y2,\alpha}$	$e'_{z2,\alpha}$	Be$_2^+$ $e'_{x3,\alpha}$	$e'_{y3,\alpha}$	$e'_{z3,\alpha}$	
1.56	0	0	0.312	0	0	0.897	0	0	0.312	COM
2.141	0	-0.013	0	0	1	0	0	-0.013	0	
3.064	0.012	0	0	-1	0	0	0.012	0	0	
4.194	0	0	-0.707	0	0	0	0	0	0.707	STR
4.284	0	0	0.634	0	0	-0.442	0	0	0.634	EGY
13.179	0	0.707	0	0	0	0	0	-0.707	0	
13.179	0	0.707	0	0	-0.019	0	0	-0.707	0	
13.963	0.707	0	0	0	0	0	-0.707	0	0	
13.963	-0.707	0	0	-0.017	0	0	-0.707	0	0	

Table 2.2: Normal mode eigenfrequencies and eigenvectors for beryllium-calcium-beryllium crystal. The single calcium secular frequencies used for the calculations are $[\omega_x, \omega_y, \omega_z] = 2\pi \times [2.6, 3.4, 1.15]$MHz. The calculated eigenfrequencies are the typical values used for the beryllium-calcium experiments presented in this thesis. In the last column I highlighted the three axial modes with the naming convention used in this thesis.

2.8.2 Basic experimental sequence

Figure 2.14 shows an oscilloscope view of a typical pulse sequence for the cooling and detection used for mixed species experiments. The structure of the experimental sequence is common for all mixed-species experiments presented in this thesis. The main differences are in the sideband cooling stage and in the qubit manipulation. The majority of the results presented in later chapters involve coupling between ions of different species. This is best achieved by addressing the axial mode of motion (usually the in-phase mode, also referred to as "COM" in this thesis) which involve a significant motion from both species, according to Table 2.1 and Table 2.2. To achieve the highest gate fidelities the axial modes of motion are usually cooled near the ground state. For the mixed-species ion chain configurations (beryllium-calcium and beryllium-calcium -beryllium), beryllium sideband cooling is typically used to ground-state cool the higher axial normal modes, due to the larger Lamb-Dicke parameter. Finally beryllium or calcium sideband cooling is used to groud-state cool the in-phase axial mode, which is the principal motional mode used for coupling the two species.

Further details about the experimental sequences will be given throughout the thesis when presenting results.

Figure 2.14: Pulse sequence diagram of a mixed-species experimental shot; At the bottom the typical length for each step of the sequence.

3 State readout

Upon completion of the experimental sequence, the qubit states are read out. For all the experiments described in this thesis, the preferred readout method is state-dependent fluorescence [79, 80, 81]. With this technique, a detection laser beam resonantly couples one of the two qubit states to an excited state via a dipole allowed transition. For an ion initially in $|\psi\rangle = a\,|\text{bright}\rangle + b\,|\text{dark}\rangle$, the detection collapses the state into the bright state with probability $|a|^2$. During detection, a bright ion fluoresces at a rate of $10^7 - 10^8$ photons/s. The wavelength of the fluorescence photons is $397\,\text{nm}$ for calcium and $313\,\text{nm}$ for beryllium. An in-vacuum objective, effectively covering 4.4% of the 4π solid angle [48], captures some of the emitted photons which are then detected with a photomultiplier tube (PMT). The PMT quantum efficiency (26.5% at $313\,\text{nm}$ and 30% at $397\,\text{nm}$), together with an estimated loss of $\approx 15\%$ in optics and vacuum chamber windows, limits the total detection efficiency to $\approx 1\%$ [48]. As a result, for a typical detection time of $200\,\mu\text{s}$, the average number of photons detected for a bright ion is 30.

Assuming that the detection of photons happens at a constant rate and independently of the time of previous detection events[1], the photon count distribution follows Poisson statistics. The Poisson distribution is defined as

$$P(n|\lambda) = \frac{\lambda^n e^{-\lambda}}{n!}\ , \tag{3.1}$$

where λ is the average number of photons detected within an detection interval t_d. Ideally, for an ion initialized in the dark state, the average number of photons is $\lambda_D = 0$. Despite this, stray light shining on the detector, electrical noise and cosmic rays contribute to an average background photon counts $\lambda_D = R_D t_d$, where R_D is the background photon counting rate. In our experiments in $200\,\mu\text{s}$ the average background counts are $\lambda_D < 0.5$. For an ion in the bright state, the average number of photons detected within the detection time t_d is $\lambda_B = (R_B + R_D)t_d$, with R_B the detected photon fluorescence rate[2].

For a single ion in state $|\psi\rangle = a\,|\text{bright}\rangle + b\,|\text{dark}\rangle$, the probability of detecting n photons within a detection interval t_d is a superposition of two Poisson distribution

$$p(n) = p_0 P(n|\lambda_D) + p_1 P(n|\lambda_B), \tag{3.2}$$

where, $p_0 = |b|^2$ is the probability that the ion collapses in the dark state and $p_1 = |a|^2$ the probability that the ion is collapsed in the bright state.

At the end of the detection, the number of photons detected by the PMT is transmitted to the control electronics that manages the experiment (see Chapter 4), where it is processed to discriminate the state of the ion. The discrimination relies on data processing, as relevant information is carried by the number of photons detected, but also the time at which they

---

[1]We expect this assumption to hold since the detection of a photon is a rare event.

[2]R_B, R_D already take into account the global detection efficiency of the setup, which depends both on the properties of the lens system (ie. numerical aperture, lens coating etc...) and on the quantum efficiency of the PMT.

are detected. For the rest of chapter whenever I talk about 'detection' I will refer to the act of measuring the ion fluorescence, while 'readout' refers to qubit state discrimination.

Within this chapter I will first describe the standard techniques used for state discrimination. I will then focus the attention to the case in which the photon counting distribution does not follow the Poisson one, due to pumping mechanisms that alter the ion population during detection. The chapter continues summarizing and presenting experimental results of readout techniques that are based on the photon arrival time. Finally, I will extend these methods to a novel technique that offers the possibility of further reducing the detection time using entropy gain as a key element.

3.1 Thresholding

Thresholding is the simplest method for discriminating a bright ion from a dark one. The state of the ion is determined by comparing the total number of photons n collected during a detection event to a threshold value n_{th}. Trials where $n \geq n_{\text{th}}$ label the qubit in the bright state, those with $n < n_{\text{th}}$ label the qubit in the dark state. At the end of a data point, the fraction of times that the ion produced fluorescence above (below) threshold gives the value for the probability of being bright (dark) $P(b)$ ($P(d)$).

For Poisson distributions, it can be shown [58] that the optimal threshold lies at the intersection of the two distributions

$$n_c = \frac{\lambda_B}{\ln\left(1 + \frac{\lambda_B}{\lambda_D}\right)} \ . \tag{3.3}$$

It follows that the discrimination error is purely statistical and it is proportional to the overlap of the two distributions.

One of the main advantages of thresholding is that it is computationally fast and allows state discrimination after a single detection shot. This feature is particularly important for advanced experiments, like teleportation and quantum error correction, which require conditional operations based on the readout within the same experimental shot. For these particular cases, single shot readout needs to be of high fidelity. Experimentally it is thus advisable to suppress the background count rate R_D as much as possible while improving the bright fluorescence rate R_B.

The thresholding method can also be extended to crystals composed of m ions of the same species. Assuming that the ions are equally illuminated by a detection beam and that no spatial resolution of the emitted photons is possible[3], the probability of detecting n photons is a linear combination of $m + 1$ Poisson distribution

$$p(n) = \sum_{i=0}^{m} p_i P(n|\lambda_i) \tag{3.4}$$

where $P(n|\lambda_i)$ is defined in Equation 3.1 and the average photon counts are approximately $\lambda_i = \lambda_0 + i(\lambda_1 - \lambda_0)$ for equally illuminated ions, where λ_0 and λ_1 are the means of the 0-th and first Poisson distributions. In this case m thresholds are needed to perform state

---

[3]Spatial resolution is possible by mapping different ions in the chain to different channels of a multi-channel PMT array [82] or to different pixels of an electron-multiplied CCD camera [83]. In all the experiments presented in this thesis, readout is done primarily through a single channel PMT.
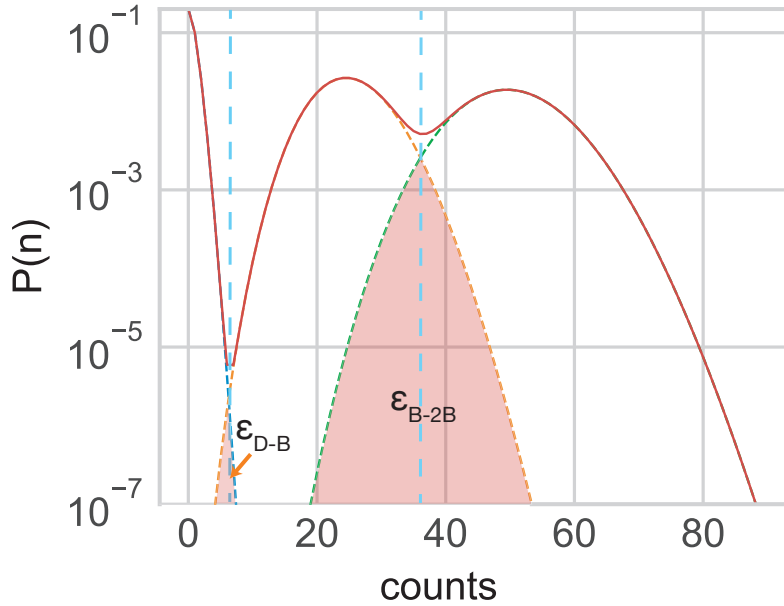
Figure 3.1: Thresholding error. The red solid curve is a simulated histogram for two ions with Poisson means $\lambda_0 = 0.5$, $\lambda_1 = 25$ and $\lambda_2 = 50$. The light blue dashed lines are the two optimal thresholds. The discrimitation error is proportional to the area where two Poisson distribution intersect. From the plot, it is clear that the largest error occurs when discriminating between one bright ion and two.

discrimination. The variance of the Poisson distribution scales as $\sqrt{\lambda_i}$. Therefore the overlap, and thus the discrimination error, is the largest between $P(n|\lambda_{m-1})$ and $P(n|\lambda_m)$. Figure 3.1 shows an example of the Poisson distributions for two equally illuminated ions, with photon means similar to the experimental ones.

3.1.1   Dealing with imperfect readout

Consider the imperfect state readout of a single ion in which there is some non-negligible overlap between the two Poisson distributions. Extracting the full information about the quantum state of the ion is still possible under the assumption that one can find the probabilities of being bright $P(b)$ and dark $P(d)$, as introduced above. Therefore this method cannot be applied for experiments that require single shot readout. The main idea is presented in the Ph.D. thesis of Jonathan Home [84].

Let's define $p = P\left(b|\,|\text{bright}\rangle\right)$ as the probability that an ion prepared in the bright state produces fluorescence above the threshold n_c, and $q = P\left(d|\,|\text{dark}\rangle\right)$ the probability the an ion in the dark states produces fluorescence below the threshold n_c. The probability $P(b)$ that an ion fluoresces above threshold, given that it has probability $P\left(|\text{bright}\rangle\right)$ of being the the bright state, and probability $P\left(|\text{dark}\rangle\right)$ of being in the dark one is

$$P(b) = pP\left(|\text{bright}\rangle\right) + (1-q)P\left(|\text{dark}\rangle\right) \ . \tag{3.5}$$

Similarly we can write the probability $P(d)$ that an ion fluoresces below the threshold.

Written in form of matrices

$$
\begin{pmatrix} P(d) \\ P(b) \end{pmatrix} = \begin{pmatrix} q & 1-p \\ 1-q & p \end{pmatrix} \begin{pmatrix} P(|\text{dark}\rangle) \\ P(|\text{bright}\rangle) \end{pmatrix} . \tag{3.6}
$$

To deduce the state of the ion after detection this matrix can be inverted, and obtain

$$
\begin{pmatrix} P(|\text{dark}\rangle) \\ P(|\text{bright}\rangle) \end{pmatrix} = \frac{1}{p+q-1} \begin{pmatrix} p & p-1 \\ q-1 & q \end{pmatrix} \begin{pmatrix} P(d) \\ P(b) \end{pmatrix} . \tag{3.7}
$$

This technique can also be generalized to the state readout of more than one ion. For the case of two ions, two thresholds are needed. Assuming no spatial resolution for the detected photons, and equal illumination of the detection beams on the two ions, it is possible to extract the populations $P(dd)$, $P(db+bd)$ and $P(bb)$ at the end of a data point, in a similar way to what described above. $P(db+bd)$ is the probability that one of the two ions is labeled bright and is defined as $P(db+bd) = P(bd) + P(db)$. The probability that both ions fluoresce above threshold, assuming that their are both initialized in the bright state, is $P(bb|\,|\text{BB}\rangle) = p^2$, where $|\text{BB}\rangle = |\text{bright}\rangle \otimes |\text{bright}\rangle$ for compactness. Similarly $P(dd|\,|\text{DD}\rangle) = q^2$. For each data point the the states can then be calculated as

$$
\begin{pmatrix} P(|\text{DD}\rangle) \\ P(|\text{DB+BD}\rangle) \\ P(|\text{BB}\rangle) \end{pmatrix} =
$$
$$
\frac{1}{(p+q-1)^2} \begin{pmatrix} p^2 & p(p-1) & (1-p)^2 \\ 2p(q-1) & 2pq-p-q+1 & 2q(p-1) \\ (q-1)^2 & (q-1)q & q^2 \end{pmatrix} \begin{pmatrix} P(dd) \\ P(db+bd) \\ P(bb) \end{pmatrix} . \tag{3.8}
$$

This readout method is also computationally fast, and just requires an initial calibration of the parameters p and q.

3.2 Histogram fitting

An alternative technique to thresholding is histogram fitting. It consists of fitting a distribution to the aggregate histogram of the counts for an experimental point. This technique is well suited when the discrimination error with thresholding is significant. It can also be advantageous when the modeled distribution is not purely Poissonian, as discussed in Section 3.3.

In our experiments, we implement the least-squares fitting of Equation 3.4 to the aggregate histograms of a data point. The calculation consists of two stages. Initially, we create a single 1D histogram composed of all the shots of a scan, and by fitting both $\{p_i\}$ and $\{\lambda_i\}$, we extract the average photon counts $\{\lambda_i\}$. In a second step, for each point of the experiment, the populations $\{p_i\}$ are fitted to the aggregate histogram while keeping the mean photon counts fixed. Experimentally, we noticed that at least 100 shots per data point are needed to have reliable fits.

Compared to the previous two methods, histogram fitting is slow, thus we use it only in post-analysis. During run-time we prefer to use thresholding or the method presented in Section 3.1.1.
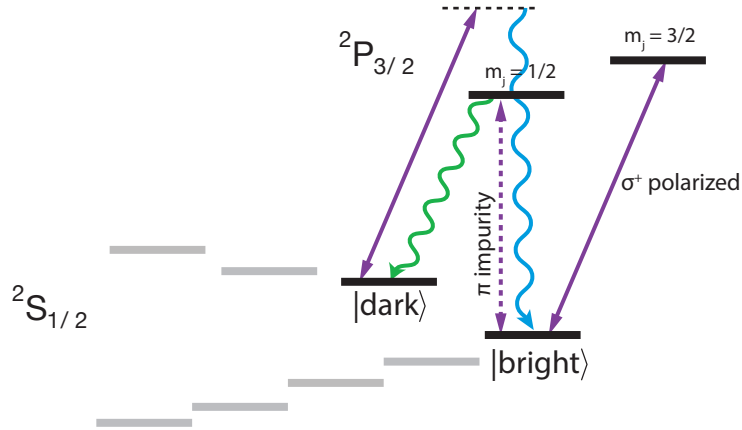
Figure 3.2: Population leakage in beryllium. In blue is shown the dark-to-bright pumping due to off-resonant scattering from the dark state, and is intrinsic to the detection technique. In green is indicated the bright to dark leakage due to polarization impurities of the detection beam.

3.3 Non Poisson statistics

In the previous sections we assumed the that the photon counting statistics is well modeled by Poisson distributions. One of the assumptions that we made is that once the state of the ion is collapsed into either the bright or the dark state, the ion continues to fluoresce at a constant rate. A change in the ion state within a detection event will modify the photon emission rate. If the time in which the ion switches state is not controlled and happens at random times, the photon counting statistics deviate from the Poissonian one.

There can be different reasons for which the state of the ion changes. In calcium the main contribution to state change is spontaneous decay. For our experiment, the dark state of calcium is the $\left|D_{5/2}, m_J = 3/2\right\rangle$ level, which has a lifetime of ~1.1 s. This means that, for a detection time of 200 μs, the probability that the dark state decays to the bright ground state during the detection is $\sim 10^{-4}$. At our current fidelities for other operations this does not provide a significant restriction.

In beryllium instead there are two different mechanisms that can change the state of the ion during detection. Those are illustrated in Figure 3.2. The first, is off-resonant pumping of a dark state into the bright one. The second, is impure polarization of the detection beam or state mixing that makes the detection transition not closed, thus leading to pumping of the bright state into the dark one.

3.3.1 Dark-to-bright leakage

To show how the distribution changes, I will follow a similar approach to the one presented in the Ph.D. theses of Chris Langer and Alice Burrel [55, 58]. Let's assume that an ion is initially prepared in the dark state, and that at time $t = 0$ it begins a detection event of duration t_b. Assuming a dark-to-bright repump rate $\omega = 1/\tau$, the probability that the ion is found in the bright state after time t $(t < t_b)$ is

$$P_{\mathrm{B}}(t) = 1 - e^{-t/\tau} \ . \tag{3.9}$$

It follows that the probability that a decay happens between t and $t + \mathrm{d}t$ is

$$p(t)\mathrm{d}t = \frac{1}{\tau}e^{-\frac{t}{\tau}}\mathrm{d}t \ . \tag{3.10}$$

If a repump event always occurs at a well-defined time t (with $t < t_b$), the number of counts n collected in within a detection interval t_b would follow a Poisson distribution with a mean of $\lambda(t)$

$$\lambda(t) = R_D t_b + R_B \left(t_b - t \right) \ . \tag{3.11}$$

In reality, the repump time t is a continuous random variable. Therefore, what we need to calculate is the density of means $p(\lambda)$. The mean photon counts λ is single valued with respect to t. We can therefore assume that

$$|p(t)\mathrm{d}t| = |p(\lambda)\mathrm{d}\lambda| \tag{3.12}$$

for $\lambda = \lambda(t)$. Using Equation 3.10 it follows that

$$p(\lambda)\mathrm{d}\lambda = p(t(\lambda))\frac{\mathrm{d}t}{\mathrm{d}\lambda}\mathrm{d}\lambda = \frac{1}{\tau}e^{-t(\lambda)/\tau}\frac{\mathrm{d}t}{\mathrm{d}\lambda}\mathrm{d}\lambda \ . \tag{3.13}$$

Extracting t from Equation 3.11, and substituting it into Equation 3.13 we derive the probability distribution $p(\lambda)\mathrm{d}\lambda$ as

$$p(\lambda)\mathrm{d}\lambda = \frac{1}{R_B\tau}\exp\left(\frac{\lambda - t_b\left(R_D + R_B\right)}{R_B\tau}\right)\mathrm{d}\lambda \ . \tag{3.14}$$

It follows that, for an ion prepared in the dark state, the probability $P_{dark}(n, t_b)$ that we detect n photons within t_b is the sum of all the Poisson distributions with mean values between $\lambda_D = R_D t_b$ and $\lambda_B = (R_D + R_B)t_b$ weighted by the density of the means $p(\lambda)$

$$
\begin{aligned}
P_{\mathrm{dark}}(n, t_b) &= P_{\mathrm{D}}(t_b)P(n|\lambda_D) + \int_{\lambda_D}^{\lambda_B} p(\lambda)P(n|\lambda)\mathrm{d}\lambda \\
&= e^{-t_b/\tau}P(n|\lambda_D) + \int_{\lambda_D}^{\lambda_B} p(\lambda)\frac{\lambda^n e^{-\lambda}}{n!}\mathrm{d}\lambda,
\end{aligned}
\tag{3.15}
$$

with

$$
\begin{aligned}
X_0(n) &\equiv \int_{\lambda_D}^{\lambda_B} p(\lambda)\frac{\lambda^n e^{-\lambda}}{n!}\mathrm{d}\lambda \\
&= \frac{e^{-\xi}}{R_B\tau}\left(\frac{R_B\tau}{R_B\tau - 1}\right)^n \left[G\left(n + 1, \xi\left(R_B\tau - 1\right)\right) - G\left(n + 1, \frac{R_D t_b}{R_B\tau}\left(R_B\tau - 1\right)\right)\right] ,
\end{aligned}
\tag{3.16}
$$

where

$$\xi = \frac{\left(R_B + R_D\right)t_b}{R_B\tau} \tag{3.17}$$

and $G(a, x)$ is the incomplete gamma function

$$G(a, x) = \frac{1}{\Gamma(a)}\int_0^x e^{-m}m^{a-1}\mathrm{d}m \ , \tag{3.18}$$

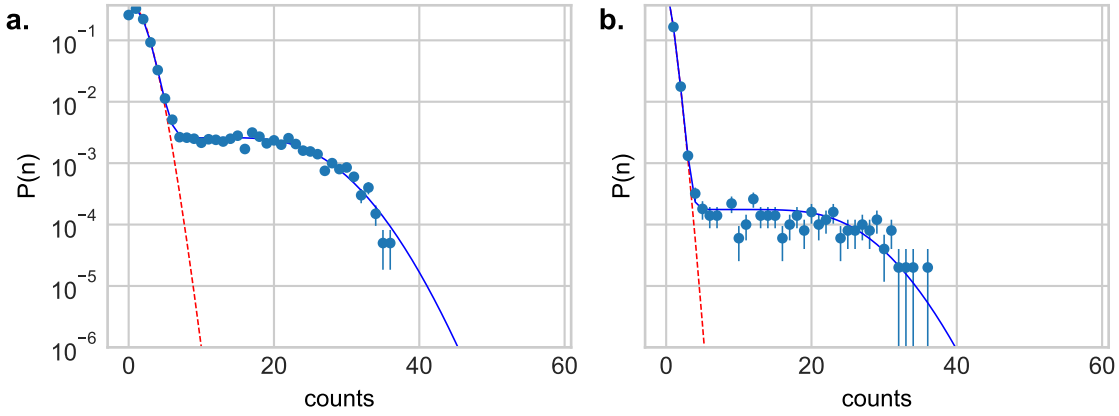with $\Gamma(a)$ is the gamma function.

Figure 3.3: Dark-to-bright leakage for a total detection time of $200\,\mu s$. Panel **a** shows a typical detection histogram for an ion prepared in the $|F = 1, m_F = 1\rangle$ state. We fit Equation 3.15 to the histograms with the dark-to-bright pumping rate $\tau = 1/\omega$ as a free parameter. The fitted pumping rate is $\omega = 10^2 \times 3.4(3)\,\mathrm{s}^{-1}$. Panel **b** is instead the histogram obtained from an ion in the shelved state $|F = 1, m_F = -1\rangle$. The fitted dark-to-bright pumping rate is $23(3)\,\mathrm{s}^{-1}$. The latter is just an approximation since 3.16 only takes into account one decay path.

Beryllium dark-to-bright pumping   For the specific case of beryllium, the rate at which a dark state is pumped into the bright state varies depending on which initial dark state is populated. A detailed description of this process following a rate-equation treatment can be found in the thesis of Hsiang-Yu Lo [48] and Chris Langer [55].

In the simple case where the initial dark state is $|F = 1, m_F = 1\rangle$, the expected pumping rate is

$$\omega = \frac{1}{\tau} = \frac{\Gamma}{2} \frac{s_0}{1 + s_0 + \frac{4\delta^2}{\Gamma^2}} c_{BR} \tag{3.19}$$

where γ is the natural linewidth of the excited $P_{3/2}$ manifold, s_0 is the saturation intensity of the detection beam, δ the detuning and c_{BR} is the coupling coefficient for scattering from the dark state into the bright one. For a beryllium ion at $119.4\,\mathrm{G}$, $\Gamma = 2\pi \times 19.4\,\mathrm{MHz}$, $2\delta/\Gamma = 128$, $s_0 = 1/2$, and $c_{BR} = \frac{2}{9}\alpha$ with $\alpha = -0.793$, the expected rate is $\omega = 240\,\mathrm{s}^{-1}$ [55]. Figure 3.3a shows an example of an histogram obtained for an ion prepared in the state $|F = 1, m_F = 1\rangle$. The fitted dark-to-bright pumping rate is $\omega = 10^2 \times 3.4(3)\,\mathrm{s}^{-1}$ (using Equation 3.15), which is compatible with a saturation intensity $s_0 \sim 0.65$.

As already mentioned in Section 2.5.1, it is possible to mitigate the off-resonant repumping by shelving the dark state in the $|F = 1, m_F = -1\rangle$ level. In this case, a minimum of four scattering events are necessary to pump the population into the bright state [55, 48]. Figure 3.3 shows the comparison of the photon count distribution for an ion prepared in the shelved $|F = 1, m_F = -1\rangle$ state compared to one initialized in $|F = 1, m_F = 1\rangle$. The fit to the dark-to-bright pumping for Figure 3.3b doesn't capture the full dynamics because this fit only assumes dark-to-bright pumping with just one scattering event. Nevertheless, it shows that shelving the dark state to the $|F = 1, m_F = -1\rangle$ reduces the pumping rate by at least one order of magnitude.

Calcium dark-to-bight pumping   Compared to beryllium, calcium suffer less from dark-to-bright pumping. The lifetime of the $D_{5/2}$ manifold is $\tau = 1.168(7)\,\mathrm{s}$ [85], corresponding

to a dark-to-bright pumping rate of $0.856(5)\,\mathrm{s}^{-1}$. This value is ≈ 425 times smaller that the measured one for beryllium in the state $|F = 1, m_F = 1\rangle$.

3.3.2 Bright-to-dark leakage

Let's now assume that the ion is prepared in the bright state and that during detection the bright state gets pumped in the dark one at a rate $\tilde{\omega} = 1/\tilde{\tau}$. Following a similar derivation to the one presented earlier, the bright photon count distribution can be shown to be:

$$P_{bright}(n) = e^{-t_b/\tilde{\tau}} P(n|\lambda_B) + X_1(n) \ , \tag{3.20}$$

in which

$$X_1(n) = \frac{e^{\xi}}{R_B \tilde{\tau}} \left(\frac{R_B \tilde{\tau}}{R_B \tilde{\tau} + 1} \right)^n \times \cdots$$
$$\cdots \left[P \left(n+1, \frac{(R_B + R_D)t_b}{R_B \tilde{\tau}} (R_B \tilde{\tau} + 1) \right) - P\left(n+1, \xi\left(R_B \tilde{\tau} + 1\right)\right) \right] \ , \tag{3.21}$$

where

$$\xi = \frac{R_D t_b}{R_B \tilde{\tau}} \ . \tag{3.22}$$

Beryllium bright-to-dark pumping In the case where the detection beam has a small component of π and σ_- polarization, the bright state $\left|S_{1/2}F = 2, m_F = 2\right\rangle$ can couple, respectively, to the states $\left|P_{3/2}, m_J = 1/2\right\rangle$ and $\left|P_{3/2}, m_J = -1/2\right\rangle$ leading to decay mechanisms outside the cycling transition.

The simplest way to analyze this effect is to assume that all polarization impurity is σ_-. Although the σ_- transition is off-resonant by $\delta_\sigma = 2\pi \times 446\,\mathrm{MHz}$, which is larger than the π transition detuning $\delta = 2\pi \times 223\,\mathrm{MHz}$ [55], it is more likely to have σ_- impurity. For this scenario, the repumping rate can be written as $\tilde{\omega} = 1/\tilde{\tau} = \epsilon_\sigma/\tau$, where ϵ_σ is the amount of σ_- polarization, and $1/\tau$ can be derived from Equation 3.19 assuming a detuning of $\delta = 2\pi \times 446\,\mathrm{MHz}$, a coupling coefficient $c_{BR} = (2/9)\alpha$ ($\alpha = 0.793$) [55] and half saturation intensity $s_0 = 1/2$. The expected repumping rate, assuming $\epsilon_\sigma = 1$, is $\tilde{\omega} \sim 0.3\,\mu\mathrm{s}^{-1}$. This theoretical prediction can be used to infer an upper bound to the amount of polarization impurity ϵ_σ. Figure 3.4a shows the measured photon counting distribution for a beryllium ion prepared in the bright state $|F = 2, m_F = 2\rangle$ together with the fit of Equation 3.20 to the data for a total detection time of $200\,\mu\mathrm{s}$. The extracted bright-to-dark pumping rate is $\tilde{\omega} = 78.4(6)\,\mathrm{s}^{-1}$ which corresponds to $\epsilon_\sigma \sim 2 \times 10^{-4}$ σ-polarization impurity. Experimentally we also verified the population leakage from the bright state by dividing the detection time into 20 bins and measuring the average number of counts per bin, as shown in Figure 3.4b. These data are then fitted with a simple exponential decay where the decay rate is kept constant at $\tilde{\omega} = 78.4\mathrm{s}^{-1}$. Except for the first few points, this simple model captures well the population dynamics.

Calcium bright-to-dark pumping A detailed analysis of the bright-to-dark pumping mechanism for calcium can be found in Alice Burrel's Ph.D. thesis [58]. For our setup, one of the largest contribution is due to magnetic field mixing. The $P_{1/2} \to D_{5/2}$ transition is normally forbidden since $\Delta J = 2$. However, a magnetic field could induce a mixing between states with the same m_J but different value of J. As a result, there is a small probability of decaying from the $P_{1/2}$ manifold to $D_{5/2}$ states, that results in an unwanted shelving during
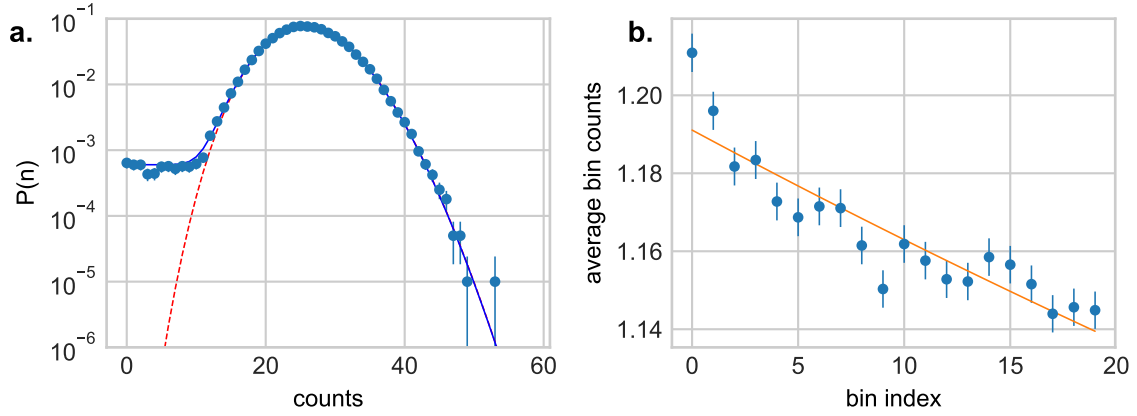
Figure 3.4: Bright to dark leakage. Total detection time $200\,\mu$s. Panel **a** shows the average histogram for an ion prepared in the bright state $|F = 2, m_F = 2\rangle$. The red dashed line is the fit to a Poisson distribution with average counts $\lambda_B = 26.44(1)$, while the blue line is the fit to Equation 3.20. The fitted bright to dark leakage rate is $\tilde{\omega} = 78.4(6)$ s^{-1}. Panel **b** plots the average number of counts detected in consecutive detection bins of $10\,\mu$s, showing the loss of population from the bright state. The solid line is a fit to an exponential decay of the form $A\exp(\tilde{\omega}t) + B$, where the decay rate $\tilde{\omega}$ is kept fixed at $\tilde{\omega} = 78.4$s^{-1}. In both cases, we plot the average of 50000 experiments.

detection. This phenomenon is more evident at large magnetic fields. In a calcium ion, it was first measured in a Penning trap experiment [86]. In their work, the authors measured the branching ratio between the two decay pathways, $\Gamma(P_{1/2} \to D_{5/2})$ and $\Gamma(P_{1/2} \to S_{1/2})$, to be

$$\frac{\Gamma(P_{1/2} \to D_{5/2})}{\Gamma(P_{1/2} \to S_{1/2})} = 4.210^{-7}B^2 = n^{-1}. \tag{3.23}$$

Here, B is the value of the magnetic field in Tesla, and n the number of emitted photons before a shelving event happens. For our experimental setup at 119 G, assuming a detection efficiency of 0.1%, and an average of 30 counts detected in $200\,\mu$s, the estimated shelving rate is $< 10^{-2}$ s^{-1}. This corresponds to less then 1 event in 5×10^6 bright state readout trials, each of duration $200\,\mu$s. Therefore, we can effectively neglect it.

3.3.3   Thresholding readout error

The two pumping mechanisms described above increase the overlap between the dark and the bright state distributions.

   To calculate the thresholding discrimination error for a beryllium ion we can consider the distributions of Figure 3.4a and Figure 3.3b. Here the total detection time is $200\,\mu$s, the leakage rates are $\tilde{\omega} = 78.4(6)$ s^{-1} and $\omega = 23(3)$ s^{-1}, respectively for the bright-to-dark and dark-to-bright leakage. From the Poisson fits to these distributions and from Equation 3.3, the optimal threshold is calculated to be $n_c = 9$. For an ion prepared in the bright state (Figure 3.4a), the error e_B is the fraction of the population that fluoresce below threshold and is $e_B = 0.54\%$. For an ion prepared in the dark state $|F = 1, m_F = -1\rangle$ (Figure 3.3a), the error e_D is $e_D = 0.31\%$. This value could be improved in various ways. One is to increase the detection efficiency, which would allow to shorten the detection time. One other way,

is to completely suppress the bright-to-dark leakage mechanisms by better optimizing the detection beam polarization.

3.4   Time of arrival of photons

The threshold method assumes that photons are collected for a fixed detection time, and state discrimination is based on the number of photons detected compared to a given threshold. In the following section, we will show an alternative readout technique that is based on the time of arrival of photons. The initial idea to use time-resolved photon counting was modeled theoretically by Langer [55] and Gambetta [87]. The method consists of dividing the detection bin t_b into N shorter sub-bins each of length t_s and record the detected number of photons in each bin $\{n_i\}$. The detection problem then reduces to understand whether a given set of counts $\{n_i\}$ originates from an ion in the bright or dark state. After each sub-bin detection, one could calculate the probabilities that an ion is in the bright or dark state. Once the confidence level associated to these probabilities goes above a user-defined threshold, the detection process can be interrupted. This readout technique is called *adaptive maximum likelihood* and compared to the threshold method it has the potential of reducing the overall detection time without sacrificing fidelity. Adaptive maximum likelihood readout has been successfully demonstrated in different experiments [36, 88], but it was always applied in post-analysis. As a result, the benefit of shortening the detection time was not used. In our experiment, we have shown real-time application of this technique, where the probability distributions where updated after each sub-bin detection in less than 2 µs. This is due to the ability to perform floating-point calculations directly on our control electronics (see Chapter 4). As it will be shown later, we are able to shorten the detection time by approximately 70%, while maintaining a comparable readout fidelity.

At the core of the adaptive maximum likelihood readout there is the evaluation of the likelihood function p_D (p_B) that the set of counts is generated by an ion in the dark (bright) state. For a set of counts $\{n_i\}$, the likelihoods p_B and p_D can be written as

$$p_B = P(\{n_i\}|\text{bright}), \text{and } p_D = P(\{n_i\}|\text{dark}) \ . \tag{3.24}$$

On top of the likelihoods, after each sub-bin detection, one needs to evaluate the estimated error probability e_B (e_D) that we have incorrectly deduced an ion to be in the bright state when $p_B > p_D$ ($p_B < p_D$). This can be calculated as:

$$e_B = 1 - P(\text{bright}|\{n_i\}) \ , \tag{3.25}$$

where $P(\text{bright}|\{n_i\})$ is the probability that an ion was prepared in the bright state given that we detected a set of counts $\{n_i\}$. The latter probability can be calculated from Bayes' rule as:

$$P(\text{bright}|\{n_i\}) = \frac{P(\{n_i\}|\text{bright})}{P(\{n_i\})} = \frac{p_B}{p_B + p_D} \ . \tag{3.26}$$

It follows that

$$e_B = \frac{p_D}{p_B + p_D} \text{ and } e_D = \frac{p_B}{p_B + p_D} \ . \tag{3.27}$$

Once the estimated readout error falls below a user-defined threshold e_c, the detection can be interrupted and the state is labeled as bright (dark) if $p_B > p_D$ ($p_B < p_D$). Convergence below this threshold is not guaranteed so it is necessary to define a sharp cutoff time $t_c \leq t_b$ to stop the detection when when the algorithm does not succeed within a standard detection time t_b.

The only thing that now remains to be defined is how to calculate the likelihoods. In the simplest case of pure Poisson distribution, the likelihood function after the detection of m sub-bins is [58]

$$p_B = \prod_{i=1}^{m} P(n_i|(R_B + R_D)t_s), \text{ and } p_D = \prod_{i=1}^{m} P(n_i|R_D t_s) , \qquad (3.28)$$

where $(R_B + R_D)t_s$ and $R_D t_s$ are the mean photon counts detected during a time bin t_s for a bright and a dark ion, respectively. A pseudo-code description of the adaptive maximum likelihood estimation algorithm is given in Algorithm 1.

Algorithm 1 Adaptive maximum likelihood

    Output State of the ion
1: **procedure** ADAPTIVE MAXIMUM LIKELIHOOD
2:     $p_B \leftarrow 1, p_D \leftarrow 1$
3:     **for** $m = 1 \leftarrow 0, N$ **do**
4:         Detect sub-bin
5:         Update likelihoods p_B, p_D
6:         Evaluate errors e_B, e_D according to Equation 3.27
7:         **if** $\min(e_B, e_D) < e_c$ **then**
8:             **if** $p_B > p_D$ **then**
9:                 Label state bright
10:             **else**
11:                 Label state dark
12:             **end if**
13:             Interrupt detection
14:         **end if**
15:     **end for**
16:     **if** $p_B > p_D$ **then**   ▷ Reaches here only if the threshold is not reached.
17:         Label state bright
18:     **else**
19:         Label state dark
20:     **end if**
21: **end procedure**

3.4.1   Non-Poisson statistics

Like in Section 3.3, pumping mechanisms from one state to the other affect the photon counting statistics and thus the definitions of the likelihood function. A detailed treatment of this scenario can be found in Alice Burrell's Ph.D. thesis [58]. Let's assume that an ion is initially prepared in the dark state, and that there is only dark-to-bright pumping at a rate $\omega = 1/\tau$. Based on the results of Section 3.3, we can also make some major simplifications by making two assumptions. The first one is that pumping rate is small compared to the sub-bin time $t_s \ll \tau$. The second is that the bin time t_s is short enough such that after a pumping event, the photon counting rate changes immediately from R_D to $(R_D + R_B)$ at the start of the next sub-bin. In other words, we assume that a leakage happens always at the beginning of a sub-bin detection and never in the middle, such that we can avoid the complicated expression of Equation 3.16. Although the validity assumption hasn't been
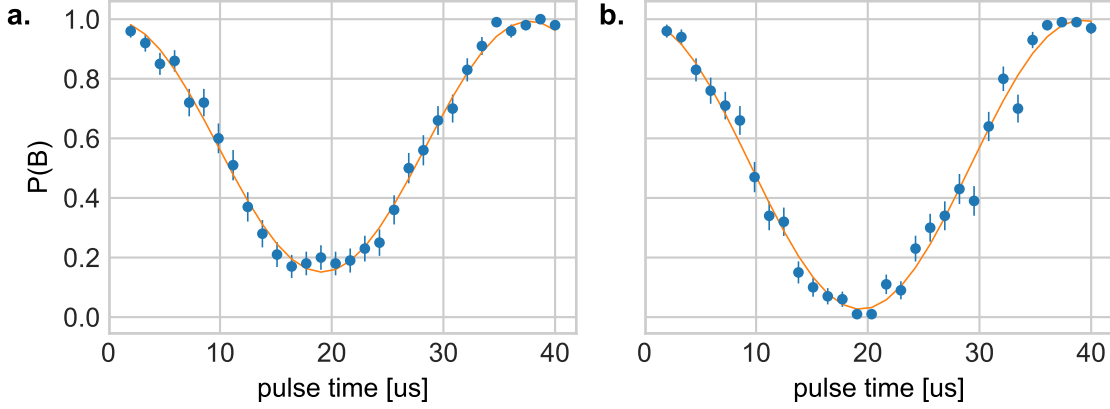
Figure 3.5: Threshold vs. adaptive maximum likelihood. In both panels, the plot of a Rabi oscillation between 0 and 2π in the FDQ manifold of beryllium. In both cases, the dark state $|F = 1, m_F = 1\rangle$ is not shelved into $|F = 1, m_F = -1\rangle$. In panel **a**, the readout method is thresholding after a detection time of $200\,\mu s$. In panel **b**, the $200\,\mu s$ detection window is divided into 20 sub-bins each of length $10\,\mu s$. The qubit populations are inferred employing the adaptive maximum likelihood technique. The dark state likelihood p_D is calculated according to Equation 3.30, with a dark-to-bright repumping rate $\omega = 1/\tau = 10^2 \times 3.4(3)\ s^{-1}$. In contrast, the bright state likelihood p_B is calculated as a product of pure Poisson distributions (Equation 3.28). On average, the time required to discriminate the state of the ion is $100\,\mu s$ in the case of adaptive maximum likelihood.

tested in simulation for our parameters, it seems to hold well looking at the quality of the results discussed later. Moreover, it increases the computational speed of the likelihood.

Under these assumptions, the probability $p_{dark}(m) = e^{-mt_s/\tau}$ that the ion remains in the dark states for m sub-bin detections, can be approximated by $1 - mt_s/\tau$. Similarly, the probability that it decays within a sub-bin is t_s/τ. With all these simplifications, the dark likelihood function p_D after m sub-bins detection can be written as

$$p_D = \left(1 - \frac{mt_s}{\tau}\right) \prod_{i=1}^{m} P\left(n_i | R_D t_s\right) + \left(\frac{t_s}{\tau}\right) \sum_{j=1}^{m} \prod_{i=1}^{j-1} P\left(n_i | R_D t_s\right) \prod_{i=j}^{m} P\left(n_i | (R_D + R_B) t_s\right) \ ,$$

(3.29)

where the first term of the sum represents the case in which the ion remains in the dark state for all the detections, while the second term involves a sum over all the possible sub-bins $j < m$ in which the dark state could have been pumped in the bright state.

The following recursive expression speeds up the real-time computation reducing it from $O(m^2)$ operations to $O(m)$ [58]:

$$p_D = \left(1 - \frac{mt_s}{\tau}\right) M_m + \left(\frac{t_s}{\tau}\right) S_m \ ,$$

(3.30)

where

$$\begin{aligned} M_0 &= 1, \quad M_k = M_{k-1} P\left(n_k | R_D t_s\right) \\ S_0 &= 0, \quad S_k = \left(S_{k-1} + M_{k-1}\right) P\left(n_k | (R_D + R_B) t_s\right) \ . \end{aligned}$$

(3.31)

In the case of bright to dark state leakage, the bright state likelihood p_B has similar expression to Equation 3.30 where the bright and dark Poisson distributions are exchanged.
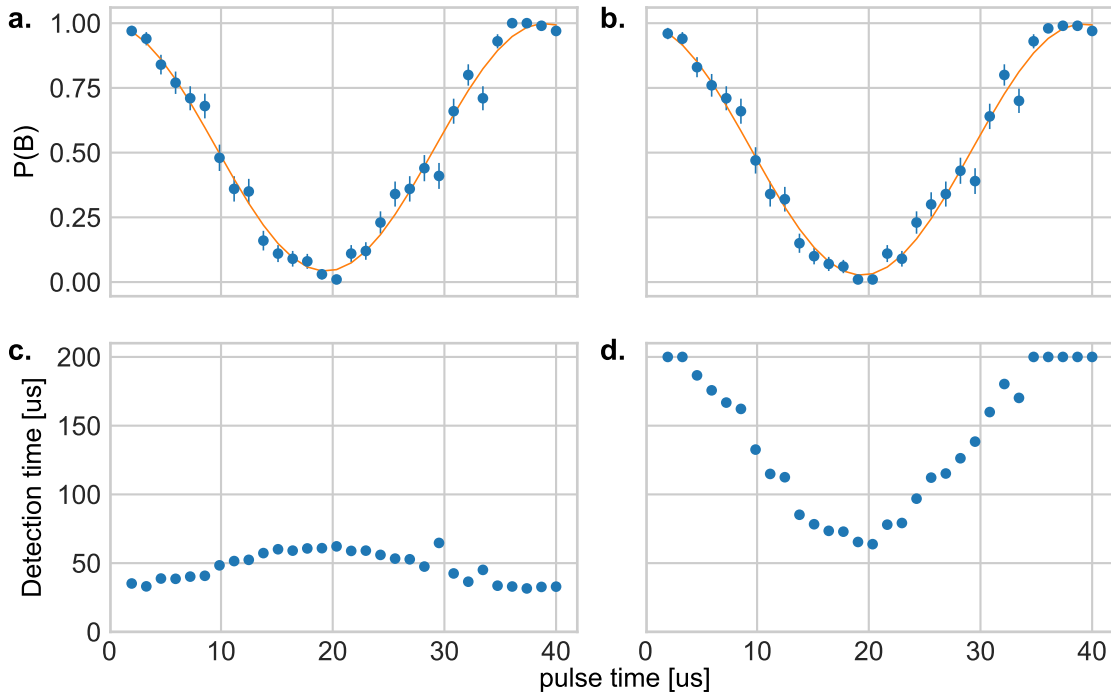
Figure 3.6: Comparison between adaptive maximum likelihood readout method with and without correction for the dark-to-bright leakage mechanisms. The experimental sequence consists of a 2π Rabi oscillation in the FDQ manifold of a single beryllium ion. The different plots originate from the same set of data which has been post-analyzed with two different methods of updating the likelihoods. The two panels on the right (panels **b** and **d**) take into account the dark-to-bright leakage and the likelihoods are updated according to Equation 3.30. The two panels on the left (panels **a** and **c**) neglect any leakage mechanism and the likelihoods are updated according to Equation 3.28. The detection window has been divided into 20 sub-bins each of $10\,\mu$s. Panels **a** and **b** show qubit population as a function of the pulse time, obtained with the two different readout algorithms. The fitted contrast of the oscillation shown in panel **a** and **b** are 96(2)% and 97(2)% respectively. Intuitively we would have expected to observe a difference in the fitted contrast since that Equation 3.30 better represent the physical dynamics. However, from simulations, we observe that our results are currently limited by Raman gate fidelities. In particular, we see that a difference between the two readout methods becomes visible only for gate fidelities $\gtrsim 99\%$. Panels **c** and **d** instead show the average discrimination time as a function of the pulse time. One clear trend is that the discrimination time gets longer if the leakage mechanism is taken into account due to the need for higher statistics.

Figure 3.5 shows a comparison between thresholding and adaptive maximum likelihood when performing a 2π Rabi oscillation on the FDQ transition of beryllium. In this experiment, the detection window has been divided into 20 sub-bins of $10\,\mu$s duration. For the adaptive maximum likelihood method we set the threshold error $e_c = 10^{-4}$, and we just took into account the dark to bright pumping mechanism. This assumption is justified from results presented in the previous section, where the dark to bright leakage rate is dominant if the dark state is the $|F = 1, m_F = 1\rangle$ level.

For this particular set of data, we deliberately did not interrupt the detection to give us more freedom in post-analysis to compare different methods. For example, we can see how the result changes if we neglect the leakage mechanism (Figure 3.6). Panels a and c in Figure 3.6 show results with adaptive maximum likelihood readout where we ignore all
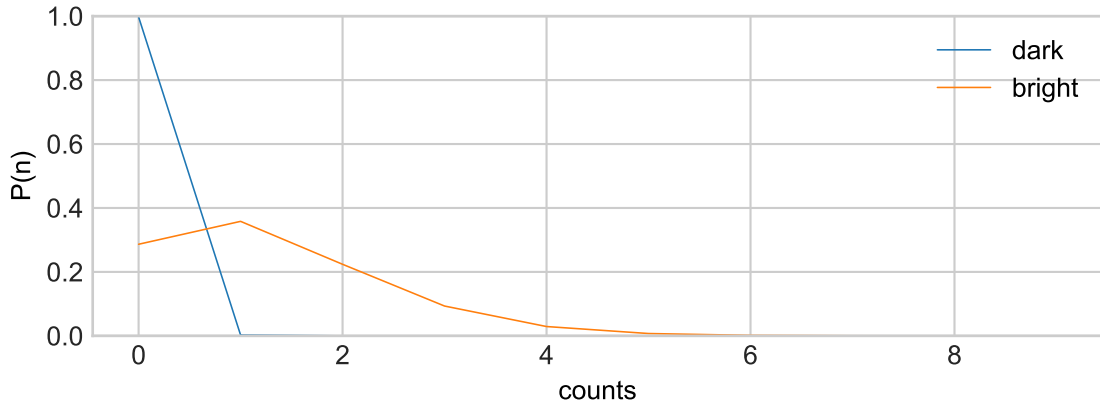
Figure 3.7: Poisson distributions within a sub-bin detection lasting $10\,\mu s$. For a bright ion it is assumed a mean photon count of 1.25, while it is 0.0025 for a dark ion. For a detection time of $200\,\mu s$ the expected counts weould be 25 and 0.05 respectively for a bright and a dark ion. These numbers are comparable to those observed experimentally. Solid lines are just a guide to the eye.

pumping mechanism, while panel b and d take into account the dark-to-bright leakage. By just considering the contrast of the Rabi oscillations (panels a and b), we can see that the difference is marginal and within errors the contrast of the Rabi oscillation is the same. From a theoretical perspective, we expect the fitted contrast to be better in the case where the leakage mechanisms are taken into account, as the real dynamics is better represented. However, from simulations, we see that a difference between the two methods becomes visible only for gate fidelities $\gtrsim 99\%$. We can then conclude that the results are currently limited by gate fidelities. Major differences appear if we compare the time required to discriminate the state of the ion, such that the estimated statistical errors are below the $e_c = 10^{-4}$ threshold (panels c and d). In this case we see that when the leakage is take into account, the average detection time is generally longer, due to the need for higher statistics. In particular, for an ion prepared in the bright state, the readout time is longer because of the bigger overlap between the histograms of a bright and dark ion (see Figure 3.3a). When leakage is neglected, the average detection time needed to readout an ion in the dark state is longer than for an ion in the bright state since consecutive events with $n = 0$ counts are needed to attain to the same level of uncertainty.

We can conclude that with the current experimental scattering rates and gate fidelities there is no clear advantage in using likelihood functions which are corrected for the leakage mechanisms. Therefore, for the future discussion we will neglect them.

3.4.2   Improving dark state readout time

One issue of dividing the detection time into smaller sub-bins is that there is a significant overlap of the bright and dark Poisson distributions for each bin. As a consequence it takes longer to readout the state of an ion prepared in $|\text{dark}\rangle$ compared to one prepared in $|\text{bright}\rangle$. Consider for example Figure 3.7. Here, we plot the Poisson distributions associated to the detection of an ion prepared in the bright or dark state with mean photon numbers that are equivalent to those of a $10\,\mu s$ sub-bin detection. The figure shows that the there is a high probability of detecting 0 photons even for an ion prepared in the bright state. It follows that to discriminate an ion in the dark state, one requires several consecutive events where

no photons are detected to increase the likelihood p_D. On the other hand, it is enough to measure one event where 2 or more photons are detected to immediately conclude that the ion is in the bright state.

It would then be advantageous to conditionally apply a π-rotation to the ion internal state before a new sub-bin detection, whenever we suspect the state of the ion is $|\text{dark}\rangle$. The decision to apply a π-rotation before the sub-bin $m + 1$ readout is based on the expected entropy gain. A similar approach, but for the calibration of quantum gates has been proposed by Andrey Lebedev [89] and experimentally realized by Brennan de Neeve [90].

After the detection of m sub-bins, the expected entropy gain for the $m + 1$ sub-bin detection is defined as

$$\Delta H^{(m+1)} = \sum_{n_i=0}^{n_{\max}} P(n_i) \left(H_\pi^{(m+1)}(n_i) - H^{(m+1)}(n_i) \right) , \tag{3.32}$$

which is a weighted sum, over all the possible detection outcomes, of the difference of the Shannon entropies H in the case where no pulse is applied $H^{(m+1)}$ compared to the case in which the π-pulse is applied H_π. The weight is the total probability $P(n_i)$ of measuring n_i photons in the $m + 1$ detection, which can be calculated from Poisson distributions as

$$P(n_i) = P(n_i|R_D t_s) + P(n_i|(R_D + R_B)t_s) . \tag{3.33}$$

Ultimately, if the entropy gain is positive ($\Delta H^{(m+1)} > 0$), the π-pulse is applied.

The Shannon entropy is defined as

$$H^{(m+1)}(n_i) = - \left(P_D^{(m+1)}(n_i) \log \left[P_D^{(m+1)}(n_i) \right] + P_B^{(m+1)}(n_i) \log \left[P_B^{(m+1)}(n_i) \right] \right) , \quad (3.34)$$

where $P_D^{(m+1)}(n_i) \equiv P(\text{dark}|\{n_0, ..., n_{m-1}, n_m, n_i\})$ and $P_B^{(m+1)}(n_i) \equiv P(\text{bright}|\{n_0, ..., n_{m-1}, n_m, n_i\})$ are the total probability that the ion is in the bright or dark state, assuming that n_i photons would be detected in the $m + 1$ sub-bin detection. These two probabilities can be calculated according to Equation 3.26 from the values of the likelihoods.

If no π-pulse is applied, the likelihoods at step $m + 1$ can be recursively calculated as

$$\begin{aligned}
p_B^{(m+1)}(n_i) &= p_B^m P\left(n_i|(R_B + R_D)t_s\right) \\
p_D^{(m+1)}(n_i) &= p_B^m P\left(n_i|R_D t_s\right) ,
\end{aligned} \tag{3.35}$$

while if a π-pulse is applied

$$\begin{aligned}
p_B^{(m+1)}(n_i) &= p_B^m P\left(n_i|R_D t_s\right) \\
p_D^{(m+1)}(n_i) &= p_B^m P\left(n_i|(R_D + R_B)t_s\right) .
\end{aligned} \tag{3.36}$$

Algorithm 2 gives a pseudo-code description of the procedure to evaluate the entropy gain which should be run prior to the $m + 1$ sub-bin detection of Algorithm 1.

Figure 3.8 shows a Monte Carlo simulation in which we compared the standard adaptive maximum likelihood detection to the new method that accounts for the information gain coming from the internal states population exchange. It shows the total discrimination time for an ion initially prepared in the bright or in the dark as a function of the total number of sub-bins that divide a detection window of $200\,\mu s$. In the presence of conditional π-pulses

---

Algorithm 2 Entropy gain's algorithm

    Input Likelihoods at step m
    Output The ion is either in the same state or in the flipped state.
1: **procedure** ENTROPY GAIN(p_B^m, p_D^m)
2:     $\Delta H^{(m+1)} = 0$
3:     **for** $n_i \leftarrow 0, n_{max}$ **do**
4:         Update likelihoods for no applied π-pulse (Equation 3.35)
5:         Shannon entropy $H^{(m+1)}(n_i)$, Equation 3.34.
6:         Update likelihoods for applied π-pulse (Equation 3.36)
7:         Calculate the Shannon entropy $H_\pi^{(m+1)}(n_i)$
8:         Calculate entropy difference difference $\delta H = H_\pi^{(m+1)}(n_i) - H^{(m+1)}(n_i)$
9:         $\Delta H^{(m+1)} += \delta H * (P(i|R_D t_s) + P(i|(R_D + R_B)t_s))$
10:     **end for**
11:     **if** $\Delta H^{(m+1)} > 0$ **then**
12:         Apply π-pulse
13:     **end if**
14: **end procedure**

(lines with triangles), the dark state discrimination time is significantly reduced. For an ion prepared in the bright state, the readout time is slightly increased as there can be specific sequences of detected counts that the algorithm mistakenly presumes as coming from an ion in the dark state, thus implementing a π pulse.

The difference between the two panels of Figure 3.8 is the background rate. In the first panel, we assumed no background, $R_D = 0$, while in the second, we assumed an average of 0.1 photons detected in 200 µs. As expected the average discrimination time is shorter in the case where $R_D = 0$ since the bright and dark Poisson distributions are less overlapped.

In the case of calcium there exist schemes for background-free detection. One possibility is presented in [91] for which an ion initialized in the ground state $S_{1/2}$ is excited into the $P_{1/2}$ states via a two-photon process through the metastable $D_{3/2}$ manifold. Once it is in the $P_{1/2}$ manifold the ion quickly decays to the ground state emitting a photon at 397 nm. For this process, two laser beams illuminate simultaneously the ion: one is at 732 nm and strongly couples the $S_{1/2}$ manifold to the $D_{3/2}$ states, and the second is the laser at 866 nm tuned on the $D_{3/2} \leftrightarrow P_{1/2}$ transition. A detailed analysis of this two photon process can be performed following a similar approach to the one described in the Ph.D. thesis of Frieder Lindenfelser [92]. There, one can find a detailed analysis of the two-photon process, but on $S_{1/2} \to D_{5/2}$ transition in calcium, to perform cooling and detection.
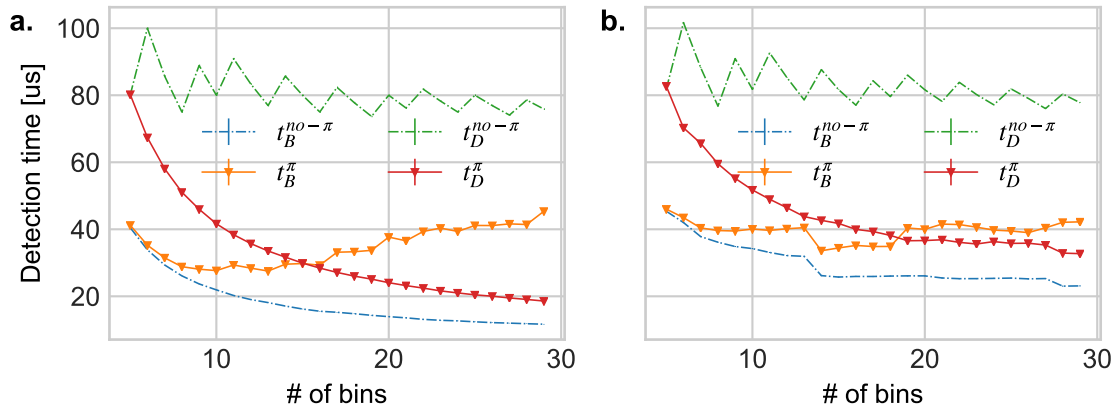
Figure 3.8: Average discrimination time as a function the total number of sub-bins that divide a detection window. Both panels show the discrimination time for bright and dark states detected with the standard adaptive maximum likelihood method (connected dots) and the one with conditional spin flips (triangles). Panel **a** is the case of no background counts and an average of 25 photons in 200 µs for a bright state. In panel **b**, the average detected photons for a dark state is 0.1 and 25 for a bright one. On average, the conditional spin-flip method outperforms the standard adaptive maximum likelihood technique in terms of speed. Note that for these simulations we assumed perfect population inversion after the application of a π pulse.

4 Mixed-species control

This chapter will be devoted to the description of the experimental tools needed to control mixed-species ion crystals. The chapter is divided into two main parts: at the beginning, I will introduce the "Modular Advanced Control of Trapped IONs" (M-ACTION) control system and the graphic interface that was developed during this thesis to address the current and expected future requirements. In previous generations of experiments, a comprehensive control system was not essential. However, current and future experiments would be unmanageable without a control system designed to specifically address all the relevant experimental requirements.

In the second part, I will instead focus on the control of the motion of an ion chain. In particular, I will introduce the apparatus and the methods needed for the transport and splitting/recombination of arbitrary ion-chains. Finally, I will present some results about single-species and mixed-species transport and splitting experiments.

4.1 Control System

4.1.1 Control System overview

The complexity of QIP experiments performed these days would be unmanageable without a robust control system that guarantees reproducible outcomes, flexibility, and automation. The requirements are two-fold: good lower-level electronics as well as a well-structured user interaction. In the spirit of the QCCD architecture [27], trapped-ion experiments require to be able to trap arbitrary strings containing multiple ion species, reconfigure their structure through transport and splitting, manipulate qubits with laser pulses and perform low-latency feedback upon detection [93]. At the lowest level, this requires regulated rf, digital and analog i/o with reproducible timing and low-latency computing capabilities that alter the control system's output based on external inputs. At a higher level, it means an Application Programming Interface (API) written in a high-level programming language that encapsulates as much of the lower level details as possible and provides a set of tools that allow the user to write and configure experiments at a high level of abstraction. The M-ACTION system developed within the group together with its Graphical User Interface (GUI) is designed to tackle those challenges. Details about the hardware and the lower level infrastructure can be found in Vlad Negnevitsky's thesis [61]. My focus has instead been on developing the GUI and improving the high level API.

Figure 4.1 shows the network topology of our control system. At its core, there is a Xilinx Zynq-7000 chip composed of two ARM CPUs controlling the experiment and connected to a medium-sized FPGA (Field Programmable Gate Array). The Zynq chip lies on a "master board", called Zedboard, which also contains various peripheries that connect to the PC and other time-critical devices.

The Zedboard is connected via a backplane connection to DDS boards (direct-digital synthesizer), which produce the rf signals required to drive the acousto-optic modulators (AOMs) that control laser pulses. Each board features four rf channels linked to an FPGA

that runs an independent firmware. The presence of an on-board FPGA avoids a continuous stream of data from the master board. Experimental sequences are loaded on each board before the execution of each data point via a low latency connection at a rate of $\approx 800-1000$ MBPS (megabits per second) [61]. For optimal control of qubits, it is also possible to shape the frequency and amplitude of each rf pulse [94] with the additional capability of phase coherence between different channels. Run-time changes to the experimental sequences are also possible thanks to a low-latency direct link to the master board ($\approx 1-3\,\mu$s latency). One extra feature that has been added recently to the DDS boards are analog inputs for in-loop stabilization of laser pulse intensities. Details will be described in Martin Stadler's Ph.D. thesis [95].

Other peripheries directly controlled by the "master" Zedboard include 32 digital outputs, used to manage rf switches and to trigger other devices, and eight digital inputs to read in the signal coming from photomultiplier tubes (PMTs). The latter are used to count the photons scattered by the ions during the detection sequence and thereby used to determine the quantum state of the ions (see Chapter 3).

The M-ACTION system also controls the custom-designed arbitrary waveform generator (AWG) boards that supply the dc electrode voltages, the Direct Ethernet-Adjustable Transport Hardware (DEATHs). Details about the design and the firmware are found in the Ph.d. thesis of Ludwig de Clerq and in the bachelor thesis of David Nadlinger [49, 96]. Each card consists of four analog channels linked to a MicroZed board, a smaller version of the Zedboard, that runs almost independently from the master Zedboard. A set of time-dependent sequences of voltages, the *waveforms*, is loaded on the Microzed's internal memory from the PC GUI via Ethernet, and each waveform is stored with an index and a unique identifier. At the beginning of an experiment point, the master board communicates via Ethernet to the DEATHS the waveforms that need to run and specifies their order, speed, and direction. Within the experimental shot, a shared digital trigger starts all the channels, ensuring a low-latency synchronous execution with the master board.

We use the Xilinx software development kit (SDK) to program and run the experimental code, written in C++, that controls the M-ACTION system. The C++ GUI, called Ionizer2 after the original used in the atomic-clock setups at NIST, provides the front-end to the experiments and also manages other devices which do not require low-latency synchronous control. These devices are usually experiment-specific, like piezo controllers or DAC boards, and are controlled by Raspberry Pis that run a python server that handles the connection with Ionizer. This concludes the overview of the control system infrastructure, Section 4.1.2 explains the higher-level tools that we developed to program complex experimental sequences, while Section 4.1.3 explains the features of Ionizer2.

4.1.2 Experiment interface

Experiments up to the repeated stabilizer measurements (Chapter 6) only required the control of ion crystals trapped in one zone. However, future experiments (and also the ones discussed in Chapter 7) involve multiple crystals of different types whose structure is continuously reconfigured through transport and splitting/recombination. For this reason, over the last year I developed with the help of Tanja Behrle a framework which comprises of different levels of abstraction. Before going to the details, I will briefly introduce the preexisting tools mostly developed by Vlad Negnevitsky with contributions from David Nadlinger and myself, upon which we built the new framework.
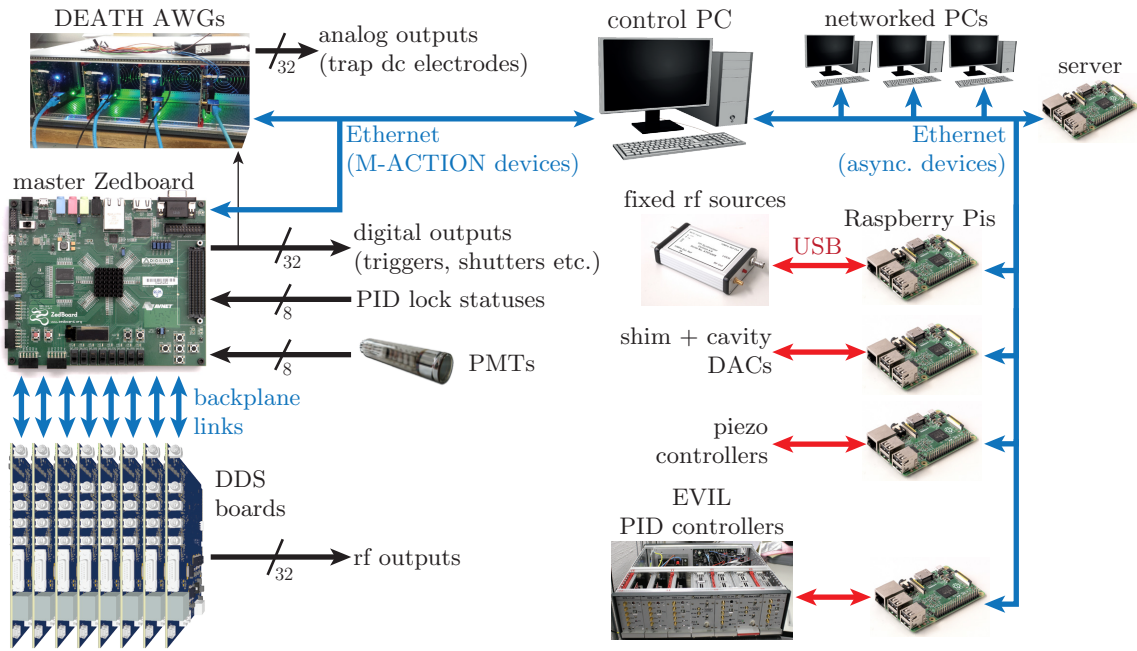
Figure 4.1: Network of the experimental control. On the left hand side is the M-ACTION system which sits on on a dedicated network and controls all the synchronous devices. In our setup it currently controls 16 rf channels, 2 PMTs and 32 analog outputs (DEATHs) and 32 digitial outputs. On the right the asynchronous devices and other PCs, which are on a separate network. Image taken from the Ph.D. thesis of Vlad Negnevitsky [61].

Preexisting API

At its core, the experiment API (Application Programming Interface) consists of three independent sets of libraries. One is the interface to program and control the DEATHs, another one defines and controls rf pulses allowing the execution of experimental sequences (with the `experiment` class at its core), and the last defines parameter objects which are controlled by the user to alter the settings of sequences (the `remote parameters` class).

The DEATHs API was mostly developed by David Nadlinger and it is discussed in his master thesis [96]. Further details about the DEATHs usage will follow in Section 4.2.

The `remote parameters` are the objects that allow the user to set the properties of an experiment. In the experiment API, these objects are treated like standard C++ types (int, double, unsigned, bool) and can, for example, be used to set the time of an rf pulse, or to trigger on and off a particular block of code. Remote parameters are defined and compiled onto the master board but are mostly controlled by the PC GUI. For this reason they extend the standard types by offering a way to customize their behavior. To each remote parameter can be assigned a unique identifier and a name string which will appear on the PC GUI as a label, and it is possible to specify extra properties like the maximum and the minimum value that the parameter can take. Remote parameters can be defined as local or global. Local parameters are defined and accessible only to specific experiments, while global parameters are shared among all experiments.

Finally, the `experiment` class is the object that executes an experimental sequence. The `run()` function acquires a data point. At first the `init_pulse_sequence()` function prepares all the devices to run a user defined sequence. This function is called only once

at the beginning of a data point. After each shot, the function `read_out_pmts()` is called to readout the PMTs and to perform real-time operations like thresholding or branching of the pulse sequence. Once a data point has been acquired, the results can be manipulated further (i.e. histogram fitting of the PMT results) and then are sent to the PC GUI for extra processing and saving. It is worth noticing that there is no concept of scans on the master board, which is only designed to acquire a data point with a specific set of parameters defined by the user. Scans are defined only on the PC GUI, which updates the value of the scanned parameter on the master board before the acquisition of a data point.

Phase coherence and reference time shifts   When performing a qubit rotation with a laser or microwave pulse controlled by a DDS, the phase of the generated rf signal controls the rotation axis. For QIP operations, it is then essential to control the phase of each pulse relative to the others in the sequence. In order to ensure phase coherence, at the beginning of each rf pulse, a hardware multiplier on each DDS board calculates and applies a phase offset. By default, the phase offset is calculated as $\phi = \omega(t - t_{\mathrm{ref}})$ where ω is the frequency of the rf pulse which we are about to apply, and t_{ref} is a reference time, which by default is the beginning of the pulse sequence.

For some particular pulse sequences, it might also be useful to be able to shifts the reference time. For the experiments described in Chapter 6, we shift the reference time to the beginning of a block of pulses. With this, we decouple the rf phase of the pulses within the block from the rest of the experimental sequence. Further details about the validity of this approach can be found in Chapter 6.

Crystal classes

The framework we developed more recently lies on top of the experiment class discussed above and introduces the concept of `crystal` classes, which are a code representation of a trapped ion chain. In particular, a crystal object has information about the ion chain composition (number of ions, species, and arrangement), the motional modes frequencies, and all the possible sequences to manipulate a specific ion chain.

One principle followed in the design phase is information hiding, which uses encapsulation to hide low-level details within higher-level tools. As a result, it minimizes the knowledge required to write an experiment and the amount of code that has to be changed in case of changes to the setup. Figure 4.2 shows a schematic of the experiment API designed for the M-ACTION system. Some elements of encapsulation were already present in the preexisting API, like the `pulse_raman_mono` (see below); the new API extends these elements and adds extra layers of abstraction.

When running an experiment, the set of operations that are run are often the same, and just the parameters differ. For instance, beryllium Raman pulses are always controlled by a specific set of AOMs in the setup. What changes, depending on the experiment, are the parameters like the frequency, the pulse time, or the phase. Therefore the first level of abstraction consists of defining functions, which run a specific pulse with parameters that are passed as an argument, hiding some information about the physical setup. For example, in the case of beryllium, Raman pulses are run through the `pulse_raman_mono` function. This function contains all the information about the physical AOM setup like the DDS channels used, the central frequency of each AOM, and which set of AOMs has to be pulsed for motion-sensitive and motion-insensitive Raman pulses. This information is hidden from the user which controls the pulse by parsing a C style structure, `param_aom_Be`, as an argument

a.

PC link

| Server |

- -

| Experiments | ↔ | crystals | ↔ | Global parameters and functions |

User code

| Phase counters |

| Transitions |

- -

API

| DEATH control | | Experiment class | | Crystal class | | Transition class | | Remote parameter class |

- -

Drivers

| Drivers |

b.

| Crystal Class |

| Crystal_BeCa | | Crystal_Ca | | Crystal_Be |

| Crystal_BeCaBe | | Crystal_2Ca | | Crystal_2Be |

c.

Crystal_BeCa

Crystal_BeCa (remote_parameters)

Detect ()
Cooling ()
state_preparation()

vector<frequency> motional_modes
vector<transition_Be> trans_be
vector<transition_Ca> trans_ca
vector<phase_counters> counters

specific_BeCa_function_1 ()
specific_BeCa_function_2 ()

Transition_Be

Transition_Be (remote_parameters,
motional_modes)

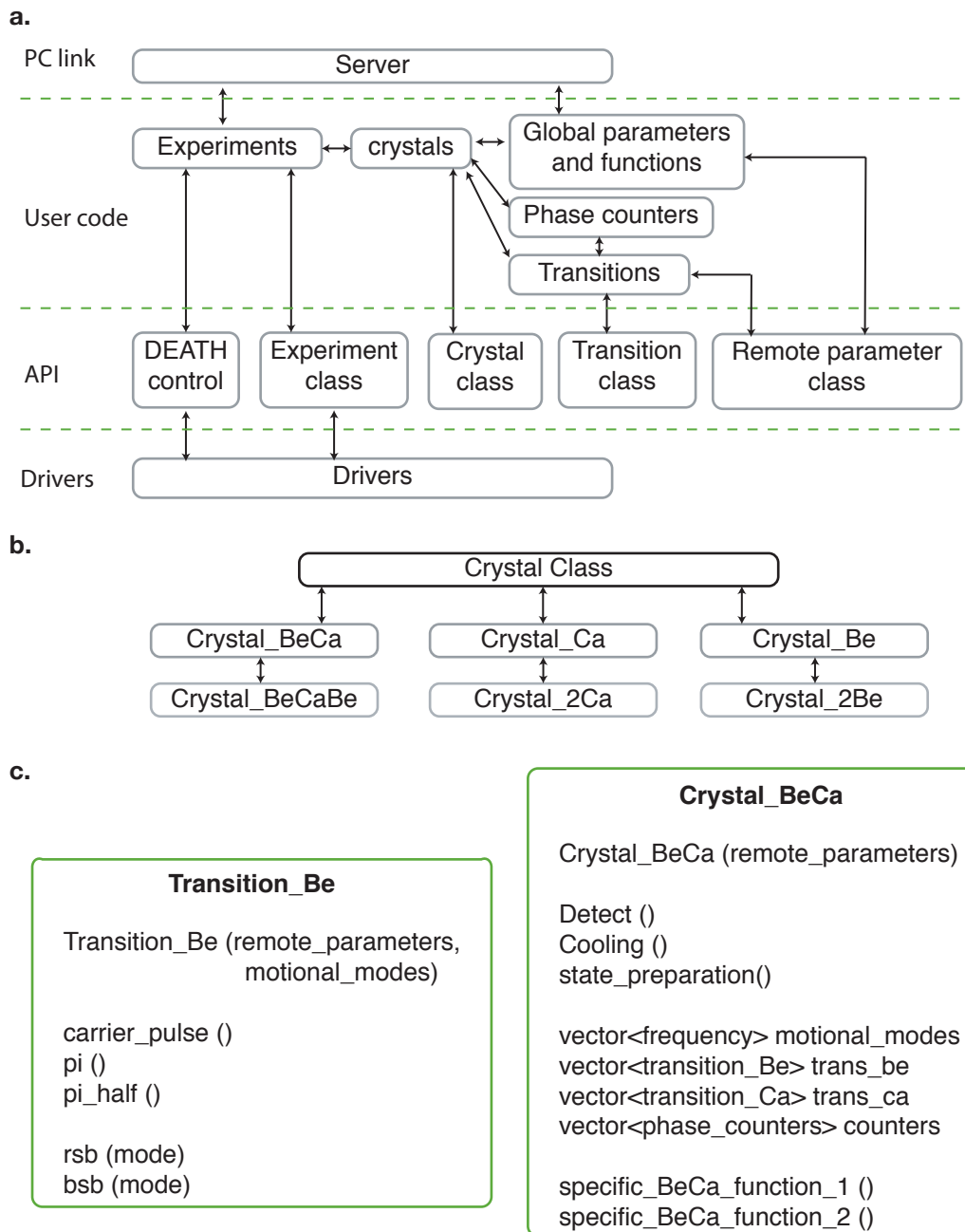carrier_pulse ()
pi ()
pi_half ()

rsb (mode)
bsb (mode)

Figure 4.2: Software hierarchy. **a** the server handles the requests coming from the control PC, altering the remote parameters and the executing experiments. Experiments are written by the users and relay crystal objects and global functions. These are created using a toolbox provided by the experiment API which also wraps the low-level drivers. **b** inheritance structure of crystal objects. At the top the most abstract crystal class. Each lower layer defines methods that child classes can inherit. **c** Pseudo-code representation of crystal and transition classes to highlight the main structure.

to the `pulse_Raman_mono` function. Within this structure, the user defines which Raman configuration to use, the transition type (an enumerator defining the transition: FDQ, FIQ, FIS), the pulse time, the phase and the frequency offset from the carrier frequency of the

desired transition. The `pulse_Raman_mono` function then interprets the information and runs the desired pulse.

The second layer of abstraction is the `transition` class. A transition object, groups together the main pulses that can be run on a particular qubit transition, together with the remote parameters that the user controls. In the example case of beryllium, there are three possible transitions: FDQ, FIQ, and FIS. Each of these is an instance of a `transition` class and contains parameters and functions to run π and $\pi/2$ pulses, arbitrary carrier, and red and blue sideband pulses. When calling any of those pulses, the transition class defines the `param_aom_Be` structure starting from the remote parameters and then calls the `pulse_Raman_mono` function.

The third level of abstraction is then provided by the `crystal` object. Depending on the ion chain configuration, it contains vectors of calcium and beryllium transition classes, and a list of functions for detection and readout, cooling of the motional modes and operations which are specific to one particular crystal object. The groups of parameters that control each operation are automatically generated and are distributed to the different objects included by the crystal class upon the creation of the crystal object. By default, parameters are global such that different instances of the same crystal share the same set of parameters. However, if needed, it is also possible to replace specific blocks of parameters in individual instances of a crystal.

An experiment then becomes a sequence of function calls on particular instances of crystal objects, interleaved by transport and splitting/recombination operations.

Phase accumulators   There can be cases in which the linearly advancing DDS phase offset introduced previously is not enough to ensure the phase coherence of two pulses in the frame of reference of the qubit. For example, in the case of ac Stark shifts, the qubit phase evolves differently with the qubit drive turned on than with it turned off. In the qubit frame of reference, this results in a phase difference between pulses that is proportional to the control pulse length.

To take account of these effects, we introduced phase accumulators which are owned by the crystal class, and are updated after each pulse of the sequence. To better understand the way they work, I will take the example case of ac Stark shifts (see Section 5.1.2 for more details). Let us define ω_0 the qubit transition frequency when the qubit drive is off, and $\omega_d = \omega_0 + \omega_{ac}$ the transition frequency of the qubit when the drive is on, with ω_{ac} the ac Stark shift induced by the drive. To achieve the highest operation fidelity, we set the DDS frequency to produce a laser frequency which is on resonance with the Stark-shifted qubit transition ω_d. Let us consider the simple pulse sequence shown in Figure 4.3a and assume that the DDS reference time coincides with the starting time of the first pulse. In the frame of reference of the laboratory, at the beginning of the second pulse, the accumulated DDS phase is $\phi_{DDS} = \omega_d(t_p + t_w)$, where t_p is the duration of the first pulse and t_w is the wait time between the two pulses. The phase accumulated by the qubit is instead $\phi_q = \omega_d t_p + \omega_0 t_w$. Therefore to ensure a fixed phase relation, an extra phase offset $\phi_{off} = (\omega_0 - \omega_d)t_w = -\omega_{ac}t_w$ has to be added to the rf signal generated by the DDSs that drive the second pulse of the sequence.

In the case of beryllium, the calculation is more complicated since the same transition can be driven with two Raman beam configurations (co-propagating and perpendicular beams), with different beam intensities and thus different Stark shifts. To take this into account, we define for each beryllium transition a phase accumulator. Consider the pulse
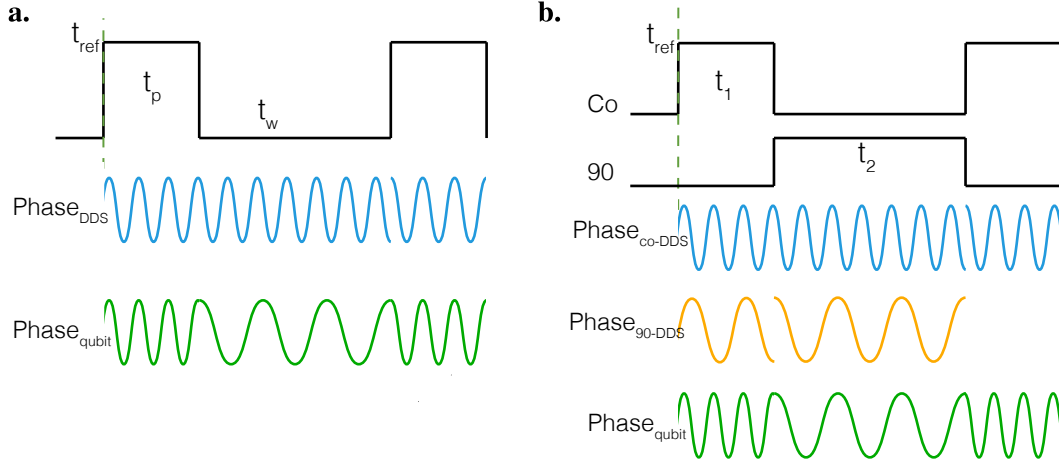
Figure 4.3: Phase accumulation. **a.** Simple scenario where one pulse is driven on resonance without the Stark-shifted transition frequency ω_d. The phase accumulated by the DDS hardware multiplier at the beginning of the second pulse is $\phi_{DDS} = \omega_d(t_p + t_w)$. The qubit phase evolves at the bare qubit frequency ω_0, and the accumulated phase at the beginning of the second pulse is $\phi_q = \omega_d t_p + \omega_0 t_w$. To maintain phase coherence with respect to the qubit, the phase accumulators of the crystal class change the DDS phase by $\phi_{off} = (\omega_0 - \omega_d)t_w$. **b.** The Stark shift associated to the motion-insentive and motion-sensitive configuration can be differnet, $\omega_d^{co}, \omega_d^{90}$. Assuming a stable phase relationship between the two, to maintain phase coherence with the qubit, two phase accumulators are updated after each pulse according to the protocol described in the text.

sequence in Figure 4.3b, and assume the ac Stark shifted qubit transition frequency for the co-propagating beams to be ω_d^{co}, and ω_d^{90} for the beams at 90°. Assume also that the relative phase between the two configurations is stable such that the only effect we have to consider is the different Stark shift [1]. At the beginning of the second co-propagating pulse the phase accumulated by the DDS is $\phi_{DDS}^{co} = \omega_d^{co}t_1 + \omega_d^{co}t_2$, while the phase accumulated by the qubit is $\phi_q = \omega_d^{co}t_1 + \omega_d^{90}t_2$, where t_1 and t_2 are the pulse duration of the first and second pulse. It follows that the phase that needs to be added to maintain the phase coherence is $\phi_{off}^{co} = t_2(\omega_d^{90} - \omega_d^{co})$.

Each phase accumulator can be activated and deactivated at any point in time by the crystal class. At the end of each pulse or wait time, the crystal class updates all the active phase counters according to the relative Stark shifts. On top of the automatic feedforward compensation of the ac Stark shifts, there is also the possibility to add a compensating phase manually. This feature could be useful when the calculation of a phase difference between the qubit and the DDSs is not trivial, like in the case of the ac Stark shift induced by bichromatic beams (Section 5.3.4) or if the ion moves through regions with different strengths of the magnetic field.

4.1.3 GUI

Throughout my Ph.D., one of the projects I have been mostly involved with is the development and maintenance of the GUI, named Ionizer2, after the first version developed at

---

[1]The latter assumption is not valid experimentally. The relative phase fluctuates at each shot due to beam path fluctuations. Chapter 6 describes in more detail this scenario, discussing how to work around it.
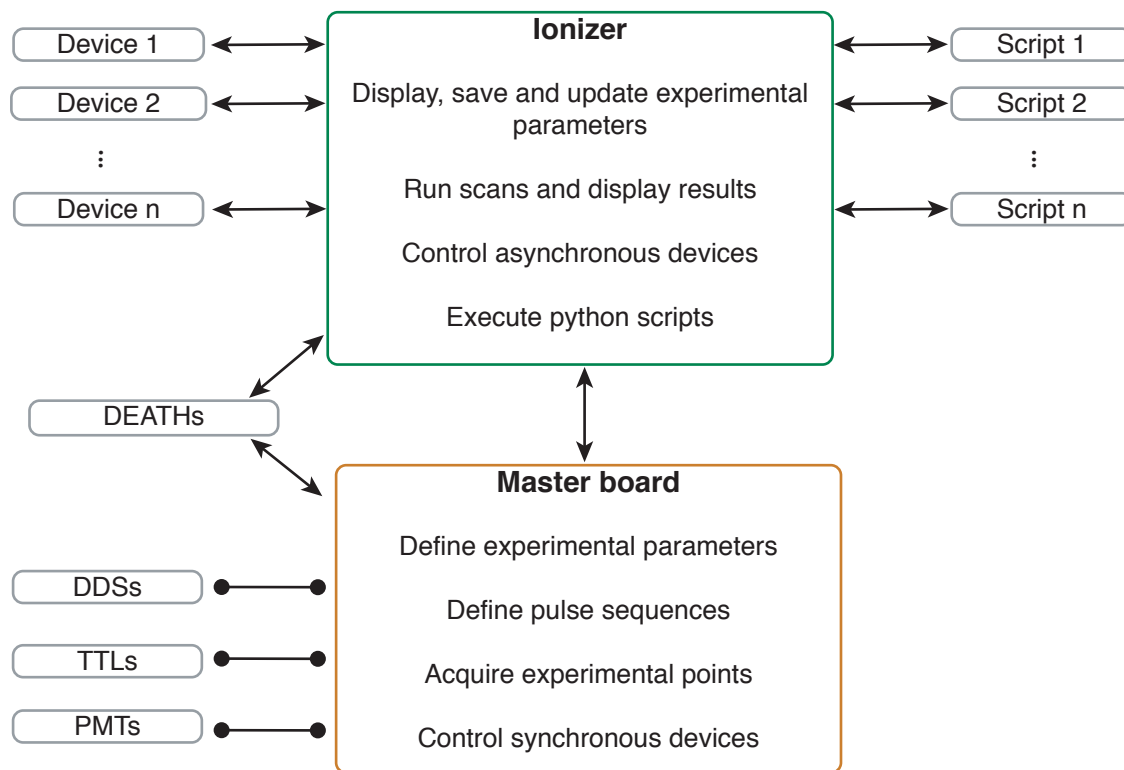
Figure 4.4: Overview of the main features of GUI, master board and their connections to external devices. The black arrows represent Ethernet links using MsgPack RPC as the communication protocol. All asynchronous devices and scripts are controlled only by Ionizer (GUI), while all synchronous devices are controlled by the master board. Details about the communication to synchronous devices (connections with the round endings) can be found in the PhD thesis of Vlad Negnevitsky [61]

NIST by Till Rosenband and co-workers. Over the years, the code base has been rewritten to the point that there is almost no residual code from the NIST version.

Ionizer2, written using the Qt C++ library, is a multi-threaded program that provides a GUI to our control system. It communicates with the master board, the DEATHs, and other asynchronous devices with an Ethernet protocol based on the MsgPack library. An overview of the main features of Ionizer and the connectivity to external devices can be found in Figure 4.4.

Since there are several experimental setups within the group, we wanted the GUI to be experiment independent to reduce fragmentation of the shared code base and to ensure a standard way of running experiments and saving data. Experiments and parameters are defined and compiled on the master board through the experiment API described before. At startup, Ionizer queries the master board for all the available experiments and the relative remote parameters (either local or global) and the status of the digital outputs. With this information, it creates a page for each experiment and populates it with the QT Widgets associated with the remote parameters. The value displayed on the GUI parameters is either the default one provided by the master board or the one loaded from a parameter database stored locally on the PC (if it exists). By changing the GUI parameters, the user can control the settings of the experiments on the master board. To minimize the amount

of communication and to ensure that the master board status is always under control, the parameters are automatically sent to the master board only before running a scan or by an active press of a button.

On top of the dynamically loaded experimental pages, it also creates static pages that control the DEATHs waveforms and the various asynchronous devices, like the shim electrodes DAC, the calcium reference cavity piezos [92] or piezo mirror mounts used to position laser beams. Generally, those devices are controlled by a Raspberry Pi, which runs a python server that handles the MsgPack connection to Ionizer. Currently, those pages are specific to particular experimental setups and require the user to write a dedicated QT page that displays the parameters and handles the connection API to the Raspberry Pi. Despite the simplicity of connecting a new device to Ionizer, it is a bad practice since it goes against the experiment independent principle. At the time of writing, there is an ongoing effort to replace these user-defined pages with a standardized plugin framework that avoids modifications of the Ionizer code. The idea is to treat each Raspberry Pi (or any other computer-like device) in a similar way to the master board. In this way, Ionizer creates pages dynamically by querying the devices about the parameters that need to be displayed and potentially scanned.

One of the most critical jobs of Ionizer is to run scans. Every remote parameter can be scanned by any experimental page, with control to the start/stop values, the number of data points, and the number of shots per data point. At the beginning of a scan, all the global remote parameters and the local ones of a particular experiment are sent to the master board and saved in a time-stamped folder, which also contains the results received by the master board. In this way, we can control and save the status of the experimental system for each scan. After each data point, the master board communicates to Ionizer the raw PMT counts and any pre-processed data, called data channel, that the user would like to display in a plot window (i.e. the average value of the thresholded PMT counts) and save them to file. When programming the experiment on the master board, the user defines how many plot windows are needed and a set of data channels that will be displayed as lines in the plot. In the case of the simultaneous scan of two parameters, Ionizer displays each data channel as a 2D color plot. At the end of a scan, Ionizer can also fit simple functions to specific data channels and update the scanned parameter with the fitted value.

Each experiment has a priority that can be changed by the user. If two or more experiments are run in parallel, a scheduler keeps switching between them at a rate proportional to the priorities of each experiment. In our experiment, a low priority continuous scan that cools and detects the ion chain is always running in the background, and is continuously interrupted for more advanced user-defined experiments.

Scripting API

To be able to automate much of the experimental operations and to provide a more sophisticated scheduler for calibration experiments, we developed a Python-based scripting interface.

In Ionizer, the path of an arbitrary number of python scripts can be saved in a dedicated page, and each script can be run by clicking a button next to its path. When Ionizer launches a script, it opens a dedicated system console and an Ethernet connection to a local port. Similarly to the connection to the Raspberry Pis described above, the flow of information is regulated by a server-client model based on the MsgPack library. If needed, it is also possible to run more then one script in parallel; in this case, a console and an ethernet

connection will be created for each script, and on the Ionizer side, they will be independent of each other.

With scripting, it is possible to reproduce any action that can be performed by hand on Ionizer. To standardize and simplify the writing of scripts, we wrote a set of libraries that help with the analysis of raw data, but also provide tools for more advanced scheduling of calibrations. Differently from the Ionizer scheduler, it is based on a queue system rather than priorities. A calibration experiment is put at the top of the queue depending on the repetition time of the other calibrations in the queue but also on the outcome of the previous calibration scan. Each calibration could have a set of dependencies (i.e. a π time calibration can have the qubit frequency as a dependency), which are scheduled to run immediately if the calibration was not successful. On the Ionizer side, a calibration scan run from a Python script is set to have the maximum priority so that no other scan can run until the calibration is over.

The goodness of a calibration depends both on the reduced $\tilde{\chi}^2$ and on heuristics set by the user, like the contrast of a resonance peak. To increase the stability and the success rate of calibrations, for frequencies or time calibrations, we also provide functions that retake scans if at first, the fit was not successful. For example, if a frequency resonance is at first not found, the code can automatically search for it by increasing the scan range and the number of data points, and then zoom back into the feature once it is found. Also in this case, the user can easily customize the search by setting the recursion depth and the range adjustment for each calibration.

In the experiment, we now make use of these tools daily both in the morning for initial calibration of parameters and throughout the day to keep them calibrated. As an example, in the morning after turning on all the lasers and loading a single Be-Ca ion chain, the calibration script automatically calibrates all the relevant parameters (carrier and motional frequencies, AC Stark shifts, π and $\pi/2$ times for all transitions), but also ground state cooling of the axial motional modes. In about 15 min, the system is ready for the manual calibration of the entangling gate and the other experiments that we want to run that day.

At the time of writing, we are also extending the scripting capabilities by allowing the user to control Ionizer from independent scripts. This is a paradigm shift, as Ionizer will not own the scripts, but on the contrary, they will own and control Ionizer. This new feature has the advantage of simplifying the process of writing and debugging scripts since one can test individual parts of code in an environment like the Jupyter notebook. On the other side, it increases the risk of fragmentation as the users could write their control system by using Ionizer only as a subroutine that talks with the master board. Group effort and careful management will, therefore, be needed to avoid this possibility.

4.2   Transport and splitting

Reliable transport, splitting and recombination of ion chains are critical requirements for the QCCD architecture [26, 27].

In our setup, initial transport experiments were performed by Ludwig deClercq [49], who also designed and built the AWG boards that control the dc electrodes, known as Direct Ethernet-Adjustable Transport Hardware (DEATHs). This allowed us to demonstrate parallel transport gates [97, 98], in which we performed parallel coherent sequences of quantum operations on two beryllium ions in different experimental zones using a single recycled laser

beam. During his Ph.D. work, transport was also used to perform ion velocimetry, which was used to improve the control of the velocities required for transport gates [99, 100]. Since then transport and splitting was used for several purposes: beam alignment (Section 5.1.2), implementing addressed operation for mixed species (Chapter 6) and also for beam profiling [61].

Each DEATH consists of a motherboard containing two dual-channel 16-bit DACs, which are run at 100 MSPS (megasamples per second). Every output is then sent to an amplification and filtering stage that produce voltages in the range between $-9.7\,$V and $9.7\,$V with a bandwidth of $50\,$MHz [49]. The two DACs are controlled by a Microzed board, which is a compact version of the Zedboard used as the "master" board in the M-ACTION system.

Transport waveforms consist of voltage samples, stored in the internal memory (BRAM with a capacity of 240 KB) of the FPGA hosted on the Microzed. When a waveform is run, the voltage samples are sent to the DAC sequentially in forward or reverse mode, with an adjustable sampling time. The sampling time (the slowdown parameter, in our coding terminology) is an integer representing the number of clock cycles, which, together with the total number of samples of a waveform, defines the execution speed of a waveform. A slowdown of 0 corresponds to the maximum speed for which the waveform is played at 100 MSPS. A typical slowdown value used in our experiments is 49, which corresponds to a 2 MSPS update rate. For a typical waveform with 500 samples, the total execution time with a slowdown of 49 is approximately $250\,$µs.

The DEATH boards are controlled both by Ionizer and by M-ACTION system. Ionizer, through a dedicated page, loads a JSON[2] file containing up to 256 waveforms, for a maximum sample size of 16384. During the loading, Ionizer sends via Ethernet the waveforms to the Microzed boards [96] and displays in a dedicated page all the details of each waveform, such as the index, the description label, number of samples and the starting and ending voltages. In Ionizer, it is also possible to manually trigger each waveform individually both in forward and reverse mode, by simply clicking a button. Within an experimental sequence, a dedicated API controls the correct execution of waveforms. From a user perspective, the most relevant object in the M-ACTION system is the `DeathSequence` class, which is used to create a sequence of waveforms. At the beginning of each data point, this sequence is sent via Ethernet to the DEATHs using a protocol based on the MessagePack RPC (Remote Call Procedure) library [96]. During the execution of an experiment shot, a digital signal triggers the execution of individual waveforms in the sequence.

4.2.1 Waveform generation

Details about the generation of waveforms can be found in the Ph.D. thesis of Vlad Negnevitsky [61]. Here I will just give an overview of the process for a better understanding of the results described in the next sections. It is worth noticing that the solver used for the waveform generation always assume single-species operations. However, the generated waveforms are then experimentally used also for mixed-species transport and splitting. In the following discussion about the solver architecture, I will assume single-species crystals.

In the segmented trap, we have a total of 30 dc electrodes. A voltage v_i on the i-th electrode generates an electric potential $V_i(x, y, z)$, which is dependent on the electrode geometry and on its surrounding environment. The potential can be expressed as

$$V_i(x, y, z) = \phi_i(x, y, z) v_j, \tag{4.1}$$

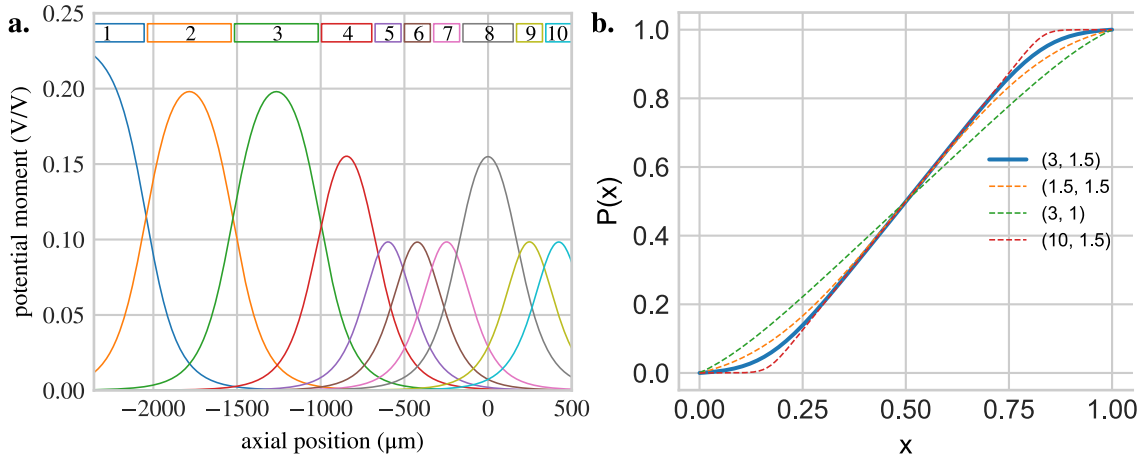[2]JavaScript Object Notation, http://json.org/.

Figure 4.5: **a** Electrode moments ϕ_i for $i \in [1, 10]$, located on the top wafer. On top of the image, the electrode widths drawn to scale. The central experimental zone is at $z = 0\,\mu m$, the left splitting region is at $z = -422.5\,\mu m$ and the loading zone at $z = -1870\,\mu m$. The electrode moments on the right side of the trap are symmteric around $0\,\mu m$. The bottom wafer is ideally the same as the top wafer. This image was taken from Vlad Negnevitsky Ph.D. thesis [61] **b.** Profile of the function $P(x)$ according to Equation 4.8 for different values of (a, b) parameters. The solid line correspond to $(a, b) = (3, 1.5)$, that is the parametrization we use for the transport operations presented in this thesis.

where the term $\phi_i(x, y, z)$ is the dimensionless potential moment, which is defined as the potential at position (x, y, z) generated by the electrode for $1\,V$ test voltage. The total electric potential and field, for a set of voltages $\{v_i\}$ on all the 30 dc electrodes of the trap, is

$$V(x, y, z) = \sum_{i=1}^{N=30} \phi_i(x, y, z) v_i, \quad \vec{E}_u(x, y, z) = \sum_{i=1}^{N=30} v_i \frac{\partial \phi_i(x, y, z)}{\partial u}, u \in \{x, y, z\}. \quad (4.2)$$

As shown in Figure 2.1e, the dc electrodes on the top and the bottom wafers are symmetric. If the same voltage is applied on opposing electrodes, the electric field in the radial direction is ideally null everywhere along the trap axis ($x = 0$ and $y = 0$). If we assume that the ion is positioned along the trap axis, and in the absence of stray dc fields in the radial plane, we can ideally suppress the x and y dependence for the total potential and the potential moments in Equation 4.2. Opposing electrodes are driven by the same DAC chip, to ensure that temperature-dependent voltage fluctuation between DACs do not cause voltage differences that could displace the ions radially.

The potential moment of each electrode is obtained from a COMSOL electrostatic boundary-element simulation of the trap and its surroundings at points on a 3D grid with $5\,\mu m$ spacing, along and around the trap axis. Figure 4.5a shows the electrode moments for the electrodes $i \in [1, 10]$ on the left side of the trap. The moments for the electrodes on the right side are mirrored around $z = 0$.

A positively charged ion of mass m, given some cooling, will settle at local minima of the total potential, since the force experienced by the single-charged ion is $F_z = -e \partial V(z)/\partial z$. The potential minimum at location $z = p$ can be engineered to be smooth over a range of tens of micrometers, and can be well approximated by a quadratic potential around the

minimum [101]. The shape of the harmonic well can then be described as

$$V_h(z) = \frac{m\omega^2}{2e}(z-p)^2 + d \,, \tag{4.3}$$

where p is the position of the minimum along the trap axis, d a constant dc offset and

$$\omega^2 = \frac{e}{m}\frac{\partial^2}{\partial z^2}V(z)\bigg|_{z=p} \tag{4.4}$$

the trapping frequency at point $z = p$. Generally, the maximum trapping frequency ω at the trapping location p is constrained by the second derivatives of the electrode moments in the trapping location $\partial^2\phi_i(z)/\partial z^2|_{z=p}$, the highest achievable electrode voltages, and the dc offset d (especially if it is positive). By design, the rf electrodes are kept at dc-ground; therefore, a variation of the dc offset d effectively changes frequencies and directions of the radial normal modes of motion due to the emergence of a static quadrupole.

Generation of transport waveforms

To be able to shuttle the ions along the trap axis, the voltages applied on the electrodes must vary with time $\{v_1(t), \dots, v_{30}(t)\}$. For simplicity, let's consider the transport of a single potential well. From Equation 4.3 we can parameterize it by the position, the frequency and the offset (p, ω, d). For general transport operations, these three quantities can change in time. Following the approach introduced in the Ph.D. of Ludwig deClerq [49] and in the master thesis of Robin Oswald [100], the set of voltages $\{v_1(t), \dots, v_{30}(t)\}$, can then be derived by solving a constrained optimization routine where the a quadratic cost function is minimized subject to hardware constraints ($v_i(t) \in [-9.7, 9.7]$ V and the slew rate, dv_i/dt, limited to $4\,\mathrm{V\,\mu s^{-1}}$). The quadratic cost function that we minimize is

$$
\begin{aligned}
C = \int_{t_0}^{t_f} \Bigg\{ & \int_{z_{\min}}^{z_{\max}} G\left(t', z'\right) D\left(t', z'\right) dz' \\
& + \sum_{i=1}^{N=30} \left[r_0 \left(v_i\left(t'\right) - v_{\mathrm{def}}\right)^2 + r_1 \left(\frac{dv_i\left(t'\right)}{dt'}\right)^2 + r_2 \left(\frac{d^2 v_i\left(t'\right)}{dt'^2}\right)^2 \right] \Bigg\} dt'
\end{aligned}
\tag{4.5}
$$

where $z_{\min}$ and $z_{\max}$ are the trap boundaries. The term $D(t, z)$

$$D(t,z) = [V(t,z) - V_h(t,z)]^2 = \left[\left(\sum_i v_i(t)\phi_i(z)\right) - \left(\frac{m}{2e}\omega^2(t)\,(z-p(t))^2 + d(t)\right)\right]^2 \tag{4.6}$$

is the discrepancy between the desired harmonic potential and the one generated by the set of voltages $\{v_i\}$ at time t. This discrepancy is minimized only in a region of interest of radius R around the potential minimum p, parameterized by a Gaussian term $G(t, z) = \exp\left(\frac{-[z-p(t)]^2}{R^2(t)}\right)$. The other terms in the cost functions are used to suppress other unwanted behaviors. The first, weighted by r_0, penalizes the voltage deviation from the defined one v_{def}, and it is used to set the voltages outside the region of interest defined by $G(t, z)$ to a default value. The other two terms, weighted by r_1 and r_2, penalize the first and second derivative of a waveform, thus limiting the slew rate requirements on the DEATHs output [100].

The value of electrodes moments ϕ_i is given at discrete points along the trap axis spaced by $5\,\mu\mathrm{m}$. As a result, we discretize the cost function C both in space and time on a

$K \times M$ grid, where K is the number of points along the trap axis (usually $K = 943$, from $z = -2355\,\mu m$ to $z = 2355\,\mu m$), and M is the number of timesteps ($1 \leq M \leq 2000$, with a time step of $20\,ns$ to match the DAC sampling rate). The constrained optimization is currently done in python using a quadratic programming algorithm [100, 61, 49], which uses the CvxPy library to automate the process of defining the problem to the Mosek[3] solver.

During transport, it is desirable to avoid motional excitations, thus reducing the number of cooling cycles required within a sequence. For the experiments discussed in this thesis, the maximum transport speed of the ion is below $v_{max} = 5\,m\,s^{-1}$. For these speeds, the motional excitation can be suppressed by parameterizing the position $p(t)$ with a smooth function that minimizes the impulse on the ion [61, 102, 103], and is written as

$$p(t) - p(t_0) = [p(t_f) - p(t_0)]\, P\left(\frac{t - t_0}{t_f - t_0}\right)\ , \tag{4.7}$$

where

$$P(x) = \frac{\rho(x) - \rho(0)}{\rho(1) - \rho(0)}, \quad \rho(x) = \ln\left|\frac{\zeta(x) - ie^{-a}}{\zeta(x) - ie^a}\right|, \quad \zeta(x) = \exp[ab(2x - 1)]\ . \tag{4.8}$$

The a parameter defines the sharpness of the position profile at the beginning and at the end of transport, while b determines the slope in the middle. Figure 4.5b shows the profile of $P(x)$ for different pairs of (a, b) parameters. The typical values used in our experiment are $a = 3$ and $b = 1.5$. The dc offset $d(t)$ and the motional frequency $\omega(t)$ follow a similar trajectory to Equation 4.7. A common choice is $P(x) = \sin^2(\pi x/2)$, however this was found to be somewhat inflexible [61]. For this reason we decided to parameterized the position as described above.

Splitting waveforms generation

To split an ion chain, the potentials need to be engineered to transition from an initial single well potential, containing the ion chain we wish to split, to a double well with the two separated strings [104]. The time-dependent dc potential around the splitting region can be well approximated by a 4-th order polynomial of the form

$$V_{\text{sep}}(z, t) = \alpha(t)(z - z_s)^2 + \beta(t)(z - z_s)^4 + \gamma(t)(z - z_s) + \delta(t), \tag{4.9}$$

where the cubic term is assumed to be negligible. This is a valid approximation as long as the electrode geometry and applied voltages are locally symmetric around the splitting point z_s. In our setup the splitting position z_s is located at -422.5 ($+422.5$) μm from the trap center, for the left (right) splitting region (Figure 2.1e). The parameter δ specifies the dc offset at z_s, while γ is an axial electric field, which is ideally zero. In practice, axial stray fields and deviation of the experimental potential moments from the model require this parameter to be calibrated experimentally. The terms α and β are instead related to the ion separation distance s and the axial center-of-mass angular frequency ω of a crystal in this potential by [104]

$$\begin{aligned} \beta s^5 + 2\alpha s^3 &= \frac{e}{2\pi\epsilon_0} \\ \omega^2 &= 2\alpha + 3\beta s^2 \frac{e}{m} \end{aligned} \tag{4.10}$$

where ϵ_0 is free-space permittivity and mass m.

---

[3]https://www.mosek.com

At the beginning of the separation process, α is positive, and β is small. During splitting, β is then increased, while α is gradually lowered to a negative value to create a double well potential. While α is decreased, it is desirable to maximize the motional frequency ω to minimize the heating generated by external noise (see Section 4.2.2). This can be achieved by keeping β as high as possible, as it can be seen from Equation 4.10.

The electrodes involved in the splitting process in the left splitting region are the one from 4 to 8 (Figure 2.1) and their symmetric counterpart on the bottom dc wafer. The solver introduced above for the generation of the transport waveforms is not optimal for the splitting process since it uses a constant number of fixed-parameter wells, and it is not designed to favor specific parameters at the expense of others [61]. Therefore, Vlad Negnevitsky [61] defined a new solver, used only for the generation of the splitting waveforms, that takes into account the 10 relevant dc electrodes around the splitting region, and accepts only continuous functions to minimize the cost function. For this purpose, the electrode moments are fitted with 4-th order polynomials over a $200\,\mu\text{m}$ region of interest [61]. For each electrode i ($i \in [4, 5, 6, 7, 8, 19, 20, 21, 22, 23]$ for the left splitting region), the fits are of the form

$$\tilde{\phi}_i\left(z\right) = \tilde{\alpha}_i(z - z_s)^2 + \tilde{\beta}_i(z - z_s)^4 + \tilde{\gamma}_i(z - z_s) + \tilde{\delta}_i + \tilde{g}_i(z - z_s)^3 \ , \qquad (4.11)$$

where the tildes is used to denote fitted values. As a result, the fitted separation potential can be written as $\tilde{V}_{\text{sep}}\left(z_s\right) = \sum_i v_i \tilde{\phi}_i\left(z_s\right)$. The $\{\alpha, \beta, \gamma, \delta\}$ parameters of Equation 4.9 can then be calculated from the following

$$\begin{bmatrix} \alpha \\ \beta \\ \gamma \\ \delta \end{bmatrix} = \begin{bmatrix} \tilde{\alpha}_4 & \ldots & \tilde{\alpha}_8 \\ \tilde{\beta}_4 & \ldots & \tilde{\beta}_8 \\ \tilde{\gamma}_4 & \ldots & \tilde{\gamma}_8 \\ \tilde{\delta}_4 & \ldots & \tilde{\delta}_8 \end{bmatrix} \begin{bmatrix} v_4 \\ \vdots \\ v_8 \end{bmatrix} \qquad (4.12)$$

The solver is then designed to minimize the cost function C defined as

$$C = \sum_{i=4}^{8} \left[q_1 \left(\alpha(t) - \tilde{\alpha}_i v_i(t) \right)^2 + q_2 \left(\gamma(t) - \tilde{\gamma}_i v_i(t) \right)^2 + q_3 \left(\delta(t) - \tilde{\delta}_i v_i(t) \right)^2 \right] - \sum_{i=4}^{8} \tilde{\beta}_i v_i(t) \ . \qquad (4.13)$$

For the left splitting zone, the cost function is minimized only for electrodes from 4 to 8 since the same voltage is then applied to the symmetric counterparts in the bottom wafer. The parameters q_1, q_2 and q_3 determine how closely the desired α, γ, δ parameters are met, while trying to maximize β.

The α parameter is lowered from a positive α_0 to a negative α_f. For the results shown in this thesis, $\alpha_0 = -\alpha_f = 5 \times 10^6$ V/m^2, which corresponds to a calcium frequency $\omega = 2\pi \times 780\,\text{kHz}$ (for $\beta = 0$), although this choice is arbitrary. During splitting, the primary goal is the minimization of the motional excitation of the ions. This can arise from heating, uncontrolled stray fields, and impulsive acceleration (due to uncontrolled waveform voltages) that can happen around the critical point ($\alpha \approx 0$) where the confinement is weak. A small value of the acceleration close to the critical point, $\ddot{s}_{\text{CP}}$, can be guaranteed by controlling the ion separation distance s [105]. Therefore, it is advantageous to re-parameterize the voltages in terms of s, instead of α. The waveform generation then proceeds as follows. Initially, the solver is run k times (typically $k = 100$) for α values between α_0 and α_f to produce a set of voltages $\vec{v}[k]$ for each $\alpha[k]$. From the $\alpha[k]$ and $\beta[k]$ parameters obtained by the solver, it is then possible to calculate a the position $s[k]$ according to Equation 4.10.

Since $s[k]$ is monotonic with respect to $\alpha[k]$, the voltages are re-parameterized by using a 4−th order spline interpolation to the coordinates sets $(x,y) = (s[k], \vec{v}[k])$, to obtain $v(s)$.

Now by defining the splitting trajectory $s(t)$ between the initial and final separation (s_0 and s_f) as

$$s(t) = s_0 + \tau(t)^\epsilon \left(s_f - s_0\right) \tag{4.14}$$

with $\tau(t) = (t - t_0)/(t_f - t_0)$, and for $\epsilon = 3$ [105, 61].

Once $s(t)$ is defined, the set of voltages $\vec{v}(t)$ can directly calculated from the function $\vec{v}(s)$.

For the results presented below, the dc offset parameter δ at position $(z - z_s)$, is not constrained and thus the cost term q_3 in Equation 4.13 is set to 0. Experimentally we observe that the dc offset tends to vary throughout the splitting process, reaching the lowest negative value ($-1.5\,\text{V}$) at the critical point to ensure the highest possible trapping frequency at the critical point for the range of output voltages that the DEATHs can supply.

For symmetric separation, the axial electric field is ideally $\gamma = 0$. Nevertheless, fluctuating stray field and deviations from the true potential moments may require a compensating axial field during splitting to reduce the motional excitation. In the current version of the solver, the γ parameter is set to be $\gamma = \gamma_{comp}$ for the entire splitting process. To fine-tune the axial dc field in the left splitting region ($-422.5\,\mu\text{m}$), we differentially add an extra voltage to the electrodes on the left (Electrodes 5 and 20) and on the right (Electrodes 7 and 22) side of the splitting zone. From the moments of electrodes $5, 20, 7, 22$, it can be shown that when we differentially add 1 V, the resulting net axial field is $1372.8\,\text{V}\,\text{m}^{-1}$.

The most recent splitting experiments apply the axial dc offset by interpolating the splitting waveform with another waveform that adds $1\,\text{V}$ to electrodes 7 and 22, and subtracts it from electrodes 5 and 20. To avoid discontinuities in the voltages, the waveform applying the differential dc offset is designed to smoothly increase (decrease) the offset voltage to reach the desired value at the critical point as shown in Figure 4.7b. Details of the interpolation procedure will be covered in the upcoming Ph.D. thesis of Francesco Lancellotti [106].

4.2.2   Single species splitting

Within this section, I will present the splitting experiments of a two-ion crystal of the same species, highlighting the procedure we followed to optimize the splitting operation in the laboratory. The figure of merit for the quality of splitting is the motional excitation induced by splitting on both ions, and the time it takes to separate the ions. The potentials for the entire waveform set used for splitting are shown in Figure 4.6.

Initially, the two ions are in a single potential well located in the experimental zone in the center of the trap, $z = 0$. Here the axial modes of motion are cooled to the ground state following a sequence similar to the one described in Chapter 2.7. After cooling and state preparation, the waveform sequence is started. First the ions are transported to the splitting region on the left side of the trap $z = -422.5\,\mu\text{m}$ from the trap center (waveform a in Figure 4.6). The ions are then separated in two different wells with waveform b, and that in the well 1 (the rightmost one) is transported to the experimental zone in the center of the trap, where we measure either the ion fluorescence or the temperature of the motional modes by applying a blue sideband pulse (Section 2.7.4). A second transport waveform c shuttles the ion in well 2 to the experimental zone for the diagnostic pulse. Finally, the
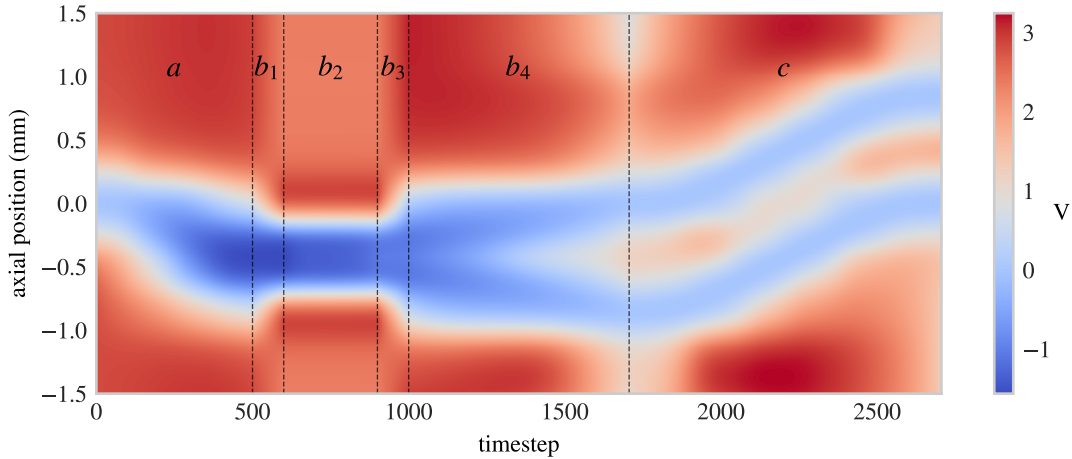
Figure 4.6: Potentials for the entire waveform set used for splitting. Waveform a shuttles the ions from the experimental zone in the center of the trap to the splitting zone. Waveform b separates them into two wells and shuttles one well to the central experimental zone while moving the second well to a storage region. Waveform c shifts the second well to the experimental zone and moves the first well to a storage region. Waveform b consists of different sections: b_2 is the actual splitting waveform generated with the polynomial solver whereas b_4 uses the regular transport solver, with b_1 and b_3 being an interpolation between the solvers. This image has been taken from the Ph.D. thesis of Vlad Negnevitsky [61]

ions are recombined in the same potential well by running the entire sequence in reverse. All waveforms are generated by the transport solver (Section 4.2.1) with the exception of a part of the splitting waveform b, labeled as b_2 in Figure 4.6 which is instead generated with the polynomial splitting solver (Section 4.2.1). To smoothly transition from the waveforms generated by one solver to the other, we add interpolation waveforms (with approximately 100 timesteps), labeled as b_1 and b_3 in Figure 4.6.

For the initial optimization of the splitting process, we run the full transport and splitting waveform, and we scan the axial field γ over a few tens of V m^{-1}. We then measure the fluorescence of the ions in the two wells to identify a range in which the two ions separate in two different wells. A typical fluorescence scan as a function fo the axial field is shown in Figure 4.7a, and is characterized by clear 'steps'. Experimentally we set γ to be in the center of the step where the two ions are in two separate wells. We further optimize the splitting parameters, like the slowdown, by measuring the axial mode temperature of the two ions after splitting using sideband probes.

The lowest axial excitation results are shown in Figure 4.8 for a two ion single-species splitting experiment performed either with calcium (panels a and b) or beryllium (panels c and d). The figure shows the blue sideband Rabi oscillation for the ion in well 1 (panels a and c) and in well 2 (panels b and d), from which we extract the average motional occupancy, according to Equation 2.38.

The initial average thermal occupancy of the axial modes before splitting is $\bar{n}_{COM} = 0.18(2)$ and $\bar{n}_{STR} = 0.11(1)$, measured by running a blue sideband Rabi oscillation on each mode before the 'single'-ion readout following splitting. The BSB Rabi oscillations are then fitted according to Equation 2.38 to extract the mean phonon occupancy for each mode. The splitting is then further optimized by tuning the DEATHs slowdown by minimizing the axial excitation of the two ions after the separation. We find that the lowest axial excitation is
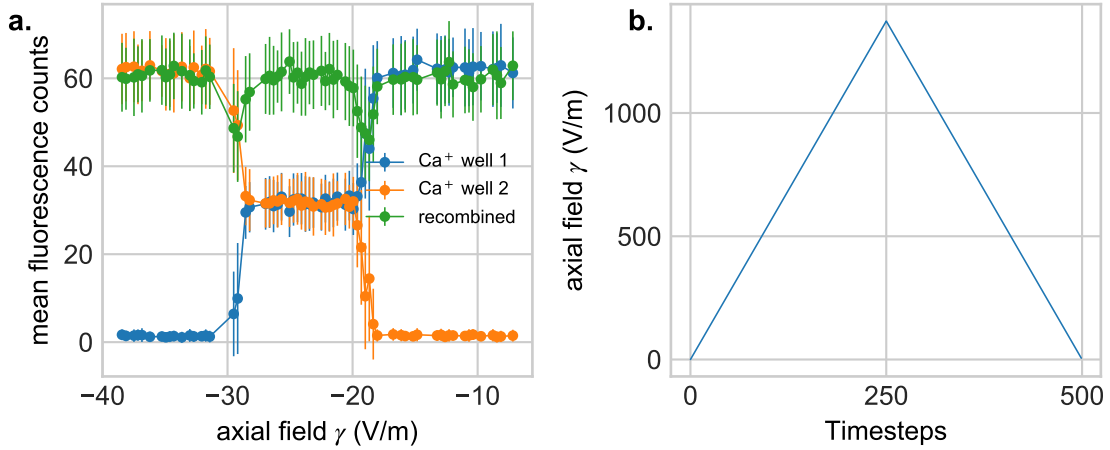
Figure 4.7: Separation of a calcium-calcium crystal. **a** The three curves represent the mean PMT counts in Well 1, 2, and after recombination. For an axial field between $-28 \leq \gamma \leq -20$ V m^{-1} there is one ion in each well. Left (right) of this region, the axial field drives both ions into Well 2 (Well 1). The recombined counts show the fluorescence for a repeated detection of the ions in a single well. **b** Axial field in the splitting reagion as a function of the waveform timesteps. The maximum field of $\gamma = 1372.8$ V m^{-1} is applied at the critical point. This waveform is interpolated with the splitting one. The smooth ramp-up and ramp-down avoid first order discontinuities in the voltages and ensure that the axial field is present mostly around the critical point.

reached for a splitting time of 350 µs for an ion separation distance of 350 µm (approximately around timestep 900 in Figure 4.6)), where the 0 time is set to be at the beginning of the splitting waveform sequence (beginning of waveform b_2 in Figure 4.6). After splitting, the fitted thermal state on the axial mode has a mean phonon number of $\bar{n}_{w1,Z} = 1.56(6)$ and $\bar{n}_{w2,Z} = 1.63(7)$, respectively for the ion in well 1 and 2.

For beryllium, the initial average thermal occupancy of the axial modes before splitting is $\bar{n}_{COM} = 0.13(2)$ and $\bar{n}_{STR} = 0.19(2)$. After splitting the fitted thermal state on the axial mode has a mean phonon number of $\bar{n}_{w1,Z} = 0.67(3)$ and $\bar{n}_{w2,Z} = 0.76(3)$, respectively for the ion in well 1 and 2. In this case, the optimal time taken to separate the two ions by 350 µm is 325 µs. The lower excitation achieved with beryllium is due to the larger axial confinement. In fact, while the the lowest normal mode frequency during the split for calcium is $\sim 2\pi \times 330$ kHz, it is almost double for beryllium.

Classical simulation and heating rate   To reproduce the results, under the assumption of an ideal model of the trap, Francesco Lancellotti performed classical simulations of the entire splitting sequence using the potentials generated by the solvers, following a similar approach to [105, 107]. Details about the simulation will be presented in his Ph.D. thesis [106], but at the time of writing, we are still not able to reproduce the experimental results. Starting from ions with no kinetic energy, the expected thermal state distribution after splitting should have an average mean phonon number of $\bar{n}_{Ca} \approx 0.2(1)$ and $\bar{n}_{Be} \approx 0.05(2)$.

The classical simulation also takes into account the heating caused by technical noise and anomalous heating, which scales inversely on frequency [108, 101]. Taking this into account is particularly important since, during splitting, the axial confinement is gradually reduced to reach a minimum at the critical point ($\omega \approx 2\pi \times 330$ kHz for calcium). The
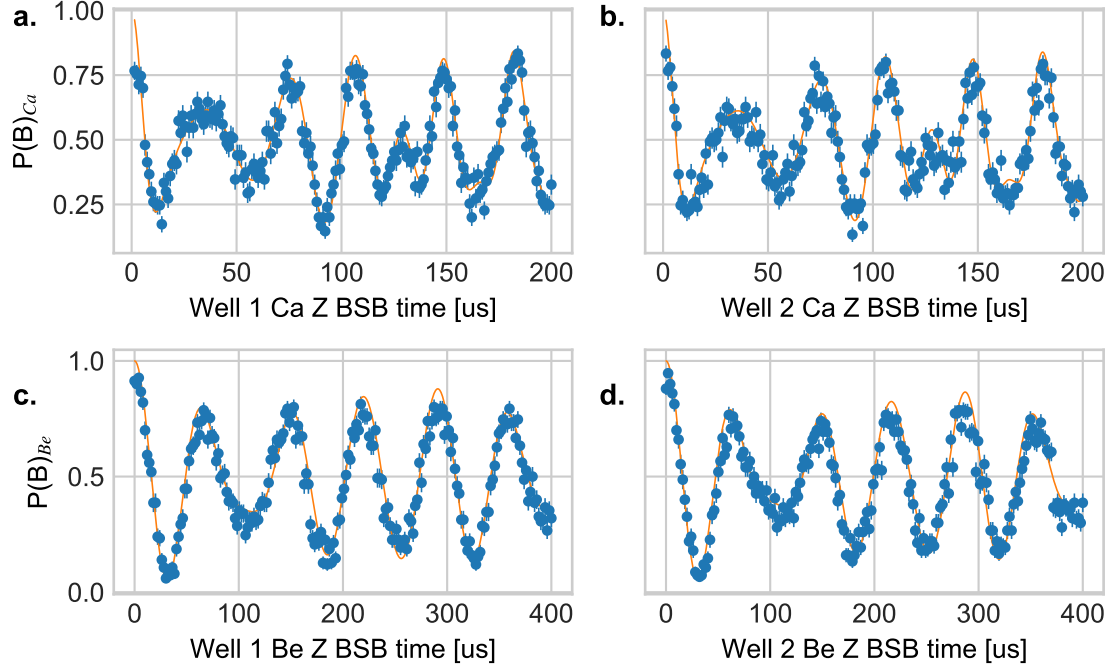
Figure 4.8: Axial blue sideband Rabi oscillation after the splitting of single-species two ion crystal. Panel **a** and **b** show the blue sideband Rabi oscillation of two calcium ions after splitting. Before splitting, the axial motional modes are cooled with interleaved sideband cooling to a thermal occupancy of $\bar{n}_{COM} = 0.18(2)$ and $\bar{n}_{STR} = 0.11(1)$. The fitted thermal states of the axial mode after splitting have a mean phonon number $\bar{n}_{w1,Z} = 1.56(6)$ and $\bar{n}_{w2,Z} = 1.63(7)$ respectively for the ion in well 1 and 2. Panel **c** and **d** the blue sideband Rabi oscillation of two beryllium ions after splitting. The initial phonon occupancy of the axial modes is $\bar{n}_{COM} = 0.13(2)$ and $\bar{n}_{STR} = 0.19(2)$. After splitting, we fit a thermal distribution to the axial mode BSB Rabi oscillation with mean $\bar{n}_{w1,Z} = 0.67(3)$ and $\bar{n}_{w2,Z} = 0.76(3)$, respectively for the ion in well 1 and 2.

measurement of the heating rate in the splitting zone is experimentally complicated and require lots of changes to the setup. For an initial estimation, we measured the heating rate in the experimental zone located in the center of the trap and assumed that the heating rate at the separation location is comparable. The results are shown in Figure 4.9. To perform these measurements, a single calcium ion is initially ground state cooled in well located in the center of the trap and with an axial frequency $\omega_z = 2\pi \times 1.1$ MHz. The axial confinement is then adiabatically modified to reach the desired axial frequency ω_z'. After leaving the ion in this configuration for a variable time, the confinement is adiabatically set back to $\omega_z = 2\pi \times 1.1$ MHz, and the temperature is measured with the blue sideband method. The heating rate for an axial frequency ω_z', is then extracted by fitting the increase of the thermal state's mean phonon number as a function of increasing time spent in the potential well with frequency ω_z'.

For the classical simulation of splitting, we calculate the expected motional heating by integrating over a time dependent heating rate [105]

$$\delta\bar{n} = \int_0^{t_f} \Gamma(\omega_z(t)) dt, \tag{4.15}$$

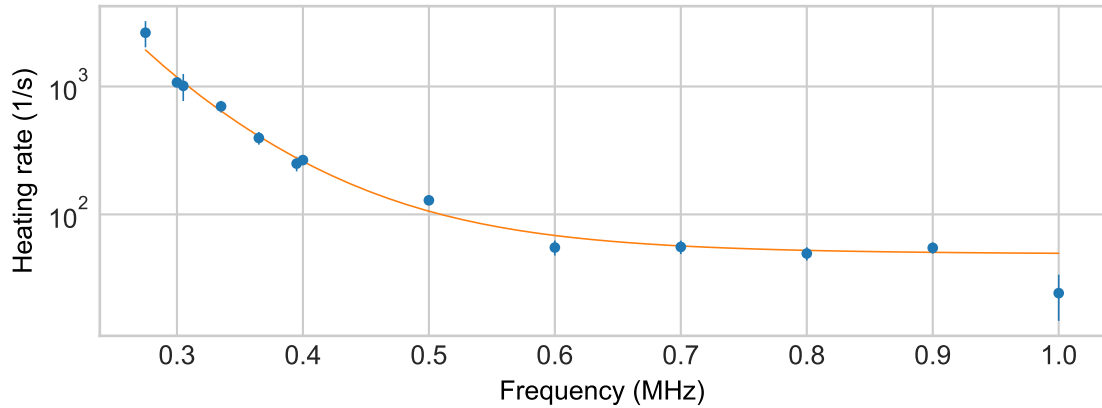where $\Gamma(\omega_z)$ is the heating rate as a function of frequency.

Figure 4.9: Heating rate as a function of axial trapping freqeuncy, measured with a single calcium ion. The experimental sequence used to extract it is described in the text. The solid line is a fit of the function $\Gamma(\omega_z) = 1/\omega_z^\alpha + c$ to the experimental data. The fitted scalig parameter is $\alpha = 5.84(5)$ and the base line is $c = 48(5)$. The presence of a baseline is probably an indication of technical noise that dominates at higher frequencies. This hypothesis could be tested measuring heating rates at higher frequencies.

At the of writing, the classical simulations, together with the heating rate values are not enough to explain the observed motional excitations. However, there is an on going effort to improve the trap model and the classical simulations.

4.2.3   Beryllium-calcium splitting

The same splitting waveform sequence was also tried for beryllium-calcium crystals. For this purpose, before running the splitting waveforms, the in-phase and out-of-phase axial modes were cooled to the ground state, and the two lowest radial modes were EIT cooled. Following a similar procedure to that described above, it was possible to find an axial field that would split the two ions in two separate wells. The splitting routine was not particularly stable and ions were lost every few hundreds of shots. As a consequence, gathering enough statistics for the temperature measurement of the motional modes after splitting was hard.

To better understand which part of the splitting sequence was causing this much instability, we first analyzed the mixed-species transport to the splitting zone. One feature of the transport waveform used for splitting is that the dc offset δ is lowered from $\delta =1.4\,\text{V}$ to $\delta =-1.5\,\text{V}$. Such a low dc-offset in the splitting zone is used to achieve the highest possible axial confinement at the critical point during splitting for the range of output voltages of the DEATHs. However, in the experimental zone, we use positive dc-offsets for stability of laser cooling. Experimentally we observed that low dc-offsets require high voltages applied to the shim electrodes to compensate micromotion in the experimental zone, and for dc offsets below $\delta =-1\,\text{V}$, the required voltage is beyond the $[-30\,\text{V},\ 30\,\text{V}]$ range allowed by the DACs controlling the shim electrodes. As a consequence, radial micromotion is not compensated during transport.

The normal modes of motion for a mixed-species crystal change in the presence of additional static fields, which does not occur for single-species chains [51]. Due to the weaker radial confinement experienced by the heavier mass ion, static radial fields displace the heavier ion from the trap axis by more than those of the lighter ion. As a result, a

varying radial field during transport could cause excitations of the motional modes of the mixed-species crystal [109].

To test whether the main cause of instability is due to the changing dc offset δ, we perform two experiments using a beryllium-calcium ion chain. In one case, we do a round trip transport from the experimental zone to the left splitting zone ($z = -422.5\,\mu m$) keeping the dc offset constant at $1.4\,V$, while, in the second case, the dc offset is gradually lowered to $-1.5\,V$ as the ions approach the splitting zone. At the end of the transport, we measure the motional occupancy of the axial and radial modes to see if there are any differences in the excitations. In both cases, the voltages applied to the shim electrodes are such that micromotion is compensated in the experimental zone in the center of the trap for a dc-offset $\delta = 1.4\,V$. Before transporting the ions, the axial modes and the two lowest radial modes are EIT and sideband cooled (see Section 2.8.1 for the modes' frequencies). The measured thermal occupancies are $\bar{n}_{Z1} = 0.005 \pm 0.01$, $\bar{n}_{Z2} = 0.01(1)$ and $\bar{n}_{Y1} = 0.18(2)$ for the in-phase ($Z1$), out-of-phase ($Z2$) and lowest radial mode respectively. To ensure adiabatic transport, the DEATHs slowdown is set to 100, corresponding to $500\,\mu s$ needed to cover $-422.5\,\mu m$.

After the round trip transport, we perform blue sideband Rabi oscillations on the three different modes to extract the thermal occupancy, as shown in Figure 4.10. A fit of Equation 2.38 to the curve, assuming a thermal distribution for the motional states, allows to extract the average motional occupancy of each mode. It is clearly visible that a varying offset introduces severe heating especially on the lowest frequency radial mode, with a final thermal state with $\bar{n}_{Y1} = 5.0(7)$. We explain this result as being due to uncontrolled radial micromotion compensation during transport, whose effect is to induce a tilt of the mixed-species crystal which causes an energy coupling between the axial and radial modes.

4.2.4 Next steps

Single species transport and splitting are reliable and well-controlled at moderate velocities. It is used daily for ion loading, beam alignment (Section 5.1.2), MS gate optimization 5.3.4 and to remove hydrides. Future improvements for single-species experiments might go in the direction of diabatic transport and splitting, though it would not be my immediate priority since mixed-species splitting is not yet as reliable.

One current limitation is that the waveform generation purely relies on the simulation model of the trap. As was performed in previous low-excitation single-species separation work [105, 110], the experimental characterization of the electrode moments may be beneficial to improve the splitting experiments also for mixed-species.

In the laboratory, we tried different approaches to precisely measure the electrode moments, and the results will be presented in the Ph.D. thesis of Francesco Lancellotti [106]. So far, the most promising method consists of measuring the radial field experienced by a single calcium ion, trapped in different locations on the trap axis, when a voltage offset is applied on a single dc-electrode. The radial field intensity and direction is extracted by measuring how much the micromotion compensation voltages change with and without the dc-offset on the single electrode. Initial results seem promising though more investigation is required to check the quality and accuracy of the results.
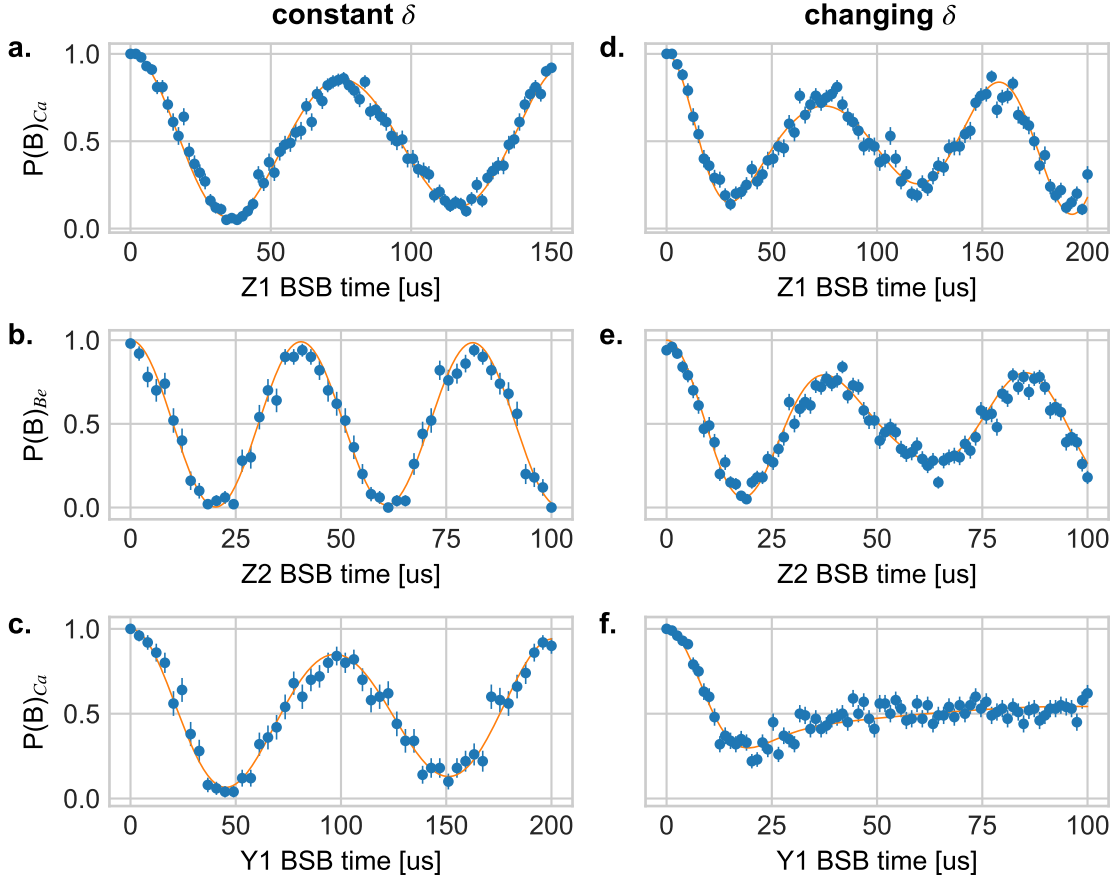
Figure 4.10: Blue sideband Rabi oscialltions on the in-phase axial mode (Z_1), out-of-phase axial mode (Z_2), and the lowest radial mode (Y_1), after round trip transport to the left splitting zone ($z = -422.5\,\mu$m). The plots on the left are taken for a transport seqeunce that kept the dc-offset constant $\delta = 1.4$ V. For the plots on the right the dc-offset was reduced from $\delta = 1.4$ V to $\delta = -1.5$ V as the ion approached the left splitting zone. The initial motional occupancy before transport was measured to be $\bar{n}_{Z1} = 0.005 \pm 0.01$, $\bar{n}_{Z2} = 0.01(1)$ and $\bar{n}_{Y1} = 0.18(2)$ for Z_1, Z_2 and $Y1$ respectively. After the round trip transport the fitted motional occupancy for the case of constant dc-offset is $\bar{n}_{Z1} = 0.21(2)$, $\bar{n}_{Z2} = 0.02(1)$ and $\bar{n}_{Y1} = 0.22(3)$, while for the varying dc-offset the fitted motional occupancyes are $\bar{n}_{Z1} = 0.71(5)$, $\bar{n}_{Z2} = 0.50(3)$ and $\bar{n}_{Y1} = 5.0(7)$.

4.3   Mixed-species reordering and recrystallization

Keeping a well-defined crystal order is required for mixed species experiments as the normal mode frequencies and amplitudes depend on the chosen crystal configuration. To maintain a given order, we follow the approach described in [51] where we make use of the mass dependence of the total potential.

In the setup, reordering is carried out in the center of the trap using the six closest dc electrodes (electrodes 7, 8, 9 and 22, 23, 24 of Figure 2.1)). It can be performed manually by triggering the respective DEATH waveforms directly in Ionizer, or it can be done automatically by the master board at the beginning of each data point.

4.3.1 Be-Ca-Be reordering

For the experiments described in Chapter 6 we use a symmetric crystal composed of a calcium ion placed between two beryllium ions. To reliably achieve this configuration, we apply a radial displacement by adding a voltage offset to the electrodes 7, 8 and 9. Due to the weaker radial confinement, the calcium ion displaces further. For axial confinement of $\omega_{Z1} = 2\pi \times \approx 1.5\,\text{MHz}$, and for an electrode voltage offset of $2\,\text{V}$, the ion chain undergoes a sudden transition to the lowest energy configuration that resembles an isosceles triangle with the calcium ion at the outer corner. By removing the radial displacement gradually while simultaneously running the Doppler cooling sequence, the ions return to the trap axis with the calcium ion placed between the two beryllium.

4.3.2 Be-Ca reordering

For this configuration, a simple radial displacement isn't enough for a deterministic reorder due to the axial symmetry of the trap. Therefore, after applying a radial displacement, we also introduce a twist in the potential [51, 101] by symmetrically increasing the voltages of electrodes 7 and 24 and reducing those of electrodes 9 and 22. The initial radial displacement shifts the two ions off-axis towards electrodes 22,23 and 24, while the twist introduces an axial displacement towards the electrode's pair 7 and 22. The lower radial confinement of calcium results in a larger radial displacement. Consequently, a larger axial displacement arises due to the higher net axial field (calcium is closer to electrodes 22, 23, 24). As a consequence, the crystal configuration is tilted towards one side of the trap axis. The reordering process is then concluded by first removing the radial displacement to bring the ions back onto the trap axis, with the calcium ion on the side of the chain. Then, as the last step, the axial displacement is removed, leaving the ion in the desired configuration. To have a reliable reordering we apply an offset voltage of $2\,\text{V}$ for the radial 'push' and a twist voltage offset of $0.9\,\text{V}$, for a well whose lowest axial frequency is $\omega_{Z1} = 2\pi \times \approx 1.3\,\text{MHz}$ and with the lowest radial frequency at $\omega_{Y1} = 2\pi \times \approx 2.4\,\text{MHz}$.

4.3.3 Recrystallization

Collisions between the ions and background gas atoms can lead to large motional excitations that bring the ions into a regime where the detection and Doppler cooling beams are far off-resonance. In our setup, the rate at which this happens is approximately one event every half a minute for the beryllium-calcium-beryllium crystal.

To detect these events, we monitor the number of photons scattered during Doppler cooling. If the photon count is below a given threshold, the master board assumes that a collision happened during the previous shot. For this reason, it automatically flags the result of the previous shot as bad and retakes it. If the counts remain below the threshold for several consecutive shots, the system assumes that the ions are in a state with large motional excitation. In this case, the master board tries to recover the ions by running a 'recrystallization' sequence that triggers a waveform with a low axial trapping frequency $\approx 400\,\text{kHz}$ (for calcium). Once the ions are in the low axial frequency potential, successive sequences of pre-cooling and Doppler cooling pulses are applied until the photons detected during Doppler cooling are again above the threshold, or until a timeout is reached. In the case of recovery, the waveform is reset to the original and the last data point is repeated. If the recrystallization did not succeed, the master board alerts the user with an error message and waits for inputs.

5 Mixed-species experimental operations

This chapter is devoted to the description of the experimental techniques used for the calibration of parameters and the characterization of mixed-species ion chains. In the beginning, I will describe the Ramsey techniques, which we use to calibrate frequencies and to estimate spin and motional coherence. I will then continue by describing the experimental characterization of mixed-species normal modes, and finally, introduce multi-qubits states and the experimental techniques to create entangled states.

5.1 Ramsey sequence and related techniques

Ramsey sequences [111] are widely used in QIP experiments and metrology. In our experiment, they are primarily used for the calibration of qubit frequencies and the measurement of the qubit and motional coherence.

Starting from a qubit in state $|\downarrow\rangle$, a carrier $\pi/2$-pulse with phase ϕ_1 prepares the qubit in a superposition state

$$|\psi\rangle = \hat{R}(\pi/2, \phi_1)|\downarrow\rangle = \frac{1}{\sqrt{2}}\left(|\downarrow\rangle - ie^{-i\phi_1}|\uparrow\rangle\right) , \tag{5.1}$$

where $\hat{R}(\theta, \phi)$ is the qubit rotation matrix defined in Equation 2.24 [1]. After this, the qubit is exposed to a Hamiltonian

$$H_R = \frac{1}{2}\hbar\delta(t)\hat{\sigma}_z \tag{5.2}$$

for an interrogation time τ, which results in a state

$$|\psi\rangle = \frac{1}{\sqrt{2}}\left(|\downarrow\rangle - ie^{-i(\phi_1 + \Phi(\tau))}|\uparrow\rangle\right) , \tag{5.3}$$

where Φ is the phase acquired by the qubit during the interrogation time, and defined as $\Phi(\tau) = \int_0^\tau \delta(t)dt$. The sequence is then concluded by applying a second carrier $\pi/2$-pulse with phase ϕ_2. The population in state $|\downarrow\rangle$ is

$$P_\downarrow(\tau, \delta\phi) = \frac{1}{2}(1 - \cos(\Phi(\tau) - \delta\phi)), \tag{5.4}$$

with $\delta\phi = \phi_2 - \phi_1$.

5.1.1 Bare qubit frequency calibration and coherence

In the simple case where the laser has a small detuning δ_0 from the qubit transition frequency, and in the absence of any source of noise that could perturb the frequency of either the qubit

---

[1]Note that in this case we assumed the rotation to be perfectly on resonance with the qubit frequency. This is a valid assumption for small frequency detunings compared to the overall Rabi frequency ($\delta \ll \Omega$), since the contrast of the Rabi oscillations is affected only to second order in δ/Ω.

transition or the laser, $\Phi(\tau) = \delta_0\tau$. The laser frequency can be calibrated to be on resonance with the qubit by minimizing $P_\downarrow(\tau, \delta\phi)$ while scanning the interrogation time τ.

If the phase $\Phi(\tau) - \delta\phi$ fluctuates, the population $P_\downarrow$ differs at each shot. In this case the average population can be described by

$$\langle P_\downarrow \rangle = \frac{1}{2}[1 - C(\tau)\cos\left(\langle\Phi(\tau) - \delta\phi\rangle\right)] \tag{5.5}$$

where $C(\tau) \in [0,1]$ accounts for the worsening of the contrast. The shape of $C(\tau)$ depends on the spectral properties of the noise. If Φ is sampled from a normal distribution $G(\Phi)$, representing the contribution to Φ of the various slow noise sources, the fluctuations in Φ are slower than the Ramsey probe time τ. In this case can then $C(\tau)$ can be modeled by a Gaussian [84]. However, if fluctuations in Φ are faster than the Ramsey probe time τ the expected shape of $C(\tau)$ is an exponential.

By fitting the decay function $C(\tau)$ to the Ramsey contrast, it is then possible to extract the dephasing rate. This technique was used to measure the coherence time of both calcium and beryllium that are presented in Section 2.5 [68, 66, 48].

5.1.2 ac Stark shift calibration

In the presence of ac Stark shifts, the qubit drive induces a frequency shift ω_{ac} to the bare qubit frequency ω_0. A standard Ramsey sequence, in the limit of long wait times and short $\pi/2$ times, does not allow the precise calibration of of ω_{ac} since during the interrogation time τ the qubit evolves according to the bare qubit frequency.

In the mixed-species experiments presented in this thesis, we handle ac Stark shifts in two different ways. In Chapter 6, the frequency of the relevant carrier rotations (beryllium FIQ transition and calcium optical transition) are calibrated to be on resonance with the bare qubit frequency ω_0, thus neglecting Stark shifts. This approach facilitates the automatic calibration of the phases $\phi = \omega_0(t - t_{ref})$ in the M-ACTION system for phase coherent pulses (see 4.1.2). Nevertheless, the laser drive is off-resonant, and therefore the fidelity of each pulse is reduced. For the simple case of a carrier π-pulse the inversion fidelity will be $p_{\text{inv}} \approx \Omega^2/(\Omega^2 + \omega_{ac}^2)$. The infidelity then scales as ω_{ac}^2/Ω^2. In our experiment, the highest infidelity is measured for the beryllium co-carrier FIQ transition, where the Rabi frequency is $\Omega \sim 2\pi{\times}100\,\text{kHz}$ and the measured ac Stark shift is $\omega_{ac} \sim 2\pi{\times}5\,\text{kHz}$, leading to infidelity below 1%.

The experiments presented in Chapter 7 take into account ac Stark shifts, such that the qubit is driven on resonance with dressed-qubit frequency $\omega_d = \omega_0 + \omega_{ac}$. In this case, the pulse fidelity is the highest, but the automatic phase calculation is less trivial and require the use of the phase accumulators described in Section 4.1.2.

Initially we tried calibrating the Stark-shifted frequency ω_d by maximizing the inversion depth of $2n$ π-pulses. Figure 5.1a shows the inversion probability after 11 consecutive π-pulses applied on a single beryllium ion, as a function of the laser frequency. The primary source of contrast loss is slow intensity noise. For a fluctuating Rabi frequency, the depth of inversion will be different at each shot, thus reducing the contrast and consequently limiting the precision of the frequency calibration.

For this particular noise source, this issue was then solved by slightly modifying the pulse sequence. For an ion initially in state $|\downarrow\rangle$, we repeat n pairs of pulses, where the second pulse of each pair undo the operation done by the first. For an initial rotation $R(\theta, \phi)$, the
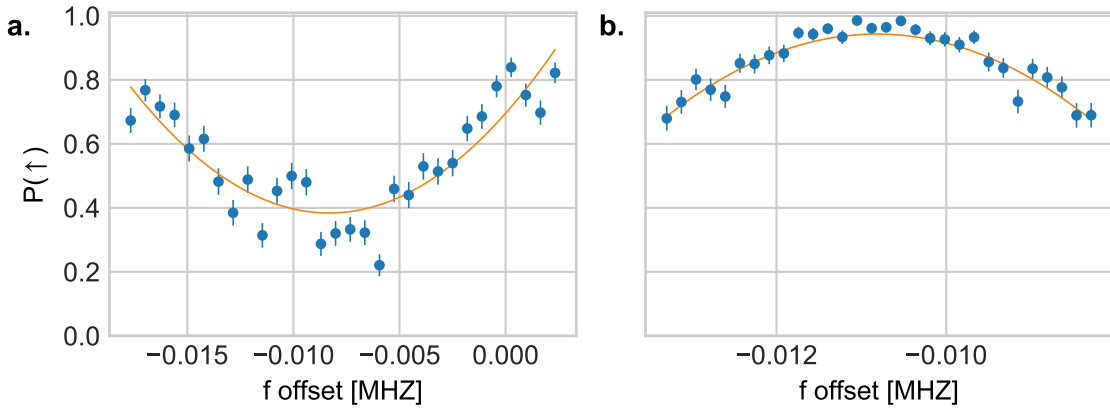
Figure 5.1: Ac Stark shift calibration for the FIQ carrier transition in beryllium. For both panels, the Stark shift is calibrated as an offset to the bare carrier frequency. Panel **a** shows the qubit population after a sequence of 22 π-pulses in-phase with each other as a function of the carrier frequency offset. In panel **b**, the qubit population after a sequence of 22 pairs of $\pi/2$ pulses, where the second pulse of the pair undo the rotation applied by the first. Compared to panel **a**, where the scan span is 20 kHz, the scan in panel **b** is less noisy and has a frequency range of 5 kHz, thus allowing a more precise calibration. The contrast loss in panel **a** is mostly due to slow Rabi frequency noise, which causes shot-to-shot changes to the qubit population. The sequence adopted in panel b is insensitive to Rabi frequency noise as long as it is slower than the timescale of each pair of pulses.

second pulse can undo the operation by doing the rotation $R(\theta, \phi + \pi)$. For this to work correctly, the rotation angle θ (thus the pulse area) of the two pulses has to be the same. If the Rabi frequency fluctuation is slow compared to the experiment time, this condition is satisfied, and the frequency can be calibrated by maximizing the $|\downarrow\rangle$ population as a function of increasing n. Figure 5.1b shows a typical scan used for calibrating the carrier ac Stark shift, where we used a sequence of 22 pairs of $\pi/2$-pulses[2]. The frequency span of the scan in panel b is 5 kHz, while the one in panel a is 20 kHz. The fitted frequency uncertainties is for both cases ~ 1 kHz. However, the points in panel b are less scattered. As a result, we expect to be able to run longer sequences before loosing contrast, thus achieving a higher frequency precision if necessary.

Beryllium Raman beams alignment

In the case of beryllium, we can measure the Stark shift produced by a single Raman beam by running a Ramsey sequence in which a single Raman beam is turned on within the interrogation time τ. Each beam alone causes a qubit phase shift ϕ_b due to the Stark effect without altering the qubit populations. Experimentally, we make use of this feature to check and optimize the alignment of each beam onto two beryllium ions. The experimental sequence works as follows: the two beryllium ions are prepared in a single potential well, where they, after cooling and state preparation, undergo a Ramsey sequence. During the Ramsey interrogation time, a pulse driven with just a single Raman beam causes a phase shift ϕ_1 and ϕ_2 (respectively for the first and second ion), which does not alter the qubit population. The value of the phase offset picked up by each ion depends on the ac Stark shift. At the end of the interrogation time τ, a final Ramsey $\pi/2$ rotation maps the phase offset

---

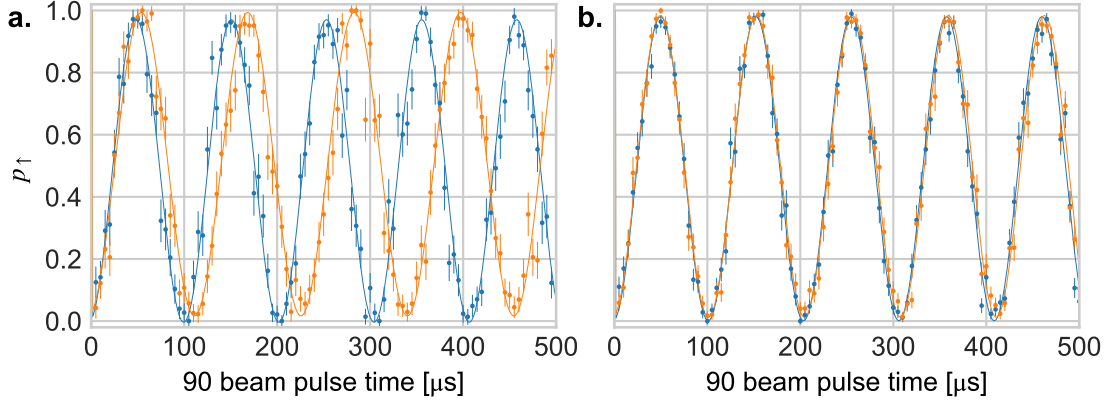[2] Experimentally we noticed that the sequence also works for longer pulse times.

Figure 5.2: FIQ 90 Ramsey beam alignment on a two beryllium chain with single-ion detection mediated by splitting. In both panels, we plot the populations measured on both ions as a function of the single-beam Raman pulse time. Applying a single Raman beam pulse withing the Ramsey interrogation time induce a phase offset ϕ_1 and ϕ_2 proportional to the ac Stark shift felt by ion 1 and 2 respectively. The beam position is adjusted until the phase offset is the same on both ions, as shown in panel **b**.

to the qubit populations. The two beryllium ions are then separated into two individual wells and detected separately to readout the acquired phase. We can then compare and equalize the differential phase shifts induced by each Raman beam in the Ramsey sequence. Figure 5.2 shows an example case in which the FIQ 90 beam is calibrated to illuminate the two ions equally. This technique is also applicable in the case where the two qubits cannot be individually detected. In this case, the joint population $p_2 = p_{1,\downarrow}p_{2,\downarrow}$ can reach 1 (0), only if both qubits simultaneously reach $|\downarrow\rangle$ ($|\uparrow\rangle$).

Another equivalent way of aligning beams is to look at the joint qubit populations while driving Rabi oscillations. We followed this approach for the experiments involving beryllium-calcium-beryllium chains. In this case, for an FDQ Rabi oscillation, the joint detection results in three populations

$$p_0 = p_{a,\uparrow}p_{b,\uparrow}, \quad p_2 = p_{a,\downarrow}p_{b,\downarrow}, \quad p_1 = 1 - p_0 - p_2 \tag{5.6}$$

where $p_{a,\uparrow}$ ($p_{a,\downarrow}$)and $p_{b,\uparrow}$ ($p_{b,\downarrow}$) are the single-ion populations of the state $|\uparrow\rangle$ ($|\downarrow\rangle$) for ion a and b, and p_0, p_1, p_2 are the joint probabilities of finding $0, 1, 2$ ions in $|\downarrow\rangle$. The two qubits evolve independently, and a misaligned beam will cause Rabi oscillations at two different Rabi frequencies Ω_a and Ω_b. Neglecting Stark shift and assuming that the two ions are on resonance, the population p_1 reads:

$$p_1 = \frac{1}{2} - \frac{1}{4}\left[\cos\left((\Omega_a - \Omega_b)\,t\right) + \cos\left((\Omega_a + \Omega_b)\,t\right)\right] , \tag{5.7}$$

which describes a rapid oscillation at $\Omega_a + \Omega_b$ superposed by a slow oscillation at $\Omega_a - \Omega_b$. The beam alignment is then optimized by minimizing the Rabi frequency difference, which is equivalent to minimizing the slow oscillations for long pulse times.

5.1.3 Mixed species spectral isolation

For mixed-species experiments, the decoherence and the Stark shift induced on one species by the laser beams used to perform detection and manipulation of the other needs to be
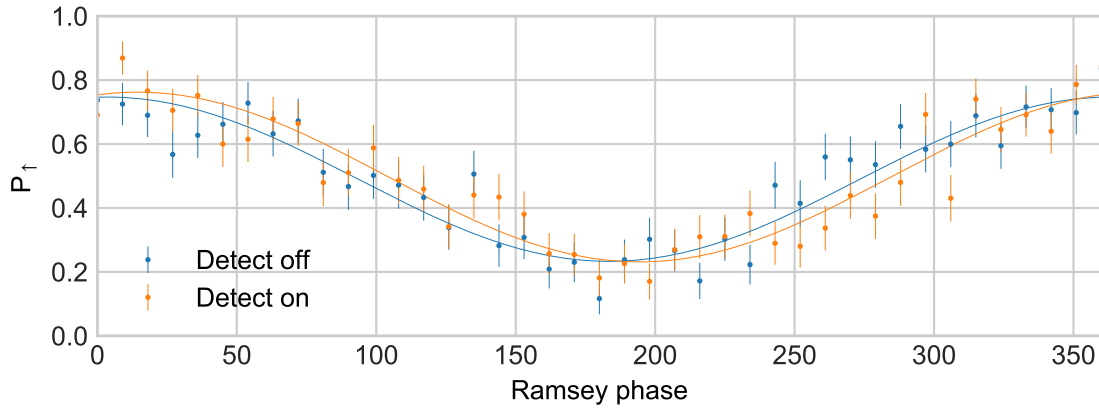
Figure 5.3: Mixed species spectral isolation. FIQ Ramsey sequence with a Ramsey wait time of 1 s. For the orange curve, the calcium detection beam (at the usual detection powers) is turned on for a 500 ms during the Ramsey probe time. The blue curve is instead the comparison Ramsey sequence where no extra pulse is on during the probe time. The fitted contrast of the oscillations is 0.51(3) and 0.53(3) for the blue and orange curve, respectively. The fitted phase offset between the two curves is 11(5) degrees. The corresponding Stark shift induced by the 397 nm laser on the beryllium FIQ transition is $\omega_{ac,397} \simeq 2\pi \times 0.06(3)$ Hz, which is negligible for all the operations discussed in this thesis.

taken into account. The protocols described in the next chapters rely on the ability to encode a quantum state in the FIQ qubit of beryllium while the calcium ion is detected and re-cooled multiple times.

To measure the influence of the 397 nm laser on the FIQ qubit, we used a Ramsey sequence where the 397 nm laser was turned on for 500 ms during a total Ramsey interrogation time of 1 s. The laser settings are the typical ones that we use during calcium Doppler cooling but for $\sim 10^3$ longer time. We compared the contrast and phase of the Ramsey trace, in which the phase of the second $\pi/2$ pulse was scanned, with and without the 397 nm laser on during the Ramsey interrogation time. The measured data are shown in Figure 5.3. The fitted Ramsey contrasts, 0.51(3) and 0.53(3) respectively for the beam off and on, are comparable within the uncertainties. However, we measure a phase shift of 11(5) degrees induced by the 397 nm beam. This corresponds to an ac Stark shift $\omega_{ac,397} \simeq 2\pi \times 0.06(3)$ Hz, which is negligible for all the operations discussed in this thesis.

Similarly, we measured the ac Stark shift induced by the 729 nm laser on the FIQ qubit, and we obtained a value consistent with 0. As a result, we do not expect a Stark shift on the beryllium FIQ transition induced by calcium sideband cooling.

The ac Stark shift on the calcium 729 nm transition induced by the beryllium motion-sensitive Raman beams is approximately $2\pi \times 3$ kHz. This effect is particularly important for the calibration of mixed-species gates (Section 5.3.4), as well as for the experiments in later chapters.

5.2 Mixed-species normal mode analysis

5.2.1 Shifts in normal modes due to additional effects

The theoretical description of normal modes presented in Section 2.2 and Section 2.8.1 assumed the potential to have the ideal quadratic form of Equation 2.5. Various experimental imperfections may lead to a real potential which deviates significantly from this. As a result, the normal modes of a mixed-species crystal can be modified, especially in the case when terms in the real potential have different effects on the individual ion species. A list of factors that have an impact on mixed-species normal modes is presented in [51], while experimental observations on beryllium-magnesium crystals in the NIST linear trap [112] can be found in [101]. Three factors that affect the mixed-species normal modes are [51] anharmonicities in the trapping potential, pseudopotential gradients, and the radiation pressure force due to the laser cooling light. In the following, I will just consider the first two factors as they are most relevant to the results presented in this thesis. If we consider an ion chain composed of two ions of different species, the radiation pressure induced by the Doppler cooling laser only modifies the motional modes when the laser illuminates one of the two ions. In the experiments discussed in this thesis, there is no quantum operation on one ion species performed in parallel with Doppler cooling on the other species. Therefore, the effect on the motional modes induced by radiation pressure can be ignored.

Anharmonicities Anharmonicities in the trapping potential have been studied theoretically and experimentally in [101]. Following the approach of [101], consider a mixed-species chain composed by two ions with mass m_1 and m_2. The axial normal modes are of primary interest in the experiments presented in this thesis. For this reason, we only consider a purely axial static potential given by $V(z) = \kappa_2 z^2 (1 + z/\lambda_3)$ [101], where $\kappa_2 = \frac{1}{2} V_{dc} \alpha_z$ according to Equation 2.1, and $\lambda_3 = \kappa_2/\kappa_3$ is a measure for the anharmonicity. Defining the mass ratio as $\mu = m_1/m_2$ (with $m_1 < m_2$), and following the approach of Section 2.2, one can show that the equilibrium positions are

$$z_\pm^0 \simeq \pm \frac{l}{2^{2/3}} \left[1 \mp \frac{3}{2^{5/3}} \frac{l}{\lambda_3} + \frac{3}{2^{7/3}} \left(\frac{l}{\lambda_3} \right)^2 \right] \tag{5.8}$$

and the eigenfrequencies

$$\omega_\pm \simeq \sqrt{\frac{2e\kappa_2}{m_1}} (1 + \mu \pm \sqrt{\mu^2 - \mu + 1})^{1/2} \left(1 \mp \frac{3}{2^{8/3}} \frac{1-\mu}{\sqrt{\mu^2 - \mu + 1}} \frac{l}{\lambda_3} \right), \tag{5.9}$$

where, in the latter equation, the positive sign is for the out-of-phase motional mode, and the negative one for the in-phase mode. In both equations, the parameter l is defined as $l = (e/8\pi\epsilon_0\kappa_2)^{1/3}$. The normal modes are

$$e_\pm' \simeq \frac{1}{\sqrt{1 + r_\pm^2}} \left(\begin{array}{c} r_\pm \left[\mp 1 - \frac{3}{2^{5/3}} \frac{1+\mu}{\sqrt{\mu^2 - \mu + 1}} \frac{1}{1 + r_\pm^2} \frac{l}{\lambda_3} \right] \\ 1 \mp \frac{3}{2^{5/3}} \frac{1+\mu}{\sqrt{\mu^2 - \mu + 1}} \frac{r_\pm^2}{1 + r_\pm^2} \frac{l}{\lambda_3} \end{array} \right) \tag{5.10}$$

where $r_\pm = [\pm(\mu - 1) + \sqrt{\mu^2 - \mu + 1}]/\sqrt{\mu}$. From these results, the corrections to the eigenvectors scale as l/λ_3, with mass-dependent coefficients.

	in-phase (COM) (MHz)	out-of-phase (STR) (MHz)
$Be^+ - Ca^+$	1.33775(8)	3.46787(9)
$Ca^+ - Be^+$	1.33718(9)	3.4753(1)

Table 5.1: Measured axial mode frequencies for beryllium-calcium and calcium-beryllium crystals. For the in-phase mode, the frequency shift is $\delta f_{\mathrm{COM}} = 2\pi \times 0.6(1)\mathrm{kHz}$, while for the out-of-phase mode is $\delta f_{\mathrm{STR}} = -2\pi \times 7.4(1)\mathrm{kHz}$.

Pseudopotential gradient   Pseudopotential gradients along the trap axis can arise from fabrication imperfections or from trap designs that deviate from the ideal linear Paul trap [108]. On a mixed-species ion chain, the effect is a differential force on ions with different mass [51]. Assuming an ion chain composed of two ions of different species with mass m_1, m_2, with $m_1 < m_2$, the force generated by a pseudopotential gradient on the ion of mass m_1 is $F_1 = -e\nabla\Phi_{\mathrm{pond}}(m_1)$, where $\Phi_{\mathrm{pond}}(m_1)$ is defined in Equation 2.6. For the other species with mass m_2, defining the mass ratio as $\mu = m_1/m_2$, the force is $F_2 = F_1/\mu$. As a result, the separation distance between the ions is changed by approximately $\pm F_1(1 - 1/\mu)/(m_1\omega^2)$, where ω is the oscillation frequency of the single ion with mass m_1, and the sign depends on the direction of the force [51]. If the force vector points from the lighter ion to the heavier ion, the separation is reduced; it is increased if the force points in the opposite direction. It follows that the frequency of the axial normal modes is shifted. In particular, the out-of-phase mode is the most affected, since it strongly depends on the Coulomb interaction, which in turn depends on the ion-ion distance.

Experimental observations   Experimentally, we observe the effects described above by measuring how the frequency of the axial normal modes shift when the order of a mixed-species two ion chain is reversed, from beryllium-calcium to calcium-beryllium. Deterministic preparation of each configuration can be achieved with the techniques described in Section 4.3.2. In the experiment, the axial modes of the mixed-species ion chain are initially sideband cooled close to the ground state. The motional frequencies are measured using the beryllium FIQ red and blue sideband transition, applying a weak sideband pulse such that the sideband π time is approximately 5 ms. Since that the pulse intensity is low, the calibrated frequency is the bare sideband frequency without a significant ac Stark shift. The calibrated motional frequencies are calculated as offsets from the carrier frequency. We suppress systematic errors coming from miscalibration of the carrier frequency by measuring both the red and the blue sideband frequencies. The measured axial frequency shifts can be found in Table 5.1.

The measured axial frequency differences are $\delta f_{\mathrm{COM}} = f_{COM,\mathrm{Be\text{-}Ca}} - f_{COM,\mathrm{Ca\text{-}Be}} = 2\pi \times 0.6(1)\mathrm{kHz}$ for the in-phase mode, and $\delta f_{\mathrm{STR}} = f_{STR,\mathrm{Be\text{-}Ca}} - f_{STR,\mathrm{Ca\text{-}Be}} = -2\pi \times 7.4(1)\mathrm{kHz}$ for the out-of-phase mode.

Figure 5.4 shows the simulated frequency difference between a beryllium-calcium and a calcium-beryllium crystal in the presence of anharmonicities (panel a), and axial pseudopotential gradient (panel b). From simulations, considering the individual contribution of just the anharmonicity term or the pseudopotential gradient is not enough to reproduce the measured frequency shifts. As a result, the measured frequency shifts are probably a result of a combination of both terms. From simulation, the measured shifts are consistent with an anharmonicity term $1/\lambda_3 \approx 220\,\mathrm{m}^{-1}$, and a pseudopotential gradient of $\approx 0.08\,\mathrm{eV\,m}^{-1}$.
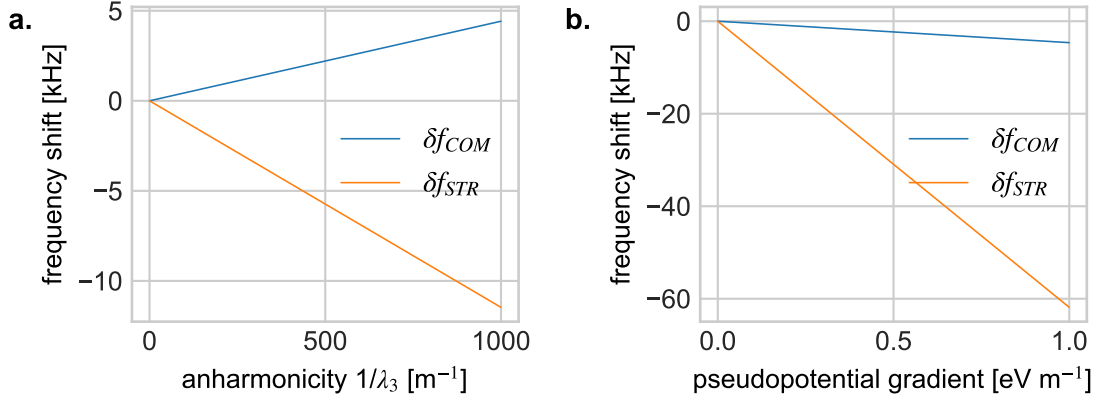
Figure 5.4: Simulated axial modes frequency difference between the two-ion mixed-species crystal in the two different orders, in the presence of **a.** anharmonicities of the trapping potential, and **b.** axial pseudo potential gradient. In both cases the frequency difference is calculated as $\delta f = f_{\text{Be-Ca}} - f_{\text{Ca-Be}}$. The calculation assumes a potential well for which the single calcium trapping frequencies are $\{\omega_x, \omega_x, \omega_z\} = 2\pi \times \{2.4, 3.6, 1.125\}$MHz. The effect of the axial pseudopotential gradient is to shift the frequency of both axial modes in the same direction. At the same time the anharmonicity term alone increases the frequency of one mode while decreasing the other.

This result is also consistent with the observed beryllium sideband Rabi oscillations on a beryllium-calcium-beryllium crystal. For this ion chain, the calculated eigenfrequencies and eigenvectors in the presence of anharmonicity ($1/\lambda_3 =220\,\text{m}^{-1}$), and axial pseudopotential gradient ($0.08\,\text{eV m}^{-1}$) are shown in Table 5.2.

Before the experiment, the axial modes of motion are ground-state cooled, and the two lower radial modes are EIT cooled. The motion-sensitive Raman beams are aligned on the beryllium ions to achieve equal illumination. The observed Rabi oscillation on the FDQ carrier transition is shown in the top plot of Figure 5.5. The populations are fitted to Rabi oscillations where two Rabi frequencies are floated, in the absence of decoherence. For the carrier Rabi oscillations, the fitted Rabi frequency imbalance is 1.4(5)%, which defines the quality of beam alignment.

Rabi oscillations on the FDQ red sidebands for the COM, STR and EGY modes (after a carrier π pulse) are shown in the other panels of Figure 5.5. A beat is seen in the

	$\omega_\alpha/2\pi$ (MHz)	Be_1^+ $e'_{z1,\alpha}$	Ca^+ $e'_{z2,\alpha}$	Be_2^+ $e'_{z3,\alpha}$	Be_1^+ η_{Be1}	Ca^+ η_{Ca}	Be_2^+ η_{Be2}
COM	1.531	0.313	0.897	0.312	0.170	0.05	0.170
STR	4.101	-0.732	-0.018	0.718	0.242	0.001	0.226
EGY	4.188	0.606	-0.441	0.662	0.199	0.015	0.217

Table 5.2: Axial modes eigenfrequencies and mass weighted eigenvectors and Lamb-Dicke parameters for beryllium-calcium-beryllium crystal in the presence of anharmonicity ($1/\lambda_3 =220\,\text{m}^{-1}$), and pseudopotential gradient ($0.08\,\text{eV m}^{-1}$). The single calcium secular frequencies used for the calculations are $[\omega_x, \omega_y, \omega_z] = 2\pi \times [2.4, 3.4, 1.125]$MHz. Note that the eigenvectors, and the Lamb-Dicke parameters of the two beryllium ions are significantly different on the STR and EGY modes.
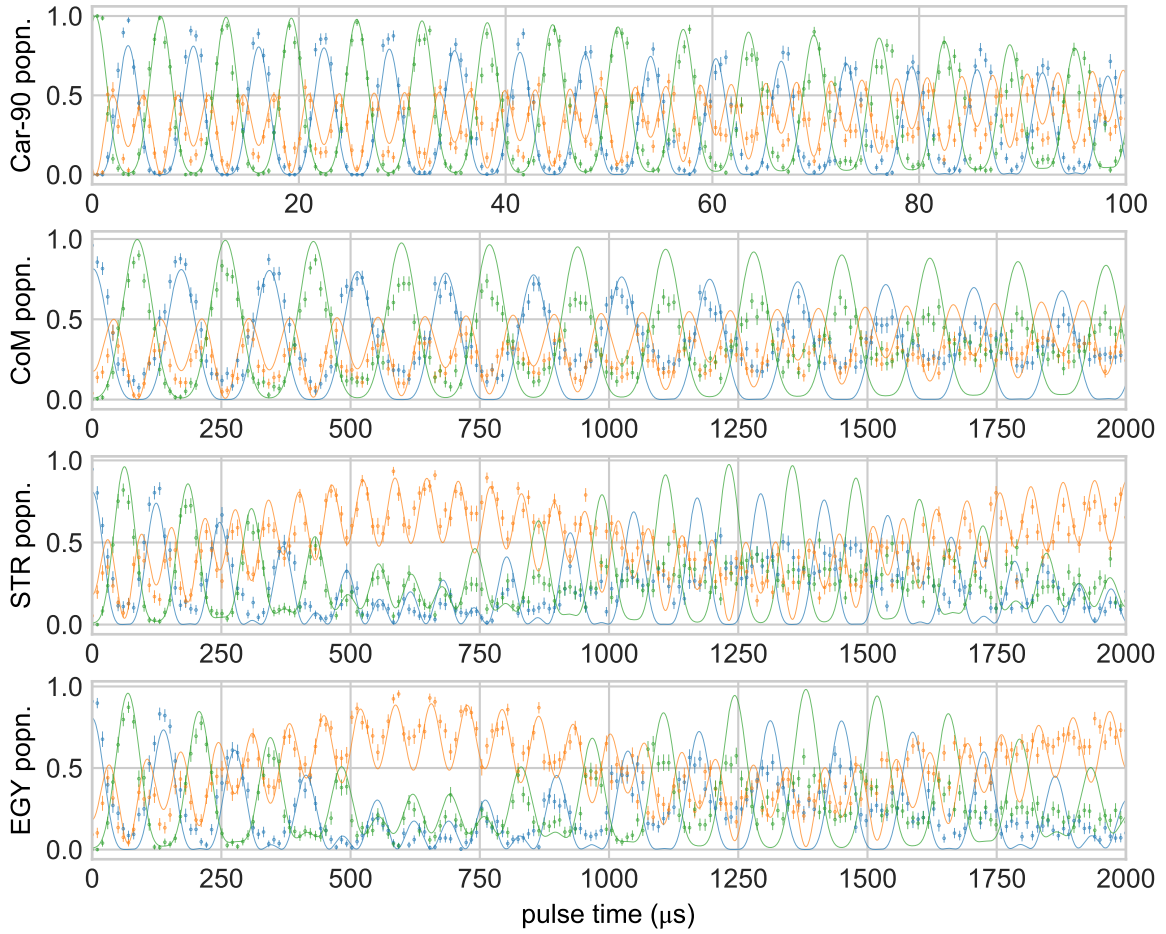
Figure 5.5: Beryllium FDQ Rabi oscillations on the carrier (top panel), and on axial center-of-mass, 'stretch' and 'Egyptian' red sideband (after a carrier π pulse) modes of the beryllium-calcium-beryllium crystal. The blue, orange and green points represent respectively the two beryllium populations where both ions are bright, one is dark, and both dark. The curves are fitted to Rabi oscillations, where two Rabi frequency Ω_1, Ω_2 are floated, under the assumptions of no decoherence. The fitted Rabi imbalance $\Omega_2/\Omega_1 - 1$ are $1.4(5)\%, 1.6(8)\%, 9.6(2)\%, 10.0(2)\%$ respectively for the Rabi flops on the carrier, and the red sidebands on the COM, STR and EGY modes. The Rabi oscillations in each plot are driven with the same pair of Raman beams.

Rabi oscillations on the STR and EGY modes, indicating a Rabi frequency imbalance of $9.6(2)\%$ and $10.0(2)\%$. Quantitatively, these results are in rough agreement with the different Lamb-Dicke parameters of the two beryllium ions given in Table 5.2, thus suggesting that the main causes for the beating are anharmonicities of the trapping potential and axial pseudopotential gradient.

For an extra confirmation it would be possible to repeat the measurements at different rf-amplitudes. This way, it would be possible to separate the two effect since only the pseudopotential gradient will be affected, but not the anharmonicity.

5.2.2   Motional coherence

The mixed-species gates described in Section 5.3.2, rely on the simultaneous manipulation of one motional mode and the internal qubit of the ion. Any dephasing of the motional mode
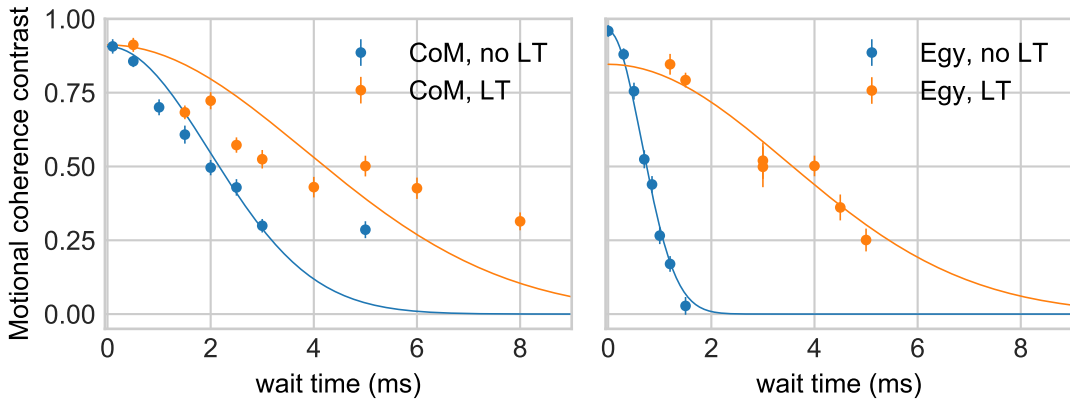
Figure 5.6:   Beryllium-calcium-beryllium axial motional coherence contrasts fitted to $a \exp[-(t/t_0)^2]$. Each point is the contrast of a calcium motional coherence sequence, obtained from Equation 5.11. Panel **a.** shows the motional coherence of the COM mode, while panel **b.** shows the motional coherence of the EGY mode. In both cases, the motional coherence is measured with and without line triggering. The measured coherence times for the COM mode with and without line triggering are $5.2(6)\,\text{ms}$ and $2.8(2)\,\text{ms}$. For the EGY mode, the measured coherence times are $0.92(2)\,\text{ms}$ and $4.9(2)\,\text{ms}$.

used during the gate leads to errors. The sources of motional dephasing are processes causing fluctuations of the trap potential, like fluctuating electric fields or currents, which change at every shot of the experiments. A detailed investigation of motional decoherence due to the coupling with different reservoirs can be found in [113]. A major source of dephasing is trap frequency fluctuations which can be modeled by the Hamiltonian $H_d(t) = \hbar \delta_m(t) \hat{a}^\dagger \hat{a}$, where $\delta_m(t)$ is the frequency fluctuation of the motional mode m and the $\hat{a}^\dagger$ ($\hat{a}$) is the rising (lowering) operator for that mode.

Motional dephasing can be probed with a Ramsey technique. For simplicity, assume that for a given ion chain, the motional quantum states are coherently coupled by a laser pulse sequence, which excites only one ion. This can be achieved with single-ion addressing [114], or, for the mixed-species ion chains used in this thesis, by addressing only one ion species. The motional mode under investigation is initially ground-state cooled, such that the initial state is $|\downarrow, 0\rangle$. As for a standard Ramsey sequence, a carrier $\pi/2$-pulse with phase ϕ_1 prepares the state in $(|\downarrow, 0\rangle - ie^{-i\phi_1} |\uparrow, 0\rangle)/\sqrt{2}$. A motion-subtracting sideband π-pulse then prepares the state in $(|\downarrow, 0\rangle - ie^{-i\phi_1} |\downarrow, 1\rangle)/\sqrt{2}$. The system is then left to evolve under the Hamiltonian $H_d(t)$ for a time τ, during which the motional states $|\downarrow, 1\rangle$ acquires a phase $e^{-i\Phi(\tau)}$, where $\Phi(\tau) = \int_0^\tau \delta_m(t)dt$. The sequence is concluded by another sideband π-pulse followed by a carrier $\pi/2$-pulse with phase ϕ_2. The population in $|\downarrow\rangle$ is

$$P_\downarrow(\tau, \delta\phi) = \frac{1}{2}(1 - \cos(\Phi(\tau) - \delta\phi)), \tag{5.11}$$

with $\delta\phi = \phi_2 - \phi_1$. The oscillation as a function of the $\delta\phi$ is similar in shape to that of Equation 5.4, with the difference that the motional mode energy fluctuation is probed.

Experimental results for single ion motional coherence measurements can be found in [47, 66]. For a single calcium ion, the axial mode coherence time is measured to be approximately $30\,\text{ms}$, while for the radial modes, it is $\approx 1\,\text{ms}$. This indicates that the radial confinement

fluctuates more than the axial one due to rf power fluctuations, as discussed in Paolo Colciaghi's Master thesis [115].

To better understand the results discussed in Chapter 6, the motional coherence of the axial modes of the beryllium-calcium-beryllium crystal was also probed. The Ramsey sequence is performed on the calcium ion, and the results are shown in Figure 5.6. As discussed in Chapter 2.8.1, the coupling of the calcium ion to the "stretch" mode is close to zero; therefore, only the COM and the EGY modes can be probed. We observed that the coherence times greatly improved when the experiment was line triggered[3]. The COM coherence time increased from $2.8(2)$ ms to $5.2(6)$ ms, while for the EGY mode it increased from $0.92(2)$ ms to $4.9(2)$ ms. This suggests, the presence of fluctuating electric fields inside the vacuum chamber in phase with the mains, either on the rf or dc electrodes, probably due to ground loops or pickup noise. At the time of writing, we have not been able to identify the source of such a ground loop in our system.

5.3 Multi-qubit gates

To achieve general-purpose quantum computation, it is necessary to be able to perform operations that span a large Hilbert space. Early theoretical work [116], showed that an arbitrary computation could decomposed into a set of single-qubit operations and a two-qubit operation, offering a universal set of gates for the control of an arbitrarily large Hilbert space. However, gates involving more than two ions can still be beneficial for quantum error correction (QEC) (see Chapter 6) [117]. The methods described in this section are valid for both two-qubit and multi-qubit operations.

For trapped ion quantum information processing, several different approaches have been proposed for the realization of deterministic quantum gates between ions [118, 119, 120, 121, 122, 123]. One of the first two-qubit gates based on the Coulomb interaction between two ions is the Cirac-Zoller gate [118, 124]. It relies on the ions to be initialized in the motional ground state and manipulated with individually-addressed red and blue sideband pulses. Under the application of the red (blue) sideband Hamiltonian, the state amplitude for $|\downarrow, n = 0\rangle$ ($|\uparrow, n = 0\rangle$) remains untouched. Conditioned on the ion states, the motional mode used during the gate is then excited with a single-ion sideband pulse, which in turn affects the internal state of the other ion when driven with red/blue sidebands. An engineered sequence of sideband pulses on each ion realizes the entanglement between the internal states of the two ions.

Current experiments usually replace the Cirac-Zoller gate with geometric phase gates that are based on the state-dependent motional displacement [119, 125, 122]. Compared to the Cirac-Zoller gate, geometric phase gates do not require individual-ion addressing, and the ions do not need to be cooled to the ground-state as long as the Lamb-Dicke approximation is valid [94, 126, 25].

Within this section, I will first introduce the definitions and the main properties of multi-qubit entangled states. I will then continue, revisiting the general theory for mixed-species Mølmer-Sørensen (MS) gates, also presenting the typical techniques used to estimate the fidelity of the states created within the experiment. Finally, I will present the main experimental results obtained for a beryllium-calcium and beryllium-calcium-beryllium MS gates, which will be useful for the later chapters.

---

[3]With line triggering each experimental shot is triggered to start at the identical phase in the mains cycle.

5.3.1 Bell and GHZ states

A general two-qubit state can be expressed in terms of a linear combination of Bell states, which form a complete basis for the Hilbert space spanned by two qubits [6]. They are defined as

$$
\begin{aligned}
|\Psi_+\rangle &= \frac{1}{\sqrt{2}}(|\downarrow\uparrow\rangle + |\uparrow\downarrow\rangle), \quad |\Psi_-\rangle = \frac{1}{\sqrt{2}}(|\downarrow\uparrow\rangle - |\uparrow\downarrow\rangle) \\
|\Phi_+\rangle &= \frac{1}{\sqrt{2}}(|\downarrow\downarrow\rangle + |\uparrow\uparrow\rangle), \quad |\Phi_-\rangle = \frac{1}{\sqrt{2}}(|\downarrow\downarrow\rangle - |\uparrow\uparrow\rangle) .
\end{aligned}
\tag{5.12}
$$

The states $|\Psi_\pm\rangle$ ($|\Phi_\pm\rangle$) are said to have an odd (even) parity. For two qubits the parity is defined as $(p_{\downarrow\downarrow} + p_{\uparrow\uparrow}) - (p_{\downarrow\uparrow} + p_{\uparrow\downarrow})$, where p_{ij} is the probability of measuring the two qubits in state $i, j \in [\downarrow, \uparrow]$. As a result, the parity of the even Bell states is 1, while it is -1 for the odd Bell states.

Following the approach described in [61], it is possible to show that with a global two-qubit carrier rotation $R_2(\theta, \phi) = R(\theta, \phi) \otimes R(\theta, \phi)$ (where $R(\theta, \phi)$ is defined in Equation 2.24), one can transform each Bell state into another with the exception of singlet state $|\Psi_-\rangle$. The two-qubit rotation matrix in the Bell state basis can be written as [61]:

$$
\begin{array}{c}
\begin{array}{cccc}
 & |\Phi_+\rangle & |\Phi_-\rangle & |\Psi_+\rangle \quad |\Psi_-\rangle
\end{array} \\
\begin{array}{c}
|\Phi_+\rangle \\
|\Phi_-\rangle \\
|\Psi_+\rangle \\
|\Psi_-\rangle
\end{array}
\begin{pmatrix}
1 - 2\cos^2\phi\sin^2\frac{\theta}{2} & -i\sin 2\phi\sin^2\frac{\theta}{2} & -i\cos\phi\sin\theta & 0 \\
i\sin 2\phi\sin^2\frac{\theta}{2} & 1 - 2\sin^2\phi\sin^2\frac{\theta}{2} & -\sin\phi\sin\theta & 0 \\
-i\cos\phi\sin\theta & \sin\phi\sin\theta & \cos\theta & 0 \\
0 & 0 & 0 & 1
\end{pmatrix}
\end{array}
$$

from which it is clear that the singlet state $|\Psi_-\rangle$ is not altered by global rotations. This feature is important for the experiments presented in Chapter 6.

To explicitly give a set of rotations, assume that the initial state is the triplet $|\Psi_+\rangle$. As it will become clear in Section 5.3.2, this is an easy state to prepare with ions. The other Bell states can then be created by

$$
\begin{aligned}
|\Phi_+\rangle &= iR\left(\frac{\pi}{2}, 0\right)|\Psi_+\rangle \\
|\Phi_+\rangle &= -iR\left(\frac{\pi}{2}, \pi\right)|\Psi_+\rangle \\
|\Phi_-\rangle &= \mp R\left(\frac{\pi}{2}, \pm\frac{\pi}{2}\right)|\Psi_+\rangle
\end{aligned}
\tag{5.13}
$$

One other property of Bell states is that they are simultaneous eigenstates of the $S_Z = Z \otimes Z$ and $S_X = X \otimes X$ operators. This property will be relevant for the experiments discussed in later chapters, where we prepared and stabilized Bell states by measuring S_Z and S_X and applying correction pulses depending on the measurement outcome.

Bell states can also be generalized to maximally entangled states with more than two ions. Examples are the Greenberger–Horne–Zeilinger (GHZ) states [127]. For n qubits one of them can be written as $|\text{GHZ}\rangle = \frac{|\downarrow\rangle^{\otimes n} + |\uparrow\rangle^{\otimes n}}{\sqrt{2}}$. GHZ states composed of 3 qubits, are particularly relevant for the work presented in this thesis, as they are used for diagnosing the beryllium-calcium-beryllium multi-qubit gate (see Section 5.3.4).

5.3.2 Mixed-species Mølmer-Sørensen gate

For the experiments discussed in this thesis, the only multi-qubit entangling gate that we used is the Mølmer-Sørensen (MS) gate [119, 25, 125], which is closely related to an alternative technique called the geometric phase gate [122]. For the description of the gate mechanism, I will assume the case in which the gate is performed between two ions of different species trapped in the same potential well. Following the two-ion case, the result will be generalized to the entanglement of N ions.

The MS gate is based on the simultaneous drive of the red and blue sideband, off-resonant from the shared motional mode with frequency ω_m. Each ion, $j = 1, 2$, is illuminated by a bichromatic beam with frequencies $\omega_{r,j} = \omega_{0,j} - \omega_m - \delta_j$ and $\omega_{b,j} = \omega_{0,j} + \omega_m + \delta_j$, with $\omega_{0,j}$ the carrier transition frequency of ion j, and δ_j the detuning from the motional sideband. In the following derivation I will assume that the ions are coupled to a single motional mode. For this assumption to hold, the laser has to be tuned close to a resonance of a single motional mode in the weak coupling regime, such that excitations on other modes can be neglected. Under these assumptions, the driving Hamiltonian in the interaction picture can be written according to Equation 2.15 as:

$$
\begin{aligned}
\hat{H}(t) = \sum_{j=1,2} \hat{H}_{\mathrm{rsb}}^{(j)} + \hat{H}_{\mathrm{bsb}}^{(j)} = \\
\sum_j \frac{\hbar}{2} \Omega_j \hat{\sigma}_+^{(j)} \left(e^{i[(\omega_m+\delta_j)t+\phi_{r,j}]} + e^{-i\left[(\omega_m+\delta_j)t-\phi_{b,j}\right]} \right) \\
\times \exp\left[i\eta \left(\hat{a} e^{-i\omega_m t} + \hat{a}^\dagger e^{i\omega_m t} \right) \right] + \mathrm{h.c.},
\end{aligned}
\tag{5.14}
$$

where the sum runs over both ions, the operator $\hat{\sigma}_+^{(j)}$ is the raising operator for ion j, ϕ_r (ϕ_b) is the phase of the red (blue) sideband, and the Rabi frequencies of the red and blue sidebands are equal.

In the Lamb-Dicke regime, making the rotating-wave approximation, the above expression can be written as:

$$
\hat{H}(t) = \sum_{j=1,2} \frac{\hbar}{2} \Omega_j \hat{\sigma}_+^{(j)} \left(\hat{a} e^{-i(\delta_j t - \phi_{r,j})} + \hat{a}^\dagger e^{i(\delta_j t + \phi_{b,j})} \right) + \mathrm{h.c.}
\tag{5.15}
$$

where $\Omega_j = \eta_j \Omega_{0,j}$ is the sideband Rabi frequency.

Equalizing the sideband Rabi frequency ($\Omega_1 = \Omega_2 = \Omega$) and the detuning ($\delta_1 = \delta_2 = \delta$), the previous expression can be written as:

$$
\hat{H}(t) = -\sum_{j=1,2} \frac{\hbar}{2} \Omega \left(\hat{a} e^{-i(\delta t + \phi_{m,j})} + \hat{a}^\dagger e^{i(\delta t + \phi_{m,j})} \right) \hat{\sigma}_{\frac{\pi}{2} - \phi_{s,j}}
\tag{5.16}
$$

with

$$
\hat{\sigma}_{\phi_{s,j}} = \hat{\sigma}_x \cos\phi_{s,j} + \hat{\sigma}_y \sin\phi_{s,j},
\tag{5.17}
$$

where we introduced the *spin phase* $\phi_{s,j} = (\phi_{r,j} + \phi_{b,j})/2$ and the *force phase* $\phi_{m,j} = (\phi_{b,j} - \phi_{r,j})/2$.

To gain an intuitive picture of the dynamics, assume that the Hamiltonian is applied to just a single ion ($j = 1$). In this case, we can write the propagator for an infinitesimal time as:

$$
e^{-iH(t)dt/\hbar} = \exp\left(d\alpha(t)a^\dagger - d\alpha^*(t)a \right) = \mathcal{D}(d\alpha(t))
\tag{5.18}
$$

where $\mathcal{D}(d\alpha(t))$ is the displacement operator and

$$d\alpha(t) = 2i\Omega\sigma_{\frac{\pi}{2}-\phi_{s,1}}e^{i(\delta t+\phi_{m,1})}dt \tag{5.19}$$

is the infinitesimal complex displacement parameter. Note that the displacement strength is proportional to Ω, and is conditional on the qubit state in the $\sigma_{\frac{\pi}{2}-\phi_{s,1}}$ basis, which explains why ϕ_s is called *spin phase*. The direction of the displacement at a given time t is instead given by

$$\arg(d\alpha(t)) = \pm\left[\pi/2 + \delta t + \phi_m\right], \tag{5.20}$$

where the $\pm$ sign is for the two eigenstates of the $\sigma_{\frac{\pi}{2}-\phi_{s,1}}$ operator. At $t = 0$ the direction of the "force" in phase space is solely determined by the *force phase $\phi_{m,1}$*.

The dynamics can then be described in the interaction picture phase space[4]. Assuming a constant drive $\Omega = const$, the displacement for an eigenstate of the $\sigma_{\frac{\pi}{2}-\phi_{s,1}}$ operator, follows a circular trajectory that closes after a period $t = \frac{2\pi}{\delta}$.

When applying the bichromatic pulses to both ions, it is important to remember that the motional mode is shared and that each ion can have a different ϕ_s and ϕ_m. Those phases can be independently set by adjusting the red and blue sideband phases. Let us assume that the sideband phases are calibrated such that $\phi_{m,1} = \phi_{m,2} = 0$ (this assumption will be justified later in the text). Then, the Hamiltonian of Equation 5.16 can be solved analytically using the Magnus expansion to get the propagator [128]

$$\hat{U}_{MS}(t) = \hat{\mathcal{D}}\left(\alpha(t)\hat{S}_{\phi_{s,1},\phi_{s,2}}\right)e^{-i\Phi(t)\hat{S}^2_{\phi_{s,1},\phi_{s,2}}} \tag{5.21}$$

where $\hat{S}_{\phi_{s,1},\phi_{s,2}} = \sigma_{\frac{\pi}{2}-\phi_{s,1}} + \sigma_{\frac{\pi}{2}-\phi_{s,2}}$ and

$$\begin{aligned}
\alpha(t) &= \frac{\Omega}{2\delta}\left(e^{-i\delta t} - 1\right)\\
\Phi(t) &= \frac{\Omega^2}{4\delta}\left(t - \frac{\sin(\delta t)}{\delta}\right)
\end{aligned} \tag{5.22}$$

are the complex displacement parameter and the geometric phase. After a gate duration $t_g = 2\pi/\delta$, the propagator reads

$$U(t_g) = \exp\left[-i\frac{\Omega^2\pi}{2\delta}\hat{S}^2_{\phi_{s,1},\phi_{s,2}}\right]. \tag{5.23}$$

If we set the sideband Rabi frequency $\Omega = \delta/2$ the propagator becomes

$$U_{MS} = \exp\left(-i\pi\hat{S}^2_{\phi_{s,1},\phi_{s,2}}/8\right) \tag{5.24}$$

which produces the following state mapping:

$$\begin{aligned}
|\uparrow\uparrow\rangle &\to \frac{1}{\sqrt{2}}\left\{|\uparrow\uparrow\rangle - ie^{i(\phi_{s,1}+\phi_{s,2})}|\downarrow\downarrow\rangle\right\}\\
|\uparrow\downarrow\rangle &\to \frac{1}{\sqrt{2}}\{|\uparrow\downarrow\rangle - i|\downarrow\uparrow\rangle\}\\
|\downarrow\uparrow\rangle &\to \frac{1}{\sqrt{2}}\{|\downarrow\uparrow\rangle - i|\uparrow\downarrow\rangle\}\\
|\downarrow\downarrow\rangle &\to \frac{1}{\sqrt{2}}\left\{|\downarrow\downarrow\rangle - ie^{-i(\phi_{s,1}+\phi_{s,2})}|\uparrow\uparrow\rangle\right\}.
\end{aligned} \tag{5.25}$$

---

[4] Defined by the position and momentum coordinates that rotate at the motional frequency ω_m with respect to the laboratory (x, p) coordinates

Therefore, initializing the two ion states in $|\downarrow\downarrow\rangle$, it is possible to create a superposition of even Bell states.

In the general case in which the force phases acting on the two ions are different, then after a gate time $t_g = 2\pi/\delta$, the geometric phase acquired by the four basis states (defined as$\{|\pm\pm\rangle\}$, with $|\pm\rangle_j$ the eigenstates of $\sigma_{\frac{\pi}{2}-\phi_{s,j}}$) is [40]

$$
\begin{aligned}
\varphi_{|++\rangle,|--\rangle} &= \frac{\pi\Omega^2}{2\delta^2}\cos^2\left(\frac{\phi_{m,1}-\phi_{m,2}}{2}\right) \\
\varphi_{|+-\rangle,|-+\rangle} &= \frac{\pi\Omega^2}{2\delta^2}\sin^2\left(\frac{\phi_{m,1}-\phi_{m,2}}{2}\right).
\end{aligned}
\tag{5.26}
$$

From these relations, assuming $\Omega = \delta/2$, the geometric phases for the different parity states differ by $\pi/8$ only if $\phi_{m,1} - \phi_{m,2} = 2n\pi$ with $n \in \mathbf{N}$.

Equation 5.21 is also valid for more than two ions, with $\hat{S} = \sum_j \sigma_{\frac{\pi}{2}-\phi_{s,j}}$. For an even number of ions, the creation of GHZ states is straightforward. For an odd number of ions, the mapping is complicated by the fact that each ion is involved in an even number of pairwise interactions with the other qubits [125, 61]. Nevertheless, the GHZ states can be created by an extra $\pi/2$ rotation with phase π applied to all qubits before or after the gate.

5.3.3   Parity oscillations and fidelity

Consider two ions initially prepared in $|\downarrow\downarrow\rangle$, that are entangled by an MS gate with spin phases $\phi_{s,1}$ and $\phi_{s,2}$. According to Equation 5.25, the final state is ideally in a superposition of the even-parity Bell state $|B\rangle = \alpha|\Phi_+\rangle + \beta|\Phi_-\rangle$. Due to experimental imperfections, the real state will not be $|B\rangle$, but can be represented by a density matrix $\hat{\rho}$. We can then extract the state fidelity as

$$
F = \langle B|\hat{\rho}|B\rangle \ .
\tag{5.27}
$$

The most general method is to perform state tomography to reconstruct the full density matrix; however, to extract the fidelity of $|B\rangle$, it is sufficient to measure only a subset of the full density matrix [129, 84].

Considering a two-ion entangled state, it is enough to measure the diagonal elements $\rho_{\downarrow\downarrow}, \rho_{\uparrow\uparrow}$ and the off-diagonal coherence elements $\rho_{\uparrow\downarrow} = \rho_{\downarrow\uparrow}^*$. The diagonal terms can be easily obtained by measuring the qubits at the end of the MS gate. To measure the off-diagonal terms, we apply a rotation $R(\pi/2, \phi)$[5] after the MS gate to both ions, which maps the off-diagonal elements to the diagonal ones [84]. We then measure the spin states. From the discussion in Section 5.3.1, for a suitable ϕ, we map the even-parity Bell state to the odd-parity state. As a result, the parity of the states oscillates as a function of ϕ. The odd-parity oscillation can then be modeled as [61]

$$
p_{\text{odd}} = \frac{1}{2} + \frac{C}{2}\cos\left(2\phi + \phi_{\text{off}}\right),
\tag{5.28}
$$

where ϕ_{off} is an offset phase that depends on the spin phases applied during the gate, and $C \in [0,1]$ is the contrast of the oscillation that also provide a measure for $|\rho_{\downarrow,\uparrow}|$.

The Bell state fidelity is calculated according to

$$
F = \frac{1}{2}\left(\rho_{\downarrow\downarrow} + \rho_{\uparrow\uparrow} + 2|\rho_{\downarrow\uparrow}|\right) = \frac{1}{2}\left(\rho_{\downarrow\downarrow} + \rho_{\uparrow\uparrow} + C\right) \ .
\tag{5.29}
$$

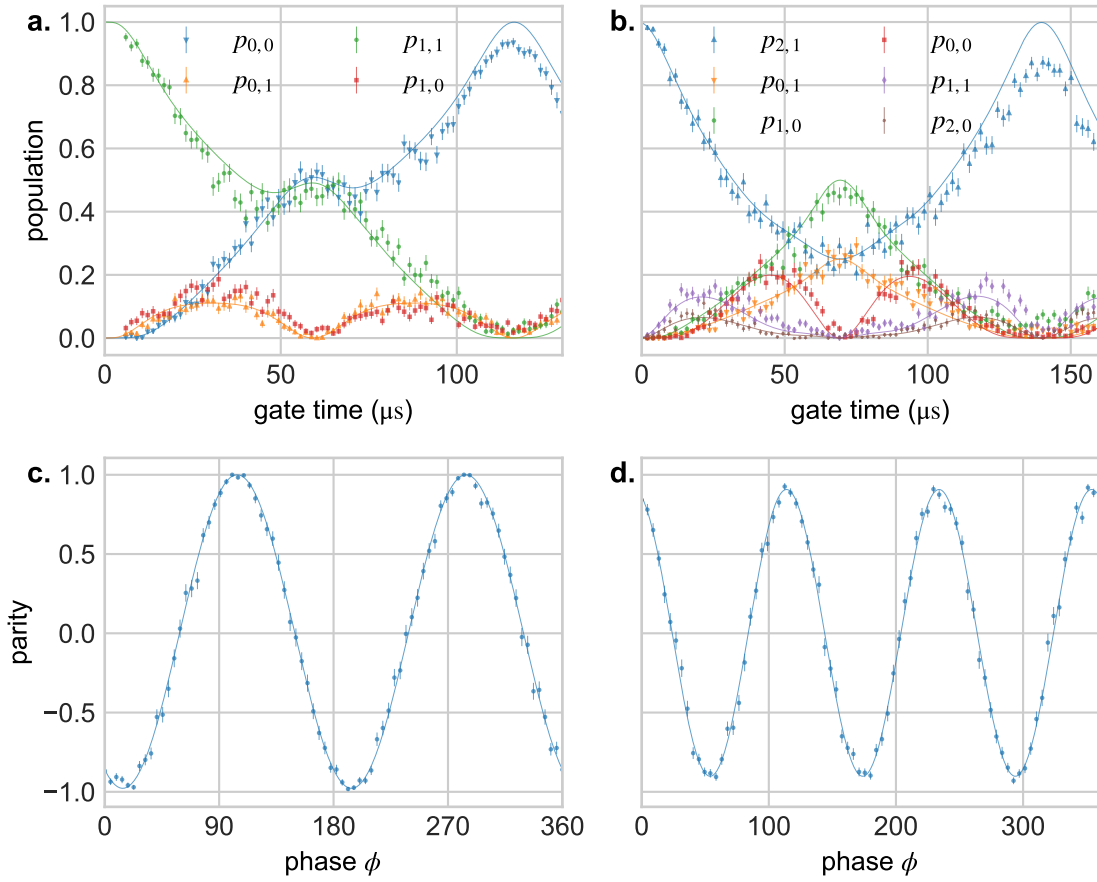[5]In the rest of this thesis, this pulse is usually referred to as *parity pulse*.

Figure 5.7: Mixed species MS gates and parity scans. The populations are labeled as $p_{i,j}$ where i (j) denotes the number of beryllium (calcium) ions measured in $|\downarrow\rangle$. In panel **a** and **b** we find the population dynamics as a function of the MS gate pulse time, respectively for beryllium-calcium and beryllium-calcium-beryllium gates. Solid lines are not a fit to the data, but MS gate simulations with the optimal parameters found in the experiment. Simulations are performed by solving the master equation, which neglects the off-resonant drive of other transitions. Panel **c** and **d** are the parity scans. The fitted contrasts are 98.9(3)% and 90.4(6)% for **c** and **d** respectively. While for beryllium-calcium gates, the parity is applied right after the MS gate, for the three-ion case an extra $\pi/2$ rotation on all ions after the gate is required to create a GHZ state.

Similar methods are also applicable for a maximally entangled state with more than two qubits [130, 129]. In the particular case of three entangled qubits, the odd parity oscillations can be modeled as

$$p_{\text{odd}} = \frac{1}{2} + \frac{C}{2} \cos\left(3\phi + \phi_{\text{off}}\right) \ . \tag{5.30}$$

Note that in this case the period of the oscillation is $2\pi/3$.

5.3.4   Mixed-species MS gate optimization

For both calcium and beryllium, the gate is implemented by applying two rf tones generated by two DDS channels to a single pass AOM, as explained in [47]. The two rf voltages applied

to the AOM are

$$V_{\mathrm{bsb/rsb}}(t) = V_0 \cos\left\{\left[\omega_{\mathrm{rf}} \pm (\omega_m + \delta) + \delta_c\right] t + \phi_s \pm \phi_m\right\} \tag{5.31}$$

where ω_{rf} is the frequency required to drive the carrier transition, δ the differential detuning defining the gate speed, and δ_c a common detuning needed to compensate the electric ac Stark shift induced by the sidebands or by the drive of the other species. The optical field amplitude is then written in terms of the amplitude modulation

$$E = E_0 \cos\left[(\omega_0 + \delta_c)\, t + \phi_s\right] \cos\left[2\left(\omega_m + \delta_m\right) t + 2\phi_m\right] \tag{5.32}$$

For mixed-species operations we use two independent sets of AOMs (one per species), and a total of four tones are required to drive the gate. As a result, the amplitudes, detunings and phases can be individually controlled for each species.

When calibrating the mixed-species MS gate, the differential detuning δ and the motional frequency ω_m are set to be equal for both species. Before the fine-tuning of the gate, the calcium and beryllium blue sideband Rabi frequencies are equalized by using the blue sideband π time as the judgment parameter. Afterward, the amplitudes of the red sidebands are set to be equal in power to the relative blue sideband amplitude. For this operation, we independently switch on the blue and red sideband pulses and adjust the red sideband optical power amplitude to match that of the blue sideband using a photodiode (one photodiode per ion species). As a final step, both sidebands are turned on simultaneously to check that the modulation depth is close to 100%. If the rf amplitude is too high the intermodulation of sideband tones mediated by non-linearities inside the AOM (or in the rf amplifier needed to drive the AOM)might create a tone at ω_{rf}, which would reduce the overall fidelity of the gate [131].

Once the amplitudes are roughly calibrated, the *force phases* of the beams acting on the two species are calibrated to be in-phase on the oscilloscope. For this purpose, we make sure that the model of the photodiodes, the gain settings and the cable length are the same for both species. This procedure defines an initial value of the phases, which are then scanned using the gate results as a proxy for the calibration. Nevertheless, we experimentally observe that the initial phases are within 10% of the calibrated ones.

Once all the relevant parameters are coarsely set, we fine-tune them by optimizing the qubit populations after driving the gate for multiple gate times. Depending on the ion crystal, the procedure is slightly different and will be explained in the next subsections.

Beryllium-calcium MS gate

For a two-qubit MS gate, we usually optimize parameters close to the gate time, using the qubit populations as a proxy. The large number of parameters to be calibrated often require heuristics and experience for the correct calibration. Often, a miscalibration of some parameters leads to a locally-optimal set of calibrated parameters. Experimentally we noticed that changing the initial state of the ion before the MS gate, often helps the calibration procedure. Different input states undergo different gate dynamics, and could show different sensitivity to the various parameters. Experimentally we calibrate the gate parameters with different input states, by applying a π pulse to one of the ions before the MS; we notice that when the set of parameters is around the global optimum, the parameter scans show the same optimal points with and without the π pulse applied.

The best beryllium-calcium MS gate observed so far is shown in Figure 5.7a and c. The measured parity contrast is 98.9(3)% with an estimated fidelity of 98.4(9)%, which is
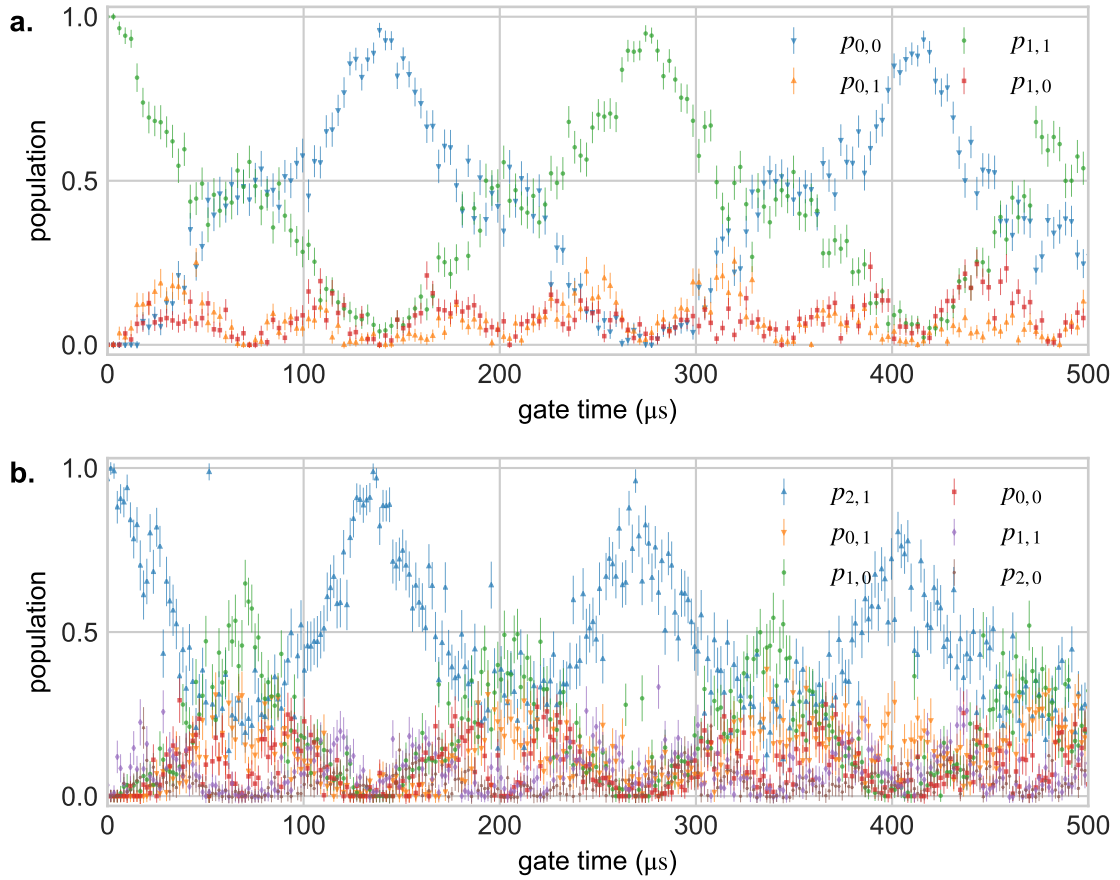
Figure 5.8: Mixed-species MS gate oscillations up to **7** gate times. Panel **a** is for a beryllium-calcium gate, while panel **b** is for a beryllium-calcium-beryllium MS gate. The populations are labeled as $p_{i,j}$ where i (j) denotes the number of beryllium (calcium) ions measured in $|\downarrow\rangle$. For the three-ion case, the rich dynamics at odd multiples of the gate time complicates the calibration process. For this reason, we mostly used the features at even multiples of the gate time, where only $p_{2,1}$ is non-zero.

in between the fidelity observed for two-beryllium and two-calcium Bell states [61]. Single-species MS gate data can be found in the Ph.D. thesis of Vlad Negnevitsky, and the observed fidelities are 97.8(4)% and 99.4(6)%, for beryllium and calcium respectively.

For the measurements in Figure 5.7, the cooling sequence is composed of EIT cooling centered on the lowest radial mode, followed by beryllium sideband cooling on the out-of-phase axial mode, and finally calcium sideband cooling on the axial in-phase mode (which is the mode used for the gate). All axial modes are cooled below $\bar{n} \leq 0.1$ quanta.

Beryllium-calcium-beryllium MS gate

In the case of beryllium-calcium-beryllium, the MS gate calibration sequence is slightly simplified. The beryllium parameters can be independently calibrated following a procedure used for single-species MS gate, which is very similar to the one described above, thus calibrating a two-beryllium MS gate. As discussed in Section 5.1.3, the calcium 729 nm laser does not induce an ac Stark shift on the beryllium ion; therefore, once the beryllium

Error sources	Infidelity
Beryllium readout	1.6%
Motional heating rate	0.4%
Motional coherence	0.2%
Raman scattering	0.2%
Calcium spin coherence	0.1%
Unequal illumination	0.05%
Debye-Waller fluctuation	0.02%
LD approximation	0.002%
Total	$\sim 2.57\%$

Table 5.3: Error sources and estimated contributions to infidelity of three-qubit GHZ state generated with a beryllium-calcium-beryllium ion chain; miscalibration errors are not included.

parameters are optimized only the calcium ones need to be adjusted. Figure 5.7b, shows the population dynamics at different times for the three-ion MS gate. Around the gate time, the presence of multiple non-zero populations complicates the calibration of the parameters since a large number of experiments are required to reduce the statistical errors. We obtained significant improvements when calibrating at even multiples of the gate time, where only on population is non-zero. A time scan up to seven gate times is shown in Figure 5.8b.

The best gate observed so far is shown in Figure 5.7. The parity contrast is 90.4(6)%, and the estimated GHZ state fidelity is 93.8(5)%, which is significantly worse than the two-ion Bell state.

For this scan, the initial cooling sequence is composed of EIT cooling optimized to predominantly cool the lowest radial mode, followed by beryllium interleaved sideband cooling on the axial STR and EGY mode, and finally calcium sideband cooling on the COM mode. Also in this the case all the modes are cooled below $\bar{n} \leq 0.1$ and the sideband Rabi oscillations are shown in Figure 5.5.

5.3.5 MS gate errors

Within this section, I will present the analysis of the error sources contributing to the GHZ and Bell state fidelities measured with beryllium-calcium-beryllium and beryllium-calcium ion chains, respectively. Finally, I will conclude this chapter highlighting how some of these errors could be experimentally reduced.

Beryllium-calcium-beryllium MS gate

Contributing error sources to the beryllium-calcium-beryllium MS gate are summarized in Table 5.3.

The leading source of infidelity is the readout error of the two beryllium ions. Beryllium qubit detection is realized by applying a resonant pulse (driving the $\left|S_{1/2}, F = 2, m_F = 2\right\rangle \leftrightarrow \left|P_{3/2}, F = 3, m_F = 3\right\rangle$ transition) for $200\,\mu s$ as described in Chapter 3, in which the $\left|\downarrow\right\rangle$ population is shelved in the $\left|F = 1, m_F = -1\right\rangle$ state. The detection laser beam size is much larger than the ion separation. As a result, the recorded histograms are drawn from a mixture of three photon-count distributions corresponding to the states $\left|\downarrow\downarrow\right\rangle$, $\left|\downarrow\uparrow\right\rangle$ or $\left|\uparrow\downarrow\right\rangle$, and $\left|\uparrow\uparrow\right\rangle$. We then infer the two-ion populations by fitting the aggregate histogram of the counts for an experimental point with a model distribution that is the sum of three Poisson dis-

tributions (see Section 3.2), with fitted averages $\lambda_0 = 0.151(1), \lambda_1 = 26.0(3), \lambda_2 = 52.1(3)$. The three Poisson distributions overlap due to the finite efficiency of our photon collection system and optical pumping during detection. Optical pumping during detection results in a photon-counting statistic that is not Poissonian (see Section 3.3). We can calculate the readout infidelity caused by fitting pure Poisson distributions, assuming the single-ion pumping rates given in Section 3.3 and extending them to the two-ion case Denoting as e_{ij} (with $i, j \in [0, 1, 2]$) the probability of mistakenly identify i bright ions as j bright ions, we calculate $e_{01} = 0.02$, $e_{02} = 0.02$, $e_{10} = 9 \times 10^{-4}$, $e_{12} = 5 \times 10^{-3}$, $e_{20} = 9 \times 10^{-5}$ and $e_{21} = 5 \times 10^{-3}$. These readout errors contribute 0.016 to our GHZ-state infidelity.

For the COM motional mode, the measured heating rate is approximately 100 quanta/s. The heating process can be modeled by a Lindblad term $L_- = \sqrt{\gamma}a$, with γ the heating rate. For the single-loop gates implemented here, this contributes an error $\epsilon_h = \gamma t_g/2$ [131], resulting in our estimate of 4×10^{-3}.

As discussed in Section 5.2.2, the COM mode motional coherence contrast is well described by a Gaussian profile. The measured motional coherence time is 2.8(2)ms (without line triggering), which is approximately 40 times longer than the gate time. We estimate the infidelity resulting from this slow motional frequency noise by numerical simulation of the GHZ-state infidelity resulting from an error in gate detuning δ during each experimental shot, sampled from a Gaussian probability density function. This results in an expectation infidelity of 2×10^{-3}.

In our setup, calcium spin coherence is ~ 1.7 ms, as discussed in the Ph.D. thesis of Christa Flühmannn [66]. The main contribution to spin dephasing is slow frequency noise arising from laser frequency fluctuations (estimated $\sigma_L \approx 2\pi \times 99$ Hz) and slow magnetic field noise, $\sigma_m \approx 81\,\mu$G (transition frequency sensitivity of 1.12 MHz/G). The GHZ state infidelity is then estimated by numerical simulation of the MS gate infidelity resulting from a shot-to-shot calcium carrier frequency offset, sampled from a Gaussian distribution with $\sigma = 190$ Hz. This results in expectation infidelity of 1×10^{-3}.

Spontaneous Raman scattering is an inelastic process that can produce leakage of the population from the qubit manifold into other hyperfine states. The resulting states will predominantly be detected as dark and will contribute to the GHZ state's fidelity as a systematic bias. Following the description found in [133, 48], one can calculate the rate of the photon scattering event from the ground-state hyperfine level $|i\rangle$ to the ground-state hyperfine level $|f\rangle$ ($i \neq f$ for Raman scattering) using the Kramers-Heisenberg formula

$$\Gamma_{i,f} = \frac{g^2}{4}\gamma \sum_q \left| \frac{a_{i \to f}^{(1/2)}}{\Delta} + \frac{a_{i \to f}^{(3/2)}}{\Delta - \Delta_F} \right|^2 \tag{5.33}$$

where g is the single-photon Rabi frequency, $\gamma = 2\pi \times 19.6$ MHz is the the natural linewidth of the $P_{1/2}$ states, and $a_{i \to f}^{(J)}$ is the transition amplitude from state $|i\rangle$ to $|f\rangle$ through an intermediate state $|q\rangle$ in the P_J manifold [133, 48]. The sum runs over all the excited states $|q\rangle$ that belong to the $P_{1/2}$ and $P_{3/2}$ manifolds. $\Delta = -2\pi \times 230$ GHz is the Raman detuning from the $P_{1/2}$ manifold, and the Δ_F is the frequency difference of the $P_{1/2}$ and $P_{3/2}$ manifolds. Assuming the Raman beams to have linear π and $\sigma_+ + \sigma_-$ polarization, respectively, it can be calculated that the the Raman scattering probability during a single-loop MS gate (73.3 μs long, and $\eta = 0.115$ the beryllium Lamb-Dicke parameter for the axial COM mode) performed on the beryllium FIQ transition is $\approx 3 \times 10^{-3}$. This contributes 2×10^{-3} to the GHZ state infidelity.

Error sources	Infidelity
Beryllium readout	0.3%
Motional heating rate	not measured
Motional coherence	0.1%
Raman scattering	0.09%
Calcium spin coherence	0.04%
Total	$\sim 0.5\%$

Table 5.4: Error sources and estimated contributions to infidelity of two-qubit Bell state generated with a beryllium-calcium ion chain; miscalibration errors are not included.

One experimental challenge was the precise alignment of the Raman beams to ensure equal illumination of the two beryllium ions (see Section 5.1.2). The top panel of Figure 5.5 shows the beryllium FDQ Rabi oscillations on the carrier transition driven with the motion-sensitive Raman beams. The fitted Rabi frequency imbalance is 1.4(5)%. From simulations, the estimated contribution of beam imbalance to the GHZ state infidelity is 5×10^{-4}.

The MS gate is generally robust against finite thermal excitation in the Lamb-Dicke regime, $\eta \ll 1$. However, this condition is not rigorously satisfied due to the small mass of the beryllium ion. The MS gate error associated with this is $\frac{\pi^2}{4}\eta^4\langle n\rangle(\langle n\rangle + 1)$ [25], where $\langle n\rangle$ is the mean of the vibrational quantum number. For an average thermal occupancy of the COM mode of $\langle n\rangle = 0.05$, the expected error is 2×10^{-5}.

Other minor contributions to the overall infidelities are the direct coupling to the spectator vibrational modes, and the indirect fluctuation in the Debye-Waller factor as the coupling strength of the COM mode is reduced due to the thermal oscillations in the spectator modes [25]. Assuming $\langle n\rangle = 0.05$, the thermal occupancy of both the STR and EGY mode, we estimate the overall contribution to the infidelity to be 2×10^{-4} [25, 132]

Other infidelity sources, such as the finite calcium qubit lifetime and the calcium spectator mode coupling to the radials modes are almost negligible. We estimate a contribution of 1×10^{-5} infidelity due to spontaneous emission and 3×10^{-6} due to the coupling to the radial spectator modes.

The effects summarized above account for about 2.57% infidelity. Part of the remaining infidelities can be related to miscalibrations. The daily procedure we followed to calibrate MS gates is described in Section 5.3.4 and consists of a sequence of scans performed manually by the experimenter. During a typical working day, MS gates have been repetitively calibrated due to parameter drifts. We observed that the variability of the GHZ state fidelity obtained by successive independent calibrations could be as large as 2%, thus putting an upper bound to the infidelity resulting from our calibrations process. This large variability is probably associated with several scans' need to reduce the statistical uncertainties due to the rich dynamics around the gate time.

Beryllium-calcium MS gate

We also estimated the contribution to the infidelity of the two-qubit Bell state, generated with a beryllium-calcium ion chain, following a similar approach to the one described above. The results are summarized in Table 5.4.

For this particular ion chain, the measured motional coherence Ramsey contrast is well described by a Gaussian profile, thus suggesting that the noise is slow compared to the

Ramsey probe time (see Section 5.2.2). The fitted axial COM mode motional coherence is 4.5(4)ms. The Bell state infidelity can then be estimated by simulating an MS gate repetitively assuming an error in gate detuning δ for each repetition, sampled from a Gaussian probability density function. This results in an expectation infidelity of 1×10^{-3}.

Unfortunately, the heating rate of the COM mode of motion ($\omega_{COM} = 2\pi \times 1.7\,\text{MHz}$) was not experimentally measured. However, based on the heating rates of single-species chains and the three-ion mixed-species chains, we expect the heating rate of the COM mode to be approximately 50 quanta/s. As a result, we expect this to contribute 1×10^{-3} to the Bell state infidelity.

Beryllium detection last $200\,\mu\text{s}$. For each data point, the beryllium qubit population is obtained by fitting a linear combination of two Poisson distributions (with means $\lambda_0 = 0.135(1)$ and $\lambda_1 = 26.3(2)$ counts) to the data. However, the non-Poisson nature of the beryllium photon-counting statistics (Section 3.3) causes readout infidelities if histograms are fitted with pure Poisson distributions. Denoting as e_{ij} (with $i, j \in [0, 1]$) the probability of mistakenly identify i bright ions as j bright ions, and assuming the single-ion pumping rates given in Section 3.3, we calculated $e_{01} = 4.2 \times 10^{-3}$ and $e_{10} = 1.3 \times 10^{-3}$. As a result, the expected contribution to the Bell state infidelity is 0.3%.

As discussed in the previous section, Raman scattering causes population leakage outside the beryllium qubit subspace. After a scattering event, the beryllium ion will predominantly be detected as dark, thus causing a systematic bias of the Bell state fidelity. From simulations, assuming a single-loop gate, we estimate that Raman scattering contributes 0.09% infidelity.

The limited calcium coherence time ($\sim 1.7\,\text{ms}$) also contributes to the overall infidelity. Similarly to before, we estimate its infidelity contribution by simulating an MS gate with a calcium carrier frequency offset, sampled from a Gaussian distribution with $\sigma = 190\,\text{Hz}$. This results in an expectation infidelity of 0.04%.

Finally, we observed variations of final the Bell state fidelity after independent calibrations of the MS gate of approximately 0.3% as an upper bound for infidelity caused by our calibration method.

Conclusions

In the two cases analyzed above, beryllium readout error is the leading source of infidelity. or single beryllium detections, better fidelities could be achieved using readout techniques based on photons' arrival time (see Section 3.4). Alternatively, it would be possible to infer qubit populations using a maximum likelihood analysis that makes use of experimental reference histograms, thus avoiding the need for a model of the count distributions [132]. For the joint detection of two beryllium ions, readout errors could be reduced either by employing splitting-based single-ion detection or extending the maximum likelihood technique to fitting two-ion histograms. Improving the readout fidelity will also be beneficial for the MS gate calibration, as it reduces systematic miscalibrations.

Another source of infidelity that could be easily reduced is Raman scattering. This could be further suppressed by increasing the detuning at the cost of more optical power to attain the same Rabi frequency value.

In general, calibration errors could be reduced by automating the calibration procedure. While writing this thesis, we have successfully employed Bayesian calibration schemes in our

experimental apparatus for the calibration of single-species two-qubit MS gates. Extending these techniques to mixed-species MS gates could be beneficial to improve the calibration time and accuracy.

This concludes the chapters dedicated to the introduction of the mixed-species techniques necessary to understand the experimental results presented in the next two chapters.

6 Mixed-species stabilizer readout

The previous chapters introduced most of the building blocks necessary to operate a mixed-species quantum processor. This chapter is devoted to the experimental demonstration of general elements required for quantum error correction (QEC), that make use of all mixed-species techniques and the power of the classical control system described before. After a general introduction about the stabilizer formalism, I will discuss the experimental sequence we used on a reduced system where a calcium ion serves as an ancillary qubit to read out the parity of two beryllium qubits. We use the full capabilities of the classical control system to feed back in real-time based on the calcium detection result to stabilize a parity subspace. The same techniques are then used to prepare and stabilize Bell states deterministically. These results are published in [42]. This work was performed together with Vlad Negnevitsky, and some details can also be found in his Ph.D. thesis [61].

6.1 Introduction and context

A primary challenge in the development of a quantum computer is dealing with errors. Errors arise from noise and imperfect gate operations and accumulate over the course of an algorithm, scrambling the state of the qubits and limiting the algorithm depth [134]. To tackle these issues, we require quantum error correction where multiple physical qubits encode one or more logical qubits. Individual errors can then be detected by repeated measurements of multi-qubit correlations on a subset of the physical qubits [135, 45, 136, 93]. The direct measurement of the physical qubits would collapse their state and destroy the stored information. Instead, they are entangled with an ancilla qubit outside the code space, that, upon measurement, collapses the state of the data qubit in an "error" or "no-error" state. The measurement outcome must then be processed in real-time to allow feedback operations that correct eventual errors. With these techniques, the system can then be stabilized for the entire computational period [93].

6.1.1 Stabilizer formalism

One general way used to describe most quantum-error correcting codes is the stabilizer formalism. To gain an intuitive picture, consider the Bell state $|\Phi_+\rangle$. It is easy to verify that $(\hat{\sigma}_x \otimes \hat{\sigma}_x)|\Phi_+\rangle = |\Phi_+\rangle$ and that $(\hat{\sigma}_z \otimes \hat{\sigma}_z)|\Phi_+\rangle = |\Phi_+\rangle$. Therefore, we say that the state $|\Phi_+\rangle$ is *stabilized* by the operators $(\hat{\sigma}_x \otimes \hat{\sigma}_x)$ and $(\hat{\sigma}_z \otimes \hat{\sigma}_z)$. More general we can say that the unitary operator U with eigenvalues ± 1 *stabilizes* a state $|\psi\rangle$, if $U|\psi\rangle = |\psi\rangle$, or in other words if the state $|\psi\rangle$ is an eigenstate of U with eigenvalue $+1$.

At the core of the stabilizer formalism lies the Pauli group G_1, which is the set of one-qubit operators generated by the multiplication of Pauli matrices. It can be shown that these operators have eigenvalues ± 1 and that they either commute or anti-commute with each other [6]. This group can be easily generalized to G_n, which consists of the n-fold tensor product of Pauli operators.

A stabilizer group S is then defined as a subset of G_n, with V_S the set of n-qubit states stabilized by all the stabilizer operators $O_S \in S$. From this definition, it follows that all operators O_S must commute, and that V_S is the intersection of the $+1$ eigenspaces of all O_S. One last condition is that $-I_n \notin S$, since $-I_n |\psi\rangle = |\psi\rangle$ only for the trivial state $|\psi\rangle = 0$.

Within this formalism, correctable errors are simply described by operators that move the state outside V_S. For this to happen, the error operation must anti-commute with one of the stabilizers[1]. By measuring the eigenvalues of the stabilizers, we can detect if an error occurred and also what type of error (or the class of degenerate errors), thus extracting the *error syndrome*. The correction is then simply an operation from the same class of errors [6].

This covers the basics to better understand the experimental results described here. Further details and examples can be found in [6].

6.1.2 Experiment on a reduced system

Limited QEC codes have been experimentally demonstrated in different systems [137, 138, 139]. However, due to incomplete set of controls, these algorithms often required to decode the encoded qubits to readout the error syndrome. For practical QEC, ideal stabilizer measurements are required [140, 141]. Such operations have been demonstrated in several platforms, including trapped-ions [142, 143, 144] and NV centers [145]. Other experiments [146, 147] also realized up to three rounds of conditional feedback upon ancilla measurements. Following the work described here, Bell state stabilization up to 12 rounds of parity measurements was realized in superconducting qubits [148].

In general, useful implementation of stabilizer readouts and feedback operations requires the following conditions:

1. The measurement time should be short compared to the relevant decoherence time of the encoded qubits

2. The measurement process should not perturb the information stored in the encoded qubits.

3. It should be possible to repeat the measurements several times. This includes the ability of re-preparing the ancilla qubit for a new round of measurements.

4. Ancilla measurement and reset rely on dissipative processes. During these operations there should be minimal crosstalk to the data qubits to prevent loss of information.

5. The classical control system should be powerful enough to apply feedback pulses upon ancilla measurement.

All these conditions have been demonstrated on a single-species trapped-ion experiment, which implements up to three consecutive measurements [149]. In this work, the information stored in the data qubits was temporarily hidden in energy levels that do not interact with the resonant light used for detection, thus minimizing crosstalk. However, such implementation in large-scale systems with high fidelity is challenging.

---

[1]There can also be errors that commute with all stabilizers. Such errors are correctable only if the error operator is itself part of the stabilizer group.

Our implementation makes use of mixed-species ion chains, where calcium is used for the ancilla qubits and beryllium to store information. Beryllium is chosen as the data qubit since it exhibits a long coherence time ($\sim$4 s) when the qubit is encoded in the FIQ transition (see Chapter 2.5.1), which is longer than the calcium coherence time ($\sim$2 ms), thus allowing for several stabilizer readouts (on average the time between two stabilizer readouts is 1 ms). Moreover, the high degree of spectral separation (see Chapter 5.1.3) enables us to satisfy the second, the third and fourth criteria, since calcium detection does not destroy the information stored in the beryllium qubits. Sympathetic cooling of the ion chain performed using laser cooling of calcium also mitigates errors coming from heating and transport. Finally, the classical control system introduced in Chapter 4 allows branching of the pulse sequence in the microseconds timescale, which is good enough to satisfy also the fifth criterion.

In this work, we implement the readout of the two-qubit stabilizers $S_Z = \hat{\sigma}_z \otimes \hat{\sigma}_z$ and $S_X = \hat{\sigma}_x \otimes \hat{\sigma}_x$. The mixed-species ion chain used in the experiment is beryllium-calcium-beryllium, and the sequence for the stabilizer readout is discussed in the next section. The S_Z (S_X) measurement projects the two beryllium qubits in a parity subspace with eigenvalues $E_Z = \pm 1$ ($E_X = \pm 1$). By continuously repeating one stabilizer measurement and applying feedback corrections upon the ancilla result, we demonstrate the stabilization of a parity subspace up to 50 cycles (see Section 6.3). As already mentioned in Section 5.3.1, Bell states are simultaneous eigenstates of S_Z and S_X; therefore, a S_Z measurement followed by a S_X readout collapses any input state in a Bell state with particular $\{E_Z, E_X\}$ values. With feedback, we can create a particular Bell state and stabilize it over more than 50 stabilizer readouts (25 pairs of S_Z and S_X measurements).

6.2 Experimental sequence and calibration

The experimental sequence used to measure the stabilizer S_Z consists of a unitary operation U_{S_Z} shown in Figure 6.1b, which together with the ancilla qubit readout forms the stabilizer measurement M_{S_Z}. For a calcium ion initially prepared in state $|\downarrow\rangle$, the multi-qubit operation U_{S_Z} maps the parity of the beryllium qubits onto the calcium measurement basis.

At the core of this operation there is the multi-qubit operation

$$U_{\text{core}} = \exp\left[\frac{i\pi}{4} Z_{\text{Ca}} \otimes X_{\text{Be}_1} \otimes X_{\text{Be}_2}\right].$$ (6.1)

Experimentally it can be realized with a pulse sequence shown in Figure 6.1a which consists of two three-qubit MS gates and a single qubit rotation on a calcium ion. Such a sequence is based on a circuit identity found in [150, 142]. Within the figures of this chapter, we changed the pulse notation to help readability. In particular, the rotation $R(\theta, \phi)$ (defined in Equation 2.24) is written as $R_\theta(\phi)$ and $P(\phi) \equiv R(\pi, \phi)$.

As discussed in Section 2.5.1, the motion-sensitive configuration of the Raman beams is not phase stable from shot-to-shot due to path difference fluctuations. This implies that the beryllium gate basis will fluctuate relative to the calcium basis, over different shots. As a result, at every execution of the sequence, the core operation has the form

$$U_{\text{core}}(\phi_b) = \exp\left[\frac{i\pi}{4} Z_{\text{Ca}} \otimes \Phi_{\text{Be}_1}(\phi_b) \otimes \Phi_{\text{Be}_2}(\phi_b)\right]$$ (6.2)

where ϕ_b is the relative phase of the Raman beams that fluctuates, and $\Phi(\phi_b) = X\cos\phi_b + Y\sin\phi_b$. This issue can be suppressed with extra $\pi/2$ rotations on the beryllium ions before
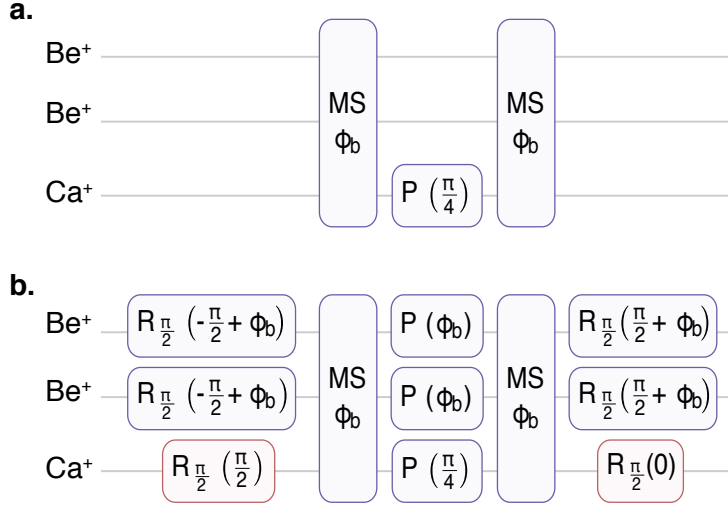
and after U_{core} (with π phase difference), which are performed with the same set of laser beams. Those pulses render the operation diagonal in the computational basis, and thus insensitive to phase fluctuations [128, 132]. For this to work, these beryllium $\pi/2$ carrier rotations have to be applied with the motion-sensitive configuration, so that the phase ϕ_b is the same for all pulses. The effect is clearly visible when we write the matrix elements associated to the core operation with and without the basis rotation pulses:

$$
\begin{pmatrix}
1 & & & ie^{-2i\phi_b} & & & & \\
 & 1 & i & & & & & \\
 & i & 1 & & & & & \\
ie^{-2i\phi_b} & & & 1 & & & & \\
 & & & & 1 & & & ie^{-2i\phi_b} \\
 & & & & & 1 & i & \\
 & & & & & i & 1 & \\
 & & & & ie^{-2i\phi_b} & & & 1
\end{pmatrix}
\rightarrow
\begin{pmatrix}
i & & & & & & & \\
 & 1 & & & & & & \\
 & & 1 & & & & & \\
 & & & i & & & & \\
 & & & & 1 & & & \\
 & & & & & i & & \\
 & & & & & & i & \\
 & & & & & & & 1
\end{pmatrix}
$$

With the $\pi/2$ carrier pulses, the operation is diagonal and independent of ϕ_b. The core operation than transforms into

$$
U_{\text{core},Z} = \exp\left[\frac{i\pi}{4} Z_{\text{Ca}} \otimes Z_{\text{Be}_1} \otimes Z_{\text{Be}_2} \right], \tag{6.3}
$$

that phase shifts the calcium qubit depending on the S_Z parity of the beryllium ions.

To map the calcium phase shift onto the measurement basis, we perform a Ramsey-like experiment, where the core operation $U_{\text{core},Z}$ is embedded between $\pi/2$ calcium rotations, whose phase difference is $\pi/2$. The compiled sequence that we apply in the experiments is depicted in Figure 6.1b. Notice that we added a set of beryllium π rotations in between the two MS gates to decouple the sequence from minor gate miscalibrations (similar idea to a spin-echo sequence). The resulting unitary is $U_{S_Z} = R^{\text{Ca}}\left(\frac{\pi}{2}, \frac{\pi}{2}\right) U_{\text{core},Z} R^{\text{Ca}}\left(\frac{\pi}{2}, 0\right)$. The measurement of the calcium qubit then completes the stabilizer measurement M_{S_Z}. For an ideal implementation of M_{S_Z}, the state of the beryllium qubits are projected into the $+1$ (-1) eigenspace of S_Z correlated with the calcium ancilla qubit in state $|{\uparrow}\rangle$ ($|{\downarrow}\rangle$)[2].

The M_{S_X} stabilizer measurements can then be performed by embedding the U_{S_Z} operation between two $\pi/2$ basis rotation pulses applied to the beryllium ions, respectively with phases $\pi/2$ and $-\pi/2$.

6.2.1   Phase reset

In the M-ACTION system, the linear advancing DDS phase offsets (Section 4.1.2) ensure phase coherence by referencing the phase of each pulse of a sequence to a common "reference" time. Neglecting Stark shifts, this scheme ensures that all carrier pulses driven with a particular beam keep a fixed relative phase relationships. Problems arise when we run MS gates. As discussed in Section 5.3.4, the red and blue sideband tones carry a common frequency offset δ_c needed to compensate Stark shifts occurring during the gate. The effect is that the phase difference between the carrier pulses and the MS gates grows with time as $(t - t_{\text{ref}})\delta_c$. As a result, for a repeated U_{S_Z} sequence, we would be implementing different unitaries at each cycle. To mitigate this effect, the reference time is shifted to the first pulse

---

[2]It assumes that the calcium qubit is initially prepared in state $|{\downarrow}\rangle$.

Figure 6.1: Circuit construction. **a** The pulse sequence that realizes the $U_{\text{core}}(\phi_b)$, where ϕ_b is the relative phase of the Raman beams which fluctuates from shot to shot. **b** Circuit implementation of U_{S_Z}. The extra beryllium π pulses are added to decouple the sequence from minor gate miscalibrations. All the beryllium pulses are realized with the motion-sensitive Raman beam configuration to ensure phase coherence. To help readability, the pulse notation is changed compared to that defined in Equation 2.24. In particular, $R_\theta(\phi) \equiv R(\theta, \phi)$ and $P(\phi) \equiv R(\pi, \phi)$.

of the U_{S_Z} sequence and then shifted back to the previous value at the end of the stabilizer measurement. Because the S_Z stabilizer readout operation is diagonal in the computational basis, the phases of the pulses in this block do not need to be referenced to the rest of the sequence [42].

The basis rotation pulses required for the M_{S_X} stabilizer measurement, are applied with the motion-insensitive Raman beams. In this configuration, the phase relationship between the beams is stable for a longer time than the motion-sensitive one, thus allowing consecutive measurements of the same stabilizer. Experimentally we estimated that the phase coherence of the motion-sensitive Raman beams is ≈ 10 ms. This value is obtained by fitting the decay of the Ramsey contrast on the FIQ transition, using the motion-sensitive Raman beams to drive the two $\pi/2$ rotations.

6.2.2 Calibration sequence

When we performed the experiment, we did not have the phase accumulators described in Section 4.1.2 to account for ac Stark shifts. Therefore the phase of each pulse in the sequence had to be calibrated by hand. As mentioned in Chapter 5.1.3, the Stark shift induced by the 729 nm laser is negligible; however, the calcium qubit experiences a few kHz Stark shift induced by the beryllium Raman lasers. The calibration sequence is then designed to first calibrate all the beryllium phases, including the MS gates, with the calcium laser off, and only at the end, we turn on the 729 nm laser and calibrate the calcium-related phases. The sequence of steps we followed can be found in [61].

It is worth noticing that there is a strong correlation between different phase settings, and it is easy to find a set of locally optimal values. For illustration purposes, we can

measure these correlations evaluating the Hessian matrix for the process fidelity. For the calculation, I will assume that each pulse in the sequence shown in Figure 6.1b realizes the correct operation but with a phase offset from the ideal one. The implemented operation is $U(\{\phi_i^{\text{off}}\})$, where $\{\phi_i^{\text{off}}\}$ is the set of phase offsets from the ideal implementation. The process fidelity can then be written as $F = \text{Tr}\left(U(\{\phi_i^{\text{off}}\})U_{S_Z}\right)/10$, that is 1 for zero phase offsets $\{\phi_i^{\text{off}} = 0\}$. The Hessian matrix $H_{i,j} = \frac{\partial F^2}{\partial\phi_i\partial\phi_j}|_{\phi=0}$ is

$$
\begin{array}{c}
\phantom{\phi_1^{Ca}} \\
\phi_1^{Ca} \\
\phi_1^{Be} \\
\phi_{MS_1}^{Ca} \\
\phi_{MS_1}^{Be} \\
\phi_2^{Ca} \\
\phi_2^{Be} \\
\phi_{MS_2}^{Ca} \\
\phi_{MS_2}^{Be} \\
\phi_3^{Be} \\
\phi_3^{Ca}
\end{array}
\begin{array}{cccccccccc}
\phi_1^{Ca} & \phi_1^{Be} & \phi_{MS_1}^{Ca} & \phi_{MS_1}^{Be} & \phi_2^{Ca} & \phi_2^{Be} & \phi_{MS_2}^{Ca} & \phi_{MS_2}^{Be} & \phi_3^{Be} & \phi_3^{Ca} \\
\left(\begin{array}{cccccccccc}
-0.4 & 0 & 0.2 & 0 & 0 & 0 & 0.2 & 0 & 0 & -0.2 \\
0 & -0.8 & 0 & 0.4 & 0 & 0 & 0 & 0 & -0.4 & 0 \\
0.2 & 0 & -0.4 & 0 & 0.4 & 0 & -0.4 & 0 & 0 & 0.2 \\
0 & 0.4 & 0 & -0.8 & 0 & 0.8 & 0 & -0.4 & 0 & 0 \\
0 & 0 & 0.4 & 0 & -0.8 & 0 & 0.4 & 0 & 0 & 0 \\
0 & 0 & 0 & 0.8 & 0 & -1.6 & 0 & 0.8 & 0 & 0 \\
0.2 & 0 & -0.4 & 0 & 0.4 & 0 & -0.4 & 0 & 0 & 0.2 \\
0 & 0 & 0 & -0.4 & 0 & 0.8 & 0 & -1 & 0.4 & 0 \\
0 & -0.4 & 0 & 0 & 0 & 0 & -0.4 & -0.8 & -0.4 & 0 \\
-0.2 & 0 & 0.2 & 0 & 0 & 0 & 0.2 & 0 & 0 & -0.4
\end{array}\right)
\end{array}
$$

where the indexes follow the pulse order. Assuming the phase offsets to be normally distributed, this Hessian matrix could be used to evaluate the covariance matrix, as the inverse of the Hessian. Consequently, the correlation coefficient of two variables is evaluated as the covariance of these variables divided by the product of the standard deviations of the same values. The correlation matrix, measures both the strength and the direction of linear relationship between two variables. This information could then be used during the calibration of parameters (or the re-calibration of a given phase following a parameter drift) as a guideline to know how the value of other phases need to be changed.

Unfortunately, this calculation was performed only at a late stage of the experimental campaign when almost all data were already acquired. As a consequence, we did not use it during the daily calibration procedure.

6.2.3 Single-shot readout

To verify the results of a single round of stabilizer measurement, we prepare input states with different parities and compare the calcium detection to the final beryllium measurement.

To prepare the input states we first create the Bell state $1/\sqrt{2}(|\!\downarrow\downarrow\rangle - i\,|\!\uparrow\uparrow\rangle)$ between the two beryllium qubits. Like for the U_{s_Z} operation, the sequence is phase insensitive [128] and makes use of an MS gate and carrier $\pi/2$ pulses as shown in Figure 6.2a (sequence labeled as "state prep."). Next, a parity pulse (Section 5.3.3) with phase ϕ_p, performed with the motion-insensitive configuration, create states with different parities. In the ideal case, a parity pulse with phase $\phi_p = 3\pi/4$ generates an input state with odd parity ($E_Z = -1$) (the triplet state $|\Psi_+\rangle$), while for $\phi_p = \pi/4$ the state has even parity $E_Z = +1$. The violet stars in Figure 6.2b show the parity[3] of the input states measured with an independent experiment.

Following the preparation of different input states, we perform a single round of the stabilizer measurement M_{S_Z}. The results for the calcium and beryllium measurements are

---

[3]we plot $(1 + \langle S_Z\rangle)/2$ to fit the plot axis.
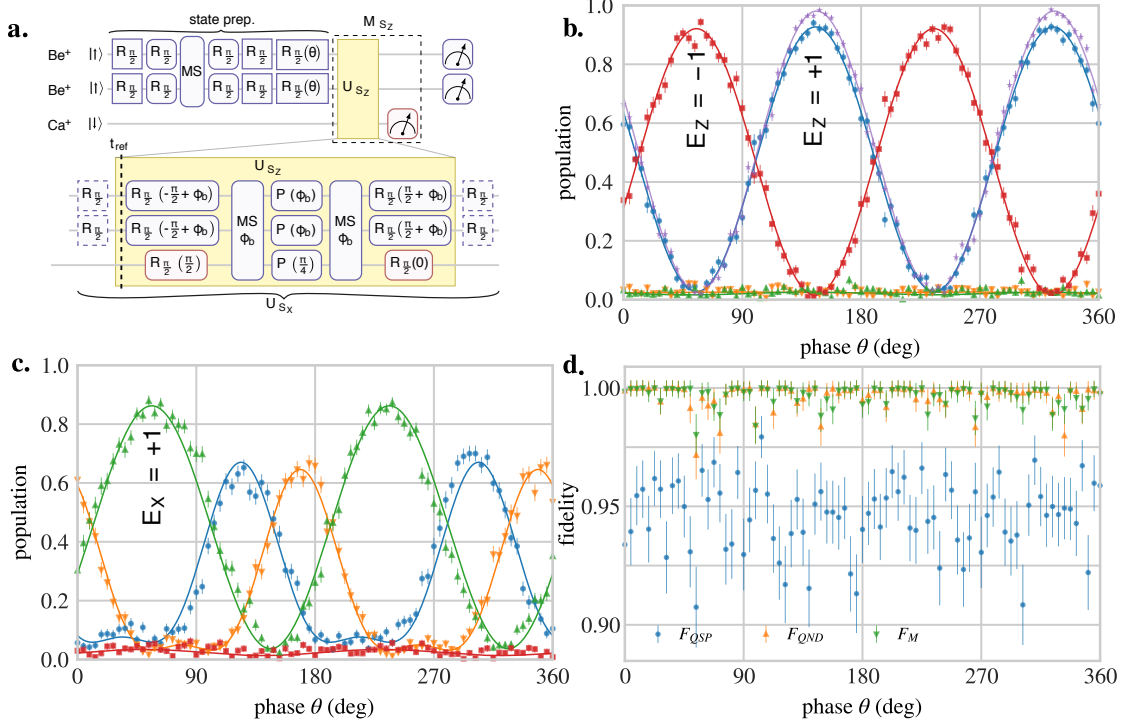
Figure 6.2: Single-round stabilizer readout. **a** Gate sequence used for beryllium state preparation and the stabilizer measurements M_{S_Z} and M_{S_X}. For the beryllium pulses, the round (sharp) rectangles indicate pulses performed with the motion-sensitive(insensitive) beam configuration. The dashed pulses are only used for the M_{S_X} readout. The parity pulse phase θ differes from the ideal pahse ϕ_p (see text) due to an uncompensated Stark shift. **b** M_{S_Z} readout. In red (blue) is the joint probability of observing calcium in $|\downarrow\rangle$ ($|\uparrow\rangle$) and beryllium in $E_Z = -1$ ($E_Z = +1$). For comparison we plot in violet the parity of the beryllium input state, plotted as $(1 + \langle S_Z \rangle)/2$. **c** M_{S_X} readout. In green the joint probability of measuring beryllium in state $|\Psi_+\rangle$ ($E_Z = +1$) and calcium in $|\uparrow\rangle$, while in blue (orange) the probability of measuring beryllium in$|\Phi_+\rangle$ ($|\Phi_-\rangle$), with $E_X = +1$ ($E_X = -1$) and calcium in state $|\uparrow\rangle$ ($|\downarrow\rangle$). **d** Fidelity estimates for M_{S_Z} as discussed in the text. In panel **c** and **d** the solid lines are fits to the expected probability distributions.

shown in Figure 6.2b. To evaluate the quality of the operations we make use of three fidelities: measurement fidelity, non-demolition fidelity and state-preparation fidelity [142, 151] defined as:

$$F_M = (\sqrt{p_{+1}^{\text{in}} p_{|\uparrow\rangle}^{m}} + \sqrt{p_{-1}^{\text{in}} p_{|\downarrow\rangle}^{m}})^2$$

$$F_{QND} = (\sqrt{p_{+1}^{\text{in}} p_{+1}^{\text{out}}} + \sqrt{p_{-1}^{\text{in}} p_{-1}^{\text{out}}})^2$$

$$F_{QSP} = p_{|\uparrow\rangle} p_{+1\||\uparrow\rangle}^{\text{out}} + p_{|\downarrow\rangle} p_{+1\||\downarrow\rangle}^{\text{out}}$$

$$= p_{+1\&|\uparrow\rangle}^{\text{out}} + p_{-1\otimes|\downarrow\rangle}^{\text{out}},$$

(6.4)

where $p_{\pm 1}^{\text{in}}$ ($p_{\pm 1}^{\text{out}}$) is the probability of measuring the beryllium parity in $E_Z = \pm 1$ before (after) the stabilizer measurement M_{S_Z}, $p_{|\uparrow\rangle}$ and $p_{|\downarrow\rangle}$ are the calcium measurement probability, and $p_{+1\||\uparrow\rangle}^{\text{out}}$ ($p_{-1\||\downarrow\rangle}^{\text{out}}$) is the conditional probability of measuring beryllium in the $E_Z = +1$ ($E_Z = -1$) having measured calcium in $|\uparrow\rangle$ ($|\downarrow\rangle$). For QEC, the state preparation fidelity is the most critical value since it takes into account the joint probabilities of the beryllium output parity and the calcium readout state.

Figure 6.2d shows the measured fidelities for different input parity states. On average we find that for the M_{S_Z} operation, the average fidelities over all the different states are $\bar{F}_M = 99.6(4)\%$, $\bar{F}_{ND} = 99.6(5)\%$ and $\bar{F}_{SP} = 94.6(2)\%$ [42]. The $\bar{F}_{SP}$ fidelity is broadly consistent with the quality of the operations measured in our system, and in particular, with the three-ion MS gate that is the primary source of infidelity. As discussed in Chapter 5.3.2, the GHZ state preparation fidelity with the three-ion MS gate is 93.8(5)%, while the fidelity for creating a Bell state between the two-beryllium qubits in the beryllium-calcium-beryllium ion chain is 97.8(4).

In a similar way we also verified the stabilizer measurement M_{S_X}, as shown in Figure 6.2c. With the state preparation method described above, we can produce the triplet state $|\Psi_+\rangle$, which is an eigenstate of S_X with eigenvalue $E_X = +1$; however, we do not create a pure $E_X = -1$ state. An example of state with $E_X = -1$ is the Bell state $|\Phi_-\rangle$, which cannot be created for any ϕ_p. The green trace in Figure 6.2c correspond to beryllium measured in state $|\Psi_+\rangle$ with $E_X = +1$ correlated with calcium being measured in $|\uparrow\rangle$. The blue (orange) points are instead for beryllium in $|\Phi_+\rangle$ ($|\Phi_-\rangle$) and $E_X = +1$ ($E_X = -1$) correlated with calcium being measured in $|\uparrow\rangle$ ($|\downarrow\rangle$).

If we compare the contrast of the $E_X = +1$ trace (green trace in Figure 6.2c) to that of the $E_Z = \pm 1$ (blue and red traces in Figure 6.2b), we observe that it is lower (82(1)% against 89(1)%). Similarly, one can also notice an asymmetry of the blue points in Figure 6.2c compared to the fitted curve (compare the region around $\theta = 90$ and $\theta = 280$). Unfortunately, we are not able to fully explain those behaviors nor to reproduce them in simulations. However we suspect that it is related to a higher susceptibility on the MS gate infidelities. One possible explanation that only partially explains the observed behavior is the following. Assume to perform an S_Z measurement, in which the beryllium ions are prepared in an even state (e.g. $|\downarrow\downarrow\rangle$). The effect of the first beryllium $\pi/2$ pulse in the S_Z sequence rotates the beryllium states in the eigenbasis of the following MS gate. As a result, we do not expect an excursion in phase space during the MS gate. On the contrary, if we perform a S_X measurement, the $\pi/2$ pulse within the S_Z block undo the rotation of the motion-insensitive $\pi/2$ pulse. Before the MS gate, the state of the beryllium qubit is still $|\downarrow\downarrow\rangle$ which is not an eigenstate of the MS operation. As a result this state will evolve in phase space while applying an MS gate, and may suffer from MS gate miscalibrations.

6.3   Repeated measurements

Calcium fluorescence detection is a dissipative process, which induces significant heating on the motional modes of motion. If not re-cooled, the performance of the subsequent three-ion MS gates will be reduced. To mitigate this heating, we red-detuned from resonance the 397 nm detection beams by approximately 8 MHz. This produces a lower scattering rate than at $\delta = 0$, but maintains the ions at lower excitation. Next, we apply a calcium cooling sequence that sympathetically cools the relevant modes of the ion chain. At first, an EIT cooling pulse (150 µs long) is used, for which the settings are optimized to cool the EGY mode and lowest radial frequency mode. The COM mode of motion is instead cooled with a second EIT cooling pulse (200 µs long) followed by ten loops of pulsed sideband cooling with the 729 nm beam. By addressing just calcium, it is not possible to cool the STR mode due to the symmetry of the ion chain (see Chapter 2.8.1); however, for the same reason, we do not expect any heating on this mode induced by photon scattering during detection. At the end of the sequence, the COM sideband Rabi oscillations were comparable to those before
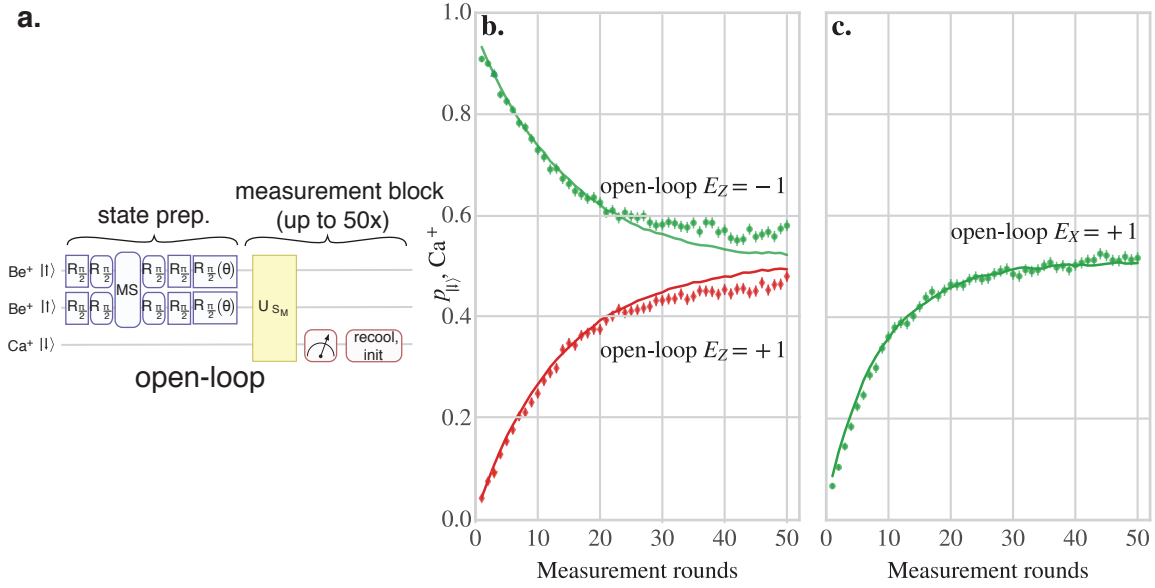
Figure 6.3: Open-loop parity measurement. **a** Pulse sequence used for beryllium state preparation and the $S_{Z/X}$ readout. **b** and **c** The calcium population as a funtion of S_Z and S_X measurement cycles, respectively. In panel **b** the green (red) points are produced by initializing beryllium in $E_Z = -1$ ($E_Z = +1$) parity state. In panel **c** the beryllium ions are initialized in the triplet state $|\Psi_+\rangle$. The solid line are produced from Monte Carlo density matrix simulations using only one free parameter (see text).

the first measurement round. This implies that that the motional excitation is comparable to the one we measure at the beginning the measurement sequence. Finally, calcium state initialization in $|\downarrow\rangle$ concludes the re-cooling sequence.

Following re-cooling and calcium state initialization, we repeat the stabilizer measurement up to 50 times. Figure 6.3a, shows the pulse sequence for the consecutive measurement of a stabilizer without feedback (open-loop sequence). For the repeated M_{S_Z}, we initialize the beryllium either in the triplet state $|\Psi_+\rangle$ ($E_Z = -1$) or in a superposition of the even Bell states $|\Phi_+\rangle$ and $|\Phi_-\rangle$ ($E_Z = +1$). In Figure 6.3b, we plot the calcium population as a function of the measurement round. The points in green are for the M_{S_Z} acting on $|\Psi_+\rangle$; the ones in red are for the measurements in which beryllium is prepared in an even parity state. The contrast loss indicates that the purity of the initial Bell state decreases over measurement rounds due to the parity readout corrupting the original state. The solid lines are from a simple Monte Carlo density matrix simulation where only one parameter is free. For more details about the model and the data analysis, refer to Section 6.4.

6.3.1 Stark shift calibration

The U_{S_X} stabilizer operation is not diagonal in the measurement basis. As a result, it is sensitive to the relative phase between $|\downarrow\rangle$ and $|\uparrow\rangle$ acquired during each pulse of the sequence (remember that all carrier pulses are on-resonance with the bare qubit frequency). To make sure that at each cycle we measure the same stabilizer operator, we shift the phase of the initial and final co-carrier $\pi/2$ pulse by $n\Phi_X$, where n is the number of times the S_X stabilizer has previously been measured and Φ_X is the Stark shift induced by a single M_{S_X} sequence. The phase Φ_X is empirically calibrated by repeating the scan in Figure 6.2c for several rounds while maximizing the measurement correlations for even-parity input states.
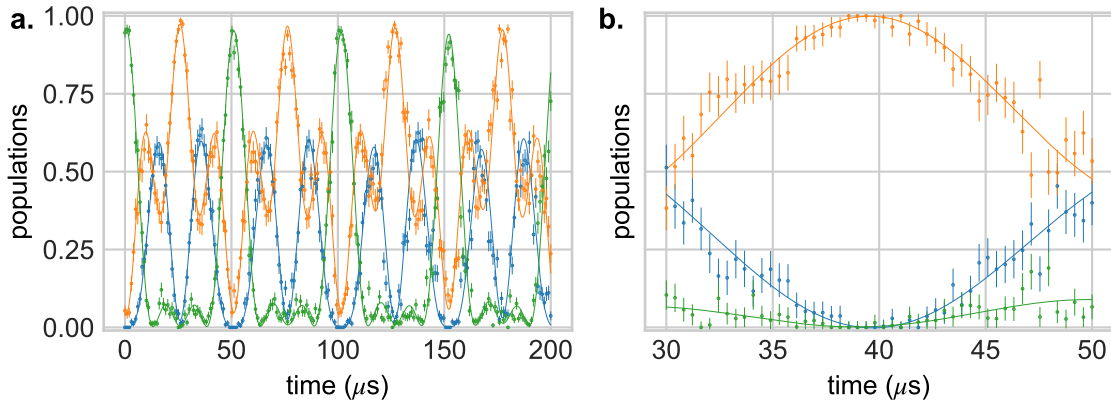
Figure 6.4: Two beryllium FIQ carrier rotation time scan with the ions non-centered in the laser beam. The orange data show the probability of only one ion being detected in the bright state, while the green (blue) data show the probability of both ions being bright (dark). **a** Rabi oscillations **b** Time scan around the optimal time for inverting only one of the two ions. At time $t = 39\,\mu$s, we perform a $\theta = 2\pi$ rotation on one ion and $\theta = \pi$ rotation on the other. The fitted inversion probability is 99.9(5)%. Fitted curves are for two ions undergoing independent Rabi oscillations with different Rabi frequencies.

6.3.2   Feedback operations and subspace stabilization

The loss of contrast measured in Figure 6.3 is to be attributed to imperfections of the stabilizer readout sequence rather than qubit decoherence (see Section 6.4). For future trapped-ion experiments, it is also likely that operations fidelity will be the main limiting factor [117], especially in the case where the qubits are encoded in a logical decoherence-free subspace [152, 153]. Using real-time feedback, we can correct parity errors and demonstrate an extra element required for more general QEC protocols. Real-time feedback is a fundamental feature of the M-ACTION system; extensive details about the software and hardware implementation can be found in Vlad Negnevitsky Ph.D. thesis [61]. When we acquired the data, the re-configuration of the pulse sequence required $\approx 50\,\mu$s. Since that data was acquired, an upgrade in the system has reduced this time to approximately $3\,\mu$s.

In the case of S_Z, our choice for the correction operator is $C_Z = -I^{(1)} \otimes \hat{\sigma}_x^{(2)}$; while it is $C_X = -I^{(1)} \otimes \hat{\sigma}_z^{(2)}$ for the S_X stabilizer. In both cases, we require a different rotation for each of the two beryllium ions. In order to realize this, for C_Z, we move the ions with respect to the Raman beam by $\approx 10\,\mu$m, such that one beryllium experiences a Rabi frequency twice as large as the other. At this position, we calibrate the pulse time to perform a $\hat{\sigma}_x$ rotation on one qubit and $-I$ on the other. Figure 6.4 shows a typical time scan of the Rabi oscillations used to calibrate the time of the C_Z correction pulse. This operation is realized with the co-propagating Raman beams.

For C_X, we embed the C_Z operation between two basis rotation $\pi/2$ pulses. In particular $C_X = R(\pi/2, 0)C_Z R(\pi/2, \pi)$, where the rotation $R(\theta, \phi)$ is common to both beryllium qubits and realized with co-propagating Raman beams.

Similarly to M_{S_Z} and M_{S_X}, also the correction pulses induce Stark shifts that have to be taken into account to realize the desired operations. The phase accumulators described in the previous section are hard-coded in the experimental sequence; however, the Stark
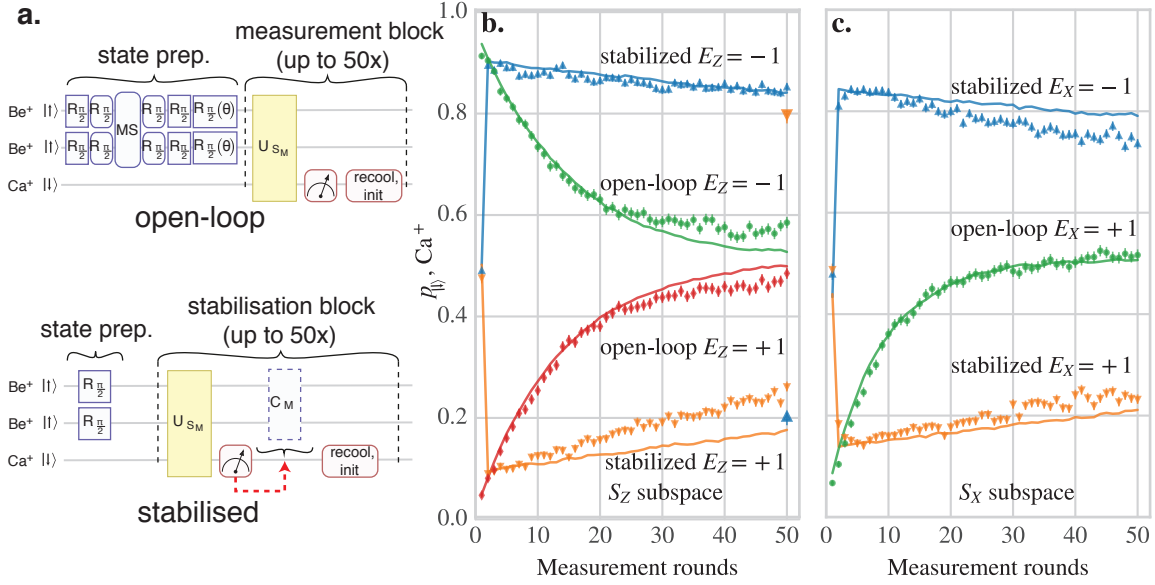
Figure 6.5: Repeated parity measurements and parity subspace stabilization. **a** On top the pulse sequence used for the open-loop repeated parity measurements. Beryllium qubits are prepared in an entangled state with a well-defined parity. Bottom: the pulse sequence used for the parity subspace stabilization. An initial $\pi/2$ pulse prepares the beryllium qubits in an equal superposition of eigenstates $E_{Z/X} = \pm 1$. Depending on the choice of stabilization, U_{S_M} is U_{S_Z} or U_{S_X} and C_M is the appropriate feedback operation. **b** Calcium detection probabilities as a function of repeated S_Z measurements. The green (red) data are the results for the sequence where no feedback is applied and for beryllium initialized in $E_Z = -1$ ($E_Z = +1$). The blue (orange) points are for the closed-loop operation where the $E_Z = -1$ ($E_Z = +1$)parity subspace is stabilized. The solid line are produced from Monte Carlo density matrix simulations using only one free parameter (see text). **c** Same as **b** but the stabilizer being measured is S_X.

shift phases coming from the correction pulses have to be dynamically applied depending on the history of the pulse sequence. To give an example, consider the stabilization of the S_X parity subspace. Defining Φ_X as the phase shift induced by U_{S_X}, Φ_{C_X} is the phase induced by the correction pulse. At the $n+1$ S_X measurement, the phase offset of the initial and final co-carrier $\pi/2$ pulses of U_{S_X} is $\phi_{\text{off}} = n\Phi_X + k\Phi_{C_X}$, where k is the number of feedback pulses applied earlier in the sequence. The calculation is done directly on the ARM CPU of the control system before the execution of the next measurement round, and the result is pushed to the DDS boards within $1-3\mu$s.

Having these techniques in place, we can then test the stabilization sequence up to 50 measurement rounds [42]. The experimental results are shown in Figure 6.5. As in the previous sets of measurements, we plot the calcium population after each stabilizer measurement. The beryllium qubits are initially prepared in an equal superposition of even and odd parities with a single $\pi/2$ rotation applied to the qubits initialized in $|\downarrow\downarrow\rangle$; as a result, we expect the calcium population at 0.5 after the first stabilizer measurement. In the case of S_Z parity stabilization (Figure 6.5b), we also plot the measured parity of the beryllium ions at the end of the stabilization sequence. The plotted quantity is $(1+\langle S_Z \rangle)/2$; therefore, for ideal operations, we expect to obtain a parity value of 1 (0) when the even (odd) parity subspace is stabilized.

The figure of merit for the improvement obtained by the stabilization is the ratio between

subspace	γ_{closed}	γ_{open}
$E_Z = +1$	0.33(1)	8.0(2)
$E_Z = -1$	0.10(1)	8.5(3)
$E_X = -1$	0.23(1)	11.3(2)
$E_X = +1$	0.22(1)	-

Table 6.1: Parity subspace decay rates (in units of percent per measurement round) for open-loop and closed loop sequences. For the open-loop, the populations are fitted to exponentials. Due to the lack of information at the many-round limit, the populations for the closed-loop version are fitted to linear decays.

the decay rates of the closed-loop data and the open-loop ones. We fit the open-loop decays to exponential, while we use linear fits for the closed-loop populations due to lack of information at the many-round limit. Table 6.1 reports the fitted decay values.

6.4   Modeling of the errors

The solid lines in Figure 6.3 and Figure 6.5 are obtained with a simple Monte Carlo simulation of the density matrix where only one parameter is free. The Monte Carlo simulation consists of thousand repetitions of the same sequence of operations. Each sequence simulates the repeated stabilizer measurement and is composed of the following steps. After beryllium state initialization in a state described by a density matrix, we apply the first stabilizer $U_{S_{Z/X}}$ to the three qubits. This operation is assumed to be ideal. We mimic imperfect operations using a depolarizing channel [6] applied to the density matrix before the calcium measurement, parameterized by a rate γ_{dep} and defined as

$$\Lambda(\rho) = (1 - \gamma_{\text{dep}})\rho + \frac{\gamma_{\text{dep}}}{2N} I_N, \tag{6.5}$$

where N is the number of qubits involved in the computation and the I_N the identity matrix. Following this step, we perform a probabilistic measurement of the calcium ion based on its populations. After the measurement, the state of the calcium ion is re-initialized in $|\downarrow\rangle$, and for the closed-loop simulations, a feedback pulse conditional on the calcium measurement is applied to the beryllium qubits. The stabilizer measurement is the concluded by applying a leakage term that simulates the Raman off-resonant scattering outside the qubit space. This term is implemented with a partial trace of one or both of the beryllium ions, happening with a probability of $\gamma_{\text{leak}} = 0.3\%$. This sequence is then repeated to simulate consecutive measurement rounds.

The leakage term is fixed for all simulations and was experimentally determined with an independent measurement of the population remaining in the qubit subspace after applying the looped sequence with just one Raman beam on at a time [42]. For this measurement, we prepared the beryllium qubit state in $|\downarrow\rangle$. We then apply a sequence of stabilizer measurement where the number of rounds is scanned. The sequence is run with just one Raman beam on. Therefore, we would not expect any effect on the qubit population. However, Raman off-resonant scattering potentially reduces the population of state $|\downarrow\rangle$. At the end of each sequence we measure the beryllium qubits population. We then fit the leaked population as a function of measurement rounds, with a simple linear fit (good approximation since the leakage probability is small). We repeat the process for the other Raman beam and also for the other qubit state. The total leakage probability per stabilizer readout is

then the sum of all those fitted results. This value is also consistent with theoretical calculations, assuming a Raman detuning of $2\pi \times 230\,\text{GHz}$ [48] and a sequence of two MS gates each lasting for $70\,\mu\text{s}$. In the calculation we do not consider the effect of single qubit operations since the length of the stabilizer sequence is dominated by the MS gate time.

In the simulations, we adjust the depolarizing rate to best fit the curves. For the open-loop data, we adjust it to best reproduce the exponential decay of the calcium populations. In particular, we use $\gamma_{\text{dep}} = 0.06$ ($\gamma_{\text{dep}} = 0.07$) for $E_Z = -1$ ($E_Z = +1$), and $\gamma_{\text{dep}} = 0.11$ for $E_X = +1$. We attribute the higher value for $E_X = +1$ measurement to the worse results observed in a single measurement round (see previous section). For the closed-loop case, the depolarizing rate is instead adjusted to fit the offset of the first few points. For $E_Z = -1$ ($E_Z = +1$) we use $\gamma_{\text{dep}} = 0.10$ ($\gamma_{\text{dep}} = 0.10$) and $\gamma_{\text{dep}} = 0.15$ ($\gamma_{\text{dep}} = 0.16$) for $E_X = +1$ ($E_X = -1$).

For the closed-loop simulations, the depolarizing rates are larger compared to those used in the open-loop. These higher values are associated with imperfections in the correction pulse. To better understand this point, consider the stabilization of the odd-parity subspace of S_Z. For an ideal implementation of measurement and feedback, the correction pulse C_Z is applied only when an additional source of noise induces a change of subspace. Because single-shot non-demolition fidelity is $\bar{F}_{QND} = 99.6(5)\%$, the effect of U_{S_Z} on the parity of the state is almost negligible. Therefore, it should be unlikely to require consecutive correction pulses. However, when the dominant error source is imperfect readout, in the steady-state, we expect a 50% probability of applying feedback in two consecutive shots because, in half of the cases, we correct an uncorrupted state. This is relevant to our experiment, because the state preparation fidelity in our case is $\bar{F}_{QSP} = 94.6(2)\%$. Figure 6.6 shows the experimental and simulated feedback correlations between successive shots. One can see that the probability of applying two consecutive correction pulses is around $30 - 40\%$, and that the simulation matches reasonably well the experimental data. This result validates the argument above, suggesting that our primary source of error is imperfect readout.

One way of mitigating imperfect readout is to repeat the stabilizer measurement multiple times and apply the correction pulse based on a majority vote. We explored this scenario in simulation, where we assumed that a single stabilizer measurement is a block of three repeated M_{S_Z} operations [4]. At the end of each block, a majority vote on the three calcium measurements decides whether or not a correction pulse has to be applied. Because the sequence mostly consists of repeated M_{S_Z} operations with no feedback, the depolarizing amplitude γ_{dep} used in the simulation is that of the open-loop case ($\gamma_{\text{dep}} = 0.06$). Figure 6.7 shows a simulation comparison between the two different approaches discussed so far. If we compare the calcium population as a function of measurement cycles, we see only marginal improvements for the case where we perform a majority vote. However, if we compare the feedback correlations between successive shots, we see that the probability of applying two consecutive corrections is greatly reduced in the case of majority vote. In conclusion, despite the small improvements, this technique is probably also limited by readout errors at the current level of fidelity.

The depolarizing model described so far cannot capture all the error sources that can occur in the complex experimental system. Nevertheless, it gives a simple single-parameter

---

[4] We chose to perform a majority vote on a block of three measurements as it is the simplest way to compare the data and do correlation measurements. In the experiment one could replace this operation by doing two consecutive measurements and if the result does not agree do a third one to decide if an error occurred or not.
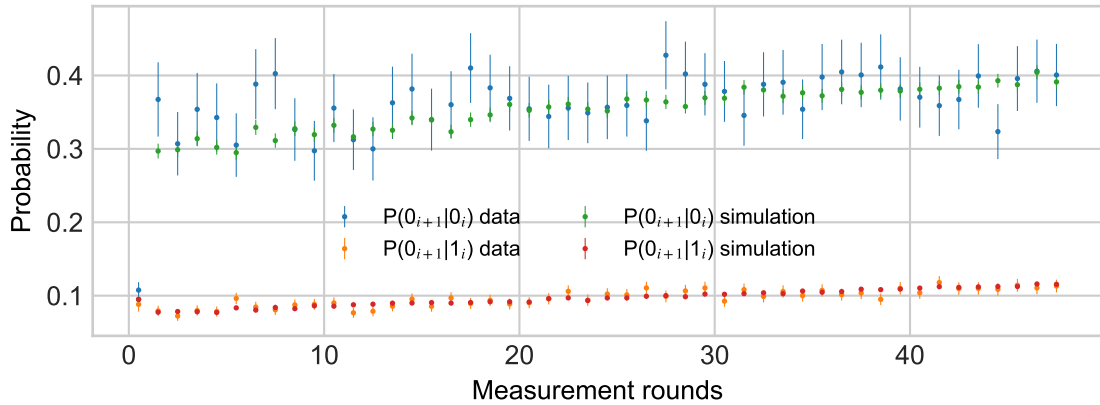
Figure 6.6: Comparison between experimental and simulated feedback correlations between successive shots. Defining $P(0_i)$ the probability of applying a correction pulse in the i-th measurement round, $P(0_{i+1}|0_i)$ is the conditional probability of two feedback operations in consecutive shots. This probability is shown in blue for the measured data and in green for the simulations. This conditional probability is compared to the one where feedback operations happen just once ($P(0_{i+1}|1_i)$). Uncertainties for $P(0_{i+1}|0_i)$ are larger than that of $P(0_{i+1}|1_i)$ due to the rarity of these events (an average of 100 events over 10,000 simulated points).

adjustment that accounts for decoherence. From Figure 6.5, we can see that especially for long sequences, the dynamics are not well described. The reason is not fully understood; however, we think that it is likely to be a systematic effect such as thermal AOM drifts due to duty cycle issues. For instance, we observed an increase of the calcium PMT counts as a function of the stabilizer readout cycle, which resulted in a drift of the optimal threshold for state discrimination from 9 counts to ≈ 11 counts. The effect was only noted after we collected the data, and caused a detection bias in the closed-loop experimental sequence. Similarly, we observed gradual changes in pulse amplitudes over the sequence length, which we were not able to compensate. In simulations, we modeled these effects as a gradual drift in the readout fidelity of the parity measurement up to $3 - 5\%$. Qualitatively, we are then able to match better all closed-loop datasets, with the exception of the $E_X = -1$ closed loop data. Unfortunately we are not able to explain the reason. More investigation is then required.

6.5 Bell state stabilization

Bell states are simultaneous eigenstates of S_Z and S_X. In our experiment we prepare one of these states by measuring M_{S_Z} followed by M_{S_X}[5] resulting in one of the four possible outcomes $\{E_Z = \pm 1, E_X = \pm 1\}$. Conditional to the calcium outcomes, we can deterministically create a particular Bell state by applying the suitable correction pulses C_Z and C_X. The sequence can then be repeated multiple times to stabilize the target state, as shown in Figure 6.8.

To ensure the same operations at every measurement cycle, the four Stark shift phases Φ_Z, Φ_X, Φ_{C_Z}, Φ_{C_X} are used to update the phases of the motion-insensitive rotations before every measurement round depending on the number of measurements and feedback opera-

---

[5]Note that the order of the measurement is not important since S_Z commutes with S_X.
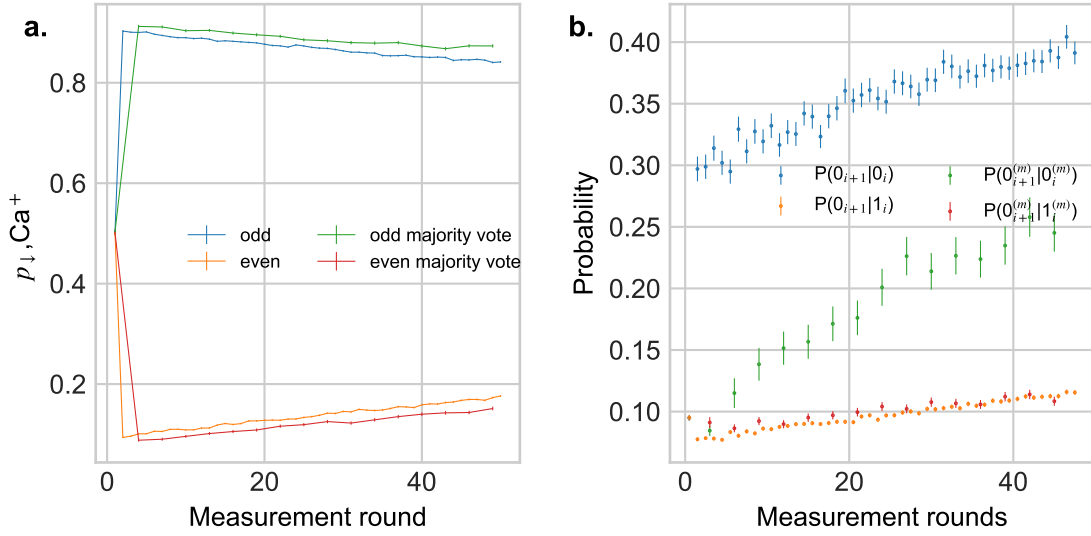
Figure 6.7: Comparison between closed-loop M_{S_Z} simulations. One simulation is the standard simulation used to describe the experimental data, where feedback pulses are conditionally applied after each calcium detection. In the second, a measurement cycle is defined as three repeated stabilizer measurements, and feedback is applied conditionally to the majority vote of the three calcium detections. In this simulation, the parameter γ_{dep} is that of the open-loop, because the sequence mostly consists of repeated M_{S_Z} operations. While the parameter $\gamma_{\text{leak}} = 0.3\%$ is the same for both simulations. **a** Calcium population as a function of the measurement round. We can see that in the case of the majority vote, the improvement is marginal. **b** Two-point correlations between successive shots. The blue and orange points are for the standard simulation, while the green and red are for the majority vote simulation. In the case of majority vote we see that the probability of applying two correction pulses in consecutive shots is greatly reduced.

tions. The Stark shift phases are pre-calibrated with the same technique as in Section 6.3.1, and optimized within the sequence to maximize the expected population of each Bell state.

At fixed points in the sequence, we also extract the Bell state fidelity, and the results are shown in Figure 6.8 with green points. To better understand the sequence, assume that we want to measure the state preparation fidelity of $|\Phi_+\rangle$. At first, we measure the population in the measurement basis to obtain $\langle S_Z \rangle$. To measure the off-diagonal terms of the density matrix, we apply a motion-insensitive $R(\pi/2, \phi)$ to both beryllium ions before measuring them. The phase ϕ is chosen to prepare either $|\Psi_+\rangle$ or $|\Phi_-\rangle$ (see Section 5.3.1). We follow this operation by a measurement of the beryllium ions in the computational basis. Note that the effect of of the $\pi/2$ pulse is equivalent to the preparation of the two states that are at the two extrema of a parity scan (see Section 5.3.3). Effectively, we measure the contrast of an equivalent parity scan by just measuring the two extrema. The same operation is also done when $|\Phi_-\rangle$ is the target state. However, in the case of $|\Psi_\pm\rangle$, we first apply $C_Z = -I \otimes \hat{\sigma}_x$ to obtain $|\Phi_\pm\rangle$, from which we extract the state fidelity with the same method described above. Although the use of the C_Z operation is not strictly necessary, this scheme reduces the number of calibrations, making the experiment easier to manage and debug. Note that also for the analysis pulse, the phase is dynamically updated according to the exact pulse sequence.

The mean Bell state fidelity after the first measurement block is 73.1(4)%, and it drops
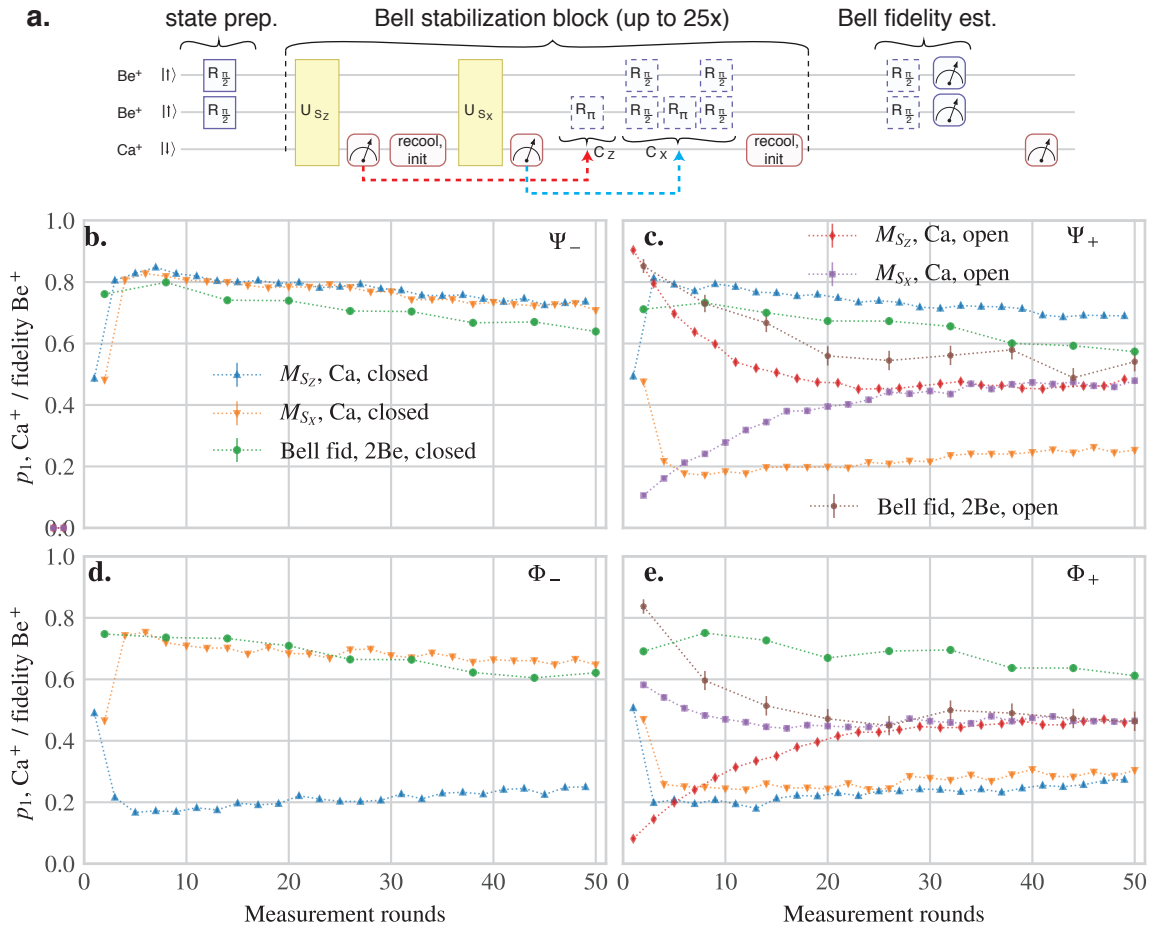
Figure 6.8: Bell state stabilization. **a** Pulse sequence. The beryllium qubits are initialized in a superposition of all Bell states. The feedback operations are applied after having measured M_{S_Z} and M_{S_X}. **b-e** Calcium population over 25 Bell state measurement rounds for a total of 50 stabilizer measurements. In green are shown the measured Bell state fidelity obtained by performing a set of measurements (see text) directly on the beryllium ions at fixed points in the sequence. In blue, we plot the calcium results after the S_Z stabilizer measurement, while in orange after M_{S_X}. For the state Ψ_+ (panel **c**), we also plot the open-loop evolution of the calcium population. In red, the calcium results after the S_Z stabilizer measurement, while in violet after M_{S_X}.

to 61.3(4)% after 25 rounds.

6.5.1   Correlations

Similarly to what we did for the parity stabilization, we can analyze the results looking at the correlations between different measurement rounds. Figure 6.9 shows the two-point correlations between consecutive parity measurements in the same basis, selected depending on the feedback operation that occurred in between them. A full correlation corresponds to a value of 1, while for perfect anti-correlation, it should be 0.

To understand the plots, consider only the curves for the stabilization of $|\Psi_-\rangle$ (Figure 6.9a). The blue (orange) triangles represent the two-point correlation of successive M_{S_Z} (M_{S_X}) measurements in the absence of any feedback. Considering the M_{S_Z} correlations, it corresponds to the sequence $M_{S_Z} - M_{S_X} - M_{S_Z}$. The violet (red) points are the correlation
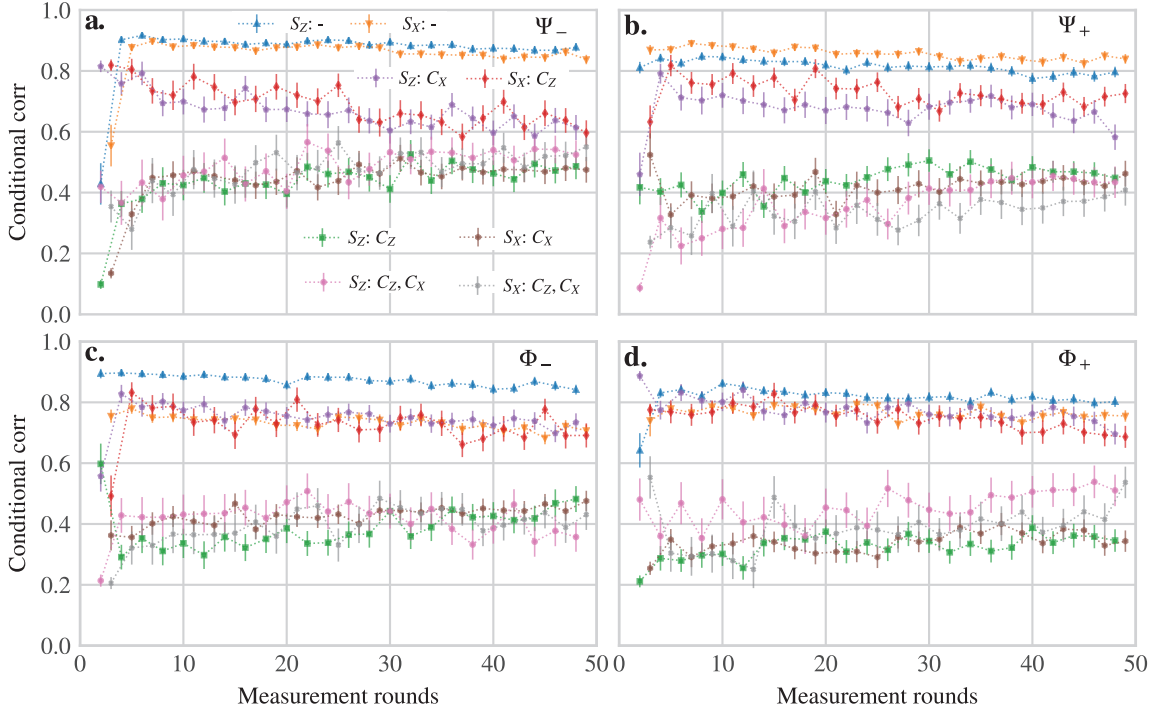
Figure 6.9: Panels **a-d** show the two-point correlations between consecutive parity measurements in the same basis, categorized by the feedback operation that occurred in between them, for different Bell states. A value of 1 (0) represent full correlation (anti-correlation). Blue (orange) points show the correlations between successive S_Z (S_X)where no feedback occurred. The violet (red) points show the correlation between consecutive M_{S_Z} (M_{S_X}) with a commuting C_X (C_Z) correction that happened in between, for which we expect full correlation. The green (brown) points show the correlation for successive M_{S_Z} (M_{S_X}) measurements where a non-commuting C_Z (C_X) correction is applied in between them. Finally the violet (grey) points are the correlations between consecutive M_{S_Z} (M_{S_X}) results where both corrections C_Z and C_X are applied.

between consecutive M_{S_Z} (M_{S_X}) measurements where a C_X (C_Z) correction happened in between. Ideally, the S_Z (S_X) and C_X (C_Z) should commute; therefore, we would expect to measure the same correlation as in the absence of the feedback pulse, i.e., the blue (orange) points. However, the violet and red curves are approximately 10% lower than the blue and orange point. This indicates that the commutation error is ≈ 10%. The source of this error is still unknown, and the error is higher than what we would expect from calibration on shorter sequences (≈ 1%). Such sequences, up to three Bell state measurement cycles, are used to calibrate the phase offset induced by the ac Stark shifts on the beryllium co-carrier pulses that define the basis rotations for the S_X measurement. During the calibration, we are able to monitor the correlation between consecutive M_{S_Z} (M_{S_X}) measurements where a C_X (C_Z) correction is either applied or not. We notice that the discrepancy between the two cases (i.e. the case in which no correction pulse is applied and when a correction pulse happens in between two measurements) is below 1%. This results disagrees with the 10% discrepancy discussed above. We suspect that on a longer sequence, we have systematic errors, such as AOM duty cycle, that alter the optimal settings over the time taken to acquire data (which is significantly longer than in the calibration experiments). We could confirm this by monitoring the correlations in real-time as the experiment is performed.

The green (brown) points are instead the two-point correlation for successive M_{S_Z} (M_{S_X})

measurements where a non-commuting C_Z (C_X) correction is applied in between. Ideally, we would expect complete anti-correlation. The idea is that the first M_{S_Z} (M_{S_X}) flags that a parity error has occurred, and that is corrected by C_Z (C_X). The second M_{S_Z} (M_{S_X}) should then give an opposite result compared to the first. Instead of measuring perfect anti-correlation, we note that the traces are at about $0.3 - 0.5$. Similarly to what discussed in Section 6.4, we think that this is a sign of imperfect readout. If imperfect readout is the dominant error source, in the steady-state, we expect a 50% probability of applying a correction pulse in two consecutive shots because, in half of the cases, we "correct" an uncorrupted state.

6.6   Conclusions and outlook

With this experiment, we demonstrated some general elements of stabilizer readout and large-scale quantum error correction, namely the ability of measuring an ancilla ion with a small perturbation of the information stored in the data qubits, the ability to re-cycle the ancilla qubit and re-prepare the system for multiple measurement rounds, and the ability of applying correction pulses upon ancilla readout. Currently, the major limitation is gate infidelities that cause errors in the stabilizer readout. At least for systematic phase miscalibrations, better results could be obtained by using the phase accumulators described in Chapter 5, where phase offsets arising from ac Stark shift can be automatically calculated. Developing and debugging this feature has been a primary task towards the realization of the experiment described in the next chapter.

Currently, the error introduced by the stabilizer readout is larger than the qubit coherence, which for beryllium is significantly longer than the $60-80$ ms necessary to complete 50 measurement rounds. However, this sequence could still be beneficial if we would let the system evolve for a duration of order of the coherence time and then stabilize it. Such experiment would be very long, but could be shortened adding artificial noise (for example off-resonant 729 nm light that causes random Stark shifts) and recover from that perturbation. One challenge would be the ability of sympathetically cool all modes using calcium during the entire sequence. For this purpose, the STR mode could be cooled by deforming the ion crystal, for example by adiabatically squeezing the ion chain into a zig-zag configuration, such that the calcium ion has some non negligible Lamb-Dicke parameter for all modes.

The techniques shown here could be extended to lattice surgery codes [154] to demonstrate a universal set of fault-tolerant quantum operations with color-codes [155]. In this framework, the fault-tolerant implementation of a logical two-qubit $CNOT$ gate [6] can be performed using an ancillary logical qubit initialized in $|\downarrow\rangle$. At the core of this operation is the following set of operations
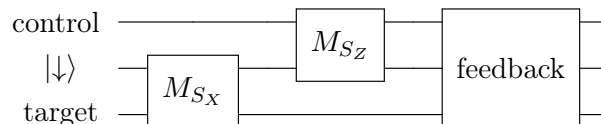
where $M_{X/Z}$ is the stabilizer measurement $S_{X/Z}$. The sequence is then completed with feedback operations on all qubits based on the measurement outcomes. A proof of principle

---

[6]The CNOT gate has two input qubits: the control and target qubits. It flips the state of the target qubit if the control is in state $|\uparrow\rangle$.

demonstration of such a gate could be realized by replacing the three logical qubits with three beryllium ions. We could then use an additional calcium qubit as an ancillary qubit for the $M_{S_{X/Z}}$ readout.

7 Measurement-based Quantum Computing

In this chapter, I will present preliminary results of the realization of general single-qubit unitary operations in the measurement-based quantum computation (MBQC) formalism. After a theoretical introduction, I will show how to construct arbitrary single-qubit gates and how these sequences can be compiled for a trapped-ion processor composed of a mixed-species ion chain. Finally, I will present preliminary results and provide an outlook for future experiments.

7.1 Theory Introduction

The circuit model for quantum computation [6] is a direct quantum generalization of the classical construct. In the ideal implementation of this framework, in the absence of quantum error correction, unitary operations are the primary mechanism for quantum information processing, and only at the end, measurements are used to convert quantum information into classical answers [156].
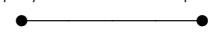
Measurement-based quantum computing (MBQC) is conceptually and practically a different paradigm for quantum computation. Although it has been demonstrated that it has equivalent computational power to the circuit model [157], it does not have a classical analog. Rather than a sequence of quantum gates, information is manipulated by a series of adaptive measurements on an entangled state of qubits. There exist two prominent examples of MBQC: the *one-way quantum computer* [158, 157] and the *teleportation-based* model [159, 160]. The latter follows an approach similar to the qubit teleportation protocol [161], where Bell state measurements are adaptively applied in a rotated Bell basis [156]; in the one-way model, universal computation is instead achieved only with single-qubit measurements. The one-way computing model is the most studied approach both theoretically and experimentally, and it became a synonym of MBQC. Within this model, the system is first prepared in an entangled quantum state, called cluster state or graph state (see later) [157]. The sequence of single-qubit measurements performed on different bases on the entangled resource state then specifies the algorithm, and gives the results [162]. To obtain the correct result, the basis for the next measurement is chosen conditionally on the previous measurement outcome. The term "one-way", reflects the fact that the graph state can only be used once, and that the computation can only be driven forward, in contrast to the reversibility of the gates in the ideal implementation of the circuit model.

Mathematically a graph state is simply a pair $\{V, E\}$ of vertices V, and their connections E. For an intuitive picture, we can imagine a vertex as a point in space, while an edge is as an arc connecting two vertices[1]. In MBQC, every vertex is associated with a qubit in state

$$|+\rangle = \frac{1}{\sqrt{2}}(|\downarrow\rangle + |\uparrow\rangle) \tag{7.1}$$

---

[1]In general vertices can be self-connected. However this case is not taken into account for applications in MBQC

and an edge is created by applying a *controlled-phase* gate (CZ) between two vertices initialized in $|+\rangle$.

$$CZ = \begin{pmatrix} 1 & 0 & 0 & 0 \\ 0 & 1 & 0 & 0 \\ 0 & 0 & 1 & 0 \\ 0 & 0 & 0 & -1 \end{pmatrix}, \quad |+\rangle \quad CZ \quad |+\rangle$$

In mathematical terms, given an ensemble of edges E connecting the qubit pair $\{i,j\}$, the graph state can be written as

$$|G\rangle = \prod_{\{i,j\}\in E} C_Z^{(i,j)} |+\rangle^{\otimes V} \tag{7.2}$$

where V is the total number of vertices.

Cluster states are a particular subset of graph states, where edges are limited to nearest neighbors. As a result, we can picture them as a d-dimensional square lattice, where each point (vertex) is connected only to its nearest neighbors (edges). In MBQC, cluster states are particularly important because it has been proven that an arbitrary quantum state can be generated on a sufficiently large 2D-cluster state, and therefore, any quantum operation [158, 163]. Finally, 3D-cluster states have been theoretically proposed for fault-tolerant quantum computation [164]. More recently, MBQC has been used to quantitatively compare the outputs of quantum circuits with different size and structure, performed on different quantum computing architectures, like NMR, superconducting devices, trapped-ion processors and photonic cluster states [165].

Initial demonstrations of MBQC have been realized in photonic systems [166] also with adaptive measurements [167]. However, the cluster states' creation is non-deterministic; scaling up these methods is then very challenging since the success probability reduces exponentially with the photon-qubit number required for the cluster state. Deterministic creation of large cluster states has been demonstrated with neutral atoms [168] and with continuous variable optical fields [169]. Experiments with trapped ions [170] demonstrated deterministic creation of cluster states and the principles of MBQC, but making use of post-processing instead of adaptive measurements. The implementation of MBQC proposed and demonstrated in this thesis makes use of the feedforward capabilities of the control system to perform adaptive measurements, as well as the ability of deterministically generate entanglement on a mixed-species ion-chain. As opposed to standard MBQC, we do not start from a large cluster state, but we create "edge" entanglement on demand when needed. In particular, we show preliminary results on the deterministic realization of arbitrary single-qubit unitaries within the MBQC formalism and provide a scheme for realizing arbitrary two-qubit gates in the near future. The approach goes in the direction of a hybrid architecture that combines the modular structure of the circuit model and the MBQC paradigm, as discussed in [171]. There, the authors propose schemes for quantum error correction and logical operations on encoded qubits, using graph states of minimal size as building blocks for quantum computation.

One other reason for doing this experiment is that it requires technical advancements in our setup, such as automatic calibrations of gates, mixed-species transport and splitting/recombination, and the ability to work with ion trapped in multiple zones. Having all those elements under control would require successful implementation of all these technical features in the current experimental setup, and demonstrate an advanced toolbox for QIP.

7.1.1   Notation

Before deriving unitary operations in the MBQC formalism, I will introduce some standard gate sequences for one and two-qubits as well as the notation I will use in the next sections.

One of the most useful single-qubit gate is the *Hadamard* gate H, whose effect is to turn the state $|\downarrow\rangle \to |+\rangle = (|\downarrow\rangle + |\uparrow\rangle)/\sqrt{2}$ and $|\uparrow\rangle \to |-\rangle = (|\downarrow\rangle - |\uparrow\rangle)/\sqrt{2}$ [6]. Its matrix and circuit representation is

$$H = \begin{pmatrix} 1 & 1 \\ 1 & -1 \end{pmatrix}, \quad \boxed{H}$$

The prototypical entangling operation acting on two qubits is the $CNOT$ gate. It has two input qubits, the *control* and *target* qubit. In terms of the computational basis, the $CNOT$ gate flips the state of the target qubit if the control qubit is in state $|\uparrow\rangle$. Its matrix and circuit representations are

$$CNOT = \begin{pmatrix} 1 & 0 & 0 & 0 \\ 0 & 1 & 0 & 0 \\ 0 & 0 & 0 & 1 \\ 0 & 0 & 1 & 0 \end{pmatrix}, \qquad \begin{array}{l} |\text{control}\rangle \\ |\text{target}\rangle \end{array}$$

Other single-qubit operations which will be used extensively in this chapter are the rotation operators about the $\hat{x}, \hat{y}, \hat{z}$ axes, defined by the Pauli matrices. In particular we can write:

$$\begin{aligned} R_X(\theta) &= \exp\left(-i\frac{\theta}{2}\hat{\sigma}_x\right) = \begin{pmatrix} \cos(\theta/2) & -i\sin(\theta/2) \\ -i\sin(\theta/2) & \cos(\theta/2) \end{pmatrix} = R(\theta, 0) \\ R_Y(\theta) &= \exp\left(-i\frac{\theta}{2}\hat{\sigma}_y\right) = \begin{pmatrix} \cos(\theta/2) & -\sin(\theta/2) \\ \sin(\theta/2) & \cos(\theta/2) \end{pmatrix} = R\left(\theta, -\frac{\pi}{2}\right) \\ R_Z(\theta) &= \exp\left(-i\frac{\theta}{2}\hat{\sigma}_z\right) = \begin{pmatrix} \exp(-i\theta/2) & 0 \\ 0 & \exp(i\theta/2) \end{pmatrix} \end{aligned} \qquad (7.3)$$

where $R(\theta, \phi)$ is defined in Equation 2.24.

7.1.2   Single-qubit unitary operations

To better understand the role of measurement and entanglement in the one-way computing paradigm, I will derive the construction of a single-qubit unitary gate step by step. In this process, I will first derive it in the circuit model representation, and then I will show how this is usually represented in the MBQC paradigm.

Let's begin by considering the simple circuit for the one-qubit teleportation [172], in which we desire to teleport the state $|\psi\rangle = \alpha |\downarrow\rangle + \beta |\uparrow\rangle$ of one qubit to a second qubit initialized in $|\downarrow\rangle$.
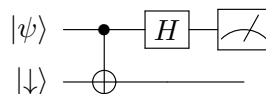
Before the measurement in the computational basis, the state of the two qubits is $|\downarrow\rangle (\alpha |\downarrow\rangle + \beta |\uparrow\rangle) + |\uparrow\rangle (\alpha |\downarrow\rangle - \beta |\uparrow\rangle)$. The measurement will then collapse the state of the second qubit into $(\alpha |\downarrow\rangle + \beta |\uparrow\rangle)$ or $(\alpha |\downarrow\rangle - \beta |\uparrow\rangle)$ with equal probability. To retrieve the initial state $|\psi\rangle$,

we would then need to apply a $Z = \hat{\sigma}_z$ Pauli rotation on the second qubit, conditional on the measurement outcome. To set the notation, we can write this operation as
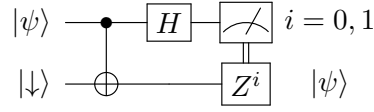
where $i = 0$ ($i = 1$) corresponds to projecting the measured qubit in $|\downarrow\rangle$($|\uparrow\rangle$).

In the MBQC formalism, the preferred gate operation is the controlled-phase gate (CZ). With the following circuit identity,
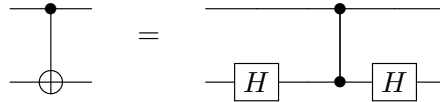
we can rewrite the one-qubit teleportation scheme as
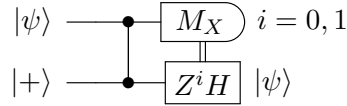
where we absorbed the Hadamard operations in the state preparation of the ancilla qubit and in the measurement basis of the first one. In the circuit above, M_X is the measurement along the X basis and for conciseness
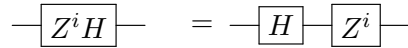
Imagine now the case in which a qubit rotation $R_Z(\alpha)$ is applied to the first qubit. This will transform the output state as
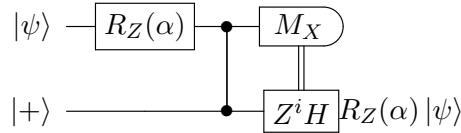
Note that the R_Z rotation can be pushed after the CZ operation since they commute, $[R_Z(\alpha), CZ] = 0$. The rotation $R_Z(\alpha)$ can be then absorbed in the measurement basis. The new rotated measurement basis is $M_\alpha = \cos(\alpha)X + \sin(\alpha)Y$. The circuit can be rewritten as:
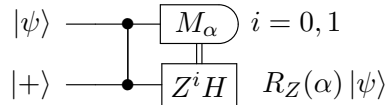
The last circuit gives a way to teleport a single qubit gate. In particular, we see that measuring the first qubit in the $\{|\alpha\rangle, |-\alpha\rangle\}$ basis effectively results in applying a $R_Z(\alpha)$ operation to the teleported state.

There are two main differences between this circuit and the one used in the MBQC formalism. The first is that the initial state is not $|\psi\rangle$ but $|+\rangle$. The second is that the final Hadamard gate in the second qubit line is not directly applied but absorbed in the final state. In particular we can write
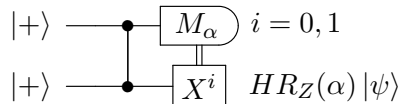
This scheme can then be generalized to the realization of an arbitrary single-qubit unitary operation, which can be written as $U = R_Z(\gamma)R_X(\beta)R_Z(\alpha)$. The following circuit provides a way to realize such gate
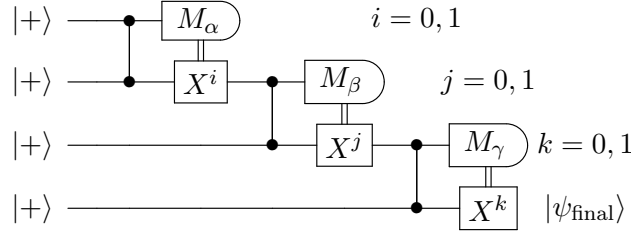
The final state $|\psi_{\text{final}}\rangle$ can then be written as

$$|\psi_{\text{final}}\rangle = X^k H R_Z(\gamma) X^j H R_Z(\beta) X^i H R_Z(\alpha) |+\rangle, \tag{7.4}$$

where we have explicitly included the conditional operations.

To show that $|\psi_{\text{final}}\rangle$ is indeed the state that we want, we need to apply some permutations. In particular, we would like to shift all the R_z rotations to the right, and all other operations to the left. For this, we need a set of equations that are easy to verify:

$$\begin{aligned} HZ^i &= X^i H \\ XZ &= -ZX \\ R_Z(\beta)X &= XR_Z(-\beta) \\ HR_Z(\beta)H &= R_X(\beta). \end{aligned} \tag{7.5}$$

One can now show that

$$|\psi_{\text{final}}\rangle = X^k Z^j X^i H R_Z\left((-1)^j\gamma\right) R_X\left((-1)^i\beta\right) R_Z\left(\alpha\right)|+\rangle \tag{7.6}$$

This means that with adaptive measurements, one can realize the general single qubit operation $U = R_Z(\gamma)R_X(\beta)R_Z(\alpha)$. This final statement could be written in the MBQC formalism in the following way

Here a cluster state of 4 qubits is measured sequentially from left to right. The angle of the measurement basis is adaptively changed depending on the previous outcome (the arrows symbolize the conditionality). On the right side of the equivalence it is given the unitary operation in the circuit model.

7.1.3 Two-qubit gates

For universal quantum computation, we require entangling two-qubit gates on top of arbitrary single-qubit unitaries. One of those gates is the CZ gate. In the MBQC framework, this gate is trivial because it is a native gate required for the creation of graph-state edges.

An example pattern in the MBQC formalism, with the equivalent circuit, is given by
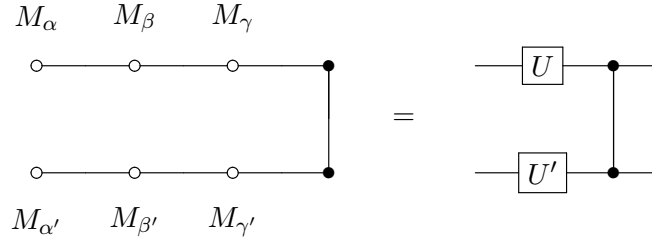
Notice that the input and output states of the CZ gate are the same (i.e. there is no measurement involved)

7.2 Experiment design

To experimentally realize a general single-qubit unitary operation, we would like to minimize the number of resources required. From the circuit representations described above, we notice two things: first, once a qubit is measured, it is not involved anymore in the computation; second, that it is not strictly necessary to start with a four-qubit cluster state. Indeed, it is possible to work on a two-qubit cluster state and build entanglement only when required. It follows that the circuits above can be written as
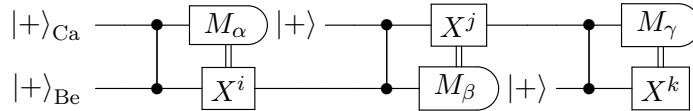
where we only use two qubits, and after a qubit has been measured, its state is re-initialized for the next measurement round.

In our setup, this circuit could be easily implemented with a calcium-beryllium crystal, where calcium is the top qubit and beryllium the lower one. The short coherence time of the calcium ion (Section 2.5), make it preferable to always keep beryllium as the data qubit and calcium as the ancilla, that is repetitively measured. This can be achieved by adding a SWAP operation at the beginning of the second measurement block. This particular circuit block could be rewritten as
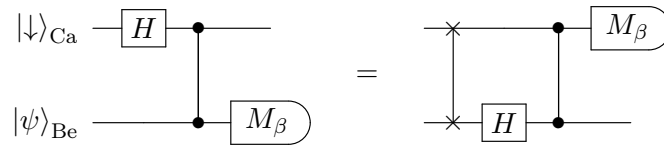
where we explicitly decomposed the calcium state preparation into state $|+\rangle_{\mathrm{Ca}}$ as $|+\rangle_{\mathrm{Ca}} = H |\downarrow\rangle_{\mathrm{Ca}}$. Using the following circuit identity for the SWAP gate
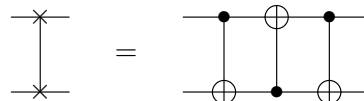
one can show that the final circuit reads
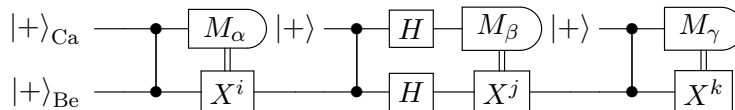
7.2.1 Compiling the protocol

The circuit found in the previous section can then be compiled to the native set of gate for trapped ions using the following circuit identities:
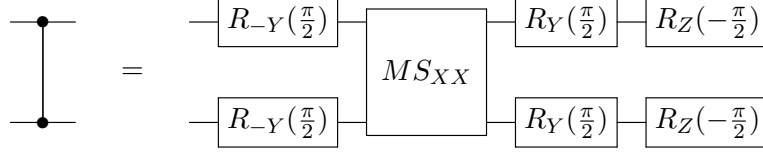
and
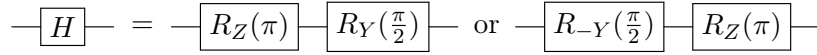
For the gate compilation, It is important to remember that the beryllium qubit, when initialized in the FIQ manifold, is in state $|\uparrow\rangle$. This assumption ensures that the definition of the rotation matrices given in Section 2.3 is the same for both calcium and beryllium qubits.

The first step of the MBQC sequence then reads
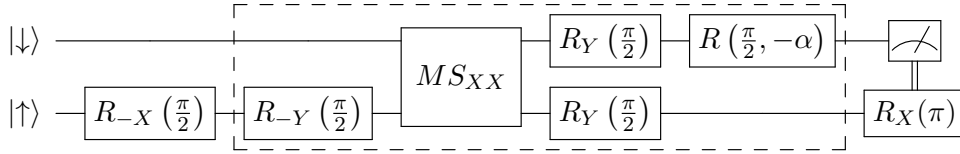
Similarly to the experiments performed in Chapter 6, the dashed box represent a block of pulses whose DDS phase accumulator is referenced to the starting time of first pulse within the box. The beryllium pulses that lie within the box are then driven with the motion-sensitive Raman configuration, while the ones outside are driven using the motion-insensitive Raman beams.

With a similar approach, we can write the second MBQC step as
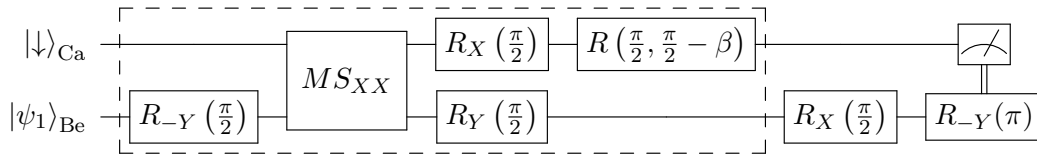
and the third as
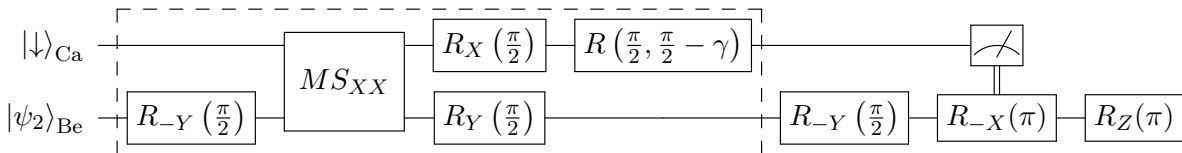
By applying the proper commutation relations, the single-qubit R_z rotations have been either shifted at the very beginning of the sequence or at the very end. The final state is:

$$|\psi_F\rangle = R_Z(\pi)HR_Z(\gamma)R_X(\beta)R_Z(\alpha)|+\rangle = R_Z(\pi)HU|+\rangle \tag{7.7}$$
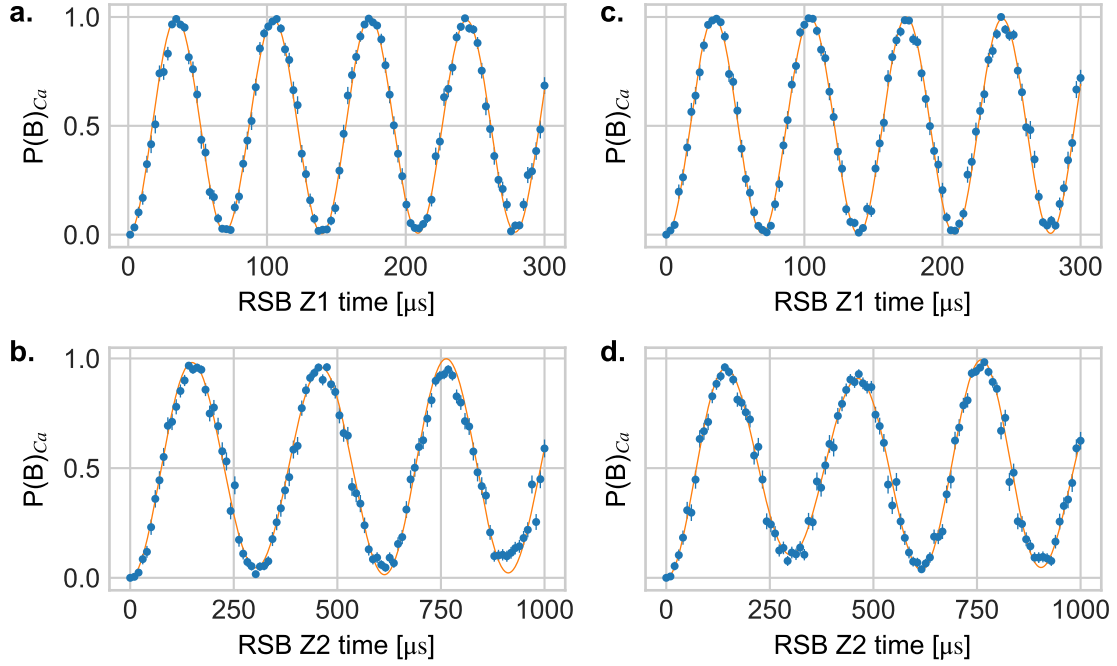
Figure 7.1: Calcium red sideband Rabi oscillations after a carrier π pulse realized in a beryllium-calcium ion chain. The plots on the left (panels **a** and **b**) are for the oscillations taken on the axial $Z1$ and $Z2$ modes (Section 2.8.1) right after initial cooling (see Section 2.8.2), those on the right (panels **c** and **d**) are taken after a calcium detection followed by one cycle of sympathetic recooling with calcium lasers. The recooling sequence consists of two consecutive bursts of EIT cooling (600 µs and 400 µs), respectively optimized for cooling the lowest frequency radial mode and the out-of-phase axial mode. The sequence is concluded with calcium sideband cooling on the in-phase axial mode and calcium state preparation. The populations are fitted according to Equation 2.38, to extract the motional occupancy of each mode. Right after the initial cooling we fit $\bar{n}_{Z1} = 0.015(4)$ and $\bar{n}_{Z2} = 0.055(9)$ for the in-phase and out-of-phase axial modes. After sympathetic recooling, we measure $\bar{n}_{Z1} = 0.008(4)$ and $\bar{n}_{Z2} = 0.13(1)$.

7.3 Preliminary results

This experiment has been the test bench for the new programming interface that makes use of the crystal classes and the phase accumulators discussed in Chapter 4 . Unlike the stabilizer experiments of Chapter 6, the frequency of the carrier pulses is calibrated to be on resonance with the Stark-shifted qubit frequency to achieve the highest gate fidelity. The exact value of carrier Stark shifts are measured using the technique discussed in Section 5.1.2, and with the phase accumulators, we pre-calculate the phase offset that should be applied to all pulses. For the preliminary results presented here, we only take into account the carrier Stark shift induced by the resonant beams that drive the transition. In other words, we do not account for the Stark shift of the calcium carrier frequency induced by the beryllium carrier pulses. However, for the pulse sequence described above, we do not expect a significant effect on the result, especially if we apply all calcium carrier rotations right after the MS gate and before the beryllium ones.

The Stark shifts induced by bichromatic beams during MS gates are manually calibrated when performing parity scans. In particular, we measure the phase offset between the parity

evolution in the ideal case compared to the one we experimentally measure. This method takes into account the Stark effect felt by the calcium ion due to the beryllium bichromatic beams.

After each calcium measurement, we sympathetically recool the crystal using just the calcium cooling beams, to not worsen the performance of the mixed-species gate. The calcium 397 nm detection beams are red detuned by $\approx 2\pi \times 3$ MHz from resonance to provide some Doppler-cooling during detection. The lowest frequency radial mode of motion is then recooled with a burst of EIT cooling lasting for 600 µs, followed by another EIT pulse of 400 µs optimized to cool the axial out-of-phase mode. Finally, 20 loops of calcium sideband cooling on the axial in-phase mode conclude the re-cooling sequence. Compared to the experiments presented in Chapter 6, the re-cooling operation takes longer. We think that the main cause is the detuning of the calcium 397 nm detection beam, which, for the experiments in Chapter 6 was $\approx 2\pi \times 8$ MHz red detuned from resonance. With this detuning we expect that Doppler cooling during detection is more effective. For the final experiments we will further detune the calcium 397 nm detection beam and reduce the re-cooling times.

We check the quality of the re-cooling by comparing the blue sideband Rabi oscillations on the axial in-phase (Z1) and out-of-phase (Z2) modes right after the initial cooling (see Section 2.8.2) and after a calcium detection followed by a single re-cooling round, as shown in Figure 7.1. A fit of Equation 2.38 to the data points, assuming a thermal distribution, allows extracting the average motional occupancy of each mode. Right after the initial cooling the measured $\bar{n}$ are $\bar{n}_{IP} = 0.015(4)$ and $\bar{n}_{OOP} = 0.055(9)$ for the in-phase and out-of-phase modes respectively. After a calcium detection and one round of sympathetic re-cooling, we measure $\bar{n}_{IP} = 0.008(4)$ and $\bar{n}_{OOP} = 0.13(1)$, which are good enough to not worsen the MS gate fidelity. It would anyway be possible to better cool the axial out-of-phase mode by running a few cycles of calcium sideband cooling on this mode before the final sideband cooling of the axial in-phase mode.

We then test the correctness of the circuit construction by realizing an arbitrary unitary operation $U(\alpha, \beta, \gamma) = R_Z(\gamma) R_X(\beta) R_Z(\alpha)$. Figure 7.2a shows the experimental realization of $U(\alpha, 0, 0)$. The trace is compared with the theoretical prediction using Equation 7.7 (Figure 7.2b). The measured contrast is 89(1)% and is consistent with the mixed-species MS gate fidelity of $\approx 97\%$ that was measured when these results were taken. More interestingly, we notice a phase offset of 16.2(8) degrees from what we would expect from simulations. This is consistent with a $1 - 2\%$ miscalibration of the co-carrier Stark shift frequency in beryllium.

7.4   Outlook

The experimental results shown in the previous section are just preliminary and require improvements of the MS gate fidelities to the levels reported in Chapter 5. It would also be interesting to perform a full process tomography of the single-qubit unitary operation to characterize the sequence better.

For future experiments, it would be exciting to realize an arbitrary two-qubit gate. For
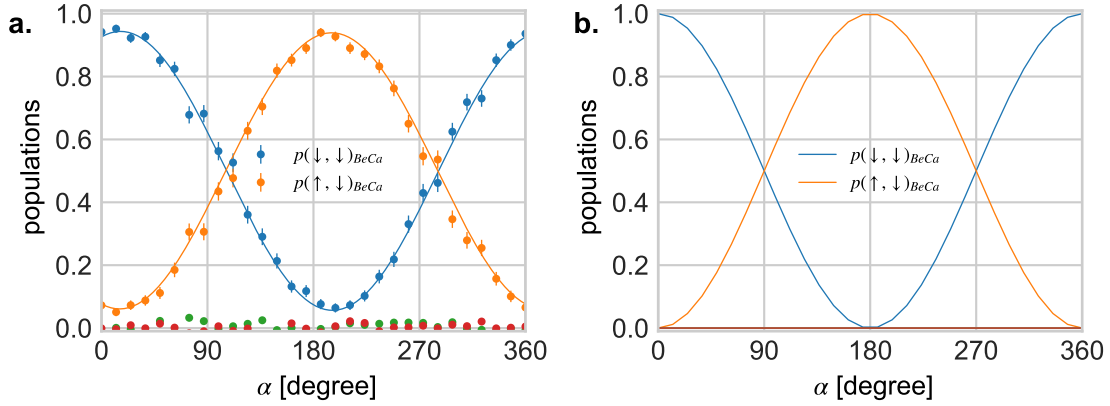
Figure 7.2: Comparison between experimental data (panel **a.**) and ideal theoretical expectation (panel **b**) for the realization fo the single-qubit unitary operation $U(\alpha, \beta, \gamma) = U(\alpha, 0, 0)$ applied on $|+\rangle$. In panel **a**, the solid lines are fits to the experimental data.The fitted contrast of the oscillations is $89(1)\%$, which is consistent with the measured MS gate fidelity of $\sim 97\%$. The phase offset ($16.2(8)$ degrees) is compatible with a $1 - 2\%$ miscalibration of the co-carrier frequency. These data are just preliminary.

the realization of the sequence[2]
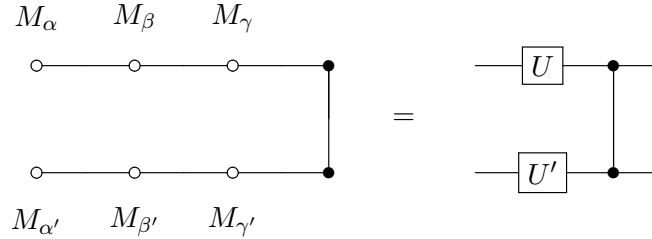
a minimum number of four ions are required (two beryllium and two calcium ions). A potential implementation would start with the four ions in a single potential well for cooling and state preparation in the calcium-beryllium-calcium-beryllium configuration. A splitting operation would then separate the chain into two smaller chains of calcium-beryllium. Following the protocol described in Section 7.2.1, we could then realize the gates U and U'. Having two pairs in the same configuration ensures that the motional frequency and beam alignment are the same, thus reducing the number of parameters that need to be calibrated. This motivates the choice of the initial four-ion chain configuration. For the final CZ operation, one possibility would be to create a beryllium-calcium-beryllium chain and apply a CZ gate on the two beryllium ions, using calcium for recooling. For this to work, the splitting/recombination operation should not heat the axial STR mode of the three ion chain. As briefly mentioned in Section 6.6, one possibility of cooling the STR mode would be to deform the ion crystal into a triangular shape by compressing the crystal axially. In this configuration, the Coulomb forces of the two outside ions stretching do not cancel out anymore, because the radial component adds up. As a result, it should be possible to sympathetically cool all the modes with a calcium ion.

---

[2]A general two-qubit gate requires a minimum of three CZ gates and three single-qubit operations as discussed in [173].

One other potential implementation of a general two-qubit gate would be to work with a symmetric beryllium-calcium-calcium-beryllium ion chain. The ordering procedure of the ions in this configuration is similar to what described in Section 4.3.1. The single qubit unitary gates could be implemented in the beryllium-calcium and calcium-beryllium sub-chains. The ions would then be recombined in the initial configuration to perform the two-qubit beryllium CZ gate. The difficulty of this implementation is in the number of parameters. Carrier Stark shifts and motional frequencies will likely be different for the two sub-chains due to the different position of the ions with respect to the laser beams and due to anharmonicities and pseudo-potential gradient (see Section 5.2.1). However, it would be possible to use scripting to automatically calibrate all parameters as discussed in Section 4.1.3.

In both cases, the experiment requires controlled splitting and recombination of arbitrary mixed-species chains and the control of multiple wells. It would also require a detailed characterization of the magnetic field homogeneity along the trap. This sequence would then exploit even more features of the segtrap experiment. It would also enable the realization of more complicated experiments, such as the simulation of physical phenomena [174, 175].

8 Conclusions and outlooks

The long term vision behind the work described in this thesis is the QCCD architecture [27] as a pathway for a scalable quantum processor based on trapped-ion technology. Within this thesis, I summarized the main features of the experimental setup and introduced the concepts for the control of mixed-species ion chains. I hope to have convinced the reader that mixed-species ion chains could be beneficial for scalable QIP experiments with trapped ions.

We used the high degree of spectral separation of calcium and beryllium ions to experimentally demonstrate quantum protocols that use mixed-species and feedback as key elements. The two main examples described are the repeated stabilizer measurements and the realization of general single-qubit unitaries in the measurement-based quantum computing paradigm. In the first experiment (Chapter 6), we demonstrated a protocol for the repeated measurement (up to 50 measurement rounds) of the parity of two beryllium ions by detection of a co-trapped calcium ion. We used the calcium readout information contained to feed back on the system and stabilize parity subspaces. With similar techniques we also deterministically prepared and stabilized Bell states. The methods used to perform this experiment could be used for stabilizer readouts in quantum error correction and metrology. The other experiment discussed in Chapter 7, used a calcium-beryllium ion chain to realize a general single qubit operation in the MBQC formalism. In this framework, operations are realized by sequential adaptive measurements on an entangled state. As opposed to standard MBQC, we create entanglement when needed to reduce the number of resources. We make use of the feedforward ability of our control system to show the deterministic implementation of an arbitrary single-qubit gate using adaptive measurements.

Future experiments will involve the manipulation of multiple crystals of different types whose structure is continuously reconfigured through transport and splitting/recombination. For this reason, in this thesis we also described a flexible interface that simplifies the writing and the calibration of such experiments. The main idea is to mimic the physical setup giving a C++ code representation of an ion crystal. Each crystal object contains information about the ion chain composition and all possible experimental sequences to manipulate that particular configuration of ions. An experiment then simply becomes a sequence of function calls on specific instances of crystal objects, interleaved by transport and splitting/recombination operations. The main features of this new interface have been tested and exploited in the experiments described in Chapter 7. Future developments of the experiment interface should go in the direction of further automation. This includes improvements of the automatic calibration of experimental parameters (for example using Bayesian schemes [61, 90]), but also a high-level interface capable of compiling QIP algorithms in experimental code that could be run by our control system.

In the spirit of the QCCD architecture we also explored the ability to transport and split/recombine mixed-species ion chains. We discussed experimental results of the splitting of chains composed of two ions of the same species. We showed average axial excitations after splitting below 1.6 quanta of motion for calcium and below 0.7 quanta for beryllium. At the time of writing, mixed-species splitting is not reliable. A careful characterization of

the trap electrode moments will likely give insight into the mixed-species separations issues.

Once we will be able to transport and split/recombine arbitrary mixed-species crystals, this would add to the toolbox that we have available, and allow more complex experiments to be realized using the current experimental setup. Examples of those experiments can be found in the outlook section of Chapter 6 and Chapter 7.

Finally, this thesis also provided a detailed analysis of ion readout in the presence of leakage mechanisms that alter the qubit population during detection. In this regard, we introduced readout techniques based on the arrival time of photons and provided experimental results . Those methods make use of the unique abilities of our classical control system to perform floating-point calculations in real time and consequently alter the pulse sequence. We showed how to reduce the detection time by approximately a factor of 3 without reducing the readout fidelity, and we also introduced a new technique, based on entropy gain, that could further reduce the detection time. These techniques could be beneficial for a large scale quantum computer based on trapped-ions.

This concludes my thesis; I hope that the reader has found it useful and informative. I also hope that the techniques developed withing this thesis will contribute to reach the goal of a hybrid universal quantum computer based on trapped ions.

Bibliography

[1] A. Turing. "On computable numbers, with an application to the entscheidungsproblem". In: *Proceedings of the London Mathematical Society* 2.42 (1936), pp. 230–65. DOI: doi:10.1112/plms/s2-42.1.230 (cit. on p. 1).

[2] D. Deutsch. "Quantum theory, the Church–Turing principle and the universal quantum computer". In: *Proceedings of the Royal Society of London. A. Mathematical and Physical Sciences* 400.1818 (8th July 1985), pp. 97–117. DOI: 10.1098/rspa.1985.0070 (cit. on p. 1).

[3] C. E. Shannon. "A mathematical theory of communication". In: *The Bell System Technical Journal* 27.3 (July 1948). Conference Name: The Bell System Technical Journal, pp. 379–423. DOI: 10.1002/j.1538-7305.1948.tb01338.x (cit. on p. 1).

[4] R. P. Feynman. "Simulating physics with computers". In: *International Journal of Theoretical Physics* 21 (1982), pp. 467–488. DOI: https://doi.org/10.1007/BF02650179 (cit. on p. 1).

[5] I. M. Georgescu, S. Ashhab and F. Nori. "Quantum Simulation". In: *Reviews of Modern Physics* 86.1 (Mar. 2014), pp. 153–185. DOI: 10.1103/RevModPhys.86.153 (cit. on pp. 1, 2).

[6] M. A. Nielsen and I. L. Chuang. *Quantum Computation and Quantum Information*. Cambridge University Press, Oct. 2000 (cit. on pp. 1, 4, 83, 95, 96, 106, 114, 116).

[7] J. Zeng, R.-Q. Zhang and H. Treutlein, eds. *Quantum Simulations of Materials and Biological Systems*. Springer Netherlands, 2012. DOI: 10.1007/978-94-007-4948-1 (cit. on p. 2).

[8] M. Reiher et al. "Elucidating reaction mechanisms on quantum computers". In: *Proceedings of the National Academy of Sciences* 114.29 (18th July 2017), pp. 7555–7560. DOI: 10.1073/pnas.1619152114 (cit. on p. 2).

[9] J. R. McClean et al. "The theory of variational hybrid quantum-classical algorithms". In: *New Journal of Physics* 18.2 (4th Feb. 2016), p. 023023. DOI: 10.1088/1367-2630/18/2/023023 (cit. on p. 2).

[10] C. Hempel et al. "Quantum Chemistry Calculations on a Trapped-Ion Quantum Simulator". In: *Physical Review X* 8.3 (24th July 2018), p. 031022. DOI: 10.1103/PhysRevX.8.031022 (cit. on p. 2).

[11] P. W. Shor. "Polynomial-Time Algorithms for Prime Factorization and Discrete Logarithms on a Quantum Computer". In: *SIAM J. Sci. Statist. Comput.* 26.1484 (1997). DOI: 10.1137/S0097539795293172 (cit. on p. 2).

[12] A. W. Harrow, A. Hassidim and S. Lloyd. "Quantum Algorithm for Linear Systems of Equations". In: *Physical Review Letters* 103.15 (Oct. 2009), p. 150502. DOI: 10.1103/PhysRevLett.103.150502 (cit. on p. 2).

[13] L. K. Grover. "From Schrödinger's Equation to the Quantum Search Algorithm". In: *Pramana* 56.2 (Feb. 2001), pp. 333–348. DOI: 10.1007/s12043-001-0128-3 (cit. on p. 2).

[14]   D. P. DiVincenzo. "The Physical Implementation of Quantum Computation". In: *Fortschritte der Physik* 48.1 (Feb. 2000), pp. 771–783 (cit. on p. 2).

[15]   M. H. Devoret and R. J. Schoelkopf. "Superconducting Circuits for Quantum Information: An Outlook". In: *Science* 339.6124 (Mar. 2013), pp. 1169–1174. DOI: 10.1126/science.1231930 (cit. on p. 2).

[16]   J. M. Gambetta, J. M. Chow and M. Steffen. "Building Logical Qubits in a Superconducting Quantum Computing System". In: *npj Quantum Information* 3.1 (Jan. 2017), p. 2. DOI: 10.1038/s41534-016-0004-0 (cit. on p. 2).

[17]   D. J. Wineland et al. "Quantum Information Processing with Trapped Ions". In: *Philosophical Transactions of the Royal Society of London A: Mathematical, Physical and Engineering Sciences* 361.1808 (July 2003), pp. 1349–1361. DOI: 10.1098/rsta.2003.1205 (cit. on p. 2).

[18]   H. Haeffner, C. F. Roos and R. Blatt. "Quantum Computing with Trapped Ions". In: *Physics Reports* 469.4 (Sept. 2008), pp. 155–203. DOI: 10.1016/j.physrep.2008.09.003 (cit. on pp. 2, 20).

[19]   C. Monroe and J. Kim. "Scaling the Ion Trap Quantum Processor". In: *Science* 339.6124 (Aug. 2013), pp. 1164–1169. DOI: 10.1126/science.1231298 (cit. on pp. 2, 3).

[20]   F. G. Major, V. N. Gheorghe and G. Werth. *Charged Particle Traps: Physics and Techniques of Charged Particle Field Confinement*. Springer Series on Atomic, Optical, and Plasma Physics. Berlin Heidelberg: Springer-Verlag, 2005 (cit. on p. 2).

[21]   W. Paul. "Electromagnetic Traps for Charged and Neutral Particles". In: *Reviews of Modern Physics* 62.3 (July 1990), pp. 531–540. DOI: 10.1103/RevModPhys.62.531 (cit. on pp. 2, 7).

[22]   J. Bollinger et al. "A 303-MHz frequency standard based on trapped Be+ ions". In: *IEEE Transactions on Instrumentation and Measurement* 40.2 (Apr. 1991). Conference Name: IEEE Transactions on Instrumentation and Measurement, pp. 126–128. DOI: 10.1109/TIM.1990.1032897 (cit. on p. 2).

[23]   Y. Wang et al. "Single-qubit quantum memory exceeding ten-minute coherence time". In: *Nature Photonics* 11.10 (Oct. 2017), pp. 646–650. DOI: 10.1038/s41566-017-0007-1 (cit. on p. 2).

[24]   N. C. Brown and K. R. Brown. "Comparing Zeeman Qubits to Hyperfine Qubits in the Context of the Surface Code: ^{174}Yb$^+$ and ^{171}Yb$^+$". In: *Physical Review A* 97.5 (May 2018), p. 052301. DOI: 10.1103/PhysRevA.97.052301 (cit. on p. 2).

[25]   A. Sørensen and K. Mølmer. "Entanglement and Quantum Computation with Ions in Thermal Motion". In: *Physical Review A* 62.2 (July 2000), p. 022311. DOI: 10.1103/PhysRevA.62.022311 (cit. on pp. 3, 82, 84, 92).

[26]   D. J. Wineland et al. "Experimental Issues in Coherent Quantum-State Manipulation of Trapped Atomic Ions". In: *Journal of Research of the National Institute of Standards and Technology* 103.3 (May 1998), p. 259 (cit. on pp. 3, 7, 13, 58).

[27]   D. Kielpinski, C. Monroe and D. J. Wineland. "Architecture for a Large-Scale Ion-Trap Quantum Computer". In: *Nature* 417.6890 (June 2002), pp. 709–711. DOI: 10.1038/nature00784 (cit. on pp. 3, 49, 58, 125).

[28] K. K. Mehta et al. "Integrated Optical Addressing of an Ion Qubit". In: *Nature Nanotechnology* 11.12 (Dec. 2016), pp. 1066–1070. DOI: 10.1038/nnano.2016.139 (cit. on p. 3).

[29] K. K. Mehta et al. "Integrated optical multi-ion quantum logic". In: *arXiv:2002.02258 [physics, physics:quant-ph]* (6th Feb. 2020). arXiv: 2002.02258 (cit. on p. 3).

[30] J. Stuart et al. "Chip-Integrated Voltage Sources for Control of Trapped Ions". In: *Physical Review Applied* 11.2 (5th Feb. 2019), p. 024010. DOI: 10.1103/PhysRevApplied.11.024010 (cit. on p. 3).

[31] C. Monroe et al. "Large-Scale Modular Quantum-Computer Architecture with Atomic Memory and Photonic Interconnects". In: *Physical Review A* 89.2 (Feb. 2014), p. 022317. DOI: 10.1103/PhysRevA.89.022317 (cit. on p. 3).

[32] N. H. Nickerson, J. F. Fitzsimons and S. C. Benjamin. "Freely Scalable Quantum Technologies Using Cells of 5-to-50 Qubits with Very Lossy and Noisy Photonic Links". In: *Physical Review X* 4.4 (Dec. 2014), p. 041041. DOI: 10.1103/PhysRevX.4.041041 (cit. on p. 3).

[33] L. J. Stephenson et al. "High-rate, high-fidelity entanglement of qubits across an elementary quantum network". In: *arXiv:1911.10841 [physics, physics:quant-ph]* (25th Nov. 2019). arXiv: 1911.10841 (cit. on p. 3).

[34] R. E. Drullinger, D. J. Wineland and J. C. Bergquist. "High-resolution optical spectra of laser cooled ions". In: *Applied Physics* 22.4 (Aug. 1980), pp. 365–368. DOI: 10.1007/BF00901058 (cit. on p. 3).

[35] D. J. Larson et al. "Sympathetic cooling of trapped ions: A laser-cooled two-species nonneutral ion plasma". In: *Physical Review Letters* 57.1 (7th July 1986), pp. 70–73. DOI: 10.1103/PhysRevLett.57.70 (cit. on p. 3).

[36] D. B. Hume, T. Rosenband and D. J. Wineland. "High-Fidelity Adaptive Qubit Detection through Repetitive Quantum Nondemolition Measurements". In: *Physical Review Letters* 99.12 (Sept. 2007), p. 120502. DOI: 10.1103/PhysRevLett.99.120502 (cit. on pp. 3, 41).

[37] C.-w. Chou et al. "Preparation and coherent manipulation of pure quantum states of a single molecular ion". In: *Nature* 545.7653 (May 2017), pp. 203–207. DOI: 10.1038/nature22338 (cit. on p. 3).

[38] P. O. Schmidt et al. "Spectroscopy Using Quantum Logic". In: *Science* 309.5735 (July 2005), pp. 749–752. DOI: 10.1126/science.1114375 (cit. on p. 3).

[39] Y. Lin et al. "Dissipative Production of a Maximally Entangled Steady State of Two Quantum Bits". In: *Nature* 504.7480 (Dec. 2013), pp. 415–418. DOI: 10.1038/nature12801 (cit. on p. 3).

[40] T. R. Tan et al. "Multi-Element Logic Gates for Trapped-Ion Qubits". In: *Nature* 528.7582 (Dec. 2015), pp. 380–383. DOI: 10.1038/nature16186 (cit. on pp. 3, 86).

[41] C. J. Ballance et al. "Hybrid Quantum Logic and a Test of Bell's Inequality Using Two Different Atomic Isotopes". In: *Nature* 528.7582 (Dec. 2015), pp. 384–386. DOI: 10.1038/nature16184 (cit. on p. 3).

[42] V. Negnevitsky et al. "Repeated multi-qubit readout and feedback with a mixed-species trapped-ion register". In: *Nature* 563.7732 (Nov. 2018), pp. 527–531. DOI: 10.1038/s41586-018-0668-z (cit. on pp. 3, 4, 95, 99, 102, 105, 106).

[43] Y. Wan et al. "Quantum gate teleportation between separated qubits in a trapped-ion processor". In: *Science* 364.6443 (31st May 2019), pp. 875–878. DOI: 10.1126/science.aaw9415 (cit. on p. 3).

[44] A. Steane. "The Ion Trap Quantum Information Processor". In: *Applied Physics B* 64.6 (June 1997), pp. 623–643. DOI: 10.1007/s003400050225 (cit. on p. 3).

[45] P. W. Shor. "Scheme for Reducing Decoherence in Quantum Computer Memory". In: *Physical Review A* 52.4 (Oct. 1995), R2493–R2496. DOI: 10.1103/PhysRevA.52.R2493 (cit. on pp. 3, 95).

[46] E. Knill et al. "Introduction to Quantum Error Correction". In: *arXiv:quant-ph/0207170* (July 2002). arXiv: quant-ph/0207170 (cit. on p. 4).

[47] D. Kienzler. "Quantum Harmonic Oscillator State Synthesis by Reservoir Engineering". Doctoral Thesis. ETH Zürich, 2015 (cit. on pp. 6, 19, 20, 23, 81, 87).

[48] H.-Y. Lo. "Creation of Squeezed Schrödinger's Cat States in a Mixed-Species Ion Trap". Doctoral Thesis. ETH Zürich, 2015 (cit. on pp. 6, 13, 15–17, 19, 20, 32, 38, 73, 91, 107).

[49] L. E. de Clercq. "Transport Quantum Logic Gates for Trapped Ions". Doctoral Thesis. ETH Zürich, 2015 (cit. on pp. 6, 50, 58, 59, 61, 62).

[50] D. Leibfried et al. "Quantum Dynamics of Single Trapped Ions". In: *Reviews of Modern Physics* 75.1 (Mar. 2003), pp. 281–324. DOI: 10.1103/RevModPhys.75.281 (cit. on pp. 7, 10, 22, 25, 27).

[51] J. P. Home. "Chapter 4 - Quantum Science and Metrology with Mixed-Species Ion Chains". In: *Advances In Atomic, Molecular, and Optical Physics*. Vol. Volume 62. Advances in Atomic, Molecular, and Optical Physics. Academic Press, 2013, pp. 231–277 (cit. on pp. 8, 9, 21, 22, 29, 68, 70, 71, 77, 78).

[52] P. Ghosh. *Ion traps*. Oxford Univeristy Press, 1995 (cit. on p. 9).

[53] C. Ospelkaus et al. "Microwave Quantum Logic Gates for Trapped Ions". In: *Nature* 476.7359 (Aug. 2011), pp. 181–184. DOI: 10.1038/nature10290 (cit. on p. 13).

[54] C. Monroe et al. "Demonstration of a Fundamental Quantum Logic Gate". In: *Physical Review Letters* 75.25 (Dec. 1995), pp. 4714–4717. DOI: 10.1103/PhysRevLett.75.4714 (cit. on p. 13).

[55] C. E. Langer. "High Fidelity Quantum Information Processing with Trapped Ions". Doctoral Thesis. University of Colorado, Boulder, 2006 (cit. on pp. 15, 36, 38, 39, 41).

[56] M. Acton et al. "Near-Perfect Simultaneous Measurement of a Qubit Register". In: *Quantum Info. Comput.* 6.6 (Sept. 2006), pp. 465–482 (cit. on p. 15).

[57] B. E. King. "Quantum State Engineering and In- formation Processing with Trapped Ions". PhD thesis. Univeristy of Colorado, 1999 (cit. on p. 15).

[58] A. H. Burrell. "High Fidelity Readout of Trapped Ion Qubits". PhD thesis. Oxford University, 2010 (cit. on pp. 15, 33, 36, 39, 42, 43).

[59] H. Uys et al. "Decoherence due to Elastic Rayleigh Scattering". In: *Physical Review Letters* 105.20 (8th Nov. 2010), p. 200401. DOI: 10.1103/PhysRevLett.105.200401 (cit. on p. 15).

[60] J. M. Amini et al. "Micro-Fabricated Chip Traps for Ions". In: *Atom Chips*. Wiley-Blackwell, 2011, pp. 395–420. DOI: 10.1002/9783527633357.ch13 (cit. on p. 16).

[61]   V. Negnevitsky. "Feedback stabilised quantum states in a mixed-species ion system". PhD thesis. ETH Zurich, 2018 (cit. on pp. 16, 49–51, 56, 59, 60, 62–65, 83, 86, 89, 95, 99, 104, 125).

[62]   A. C. Wilson et al. "A 750 mW, Continuous-Wave, Solid-State Laser Source at 313 Nm for Cooling and Manipulating Trapped 9Be+ Ions". In: *arXiv:1105.5356* (May 2011). arXiv: 1105.5356 (cit. on p. 17).

[63]   Y. Colombe et al. "Single-Mode Optical Fiber for High-Power, Low-Loss UV Transmission". In: *Optics Express* 22.16 (Aug. 2014), pp. 19783–19793. DOI: 10.1364/OE.22.019783 (cit. on p. 17).

[64]   S. C. Webster. "Raman sideband cooling and coherent manipulation of trapped ions," PhD thesis. Oxford University, 2005 (cit. on p. 18).

[65]   C. Flühmann et al. "Sequential Modular Position and Momentum Measurements of a Trapped Ion Mechanical Oscillator". In: *Physical Review X* 8.2 (Apr. 2018), p. 021001. DOI: 10.1103/PhysRevX.8.021001 (cit. on p. 18).

[66]   C. Flühmann. "Encoding a qubit in the motion of a trapped ion using superpositions of displaced squeezed states". PhD thesis. ETH Zürich, 2019 (cit. on pp. 19, 73, 81, 91).

[67]   D. Kienzler et al. "Quantum Harmonic Oscillator State Synthesis by Reservoir Engineering". In: *Science* 347.6217 (Jan. 2015), pp. 53–56. DOI: 10.1126/science.1261033 (cit. on p. 19).

[68]   D. Kienzler et al. "Observation of Quantum Interference between Separated Mechanical Oscillator Wave Packets". In: *Physical Review Letters* 116.14 (Apr. 2016), p. 140402. DOI: 10.1103/PhysRevLett.116.140402 (cit. on pp. 19, 73).

[69]   D. Kienzler et al. "Quantum Harmonic Oscillator State Control in a Squeezed Fock Basis". In: *Physical Review Letters* 119.3 (July 2017), p. 033602. DOI: 10.1103/PhysRevLett.119.033602 (cit. on p. 19).

[70]   H.-Y. Lo et al. "Spin-Motion Entanglement and State Diagnosis with Squeezed Oscillator Wavepackets". In: *Nature* 521.7552 (May 2015), pp. 336–339. DOI: 10.1038/nature14458 (cit. on p. 19).

[71]   C. Flühmann et al. "Encoding a qubit in a trapped-ion mechanical oscillator". In: *Nature* 566.7745 (Feb. 2019), pp. 513–517. DOI: 10.1038/s41586-019-0960-6 (cit. on p. 19).

[72]   D. J. Wineland et al. "Double-Resonance and Optical-Pumping Experiments on Electromagnetically Confined, Laser-Cooled Ions". In: *Optics Letters* 5.6 (June 1980), pp. 245–247. DOI: 10.1364/OL.5.000245 (cit. on p. 19).

[73]   D. J. Wineland and W. M. Itano. "Laser cooling of atoms". In: *Physical Review A* 20.4 (1st Oct. 1979), pp. 1521–1540. DOI: 10.1103/PhysRevA.20.1521 (cit. on pp. 21, 26).

[74]   R. Loudon. *The quantum theory of light.* Oxford science publications, 2000 (cit. on p. 21).

[75]   C. F. Roos et al. "Experimental Demonstration of Ground State Laser Cooling with Electromagnetically Induced Transparency". In: *Physical Review Letters* 85.26 (Dec. 2000), pp. 5547–5550. DOI: 10.1103/PhysRevLett.85.5547 (cit. on pp. 24, 25).

[76] G. Morigi, J. Eschner and C. H. Keitel. "Ground State Laser Cooling Using Electro-magnetically Induced Transparency". In: *Physical Review Letters* 85.21 (Nov. 2000), pp. 4458–4461. DOI: 10.1103/PhysRevLett.85.4458 (cit. on pp. 25, 26).

[77] H. R. Gray, R. M. Whitley and C. R. Stroud. "Coherent trapping of atomic populations". In: *Optics Letters* 3.6 (1978), p. 218. DOI: 10.1364/OL.3.000218 (cit. on p. 25).

[78] G. Janik, W. Nagourney and H. Dehmelt. "Doppler-free optical spectroscopy on the Ba mono-ion oscillator". In: *Journal of the Optical Society of America B* 2.8 (1985), p. 1251. DOI: 10.1364/JOSAB.2.001251 (cit. on p. 25).

[79] W. Nagourney, J. Sandberg and H. Dehmelt. "Shelved optical electron amplifier: Observation of quantum jumps". In: *Physical Review Letters* 56.26 (30th June 1986), pp. 2797–2799. DOI: 10.1103/PhysRevLett.56.2797 (cit. on p. 32).

[80] T. Sauter et al. "Observation of Quantum Jumps". In: *Physical Review Letters* 57.14 (6th Oct. 1986), pp. 1696–1698. DOI: 10.1103/PhysRevLett.57.1696 (cit. on p. 32).

[81] J. C. Bergquist et al. "Observation of Quantum Jumps in a Single Atom". In: *Physical Review Letters* 57.14 (6th Oct. 1986), pp. 1699–1702. DOI: 10.1103/PhysRevLett.57.1699 (cit. on p. 32).

[82] S. Debnath et al. "Demonstration of a Small Programmable Quantum Computer with Atomic Qubits". In: *Nature* 536.7614 (Aug. 2016), pp. 63–66. DOI: 10.1038/nature18648 (cit. on p. 33).

[83] J. Zhang et al. "Observation of a many-body dynamical phase transition with a 53-qubit quantum simulator". In: *Nature* 551.7682 (Nov. 2017), pp. 601–604. DOI: 10.1038/nature24654 (cit. on p. 33).

[84] J. P. Home. "Entanglement of Two Trapped-Ion Spin Qubits". Doctoral Thesis. Oxford University, 2006 (cit. on pp. 34, 73, 86).

[85] P. A. Barton et al. "Measurement of the Lifetime of the \[$D_{5/2}$\] State in calcium 40". In: *Physical Review A* 62.3 (Aug. 2000), p. 032503. DOI: 10.1103/PhysRevA.62.032503 (cit. on p. 38).

[86] D. R. Crick et al. "Magnetically induced electron shelving in a trapped Ca + ion". In: *Physical Review A* 81.5 (10th May 2010), p. 052503. DOI: 10.1103/PhysRevA.81.052503 (cit. on p. 40).

[87] J. Gambetta et al. "Protocols for optimal readout of qubits using a continuous quantum nondemolition measurement". In: *Physical Review A* 76.1 (24th July 2007), p. 012325. DOI: 10.1103/PhysRevA.76.012325 (cit. on p. 41).

[88] A. H. Myerson et al. "High-Fidelity Readout of Trapped-Ion Qubits". In: *Physical Review Letters* 100.20 (May 2008), p. 200502. DOI: 10.1103/PhysRevLett.100.200502 (cit. on p. 41).

[89] A. Lebedev. *Metrology Protocol Notes*. 2015 (cit. on p. 46).

[90] B. MacDonald-de Neeve. "Calibrating an Ion Trap Quantum Computer". Masters Thesis. ETH Zürich, 2017 (cit. on pp. 46, 125).

[91] F. Zhou et al. "Background-Free Doppler Cooling of Trapped Ions Using Quadrupole Transition". In: *Chinese Physics Letters* 30.3 (Mar. 2013), p. 033701. DOI: 10.1088/0256-307X/30/3/033701 (cit. on p. 47).

[92] F. Lindenfelser. "Broadband Cooling on a Forbidden Transition in a Novel High-Optical-Access Ion Trap". Doctoral Thesis. ETH Zürich, 2017 (cit. on pp. 47, 57).

[93] A. M. Steane. "Overhead and Noise Threshold of Fault-Tolerant Quantum Error Correction". In: *Physical Review A* 68.4 (Oct. 2003), p. 042322. DOI: 10.1103/PhysRevA.68.042322 (cit. on pp. 49, 95).

[94] C. F. Roos. "Ion Trap Quantum Gates with Amplitude-Modulated Laser Beams". In: *New Journal of Physics* 10.1 (Jan. 2008), p. 013002. DOI: 10.1088/1367-2630/10/1/013002 (cit. on pp. 50, 82).

[95] M. Stadler. "Title undecided". PhD thesis. ETH Zurich, 2023 (cit. on p. 50).

[96] D. Nadlinger. "Experimental Control and Benchmarking for Single-Qubit Trapped-Ion Transport Gates". Semester Thesis. ETH Zürich, 2016 (cit. on pp. 50, 51, 59).

[97] L. E. de Clercq et al. "Parallel Transport Quantum Logic Gates with Trapped Ions". In: *Physical Review Letters* 116.8 (Feb. 2016), p. 080502. DOI: 10.1103/PhysRevLett.116.080502 (cit. on p. 58).

[98] D. Leibfried et al. "Transport Quantum Logic Gates for Trapped Ions". In: *Physical Review A* 76.3 (Sept. 2007), p. 032324. DOI: 10.1103/PhysRevA.76.032324 (cit. on p. 58).

[99] L. E. de Clercq et al. "Estimation of a General Time-Dependent Hamiltonian for a Single Qubit". In: *Nature Communications* 7 (Apr. 2016), p. 11218. DOI: 10.1038/ncomms11218 (cit. on p. 59).

[100] R. Oswald. "Velocity Control of Trapped Ions for Transport Quantum Logic Gates". Masters Thesis. ETH Zürich, 2015 (cit. on pp. 59, 61, 62).

[101] J. P. Home et al. "Normal Modes of Trapped Ions in the Presence of Anharmonic Trap Potentials". In: *New Journal of Physics* 13.7 (July 2011), p. 073026. DOI: 10.1088/1367-2630/13/7/073026 (cit. on pp. 61, 66, 71, 77).

[102] M. A. Rowe et al. "Transport of Quantum States and Separation of Ions in a Dual RF Ion Trap". In: *Quantum Info. Comput.* 2.4 (June 2002), pp. 257–271 (cit. on p. 62).

[103] M. D. Barrett et al. "Deterministic Quantum Teleportation of Atomic Qubits". In: *Nature* 429.6993 (June 2004), pp. 737–739. DOI: 10.1038/nature02608 (cit. on p. 62).

[104] J. P. Home and A. M. Steane. "Electrode Configurations for Fast Separation of Trapped Ions". In: *Quantum Information and Computation* 6.4 (July 2006), pp. 289–325 (cit. on p. 62).

[105] H. Kaufmann et al. "Dynamics and Control of Fast Ion Crystal Splitting in Segmented Paul Traps". In: *New Journal of Physics* 16.7 (2014), p. 073012. DOI: 10.1088/1367-2630/16/7/073012 (cit. on pp. 63, 64, 66, 67, 69).

[106] F. Lancellotti. "Title undecided". PhD thesis. ETH Zurich, 2022 (cit. on pp. 64, 66, 69).

[107] K. Singer et al. "Colloquium: Trapped Ions as Quantum Bits – Essential Numerical Tools". In: *Reviews of Modern Physics* 82.3 (Sept. 2010), pp. 2609–2632. DOI: 10.1103/RevModPhys.82.2609. arXiv: 0912.0196 (cit. on p. 66).

[108] J. M. Amini et al. "Toward Scalable Ion Traps for Quantum Information Processing". In: *New Journal of Physics* 12.3 (2010), p. 033031. DOI: 10.1088/1367-2630/12/3/033031 (cit. on pp. 66, 78).

[109] R. Bowler et al. "Arbitrary Waveform Generator for Quantum Information Processing with Trapped Ions". In: *arXiv:1301.2543* (Jan. 2013). arXiv: 1301.2543 (cit. on p. 69).

[110] T. Ruster et al. "Experimental Realization of Fast Ion Separation in Segmented Paul Traps". In: *Physical Review A* 90.3 (Sept. 2014), p. 033410. DOI: 10.1103/PhysRevA.90.033410 (cit. on p. 69).

[111] N. F. Ramsey. *Spectroscopy with coherent radiation: selected papers of norman ramsey with commentary.* World Scientific and Singapore, 1998 (cit. on p. 72).

[112] J. D. Jost. "Entangled Mechanical Oscillators". PhD thesis. University of Colorado, 2010 (cit. on p. 77).

[113] Q. A. Turchette et al. "Decoherence and Decay of Motional Quantum States of a Trapped Atom Coupled to Engineered Reservoirs". In: *Physical Review A* 62.5 (Oct. 2000), p. 053807. DOI: 10.1103/PhysRevA.62.053807 (cit. on p. 81).

[114] C. F. Roos et al. "Nonlinear Coupling of Continuous Variables at the Single Quantum Level". In: *Physical Review A* 77.4 (Apr. 2008), p. 040302. DOI: 10.1103/PhysRevA.77.040302 (cit. on p. 81).

[115] P. Colciaghi. "Towards the realization of transport entangling gates with trapped ions". Masters Thesis. ETH Zurich, 2018 (cit. on p. 82).

[116] A. Barenco et al. "Elementary gates for quantum computation". In: *Physical Review A* 52.5 (1st Nov. 1995), pp. 3457–3467. DOI: 10.1103/PhysRevA.52.3457 (cit. on p. 82).

[117] A. Bermudez et al. "Assessing the Progress of Trapped-Ion Processors towards Fault-Tolerant Quantum Computation". In: *Phys. Rev. X* 7.4 (2017). DOI: https://doi.org/10.1103/PhysRevX.7.041061 (cit. on pp. 82, 104).

[118] J. I. Cirac and P. Zoller. "Quantum Computations with Cold Trapped Ions". In: *Physical Review Letters* 74.20 (May 1995), pp. 4091–4094. DOI: 10.1103/PhysRevLett.74.4091 (cit. on p. 82).

[119] A. Sørensen and K. Mølmer. "Quantum Computation with Ions in Thermal Motion". In: *Physical Review Letters* 82.9 (Mar. 1999), pp. 1971–1974. DOI: 10.1103/PhysRevLett.82.1971 (cit. on pp. 82, 84).

[120] D. Jonathan, M. B. Plenio and P. L. Knight. "Fast quantum gates for cold trapped ions". In: *Physical Review A* 62.4 (13th Sept. 2000), p. 042307. DOI: 10.1103/PhysRevA.62.042307 (cit. on p. 82).

[121] M. Šašura and A. M. Steane. "Fast quantum logic by selective displacement of hot trapped ions". In: *Physical Review A* 67.6 (30th June 2003), p. 062318. DOI: 10.1103/PhysRevA.67.062318 (cit. on p. 82).

[122] D. Leibfried et al. "Experimental Demonstration of a Robust, High-Fidelity Geometric Two Ion-Qubit Phase Gate". In: *Nature* 422.6930 (Mar. 2003), pp. 412–415. DOI: 10.1038/nature01492 (cit. on pp. 82, 84).

[123] A. Bermudez et al. "Robust Trapped-Ion Quantum Logic Gates by Continuous Dynamical Decoupling". In: *Physical Review A* 85.4 (Apr. 2012), p. 040302. DOI: 10.1103/PhysRevA.85.040302 (cit. on p. 82).

[124] F. Schmidt-Kaler et al. "Realization of the Cirac–Zoller Controlled-NOT Quantum Gate". In: *Nature* 422.6930 (Mar. 2003), pp. 408–411. DOI: 10.1038/nature01494 (cit. on p. 82).

[125] K. Mølmer and A. Sørensen. "Multiparticle Entanglement of Hot Trapped Ions". In: *Physical Review Letters* 82.9 (Mar. 1999), pp. 1835–1838. DOI: `10.1103/PhysRevLett.82.1835` (cit. on pp. 82, 84, 86).

[126] G. J. Milburn, S. Schneider and D. F. V. James. "Ion Trap Quantum Computing with Warm Ions". In: *Fortschritte der Physik* 48.9 (Sept. 2000), pp. 801–810. DOI: `10.1002/1521-3978(200009)48:9/11<801::AID-PROP801>3.0.CO;2-1` (cit. on p. 82).

[127] D. M. Greenberger, M. A. Horne and A. Zeilinger. "Going Beyond Bell's Theorem". In: *Bell's Theorem, Quantum Theory and Conceptions of the Universe*. Fundamental Theories of Physics. Springer, Dordrecht, 1989, pp. 69–72. DOI: `10.1007/978-94-017-0849-4_10` (cit. on p. 83).

[128] P. J. Lee et al. "Phase Control of Trapped Ion Quantum Gates". In: *Journal of Optics B: Quantum and Semiclassical Optics* 7.10 (2005), S371. DOI: `10.1088/1464-4266/7/10/025` (cit. on pp. 85, 98, 100).

[129] C. A. Sackett et al. "Experimental Entanglement of Four Particles". In: *Nature* 404.6775 (Mar. 2000), pp. 256–259. DOI: `10.1038/35005011` (cit. on pp. 86, 87).

[130] T. Monz et al. "14-Qubit Entanglement: Creation and Coherence". In: *Physical Review Letters* 106.13 (Mar. 2011), p. 130506. DOI: `10.1103/PhysRevLett.106.130506` (cit. on p. 87).

[131] C. J. Ballance. "High-Fidelity Quantum Logic in Ca⁺". PhD thesis. Oxford University, 2014 (cit. on pp. 88, 91).

[132] J. P. Gaebler et al. "High-Fidelity Universal Gate Set for Beryllium Ion Qubits". In: *Physical Review Letters* 117.6 (Aug. 2016), p. 060505. DOI: `10.1103/PhysRevLett.117.060505` (cit. on pp. 92, 93, 98).

[133] R. Ozeri et al. "Hyperfine Coherence in the Presence of Spontaneous Photon Scattering". In: *Physical Review Letters* 95.3 (14th July 2005), p. 030403. DOI: `10.1103/PhysRevLett.95.030403` (cit. on p. 91).

[134] B. M. Terhal. "Quantum Error Correction for Quantum Memories". In: *Reviews of Modern Physics* 87.2 (Apr. 2015), pp. 307–346. DOI: `10.1103/RevModPhys.87.307` (cit. on p. 95).

[135] A. M. Steane. "Error Correcting Codes in Quantum Theory". In: *Physical Review Letters* 77.5 (July 1996), pp. 793–797. DOI: `10.1103/PhysRevLett.77.793` (cit. on p. 95).

[136] A. R. Calderbank and P. W. Shor. "Good Quantum Error-Correcting Codes Exist". In: *Physical Review A* 54.2 (Aug. 1996), pp. 1098–1105. DOI: `10.1103/PhysRevA.54.1098` (cit. on p. 95).

[137] D. G. Cory et al. "Experimental Quantum Error Correction". In: *Physical Review Letters* 81.10 (Sept. 1998), pp. 2152–2155. DOI: `10.1103/PhysRevLett.81.2152` (cit. on p. 96).

[138] J. Chiaverini et al. "Realization of Quantum Error Correction". In: *Nature* 432.7017 (Dec. 2004), pp. 602–605. DOI: `10.1038/nature03074` (cit. on p. 96).

[139] M. D. Reed et al. "Realization of Three-Qubit Quantum Error Correction with Superconducting Circuits". In: *Nature* 482.7385 (Feb. 2012), pp. 382–385. DOI: `10.1038/nature10786` (cit. on p. 96).

[140]   D. Gottesman. "Theory of Fault-Tolerant Quantum Computation". In: *Physical Review A* 57.1 (Jan. 1998), pp. 127–137. DOI: 10.1103/PhysRevA.57.127 (cit. on p. 96).

[141]   A. M. Steane. "Efficient Fault-Tolerant Quantum Computing". In: *Nature* 399.6732 (May 1999), pp. 124–126. DOI: 10.1038/20127 (cit. on p. 96).

[142]   J. T. Barreiro et al. "An Open-System Quantum Simulator with Trapped Ions". In: *Nature* 470.7335 (Feb. 2011), pp. 486–491. DOI: 10.1038/nature09801 (cit. on pp. 96, 97, 101).

[143]   P. Schindler et al. "Experimental Repetitive Quantum Error Correction". In: *Science* 332.6033 (May 2011), pp. 1059–1061. DOI: 10.1126/science.1203329 (cit. on p. 96).

[144]   D. Nigg et al. "Quantum Computations on a Topologically Encoded Qubit". In: *Science* 345.6194 (July 2014), pp. 302–305. DOI: 10.1126/science.1253742 (cit. on p. 96).

[145]   W. Pfaff et al. "Demonstration of Entanglement-by-Measurement of Solid-State Qubits". In: *Nature Physics* 9.1 (Jan. 2013), pp. 29–33. DOI: 10.1038/nphys2444 (cit. on p. 96).

[146]   D. Ristè et al. "Deterministic Entanglement of Superconducting Qubits by Parity Measurement and Feedback". In: *Nature* 502.7471 (Oct. 2013), pp. 350–354. DOI: 10.1038/nature12513 (cit. on p. 96).

[147]   J. Cramer et al. "Repeated Quantum Error Correction on a Continuously Encoded Qubit by Real-Time Feedback". In: *Nature Communications* 7 (May 2016), p. 11526. DOI: 10.1038/ncomms11526 (cit. on p. 96).

[148]   C. K. Andersen et al. "Entanglement stabilization using ancilla-based parity detection and real-time feedback in superconducting circuits". In: *npj Quantum Information* 5.1 (Dec. 2019), p. 69. DOI: 10.1038/s41534-019-0185-4 (cit. on p. 96).

[149]   T. Monz et al. "Realization of a Scalable Shor Algorithm". In: *Science* 351.6277 (Mar. 2016), pp. 1068–1070. DOI: 10.1126/science.aad9480 (cit. on p. 96).

[150]   M. Müller et al. "Simulating Open Quantum Systems: From Many-Body Interactions to Stabilizer Pumping". In: *New Journal of Physics* 13.8 (2011), p. 085007. DOI: 10.1088/1367-2630/13/8/085007 (cit. on p. 97).

[151]   T. C. Ralph et al. "Quantum Nondemolition Measurements for Quantum Information". In: *Physical Review A* 73.1 (Jan. 2006), p. 012113. DOI: 10.1103/PhysRevA.73.012113 (cit. on p. 101).

[152]   D. Kielpinski et al. "A Decoherence-Free Quantum Memory Using Trapped Ions". In: *Science* 291.5506 (Sept. 2001), pp. 1013–1015. DOI: 10.1126/science.1057357 (cit. on p. 104).

[153]   T. Monz et al. "Realization of Universal Ion-Trap Quantum Computation with Decoherence-Free Qubits". In: *Physical Review Letters* 103.20 (Nov. 2009), p. 200503. DOI: 10.1103/PhysRevLett.103.200503 (cit. on p. 104).

[154]   A. J. Landahl and C. Ryan-Anderson. "Quantum computing by color-code lattice surgery". In: *arXiv:1407.5103 [quant-ph]* (18th July 2014). arXiv: 1407.5103 (cit. on p. 112).

[155]   H. Bombin and M. A. Martin-Delgado. "Topological Quantum Distillation". In: *Physical Review Letters* 97.18 (Oct. 2006), p. 180501. DOI: 10.1103/PhysRevLett.97.180501 (cit. on p. 112).

[156] R. Jozsa. "An introduction to measurement based quantum computation". In: *arXiv:quant-ph/0508124* (20th Sept. 2005). arXiv: `quant-ph/0508124` (cit. on p. 114).

[157] R. Raussendorf, D. E. Browne and H. J. Briegel. "Measurement-based quantum computation on cluster states". In: *Physical Review A* 68.2 (25th Aug. 2003), p. 022312. DOI: `10.1103/PhysRevA.68.022312` (cit. on p. 114).

[158] R. Raussendorf and H. J. Briegel. "A One-Way Quantum Computer". In: *Physical Review Letters* 86.22 (May 2001), pp. 5188–5191. DOI: `10.1103/PhysRevLett.86.5188` (cit. on pp. 114, 115).

[159] D. Gottesman and I. L. Chuang. "Demonstrating the Viability of Universal Quantum Computation Using Teleportation and Single-Qubit Operations". In: *Nature* 402.6760 (Nov. 1999), pp. 390–393. DOI: `10.1038/46503` (cit. on p. 114).

[160] M. A. Nielsen. "Quantum computation by measurement and quantum memory". In: *Physics Letters A* 308.2 (24th Feb. 2003), pp. 96–100. DOI: `10.1016/S0375-9601(02)01803-0` (cit. on p. 114).

[161] C. H. Bennett et al. "Teleporting an unknown quantum state via dual classical and Einstein-Podolsky-Rosen channels". In: *Physical Review Letters* 70.13 (29th Mar. 1993), pp. 1895–1899. DOI: `10.1103/PhysRevLett.70.1895` (cit. on p. 114).

[162] D. E. Browne and H. J. Briegel. "One-way Quantum Computation - a tutorial introduction". In: *arXiv:quant-ph/0603226* (3rd Oct. 2006). arXiv: `quant-ph/0603226` (cit. on p. 114).

[163] M. Van den Nest et al. "Universal Resources for Measurement-Based Quantum Computation". In: *Physical Review Letters* 97.15 (13th Oct. 2006), p. 150504. DOI: `10.1103/PhysRevLett.97.150504` (cit. on p. 115).

[164] R. Raussendorf, J. Harrington and K. Goyal. "A fault-tolerant one-way quantum computer". In: *Annals of Physics* 321.9 (1st Sept. 2006), pp. 2242–2270. DOI: `10.1016/j.aop.2006.01.012` (cit. on p. 115).

[165] C. Greganti et al. "Cross-verification of independent quantum devices". In: *arXiv:1905.09790 [quant-ph]* (8th Jan. 2020). arXiv: `1905.09790` (cit. on p. 115).

[166] P. Walther et al. "Experimental one-way quantum computing". In: *Nature* 434.7030 (Mar. 2005), pp. 169–176. DOI: `10.1038/nature03347` (cit. on p. 115).

[167] R. Prevedel et al. "High-speed linear optics quantum computing using active feedforward". In: *Nature* 445.7123 (Jan. 2007), pp. 65–69. DOI: `10.1038/nature05346` (cit. on p. 115).

[168] O. Mandel et al. "Controlled collisions for multi-particle entanglement of optically trapped atoms". In: *Nature* 425.6961 (Oct. 2003), pp. 937–940. DOI: `10.1038/nature02008` (cit. on p. 115).

[169] W. Asavanant et al. "Generation of time-domain-multiplexed two-dimensional cluster state". In: *Science* 366.6463 (18th Oct. 2019), pp. 373–376. DOI: `10.1126/science.aay2645` (cit. on p. 115).

[170] B. P. Lanyon et al. "Measurement-Based Quantum Computation with Trapped Ions". In: *Physical Review Letters* 111.21 (Nov. 2013), p. 210501. DOI: `10.1103/PhysRevLett.111.210501` (cit. on p. 115).

[171] M. Zwerger, H. J. Briegel and W. Dür. "Hybrid architecture for encoded measurement-based quantum computation". In: *Scientific Reports* 4.1 (May 2015), p. 5364. DOI: `10.1038/srep05364` (cit. on p. 115).

[172]   X. Zhou, D. W. Leung and I. L. Chuang. "Methodology for quantum logic gate construction". In: *Physical Review A* 62.5 (18th Oct. 2000), p. 052316. DOI: `10.1103/PhysRevA.62.052316` (cit. on p. 116).

[173]   D. Hanneke et al. "Realization of a programmable two-qubit quantum processor". In: *Nature Physics* 6.1 (Jan. 2010), pp. 13–16. DOI: `10.1038/nphys1453` (cit. on p. 123).

[174]   C. W. Bauer et al. "A quantum algorithm for high energy physics simulations". In: *arXiv:1904.03196 [hep-ph, physics:quant-ph]* (24th Dec. 2019). arXiv: `1904.03196` (cit. on p. 124).

[175]   R. Somma et al. "Simulating physical phenomena by quantum networks". In: *Physical Review A* 65.4 (9th Apr. 2002), p. 042323. DOI: `10.1103/PhysRevA.65.042323` (cit. on p. 124).